

Coke Formation on Metal Surfaces

Coke Formation on Metal Surfaces

Lyle F. Albright, EDITOR
Purdue University

R. T. K. Baker, EDITOR
*Exxon Research and
Engineering Company*

Based on a symposium jointly sponsored
by the ACS Divisions of Petroleum and
Industrial and Engineering Chemistry
at the 182nd Meeting
of the American Chemical Society
New York, New York,
August 27, 1981.

A C S S Y M P O S I U M S E R I E S **202**

AMERICAN CHEMICAL SOCIETY
WASHINGTON, D. C. 1982



Library of Congress Cataloging in Publication Data

Coke formation on metal surfaces.

(ACS symposium series, ISSN 0097-6156; 202)

"Based on a symposium jointly sponsored by the ACS Divisions of Petroleum and Industrial and Engineering Chemistry at the 182nd Meeting of the American Chemical Society, New York, New York, August 23-28, 1981."

Includes bibliographies and index.

1. Metals—Surfaces—Congresses. 2. Metals at high temperatures—Congresses. 3. Coke—Congresses.

I. Albright, Lyle Frederick, 1921- . II. Baker, R. T. K., 1938- . III. American Chemical Society Division of Petroleum Chemistry. IV. American Chemical Society. Division of Industrial and Engineering Chemistry. V. American Chemical Society. National Meeting (182:1981:New York, N.Y.) VI. Series.

TA459.C545 1982 665.5'3 82-16335
ISBN 0-8412-0745-3 ACSMC8 202 1-318
1982

Copyright © 1982

American Chemical Society

All Rights Reserved. The appearance of the code at the bottom of the first page of each article in this volume indicates the copyright owner's consent that reprographic copies of the article may be made for personal or internal use or for the personal or internal use of specific clients. This consent is given on the condition, however, that the copier pay the stated per copy fee through the Copyright Clearance Center, Inc. for copying beyond that permitted by Sections 107 or 108 of the U.S. Copyright Law. This consent does not extend to copying or transmission by any means—graphic or electronic—for any other purpose, such as for general distribution, for advertising or promotional purposes, for creating new collective work, for resale, or for information storage and retrieval systems. The copying fee for each chapter is indicated in the code at the bottom of the first page of the chapter.

The citation of trade names and/or names of manufacturers in this publication is not to be construed as an endorsement or as approval by ACS of the commercial products or services referenced herein; nor should the mere reference herein to any drawing, specification, chemical process, or other data be regarded as a license or as a conveyance of any right or permission, to the holder, reader, or any other person or corporation, to manufacture, reproduce, use, or sell any patented invention or copyrighted work that may in any way be related thereto.

PRINTED IN THE UNITED STATES OF AMERICA

**American Chemical
Society Library**

1155 16th St. N. W.

In Coke Formation on Metal Surfaces; Albright, Lyle, et al.;
ACS Symposium Series; American Chemical Society: Washington, DC, 1983.

Washington, D.C. 20036

ACS Symposium Series

M. Joan Comstock, *Series Editor*

Advisory Board

David L. Allara

Robert Baker

Donald D. Dollberg

Robert E. Feeney

Brian M. Harney

W. Jeffrey Howe

James D. Idol, Jr.

Herbert D. Kaesz

Marvin Margoshes

Robert Ory

Leon Petrakis

Theodore Provder

Charles N. Satterfield

Dennis Schuetzle

Davis L. Temple, Jr.

Gunter Zweig

FOREWORD

The ACS SYMPOSIUM SERIES was founded in 1974 to provide a medium for publishing symposia quickly in book form. The format of the Series parallels that of the continuing ADVANCES IN CHEMISTRY SERIES except that in order to save time the papers are not typeset but are reproduced as they are submitted by the authors in camera-ready form. Papers are reviewed under the supervision of the Editors with the assistance of the Series Advisory Board and are selected to maintain the integrity of the symposia; however, verbatim reproductions of previously published papers are not accepted. Both reviews and reports of research are acceptable since symposia may embrace both types of presentation.

PREFACE

COKE FORMATION IS AN UNDESIRABLE SIDE EFFECT of many chemical operations because it leads to costly decoking steps, reduced efficiency of operation, and increased rates of metal corrosion and erosion. There is, therefore, a tremendous incentive to minimize or at least better control coke deposition in numerous commercial units.

A symposium about coke formation on metal surfaces has been long overdue, so we were delighted when the Divisions of Petroleum Chemistry and of Industrial and Engineering Chemistry of the American Chemical Society agreed to sponsor such a symposium. Our objective was to gather key experts from around the world to promote a valuable interchange of ideas. In addition, we hoped that the results could be published and made available to individuals who could not attend the symposium.

Ten of the papers included in this book were presented at the original symposium. In each case, the paper has been reviewed and, in several cases, been modified to include 1982 findings. Five papers were added to describe coking results that are considered highly important. Consequently, this book discusses recent investigations and the latest thinking on coke formation due to thermal and catalytic processes on metal surfaces.

In conclusion, we want to thank all who made possible the symposium and this subsequent publication: the Divisions of Petroleum Chemistry and of Industrial and Engineering Chemistry for their sponsorship; the authors without whom it could never exist; the reviewers; and finally those who worked behind the scenes. In this latter category are our two secretaries, Mrs. Phyllis Beck (West Lafayette) and Mrs. M. Evan (Linden) who as a result, were burdened with considerably more than their normal duties require.

LYLE F. ALBRIGHT
Purdue University
School of Chemical Engineering
West Lafayette, IN 47907

R. T. K. BAKER
Exxon Research and Engineering Company
Corporate Research Science Laboratories
Linden, NJ 07036

July 1982

Filamentous Carbon Formation over Iron Surfaces

R. T. K. BAKER and D. J. C. YATES

Exxon Research and Engineering Company, Corporate Research Science Laboratories,
Linden, NJ 07036

J. A. DUMESIC

University of Wisconsin, Chemical Engineering Department, Madison, WI 53706

It is well known that the surface state of a metal can have a profound effect on its ability to catalyze the formation of carbon during a hydrocarbon conversion process. In this work we have examined the effect of oxygen and steam pretreatments of iron surfaces on their ability to catalyze carbon filament formation during reaction of such surfaces with hydrocarbons. Pretreatment of iron in steam at 700°C resulted in the conversion of the metal to FeO, and this oxide was found to be a tremendously active catalyst for carbon filament growth when reacted with acetylene or ethane at 700°C. On the other hand, the activity of Fe₂O₃, formed by reaction of iron with oxygen, was about the same as that of the metal when treated with these hydrocarbons. From this study it is concluded that the key to the high FeO activity is that it is a precursor for a high surface area Fe catalyst formed in situ. It was also found that Fe₃C is not an active catalyst for carbon filament formation.

The accumulation of carbon on metal surfaces when heated in the presence of carbon containing gases is a serious problem encountered in a number of commercial processes. Although carbon appears to deposit on most surfaces there are some materials which are more vulnerable than others since they contain constituents which catalyze carbon formation. The highest catalytic activity is exhibited by the ferromagnetic metals and in particular, iron. Furthermore it is well known that the surface state of such metals can have a dramatic effect on their ability to catalyze the formation of carbon.

0097-6156/82/0202-0001\$06.50/0

© 1982 American Chemical Society

Carbon deposits normally have a complex structure containing several different growth forms, which can be grouped under three headings: amorphous, filamentous, and graphitic platelets (1, 2, 3).

Of these three forms the least understood is amorphous carbon. Available evidence suggests that condensation and polymerization reactions play a major role in amorphous carbon formation. Although some hydrogen is removed during condensation, a significant amount remains in the deposit, but as the temperature is raised, dehydrogenation reactions reduce the hydrogen content to <1% (4). Although there does not appear to be any general method of preventing amorphous carbon accumulation on a surface, there is little doubt that such material would be readily removed by treatment in air at 500°C.

Filamentous carbon is produced by the catalytic decomposition of carbon containing gases on small metal particles. Figure 1 is the typical appearance of carbon filaments illustrating the catalyst particle located at the tip of the filament, which during the reaction was carried away from the support surface by the growth process. Although it is not difficult to accept that such growths could occur on a supported metal catalyst system, where metal crystallites (0.5 to 5.0 nm diameter) are dispersed on non-metallic oxide supports, it is hard to understand how the filaments are produced on bulk metal surfaces. This is an area which obviously requires a great deal of work and before solving the problem it will first be necessary to establish the criteria controlling the nucleation of small particles on metal surfaces.

A mechanism has been postulated to account for the growth of filamentous carbon produced from metal catalyzed decomposition of acetylene (5, 6). This mechanism, which is outlined in the schematic diagram, Figure 2, involves the diffusion of carbon through the catalyst particle from the hotter leading face, on which exothermic decomposition of the hydrocarbon occurs, to the cooler trailing faces, at which carbon is deposited from solution. Excess carbon buildup occurs at the exposed particle face and is transported by surface diffusion around the peripheral surfaces of the particle to form an outer skin on the filament. If filament skin formation is slow because surface diffusion of carbon is slow, the available catalyst surface for sorption and decomposition of hydrocarbon decreases; the temperature gradient and the carbon diffusion rate are both reduced slowing the growth rate. Eventually growth ceases when the leading face is covered by a layer of carbon, preventing further hydrocarbon decomposition. The postulate that diffusion of carbon through the particle is the rate-controlling step in the process is supported by measurements of the activation energy for filament growth, which correlate with those for diffusion of carbon through the corresponding metals, Table 1. A major criticism of this mechanism being accepted as a general explanation for the filament growth process is that it fails to account for filaments produced by pyrolysis of methane, an endothermic decomposition (7).

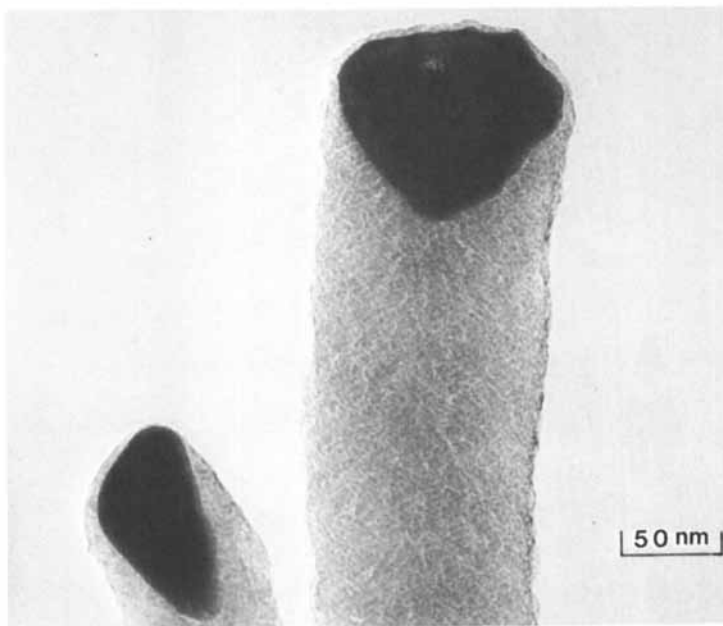


Figure 1. Transmission electron micrograph of filaments showing the catalyst particles at their heads.

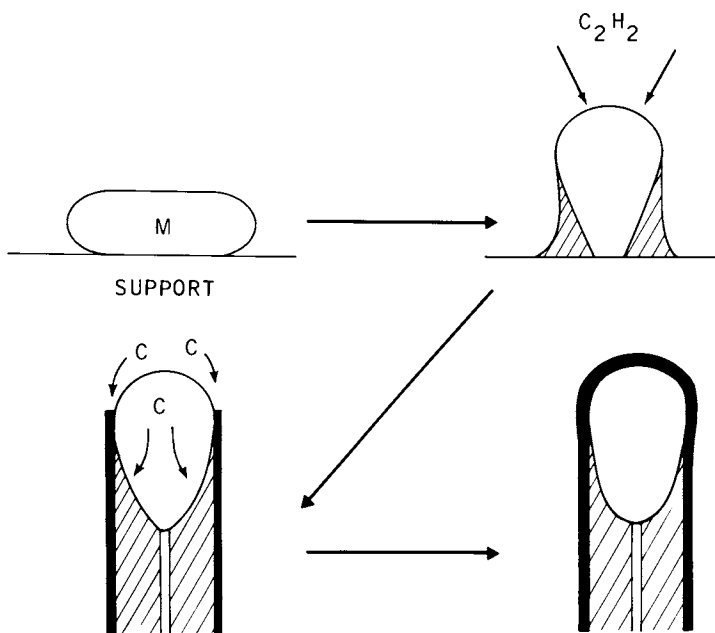


Figure 2. Schematic of the proposed mechanism of carbon filament formation.

Table I
Comparison of Measured Activation Energies for
Filament Growth with Those for Carbon
Diffusion in the Corresponding Metal Catalysts

<u>CATALYST</u>	<u>ACTIVATION ENERGY FOR</u>	
	<u>CATALYZED FILAMENT</u>	<u>DIFFUSION</u>
	<u>GROWTH</u>	<u>OF CARBON</u>
	<u>(KCAL MOLE⁻¹)</u>	<u>(KCAL MOLE⁻¹)</u>
NICKEL	34.7 (5)	33.0-34.8 (15)
α-IRON	16.1 (6)	10.5-16.5 (16)
NICKEL-IRON	33.6 (8)	34.0 (17)
COBALT	33.0-33.3 (6)	34.7 (18)
VANADIUM	27.6 (21)	27.8 (19)
MOLYBDENUM	38.8 (21)	41.0 (20)
CHROMIUM	27.1 (6)	26.5 (22)

Other mechanisms have been proposed for filamentous carbon growth, and other filament structures have been observed. One of the most common variations in the basic filament type is the spiral conformation, examples of which are shown in Figure 3. Boehm (8) has put forward an interesting approach to account for growth of spiral filaments produced during the iron-catalyzed disproportionation of carbon monoxide, which is shown schematically in Figure 4. He suggests that spirals occur when the diffusion path length in the catalyst particle varies; this is probably true, but spirals will also form if the variation of diffusion path length is not symmetrical about the axis of symmetry of the particle. Two situations where this condition would arise are (a) if the catalyst particle is not symmetrical, or (b) if the particle is symmetrical but the flux of carbon atoms is between non-parallel faces. Then, provided the particle maintains its shape, the pitch will be constant along its length.

A further modification in the growth process is encountered with filaments which are formed by an extrusion mode. In this case, filaments do not grow from a free particle but from a particle which remains attached to the support surface. This situation probably arises from a strong interaction between the metal particle and the support. A mechanism was proposed by Baker and Waite (9) for the extrusion filaments produced from the Fe-Pt/C₂H₂ system depicted schematically in Figure 5. In this system, Pt was believed to segregate to the particle surface and form an apron around a core of Fe. It was assumed that, under the prevailing reaction conditions, decomposition of acetylene occurred predominantly on the Pt-rich region of the particle. They suggested that transport of carbon through the catalyst took place by a consecutive process: rapid diffusion through Pt followed by slower diffusion through the Fe component to be precipitated on the upper surface of the particle as a filament.

In a recent study, Baker and Chludzinski (10) used the basis of this proposed mechanism to develop methods of inhibiting the growth of filamentous carbon. The approach was aimed at the introduction of additives into the metal catalyst particles, which had the potential of reducing the rate of the critical steps involved in the growth process i.e., carbon solubility or carbon diffusion through the catalyst particle. Among several additives investigated, silica was the most effective as it reduced the rates of both of these processes.

The graphite platelet deposit is formed indirectly, at the expense of the other two deposit forms and also requires the participation of a metal catalyst. It has been found that if the temperature of a metal foil, coated with carbon deposit, is raised to about 1000°C, a significant fraction of the carbon is taken into solution by the metal. On subsequent cooling this carbon is precipitated as highly crystalline graphite, underlying excess amorphous and filamentous material remaining on the surface. This platelet deposit is the most oxidation resistant of the three

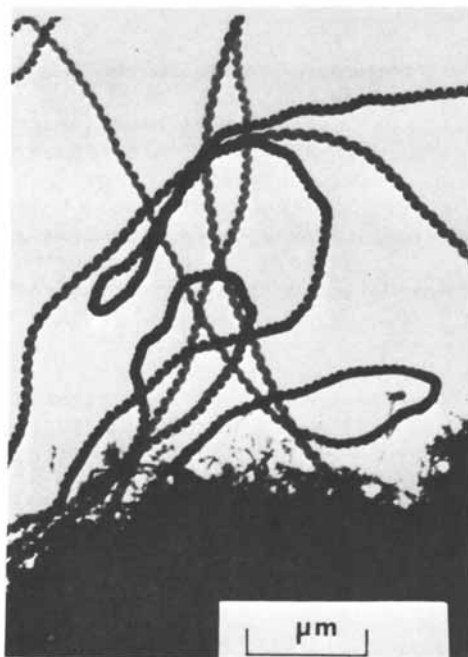


Figure 3. Spiral filaments produced from the cobalt-acetylene system.

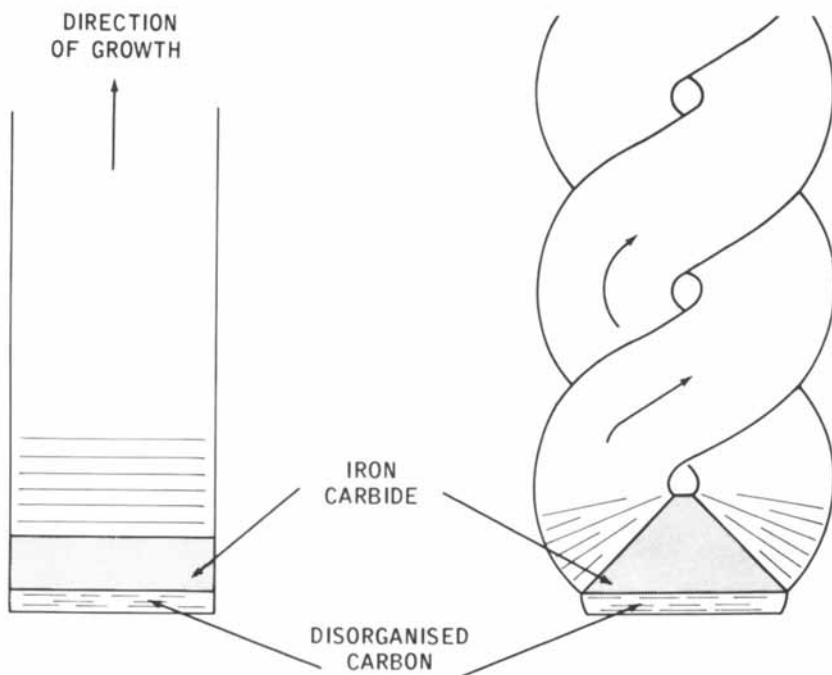


Figure 4. Schematic of growth mechanism of filamentous carbon on iron carbide. Key: left, on rectangular carbide particle; and right, on carbide particle with two active faces at oblique angles. (Reproduced, with permission, from Ref. 8.)

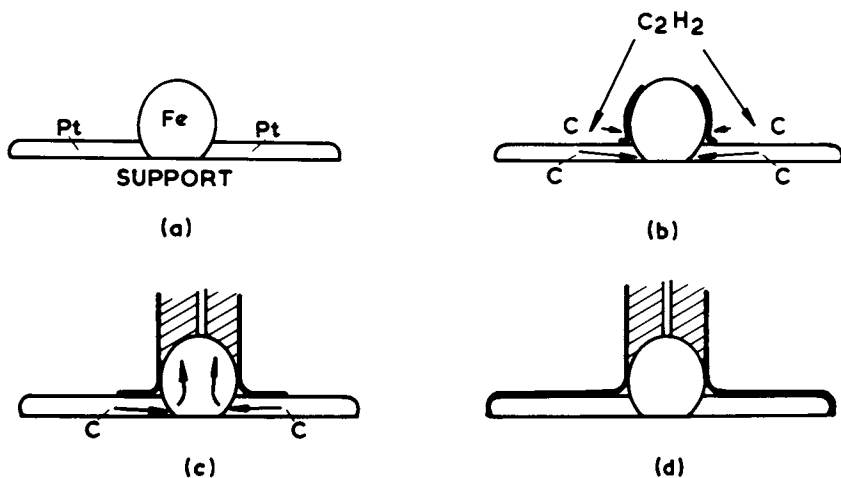


Figure 5. Stages in the growth of filaments via the extrusion mode from Pt-Fe/ C_2H_2 . (Reproduced, with permission, from Ref. 9. Copyright 1975, *Journal of Catalysis*.)

forms of carbon described here and it is unlikely that it would be all removed during a commercial decoking operation. If, however, oxygen can gain access to the graphite/metal interface, then the latter may function as a catalyst for carbon gasification and enhance carbon removal.

Figure 6 is a hypothetical plot showing the relative rates of formation of the three types of carbon as a function of reaction temperature and provides an indication of the typical composition of the carbonaceous deposit produced on a metal surface when exposed to a hydrocarbon environment at a given temperature.

One of the most useful tools available for characterizing carbonaceous deposits is controlled atmosphere electron microscopy (CAEM) (11). This technique enables one to follow the changes taking place in a solid while it is undergoing reaction with a gaseous environment at elevated temperatures. Capitalizing on the different oxidation characteristics of the three types of deposit it is possible to selectively remove each carbonaceous constituent until only a metal residue remains. In this way an overall picture can be built-up of which components were present in the original coke deposit and in some cases gain an insight into the mechanism of its formation.

In the present investigation a variety of in situ techniques, including CAEM, have been used along with the more conventional bulk approaches to compare the catalytic reactivity of Fe, FeO and Fe₂O₃ precursors for the formation of filamentous carbon from ethane and acetylene.

Experimental

Controlled Atmosphere Transmission Electron Microscopy. Details of the CAEM technique are already well documented(11), so only a brief description will be given here. The key design feature is the ability to operate at relatively high gas pressure in the specimen region while maintaining very low pressure in the rest of the microscope. This condition is attained by the incorporation of a gas-reaction stage into a JEM-120 transmission electron microscope. With this arrangement it is possible to contain gas in the vicinity of the specimen at pressures up to 400 Torr and also heat the specimen at temperatures up to 1300°C. Part of the transmission image passes through a hole in the standard viewing screen and impinges on a high sensitivity phosphor screen. The image is focussed onto a "Plumbicon" television camera located outside the vacuum chamber. The output from the camera is displayed on a TV monitor and simultaneously recorded on video tape. This facility provides immediate recall of information and the provision of making permanent records on 16 mm cine film.

The technique not only provides a qualitative picture of the changes in appearance of the specimen undergoing reaction, but in many cases it is possible to perform detailed kinetic analysis on

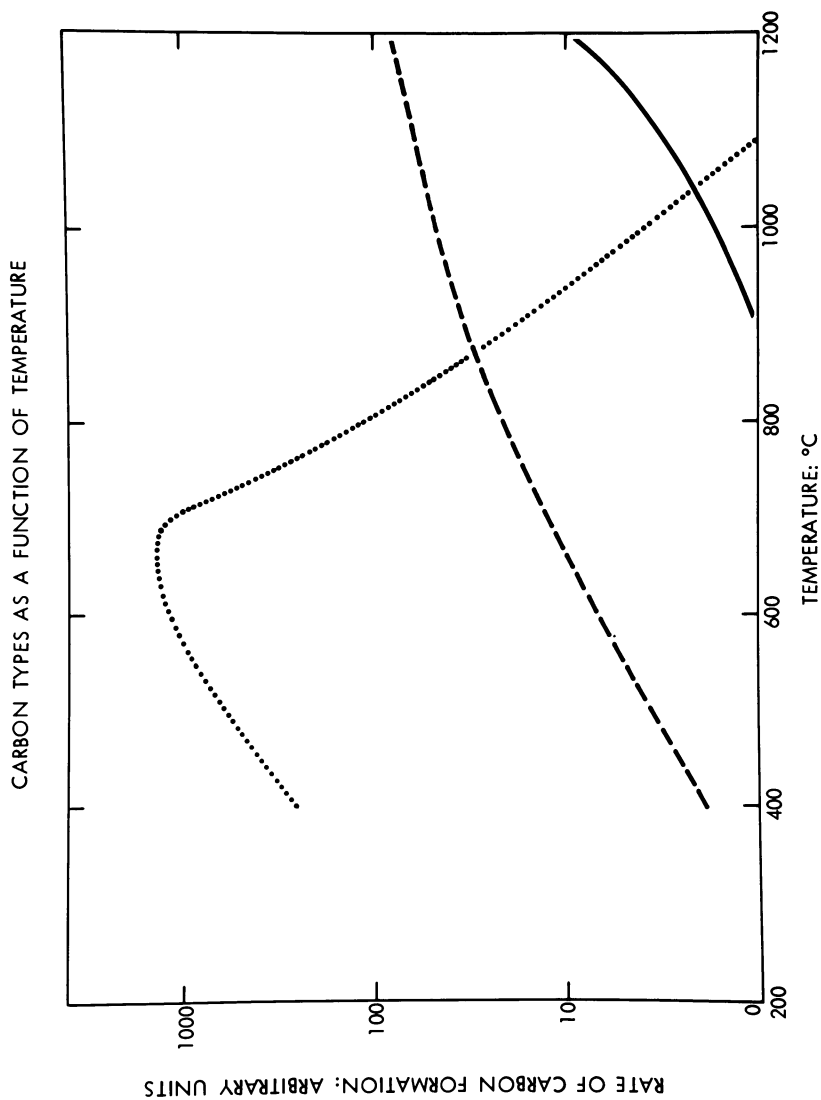


Figure 6. Hypothetical plot showing the relative rates of formation of three types of carbon deposit as a function of temperature. Key: —, graphitic; - - -, amorphous; and · · ·, filamentous.

such sequences. Unfortunately the modifications which have to be made to the microscope to accommodate the gas-reaction stage and the presence of a gas limit the resolving power of the instrument to 2.5 nm.

Single crystal graphite obtained from Ticonderoga, New York State, was used as the support medium of the reactions studied in this investigation. The crystals were released from the pyroxene mineral in which they were embedded by the method described by Hennig (12). They were first cleaved between glass slides coated with 'Britfix' polystyrene cement, and then released and washed with acetone. The crystals were mounted on glass slides with aqueous polyvinyl-pyrrolidone (PVP) adhesive. The PVP was allowed to dry and the crystals further cleaved with "Scotch" tape. Successive layers were removed until an optically transparent portion of the crystal remained affixed to the slide. Such crystals were good electron transmission specimens. The cleaved crystals were released from the slide onto a clean water surface and picked up on the microscope specimen heater ribbons and dried. Specimens were prepared according to two procedures. In the first, particles of bulk FeO derived from the macro-scale experiments and Fe_3C , which was prepared as a powder, were separately deposited onto transmission sections of single crystal graphite substrates by a dusting technique. In the second method iron was deposited as a thin film on graphite from a spectrographically pure wire, at a residual pressure of 5×10^{-6} Torr from a heated tungsten filament. The desired starting state of the iron was obtained by (a) nucleating in hydrogen at 675°C to ensure iron was in the completely reduced state, or (b) treatment in 5 Torr oxygen at 600°C for 1 hour to form Fe_2O_3 . All specimens were subsequently reacted in 2 Torr acetylene.

In a separate set of experiments carbonaceous deposits produced in the macro-scale studies were characterized by oxidizing the materials under controlled conditions in the CAEM. These samples were made by sprinkling loose fragments of the deposit onto the transmission specimens of graphite. Every effort was made to prevent the introduction of any foreign matter into the samples.

Mössbauer Spectroscopy. The Mössbauer spectroscopy cell used in this work was constructed with 131 Teflon-coated Kapton (Dupont) windows which allowed for transmission by γ -rays. Constant acceleration spectra were obtained with an Austin Science Associates, Inc. S-600 Mössbauer spectrometer equipped with an electromagnetic Doppler velocity motor. The source was 50 m Ci of ^{57}Co diffused into a palladium matrix, and it was obtained from New England Nuclear, Inc. The pulses from the proportional counter detector (Reuter Stokes) were amplified, shaped and gated using Austin Science Associates electronics. These shaped pulses were then sent to a Tracor Northern NS-900 multichannel analyzer. The MCA was interfaced directly to a PDP-11 mini-computer, greatly facilitating data storage and analysis.

The sample was a 0.0127 mm thick iron foil, of 99.99% purity, cut into disks (2.5 cm diameter). Room temperature Mössbauer spectra were taken in the initial state, after treatment at 800°C for 30 minutes in 1 atm. argon saturated with water at room temperature, and finally after reaction in 1 atm. acetylene at 750°C for 0.5 minute. Velocities were calibrated using the known Mössbauer parameters of metallic iron at 25°C, and zero velocity is with respect to this standard absorber.

Macro-Scale Experiments. For studying filamentous carbon formation on a macro-scale, the following apparatus was used. The reactor was a fused silica tube (2.54cm in diameter) which was 90cm long and externally heated via a three zone furnace, which was 61cm long overall. The center zone was 46cm long and it could be held at a set temperature to within $\pm 1^\circ\text{C}$.

The metallic iron used for these experiments was in the form of a foil, 0.013 cm thick and had a stated purity of 99.99% (Materials Research Corp., Orangeburg, NY). The foil was cut into pieces 3 cm x 0.6 cm. Before each experiment the metal foils were cleaned according to the following procedure: initial immersion in 190 proof ethyl alcohol, treatment in toluene, then ethyl alcohol again, washing in boiling distilled water, and then ethyl alcohol, and finally drying in air.

Well-defined samples of FeO were prepared by treating the iron foils with steam at temperatures above 700°C. Identification of the oxide was accomplished using Mössbauer and Auger electron spectroscopies, and x-ray diffraction techniques. Auger spectra of the foils were obtained using a Physical Electronics Model 549 combination ESCA-Auger Spectrometer. Spectra were taken using a 5KV primary beam voltage and the relative atomic concentrations of Fe and O were obtained by measuring the peaks at 703eV for Fe, and at 503eV for O. The procedure outlined in reference (13) was followed for calculating the quantitative compositions of these two elements.

As most Auger electrons have energies below 1000eV(14), their escape depth is small, usually less than 5 nm, which has the consequence that the Auger spectrum is an average composition of the surface of the sample down to this depth. Nevertheless, the spectral information is obtained mainly from the first 2 or 3 layers of the sample. Data collected in this manner showed that for depths down to 600 nm the composition was in the range FeO_{0.90} to FeO_{0.92}. A typical spectrum is shown in Figure 7, which was obtained after 25 minute argon ion sputtering, at a depth of 325 nm. Apart from a small peak due to embedded Ar atoms, the only peaks other than Fe and O, are very small peaks of Si and C. This particular sample had a composition of FeO_{0.92}.

Other portions of these samples were ground to a powder and examined by conventional x-ray diffraction techniques, which showed only peaks due to FeO. The Fe₂O₃ used in this work was initially in the form of a powder, stated purity 99.8% (Fischer

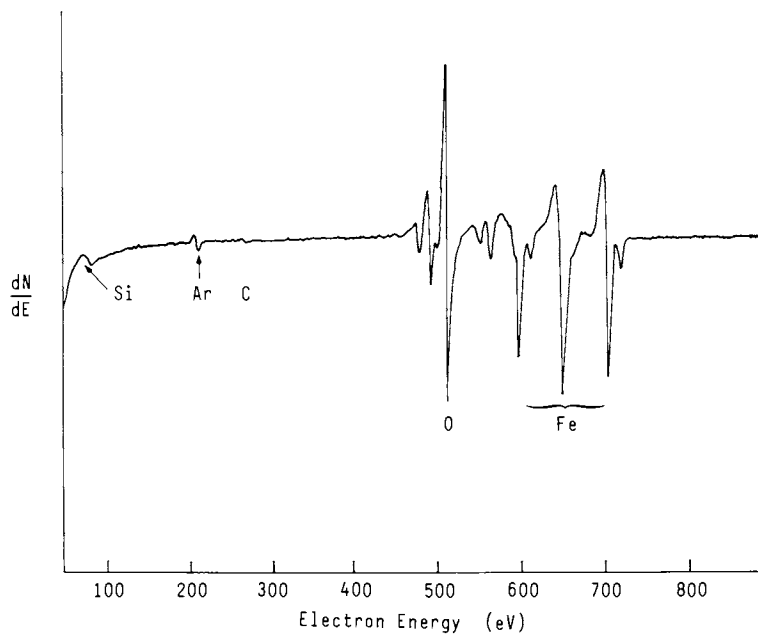


Figure 7. Auger spectrum of an FeO sample.

Scientific Co.) and was pressed into self-supporting wafers, 2.5 cm in diameter.

After the specimens were loaded into the furnace tube, they were heated in N_2 to $700^\circ C$, prior to introduction of ethane. With the tube still maintained at $700^\circ C$, ethane was admitted at a flow rate of $94 \text{ cm}^3/\text{min}$ and the reaction allowed to continue for periods of between 1.0 to 6.0 hours. The weight of deposited carbon was determined by difference of the starting and final specimen weights. In addition, the chemical state of iron in the FeO and Fe_2O_3 precursors was determined by room temperature Mössbauer spectroscopy after 2.0h of reaction in ethane at $700^\circ C$.

RESULTS

Controlled Atmosphere Transmission Electron Microscopy. In initial experiments micro-sized pieces of FeO, supported on graphite, were heated directly in 2 Torr acetylene. At $500^\circ C$ the first signs of a change in the profile of the oxide were detected and this became more rapid at $575^\circ C$ as filaments started to appear from the edges. These filaments, which ranged from 2.5 to 5 nm in width and up to 5000 nm in length, grew by rapid extrusion, with the catalyst particle remaining embedded in the FeO mass. As the temperature was gradually raised filamentous growth became more prolific and the vehemence of the reaction often resulted in rupture and fragmentation of the FeO sections into smaller particles, which resulted in the exposure of further active regions. Experiments were terminated at $800^\circ C$ as the amount of deposit was so heavy that it was impossible to discern the growth of individual filaments.

In a second series of experiments, an evaporated iron film on graphite was heated in 1.0 Torr H_2 at $675^\circ C$ for 1 hour to ensure complete reduction to the metallic state. After evacuation of the H_2 , and cooling to room temperature, acetylene was introduced at a pressure of 2.0 Torr. Upon subsequent reheating, filaments were observed at $615^\circ C$. These filaments all grew by the commonly observed mode; i.e. the catalyst particle responsible for the growth remained at the head of a filament so that during the growth process it was carried away from the support. In this case there was a significantly wider size range of filaments compared to those formed on FeO, being 2.5 to 50 nm at $650^\circ C$. Although the number and size of filaments increased as the temperature was slowly raised to $825^\circ C$, it was quite apparent that the number of filaments formed in this system was far less than that produced from the interaction of FeO with acetylene.

The remainder of the specimens were pretreated in 5 Torr O_2 at $600^\circ C$ for 1 hour, conditions where the metal is expected to form Fe_2O_3 . When these specimens were exposed to 2 Torr acetylene, filamentous carbon formation was not detected until $700^\circ C$. Even at this temperature, reaction was restricted to only

a few particles, the majority remaining quite inactive even at temperatures up to 900°C. The filaments that were formed grew by the extrusion mode, as with FeO.

Finally, particles of Fe₃C, supported on graphite were reacted in 2 Torr acetylene. In contrast to the behavior of previous systems, Fe₃C did not catalyze the formation of filamentous carbon. Indeed the particles showed very little change in appearance on heating up to 900°C.

The CAEM technique was also used to characterize the carbonaceous deposits produced in the macroscale studies. In this case fragments of the various deposits were dispersed onto transmission specimens of graphite and subsequently heated in 5 Torr O₂. During this reaction the various carbonaceous components of the deposit oxidized at different rates and numerous details became evident. At 600°C the amorphous carbon was removed leaving behind a predominantly filamentous carbon residue. These structures, which formed an interconnected network, varied in width from 5 to 35 nm, and were up to 1x10⁴nm in length. Upon further oxidation up to 750°C, virtually all the carbonaceous material had disappeared leaving a residue of metal or metal oxide particles.

Mössbauer Spectroscopy Experiments. The Mössbauer spectrum of the as received iron foil is presented in Figure 8A and shows the six-peaked pattern characteristic of the pure metal. Figure 8B is the spectrum recorded after treatment with steam at 800°C and clearly demonstrates the dramatic change in the nature of the specimen. Although the six-peak spectral pattern of metallic iron still remains, it is clear that it is now no longer the major component; the majority of iron has been converted to another phase.

The corresponding spectral component is a quadrupole-split doublet having the following Mössbauer parameters: quadrupole splitting of 0.58 mms⁻¹ and isomer shift relative to metallic iron of 0.94 mms⁻¹. These parameters are identical to those of FeO (23, 24). Measurements of the total areas under the Fe and FeO peaks showed that only 12% of the iron remained in the metallic state after the steam treatment, assuming that Fe and FeO have equal recoil-free fractions. Finally, the specimen was heated in 1 atm acetylene at 750°C and the spectrum shown in Figure 8C was recorded. Compared to the spectrum collected after treatment in steam, the acetylene treatment leads to an increase in the amount of metallic iron at the expense of FeO. This can be made more quantitative from measurements of the areas under the Mössbauer spectra peaks which shows that Fe now accounts for 23% of the Fe species present. Also apparent in Figure 8C is a small amount of the six-peak pattern characteristic of Fe₃C (25), as shown by the stick-diagram in this Figure.

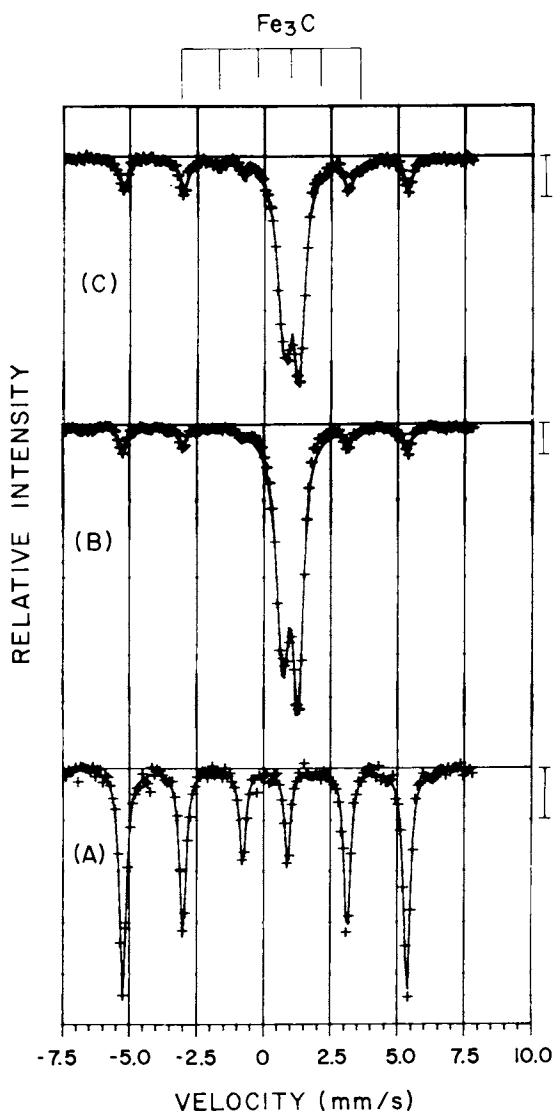


Figure 8. Room temperature Mössbauer spectra of a metallic iron foil after treatments in steam and acetylene. Key: A, metallic iron foil as received; B, from foil after treatment in steam at 800°C; and C, sample of B after treatment in acetylene at 7500°C.

Macro-Scale Experiments. Figure 9 shows a comparison of the visual changes in appearance of Fe and FeO foils accompanying the deposition of carbon from ethane at 700°C. Inspection of the deposit derived from FeO showed no traces of the original foil. Evidently during the reaction the foil had undergone complete disintegration into small particles intimately mixed with carbon. Table 2 summarizes the yields of carbon which were measured on the three types of specimens studied. It should be emphasized that the data obtained for Fe₂O₃ are probably higher than they should be as the initial surface area of the starting powder was much higher than that of either of the foil specimens. Nevertheless, it is obvious that FeO is by far the most active surface for carbon growth. Portions of all these deposits were subsequently oxidized in the CAEM where the carbon was found to be predominantly filamentous.

The Mössbauer spectroscopic analyses of the FeO and Fe₂O₃ precursors after reaction in ethane for 2 hours showed the presence of only metallic iron and iron carbide (Fe₃C) in both samples, as can be seen in Figure 10. Important is the observation that neither FeO nor Fe₂O₃ can be detected in either sample. For the FeO precursor, 14% of the iron is present as metallic iron after reaction in ethane, while less than 5% of the iron is metallic for the Fe₂O₃ precursor. (It is not known at present, however, whether the difference in the amount of metallic iron for the FeO and Fe₂O₃ precursors is significant since the amount of metallic iron for a given precursor varied from sample to sample).

Discussion

The macro-scale investigations showed that pretreatment of an iron surface with steam at 700°C induces a dramatic increase in the catalytic activity for carbon deposition from hydrocarbons. Spectroscopic analysis (Auger and Mössbauer) combined with weight increase measurements prove that treatment of iron with steam at 700°C results in the conversion of the surface of the iron to FeO. At 800°C, this process is not just limited to the uppermost surface layers but penetrates to an appreciable depth of the material after a three hour treatment. Indeed Mössbauer spectroscopy data shows that nearly all of a 0.013 cm Fe foil is transformed to FeO in this time at 800°C. It should be mentioned that the reaction of steam with iron to produce FeO may be possible at temperatures above 570°C (3). The nonstoichiometric nature of FeO has been the subject of a considerable number of papers. It is known, however, that the defects present in this material are vacant cation sites and trapped positive holes (26).

Comparison of the carbonaceous deposits produced on the macro- and micro-scale specimens shows that they are very similar in nature, the major constituent being filamentous carbon. Previous work on the formation of this type of carbon on supported

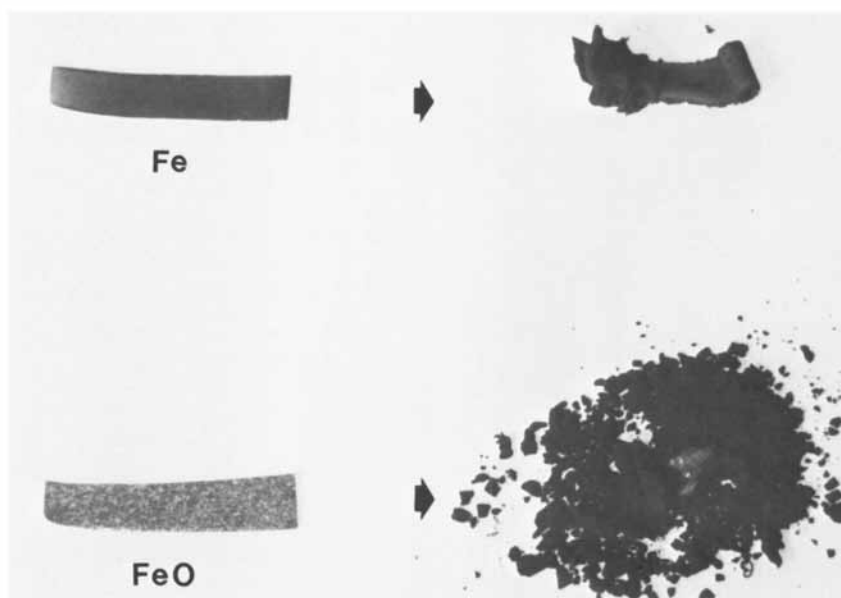


Figure 9. Changes in appearance of Fe and FeO foils accompanying the deposition of carbon from ethane at 700°C.

Table II

Carbon Formation from Catalyzed
Decomposition of Ethane at 700°C

<u>State of Iron</u>	<u>Carbon Formed 10^{-4} g/cm²/h</u>		
	<u>Average</u>	<u>High</u>	<u>Low</u>
Fe	114	148	60
FeO	1380	1870	1080
Fe ₂ O ₃ *	271	440	174

*Note: The Fe₂O₃ was used as a pressed powder, with quite a high surface area, while the Fe and FeO were foils of essentially geometric surface area. The rates are calculated on the external area of the wafers and thus the rates given above for Fe₂O₃ are probable too high on a per cm² basis.

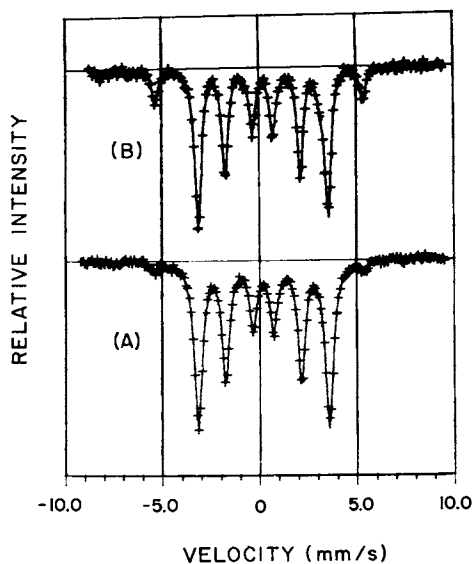


Figure 10. Room temperature Mössbauer spectra of the Fe_2O_3 and FeO precursors after reaction in ethane at 700°C for 2 hours. Key: A, Fe_2O_3 precursor; and B, FeO precursor.

metal particles thus becomes extremely relevant to the current investigation. A considerable body of information concerning this type of carbonaceous deposit has been built up over recent years (2).

In the present macro-scale experiments the filaments have been formed following reaction of ethane with iron and iron oxides. The decomposition of ethane to elemental carbon and hydrogen is endothermic (27) and so, at first sight, it appears that the experimental results are in conflict with the above mechanism of filament growth. However, earlier work (28) has shown that the majority of carbon formed from ethane arises from the decomposition product ethylene. The latter decomposes exothermically (27) ($-\Delta H$ for C_2H_4 at $725^\circ C$ is $9.2 \text{ kcal. mole}^{-1}$) so that this mechanism is not contravened. A similar rationale was used by Keep, Baker and France (29) to account for the formation of carbon filaments during the nickel catalyzed decomposition of propane.

The key to the extremely high activity for filament production found with FeO may well reside in the defect structure of this compound. In such a structure the oxygen atoms in the surface will be readily accessible to extraction by protons generated by the hydrocarbon decomposition reaction and as a result the oxide could rapidly attain at the surface an iron rich sponge-like arrangement i.e. the role of FeO is that of a precursor for a high surface area Fe catalyst formed *in-situ*. This hypothesis is supported by the Mössbauer spectroscopy data which clearly shows that Fe is being produced at the expense of FeO as carbon is being deposited. In addition, the iron in both the FeO and Fe_2O_3 precursors is present as metallic iron and iron carbide after reaction in ethane, indicating that the chemical state of iron is essentially the same in both samples after reaction; therefore the dramatic differences in reactivity of these two precursors for carbon deposition must be traced to differences in effective surface areas. This is despite the fact that the FeO was prepared from a low surface area foil of metallic iron while the Fe_2O_3 was present as a higher surface area powder. This suggests that small metallic particles are formed from the FeO precursor. This leads to the rapid production of many thin carbon filaments having small iron particles at their growing tips. The metallic iron particles formed from the Fe_2O_3 precursor, on the other hand, are evidently much larger than those formed from FeO. This leads to the slower growth of a smaller number of wider carbon filaments. A similar concept was proposed by Guinot *et al* (30) who suggested that fragmentation of an iron-nickel low surface area catalyst by the carbon deposition from CO disproportionation was a necessary step in order to account for the high rate of reaction.

Finally, the CAEM studies show that Fe_3C is not an active catalyst for carbon filament formation. This observation is also supported by the Mössbauer spectroscopy data which show that the

iron carbide concentration increases as catalytic activity declines. This finding does not preclude the possibility that Fe_3C might catalyze the formation of other forms of carbon deposit.

Acknowledgments

The authors would like to thank M. Estadt and J.J. Chludzinski for their assistance with the microscopy studies; J. McHenry who carried out the macro-scale experiments; and J. Phillips and W.M. Shen (University of Wisconsin) who kindly performed the Mössbauer spectroscopy work presented here.

Literature Cited

1. Palmer, H. B. and Cullis, C. F. "Chemistry and Physics of Carbon"; Vol. 1, (P. L. Walker, Jr. ed.), p.265, Dekker, New York, 1965.
2. Baker, R. T. K. and Harris, P.S. "Chemistry and Physics of Carbon"; Vol. 14, (P. L. Walker, Jr. and P. A. Thrower, eds.), p. 83, Dekker, New York, 1978.
3. Gaaney, B. W.; U.S. Energy Research and Development Admin. Report GA-A13982, UC-77.
4. Lahaye, J., Badie, P., and Ducret, J.; Carbon (1977), 15, 87.
5. Baker, R. T. K., Barber, M. A., Feates, F. S., Harris, P. S., and Waite, R. J.; J. Catal. (1972), 26, 51.
6. Baker, R. T. K., Harris, P. S., Thomas, R. B., and Waite, R. J., J. Catal. (1973), 30, 86.
7. Rostrup-Neilson, J. R. "Steam Reforming Catalysts", Teknisk Forlag A/S (Danish Technical Press, Inc.), Copenhagen, 1975.
8. Boehm, H. P.; Carbon (1973), 11, 583.
9. Baker, R. T. K. and Waite, R. J.; J. Catal. (1975), 37, 101.
10. Baker, R. T. K. and Chludzinski, J. J., Jr.; J. Catal. (1980), 64, 464.
11. Baker, R. T. K. and Harris, P. S.; J. Phys. E. (1970), 5, 793.
12. Hennig, G. R. "Chemistry and Physics of Carbon", Vol. 2 (P. L. Walker, Jr., ed.), Dekker, p. 1, New York, 1966.
13. Davis, L. E. "Handbook of Auger Electron Spectroscopy", 2nd Ed., Publ. Physical Electronics Industries Inc., Eden Prairie, Minn., 1976.
14. Chang, C. C.; Surf. Sci. (1971), 25, 53.
15. Diamond, S. and Wert, C.; Trans. AIME (1967), 239, 705.
16. Morgan, D. W. and Kitchener, J. A.; Trans. Faraday Soc. (1964), 50, 51.
17. Smith, R. P.; Trans. Met. Soc. AIME (1966), 236, 1224.
18. Kovenskuj, J. J.; Phys. Metlas Metallage (USSR) (1963), 16, 107.
19. Schmidt, F. A. and Warner, J. C.; J. Less-Common Metals (1972), 26, 325.
20. Rudman, P.S.; Trans. Met. Soc. AIME (1967), 239, 1949.

21. Baker, R. T. K., Dudash, M. S., Chludzinski, J. J., Jr. and Simoens, J. A. Unpublished results.
22. Barison, E. V., Gruzin, P. L. and Zemskii, S. V.; *Zashch. Pokrytiya Metal* (1968), 2, 104.
23. Johnson, D. P.; *Solid State Comm.* (1969), 7, 1785.
24. Greenwood, N. N. and Gibb, T. C. *Mössbauer Spectroscopy*, Chapman and Hall Ltd., London 1971.
25. Raupp, G. B. and Delgass, W. N.; *J. Catal.* (1979), 58, 348.
26. Jette, E. R. and Foote, F.; *J. Chem. Phys.* (1933), 1, 29.
27. Stull, D. R., Westrum, E. F., and Sinke, G. G. "The Chemical Thermodynamics of Organic Compounds", Wiley, New York, 1969.
28. Albright, L. F., and McConnell, C. F. "Thermal Hydrocarbon Chemistry" (Eds. A. G. Oblad, H. G. Davis, and R. T. Eddinger) *Advances in Chemistry Series 183*, p. 205, Amer. Chem. Soc., Washington, D.C. (1979).
29. Keep, C. W., Baker, R. T. K., and France, J. A.; *J. Catal.* (1977), 47, 232.
30. Guinot, J., Audier, M., Coulon, M., and Bonnetain, L.; *Carbon* (1981), 19, 95.

RECEIVED July 30, 1982.

Inhibition of Coke Formation in Ethylene Steam Cracking

D. E. BROWN, J. T. K. CLARK, A. I. FOSTER, J. J. McCARROLL and M. L. SIMS

The British Petroleum Company p.l.c., Research Centre Sunbury, Chertsey Road, Sunbury-on-Thames, Middlesex, United Kingdom

This paper describes the derivation and evaluation of a silica coating process to reduce the rate of coke formation in the pyrolysis section of ethylene steam crackers (ESC). The coating process utilises the chemical vapour deposition of an alkoxysilane in steam carrier gas to produce a thin, impervious, adherent and amorphous silica film on the internal surfaces of high alloy steel tubing at 700–800°C. Evaluation in a laboratory scale ethylene steam cracking reactor employing a typical ESC feedstock (LDF 160) has revealed that the coking rate can be reduced by up to x10 in short term tests and by x3–4 in longer term tests.

The steam cracking of hydrocarbons (eg naphtha) to produce the lower olefins (ethylene, propylene, butenes) and butadiene is the basic petroleum chemicals operation. Such steam cracking plant suffers coke deposition problems that restrict performance. The cracking operation involves heating naphtha diluted with steam in radiantly heated coils of high alloy steel tubing to temperatures of typically 850°C. During cracking, coke deposition occurs in the coils and associated downstream exchangers. The coke, which forms to depths of several mm, reduces heat transfer and normally limits run length to four to eight weeks. The cracking furnace must then be taken off-stream for decoking, usually by steam-air oxidation, with consequential loss of production. Also, frequent decoking operations present additional fuel and utilities costs, and probably affect coil life. A research programme was undertaken to investigate the coke deposition phenomena and to develop a potential method for its inhibition.

0097-6156/82/0202-0023\$06.50/0
© 1982 American Chemical Society

ESC Plant Materials Investigation

The research programme was initiated through an investigation of radiant coil alloys and deposited coke. Radiant coils are constructed in high alloy steels (eg Incoloy 800, HK 40, 34 CT), with iron, nickel and chromium as major components and a range of minor constituents such as silicon, titanium and manganese. Soft X-ray appearance potential spectroscopy (SXAPS) studies of radiant coil alloys were carried out to determine surface compositions resulting from exposure to a range of environments. In particular, the oxide surface films generated in oxidising conditions at high temperatures (>800°C) revealed the segregation to the surface of metals forming stable oxides in preference to metals forming less stable oxides. This effect was also found on the internal surfaces of an aged Incoloy 800 radiant coil from a commercial ESC, which had continually been exposed to high temperature steam cracking/decoking cycles. Figure 1 shows the SXAPS spectrum of the surface oxide, which (taken together with the bulk alloy composition) demonstrates the general observation of a trend in the ratio of surface oxide composition to bulk metal composition for the metallic alloying elements of Ti > Cr > Fe > Ni, in line with decreasing oxide stability.

Coke deposits from a commercial ESC plant were also examined. Bulk metals concentrations were determined by ashing at 900°C prior to emission spectroscopy analysis. High levels of metals were found at the radiant coil-coke interface due, presumably, to oxide spallation, but concentrations of metals (primarily chromium, iron and titanium, totalling ca 200 ppm) were also found into the bulk of the coke and at the coke-process stream interface (Table I). SXAPS examination of coke heated under vacuum for several hours at 900°C also revealed the appearance of up to 1% concentration of metals at the surface of some coke samples, and significantly chromium, iron and titanium were again the metals observed.

TABLE I
BULK ANALYSIS OF METALS IN COKE DEPOSITS FROM COMMERCIAL
ETHYLENE STEAM CRACKER (IN ppm)

Sample	Ca	Ti	Cr	Mn	Fe	Ni
Coke from central section between metal tube and gas phase interfaces	82	27	105	5	53	6
Coke from gas phase interface	11	3	22	3	175	<1

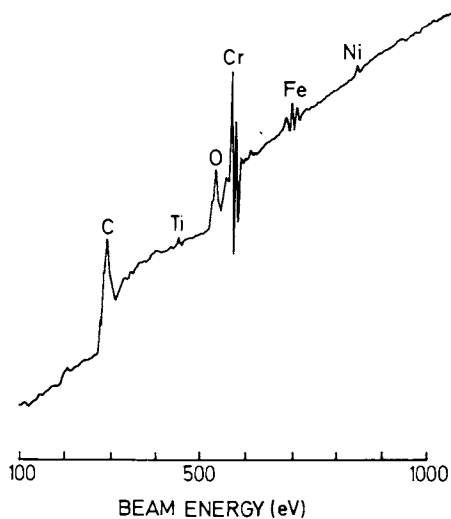


Figure 1. SXAPS of Incoloy 800 alloy aged in a steam cracker.

The presence of metals in ESC plant coke has been reported by Albright and coworkers (1), who have demonstrated that such metals can catalyse the formation of additional coke. Baker and coworkers (2,3,4) have provided insight into one mechanism for the propagation of coke deposition from model hydrocarbons (eg C_2H_2 , C_3H_8) onto metal foils. Using controlled atmosphere electron microscopy it was revealed that metal catalyst particles can become detached from the surface and be carried away by the growth of filamentous carbon, with the particles remaining at the filament tips. Other researchers have observed a wide range of coke morphologies in pyrolysis (5) and steam cracking (6) of a range of hydrocarbons over steel surfaces, suggesting that the overall deposition process in commercial steam cracking is complex.

Several studies (7,8) have indicated that the propensity of transition metals for catalysing coke formation increases with decreasing stability of the metal carbide - ie increasing propensity along the series $Ti < Cr < Fe < Ni$. However, the examination of the ESC radiant coil revealed only low levels of nickel in the surface oxide and more particularly virtually no nickel in the coke samples. Therefore, iron and possibly chromium, which are both present at the cracker coil surface and within the coke, are more likely to be responsible for catalysed coke formation. This is supported by research of Albright and coworkers (5) on the pyrolysis of hydrocarbons over Incoloy 800 surfaces, which found iron to be the predominant metal in the coke.

In summary, these investigations suggested that coke deposition in ESC plant is enhanced by catalytic interaction of metals from the radiant coil walls, a view later supported by high resolution TEM studies. This led to an examination of means of passivating alloy surfaces.

Surface Passivation of ESC Radiant Coil Alloys

Methods have been suggested for the passivation of reactors. Presulphiding treatments have been reported (9) to reduce coke formation during ethane and propane pyrolysis. However, although LDF feedstock contains small quantities of sulphur, commercial ESC plant normally relies on preoxidation during the steam/air decoking operations to produce a protective surface oxide film. Conoco (10) have claimed that high temperature steam pretreatments are particularly effective for heat-resisting alloy steels containing at least 1% silicon. This research demonstrated that steam oxidation of a range of HK and HU alloys produced increasing resistance to carburisation with increasing silicon content over the range 1-2.5%. Most particularly, several hours pretreatment with steam at 955°C of an ethane cracking furnace in 2.0% Si HK alloy significantly increased plant on-stream time through reduced coke deposition. It was presumed that these

improvements were associated with the formation of a surface film comprising silicon oxidation compounds.

A programme of work to examine the effects of steam oxidation on commercial ESC plant alloys was therefore carried out, in which the composition of the surface films was probed by X-ray photoelectron spectroscopy (XPS or ESCA). Coupons of 18/8 stainless steel, Incoloy 800, HK 40 and subsequently tubes of a high silicon-containing drawn alloy (Immaculate 5) were treated for several hours in steam at temperatures in excess of 900°C. In all cases the oxide surface was enriched in silica through segregation from the bulk alloy. Figure 2 displays the XPS spectrum of steam-treated HK 40, the alloy which showed the highest surface concentrations of silica. It may also be noticed that nickel was completely removed (<1%) from the oxide surface, though substantial concentrations of iron, manganese and chromium were still present.

These experiments demonstrated that the passivating qualities of steam pretreatment may be partially associated with the generation of a silica-rich oxide. However, brief attempts to increase the surface concentration to approach a continuous silica layer excluding all the alloying metals (by variations in preoxidation conditions) met with failure, exhibiting bulk inhomogeneity and oxide spallation problems. Further, many ESC plants are constructed with radiant coil alloys low in silicon content, and so preoxidation can only be considered a partial palliative. Hence, attention turned to the prospect of coating the internal surfaces of radiant coils with a thin, continuous layer of silica.

Silica Coating of Steel Alloys

Simultaneous development was undertaken of a method for silica coating steels and a test to demonstrate that the coke formation reaction was surface sensitive and reduced by the deposition of a silica film.

Mindful of the difficulty of coating the internal surfaces of long ESC radiant coils, a chemical vapour deposition (CVD) route was seen as presenting the best approach. The deposition of silica by CVD onto silicon is well known in the electronics industry (11), but had not been extensively applied to metals. A process was conceived (12,13) whereby a silica coating is produced on preoxidised steel substrates by the decomposition of an alkoxysilane in a carrier gas. This process offers the advantages that thin, adherent and impervious films of silica can be deposited at high temperatures, using steam as a carrier gas under conditions similar to decoking/cracking operations. Reaction of the organo-silicon compounds with an oxidising agent is not required.

An apparatus for silica coating steel coupons by this method is shown in Figure 3. Briefly, an alkoxysilane (eg tetraethyl-

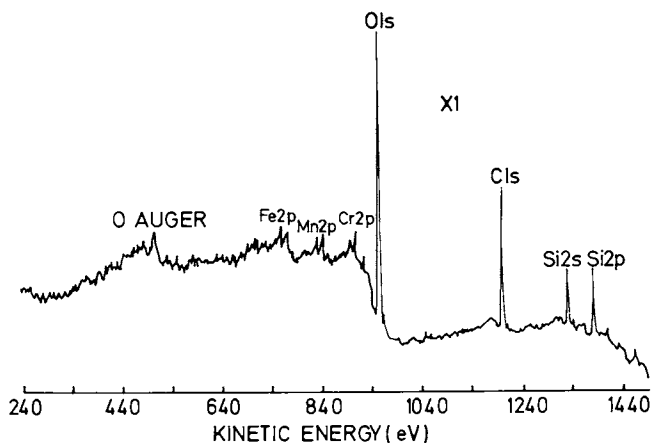


Figure 2. XPS of steam treated HK 40.

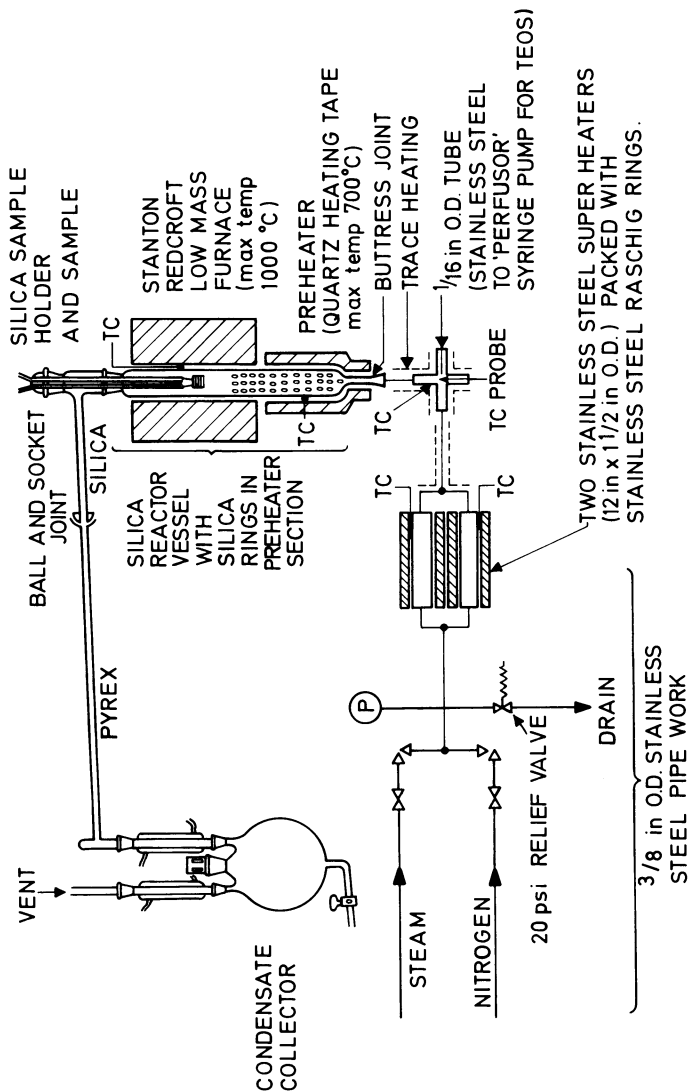


Figure 3. Apparatus used for silica coating steel coupons.

orthosilicate) is injected (1% by weight) into a preheated steam flow which passes into the coating vessel where steel substrates are radiantly heated to 600–850°C. Silica films, largely amorphous in character, have been deposited with a wide range of thicknesses, although protective, continuous coatings with a fused ball-like top surface (Figure 4) can be produced as thin as 1 micron or less.

Preoxidation of the steel substrate is an essential feature to maintain coating adherence over the wide temperature ranges and hostile environments experienced in tests; this can be accomplished in a controlled manner within the coating apparatus or separately prior to sample introduction. Metallurgical examination of silica coated steels has revealed no deleterious action on the bulk alloy, as would be predicted since the coating is deposited directly as the inert oxide. Indeed silica coating has been found to protect the steel surface from oxidative attack in high temperature steaming and cracking operations. Although no detailed study has been carried out, it would also appear possible that the impervious silica films will reduce degradation of the alloy mechanical properties by preventing carburisation.

A test to demonstrate that the coke formation reaction was surface sensitive was developed, being based around a Satorius 4102 microbalance using flowing hydrocarbon: steam atmospheres. A schematic diagram of the apparatus is shown in Figure 5. Coking rate measurements were made on HK 40, Incoloy 800, nickel foil, quartz and silica coated HK 40, from 57% (wt) steam: ethane, 72% (wt) steam: ethane, and 49% (wt) steam: 32% (wt) hexane:ethane mixtures. High steam concentrations were used in an attempt to compensate for the relatively long hot-zone residence times of several seconds. The procedure involved a temperature programme of:– 900°C for one hour to allow equilibration of the system, followed by 860°C, 880°C, 920°C, 940°C, 980°C, etc for the time necessary to measure the coking rate (10–60 minutes); occasional repeat measurements of the low temperature rates were made. Figure 6 shows the Arrhenius plot obtained for the steam: hexane:ethane mixture on both coated and uncoated HK 40, and typifies the results obtained for all gas compositions. Below a certain temperature, which depended on such factors as the steam concentration and residence time, the plots diverged with the coking rates on the metal surfaces higher than on the quartz and silica coated surfaces. Hence in the Figure shown the rate on HK 40 was four to six times higher than that on silica coated HK 40 at 830°C. From these tests it became clear that under certain conditions of temperature, steam concentration and flow rate, coke formation was catalysed by the metal substrate and a silica coating would considerably reduce the rate of coking. However, more complex feedstocks and lower residence times (0.1–0.2 s) are typically used in commercial ESC plant, making a detailed investigation of coating performance in a laboratory simulated ESC reactor necessary.

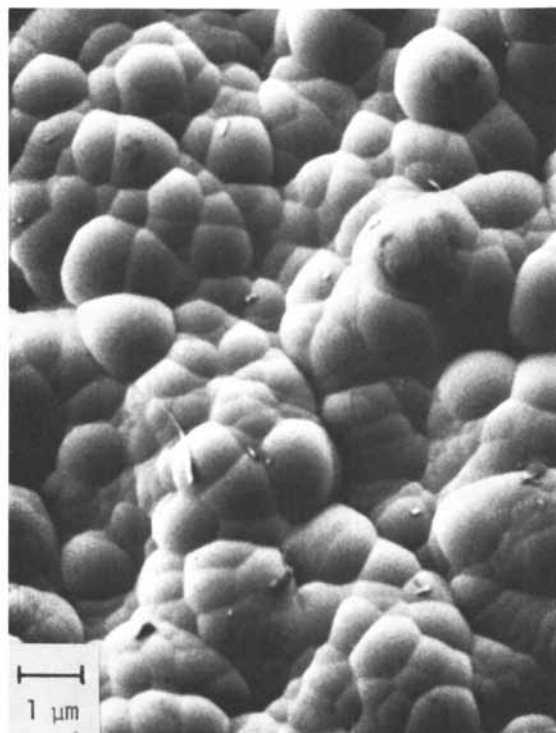


Figure 4. SEM of silica coated steel.

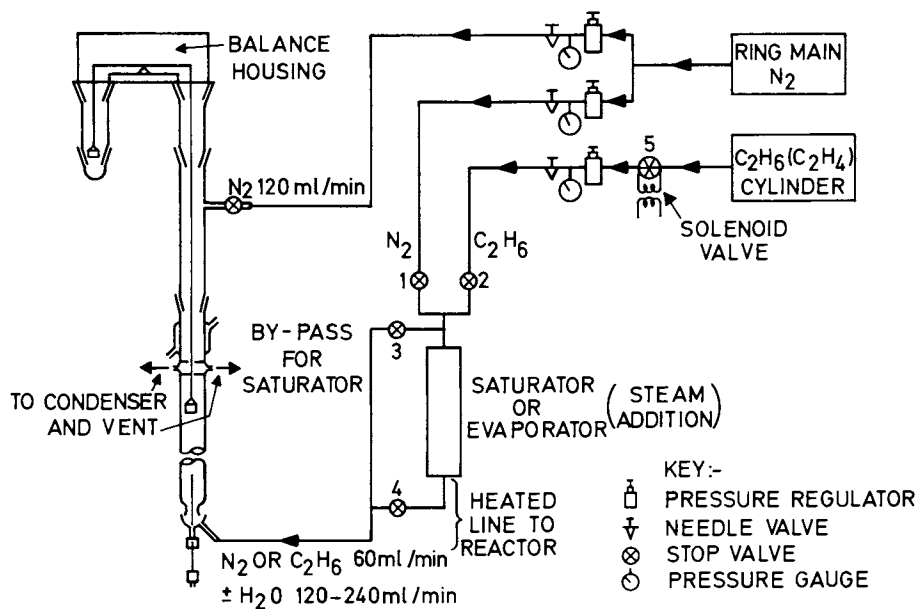


Figure 5. Schematic of microbalance system for coking studies under flowing conditions on coupons.

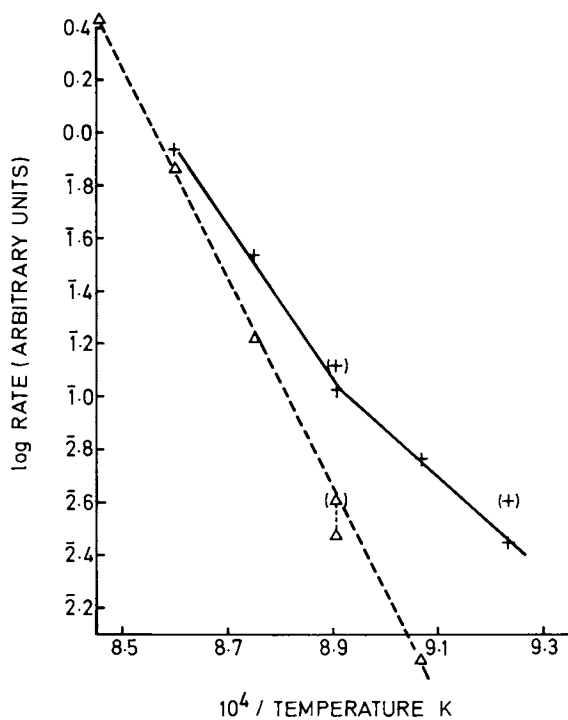


Figure 6. Microbalance coking runs in ethane:hexane:steam (49 wt%). Key: + — +, uncoated HK 40; and Δ — Δ, SiC 51 silica coated HK 40.

Coke Inhibition in a Laboratory ESC Reactor

The laboratory ESC reactor is shown in Figure 7. With this apparatus it was possible to carry-out in situ consecutive silica coating, steam cracking, and decoking operations in a 2 ft long 3/8" OD cracker tube. Most of the work was carried out using Incoloy 800 tubing, though a few runs were also carried out using Immaculate 5 tubing, which is equivalent to an AISI 310 specification with a composition similar to cast HK 40 alloy.

Silica coating was carried out as with coupons, by injecting 1% by weight tetraethoxysilane into steam just prior to the preoxidised cracker tube to produce 0.5-1.0 μm thick coatings along the whole of the tube hot zone. The steam cracking runs used a typical ESC feedstock, LDF 160 (36% iso-paraffins, 23% n-paraffins, 34% naphthenes, 7% aromatics, 78 ppm sulphur with a total fraction boiling point of 188°C). A residence time in the cracking zone of 0.12 s with 37.5% steam: LDF was selected for the cracking conditions. The cracked gas composition for different cracking temperatures was measured by gas chromatography and is shown in Figure 8. Clearly, cracking severity increased with temperature, and cracking in the temperature range 800-900°C was taken to represent a reasonable simulation of commercial ESC plant. Finally, the decoking operation, when used, utilised air at 600-800°C.

Coke deposition measurements were made on both uncoated and coated tubes, normally by measurement of weight difference before and after standard six hour steam cracking runs. In all cases the untreated tubes were pretreated in steam for at least one hour at 750-850°C before cracking began to form a surface oxide layer in a similar manner to that found in ESC plant. The coke yields observed, expressed as ppm of the total feedstock, over both uncoated and silica coated tubes at various cracking temperatures are shown in Figure 9. A fast, catalysed, coking reaction with an apparent activation energy of about 27 kcal/mol was observed in the uncoated Incoloy 800 tubes. Only a low coke formation rate was observed on the silica coated tubes up to 900°C. Thus at 850°C, up to a factor of 10 reduction in coking rate was obtained by silica coating. Above 900°C the coating was less efficient, and this was subsequently partially ascribed to severe deformation of the cracker tube causing coating spalling. This situation was to some extent alleviated by preannealing the tube at the cracking temperature prior to silica coating.

The effect of the decoking operation on coke formation in subsequent cracking runs was also studied and the results shown pictorially in Figure 10. On an uncoated Incoloy 800 tube, the high coke yield remained approximately constant throughout four successive steam cracking/air decoking cycles. This tube was subsequently coated with silica to produce an immediate x10

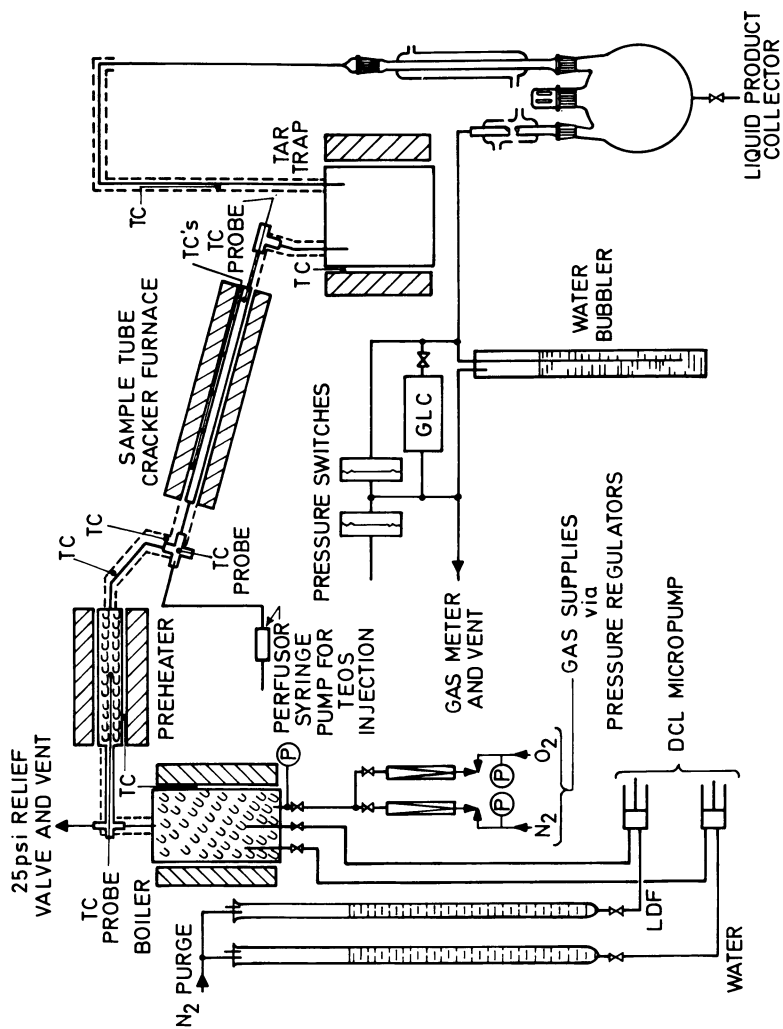


Figure 7. Laboratory-scale ethylene steam cracker.

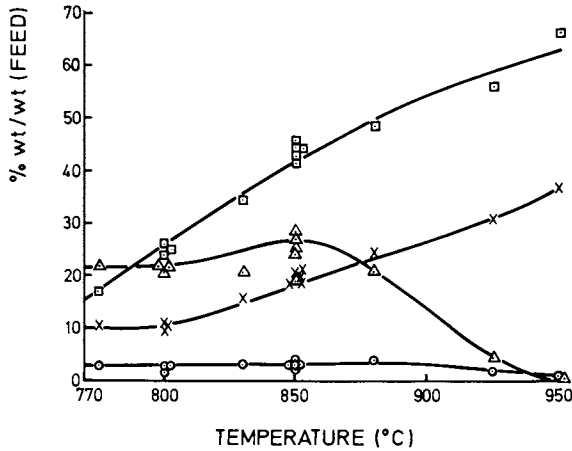


Figure 8. Product gas composition vs. cracking temperature with Incoloy 800. Key: \circ , ethane; \times , methane; \square , ethylene; and \triangle , propylene.

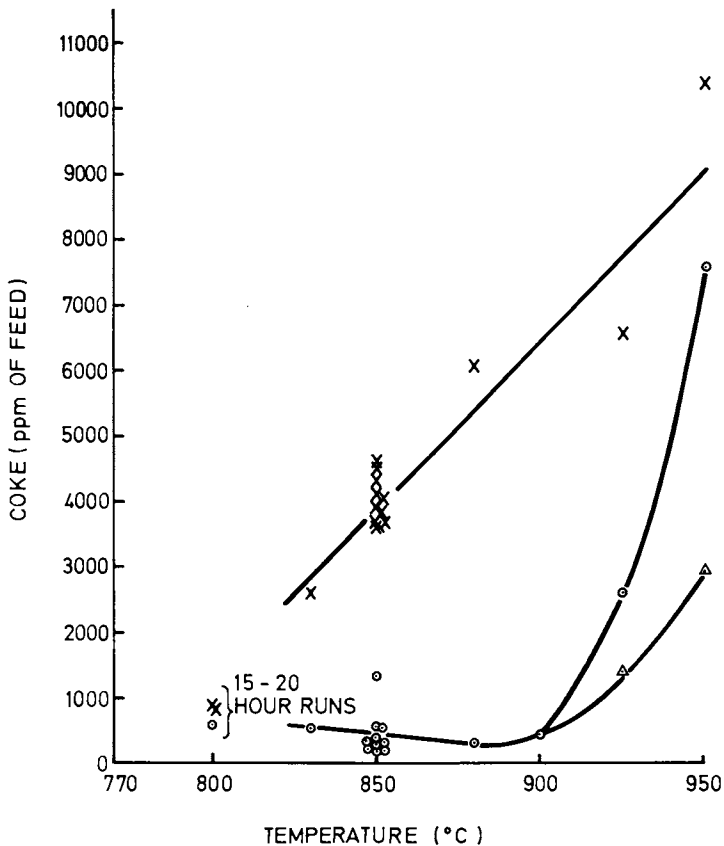


Figure 9. Coke yield vs. cracking temperature. Key: \times , uncoated Incoloy 800; \circ , silica coated Incoloy 800; and \triangle , silica coated Incoloy 800 preannealed at running temperature.

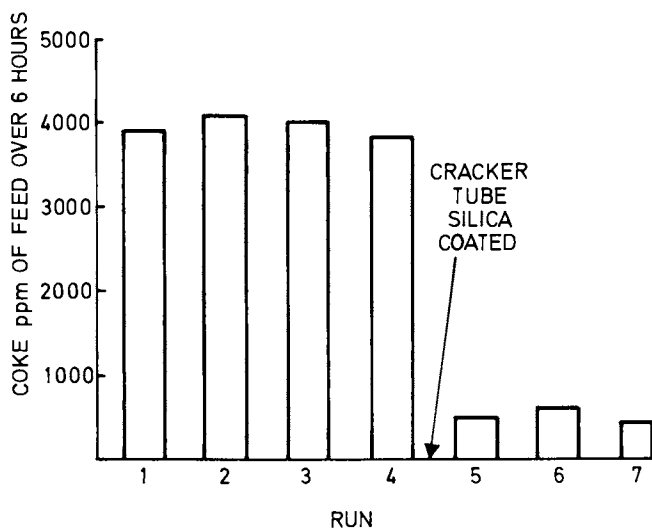


Figure 10. Coke yields at 850°C in successive steam cracking/air decoking cycles in Incoloy 800 tube.

reduction in coke formation which was broadly maintained over three further steam cracking/air decoking cycles, indicating no deleterious action upon the coating.

An opportunity was taken to examine the structure of the coke deposits using optical microscopy, SEM and high resolution TEM. The latter facility was provided by Dr G.R. Millward of the University of Cambridge, using a Phillips EM 300 fitted with a high resolution stage. The initial coke deposition during the first few hours of cracking produced a smooth, hard carbon skin, which was thicker and more brittle in the uncoated tube (Figure 11). TEM studies of the deposit from the uncoated tube revealed both poorly ordered carbon and a minority component of relatively well ordered graphitic carbon (Figures 12 and 13), whereas the deposit from the silica coated tube revealed only the poorly ordered carbon. The greater degree of ordering in the coke from uncoated tubes would appear consistent with a catalysed formation process.

Subsequently, with longer cracking times, cracks appeared in the hard carbon skin with further coke growth emanating along these cracks. After 70 hours on stream this secondary coke growth, which had a less dense whiskery nature, completely covered the uncoated tube but was still localised on the silica coated tube (Figure 14). TEM examination of this secondary deposit occasionally revealed well-defined filamentous type deposits with particles at the filament tips (Figure 15) as observed by Baker and coworkers (2,3,4). However, under the TEM the deposit still primarily revealed the poorly and relatively well ordered carbon seen in Figures 12 and 13, possibly through filament thickening by a condensation mechanism (14).

Thus, silica coating appears to retard both the formation of the hard carbon skin and the growth of the secondary (less dense) coke deposit at cracks in the skin, with the overall result that in cracking runs up to three days in length in the laboratory ESC reactor the coke formation is inhibited by a factor of 3-4 compared to uncoated tubes.

Conclusion

A process for forming thin, adherent silica coatings in high alloy steel tubing has been developed. The silica coatings substantially reduce the rate of coke formation in laboratory pyrolysis tubes operating under ethylene steam cracking conditions.

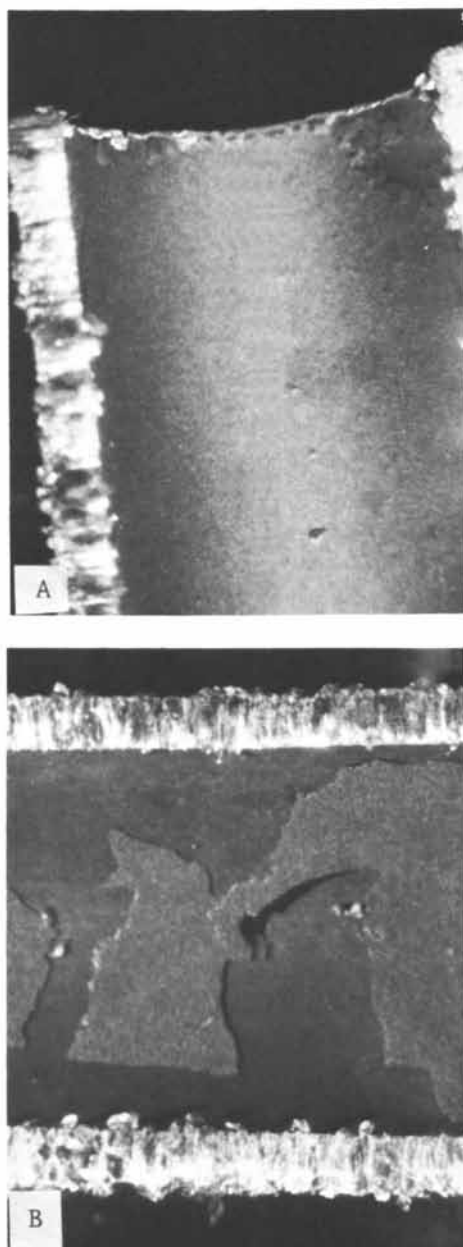


Figure 11. Optical micrographs of coke deposits after six hours cracking. Key: A, silica coated; and B, uncoated.



Figure 12. TEM of hard coke skin from uncoated Incoloy 800 tube.

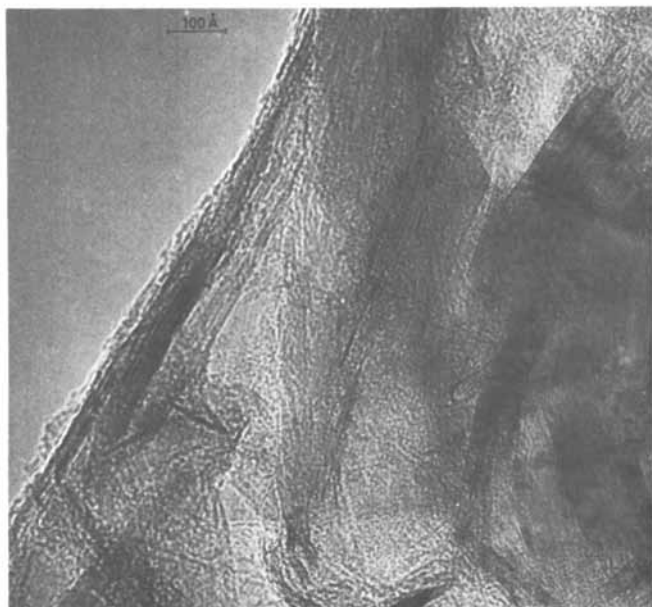


Figure 13. TEM of hard coke skin from uncoated Incoloy 800 tube.

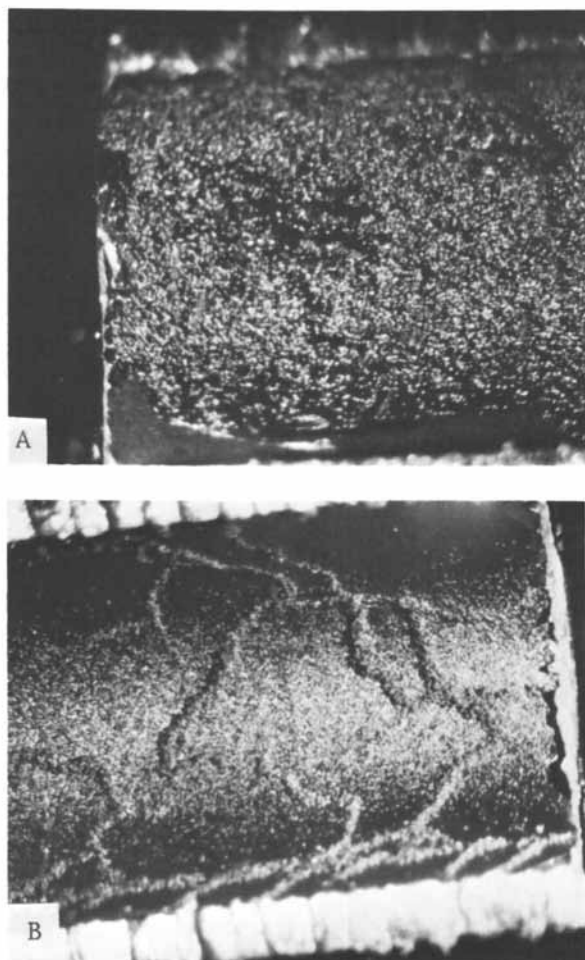


Figure 14. Optical micrographs of coke deposits after 70 h cracking. Key: A, uncoated; and B, silica coated.

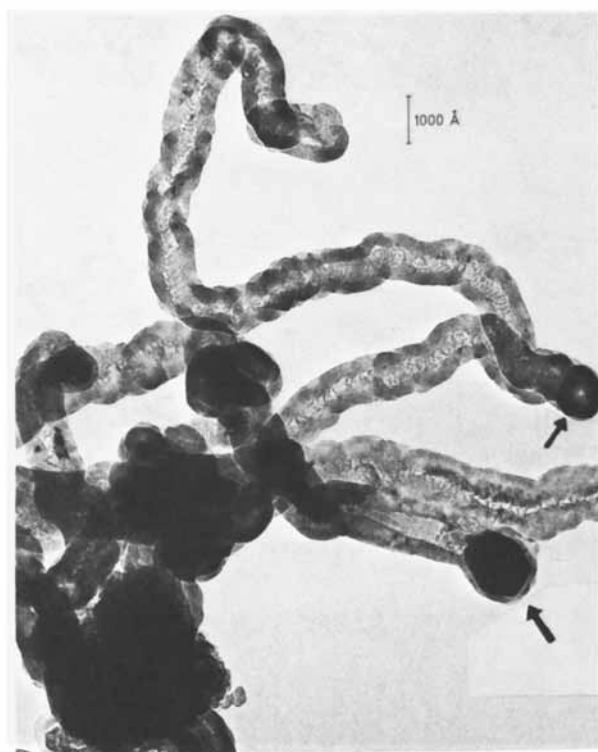


Figure 15. TEM of filamentous coke deposit (particles arrowed).

Literature Cited

1. Albright, L.F.; Yu, Y.C.; Welther, K.; Proc. 85th American Institute of Chemical Engineers National Meeting, 4th June 1978.
2. Baker, R.T.K.; Barber, M.A.; Feates, F.S.; Harris, P.S.; Waite, R.J.; J. Catalysis (1972) 26, 51.
3. Baker, R.T.K.; Harris, P.S.; Thomas, R.B.; Waite, R.J.; J. Catalysis (1973) 30, 86.
4. Keep, C.W.; Baker, R.T.K.; France, J.A. J. Catalysis (1977) 47, 232.
5. Albright, L.F.; McConnell, C.F.; Welther, K.; Thermal Hydrocarbon Chemistry, Editors, A.G. Oblad, H.G. Davis, and R.T. Eddinger, Advances in Chemistry Series #188, pp 175-191, Amer. Chem. Soc., Washington, D.C., 1979.
6. Lahaye, J.; Badie, P.; Ducret, J. Carbon (1977) 15, 87.
7. Tama, Y.; Nishiyama, Y.; Takahashi, G. Kogyo Kagaku Zasshi (1967) 70, 889.
8. Lobo, L.S.; Trim, D.L.; Figueiredo, J.L. Proc. Fifth International Congress on Catalysis, Miami Beach 1972, Paper 79.
9. Crynes, B.K., Albright, L.F., Ind. Eng. Chem. Process Develop (1969) 8, 25.
10. Continental Oil Company, UK Patent 1 332 569 Published 3 Oct 1973.
11. See for example Gregor, L.V., Physics of Thin Films (1966) 3, 131.
12. Brown, D.E.; Clark, J.T.K.; McCarroll, J.J.; Sims, M.L.; (The British Petroleum Co Ltd), UK Patent 1 483 144, Published 17 Aug 1977.
13. Brown, D.E.; Clark, J.T.K.; McCarroll, J.J.; Sims, M.L.; (The British Petroleum Co Ltd), US Patent 4 099 990, Published 11 July 1978.
14. Oberlin, A.; Endo, M., J. Crystal Growth (1976), 32, 335.

RECEIVED June 28, 1982.

Surface Effects on the Steam Cracking of Propane

A. HOLMEN and O. A. LINDVAAG

Norwegian Institute of Technology, Department of Industrial Chemistry,
N-7034 Trondheim-NTH Norway

D. L. TRIMM

University of New South Wales, School of Chemical Engineering and Industrial Chemistry,
P.O. Box 1, Kensington, 2033 Australia

The effect of surfaces on the gaseous and solid products of the steam cracking of propane has been studied. The chemical nature of the surface near the reactor inlet has a significant effect on the reaction products while the surface near the exit does not. The material of the reactor tube appears to catalyze gas phase reactions as well as coke formation and gasification. Pretreatment of the reactor tube alters the chemical nature of the surface and, as a result, alters the effect of the material on the reaction products.

The steam cracking of hydrocarbons is one of the most important sources of light olefins for the chemical industry (1). The overall reaction is a high temperature pyrolysis process in which a range of products are formed in the gas phase as a result of a free radical chain reaction. Tars and coke are also formed as side products to the main reaction. Steam is present mainly as an inert diluent (2), although it may help to gasify tars and carbon produced during the reaction (1, 3). Because of the formation of coke deposits on industrial reactor surfaces, the reactor must be removed from operation from time to time and the coke layer burned out with oxygen/steam mixtures.

Although the major reactions occur in the gas phase, surface reactions can be very important in these systems. The absence or presence of a surface plays an important role in the formation of solid products such as coke (4 - 8). There is also good evidence that the wall can have a significant effect on gas phase reactions, at least in part as a result of the initiation or termination of free radical chains thereon (9, 10). Given the nature of the free radical chains, both the chemical nature and the physical form (11 - 16) of the surface can influence the reaction and its products.

0097-6156/82/0202-0045\$06.00/0

© 1982 American Chemical Society

The present studies were initiated in order to investigate the effect of the reactor surface on the product distribution and on the tendency for coke formation during the steam cracking of propane in a tubular reactor. Attention has been focused on correlating various effects which can arise in the system. Previous studies of the pyrolysis of propane has been reviewed recently (17, 18), and the findings of the present work are related to these studies later in this paper.

Coke formation will always be a potential problem in any high temperature process involving hydrocarbons. Coke and tars formed during reaction can deposit on reactor surfaces or in quench heat exchangers, and several effects have been observed in a steam cracker tube (4, 9). As the reaction proceeds the tube will accumulate coke towards the reactor exit, while the inlet zone remains relatively coke free, as a result of the induction time associated with the formation of tars and coke (19). Gas phase reactants may adsorb and react on this bare metal, and the components of the gas phase in the reactor should and do reflect this interaction (4, 9, 10). Since carbon formation depends on the nature of the gas phase species, these interactions should also influence coke formation towards the exit of the reactor. Again, this is found to be the case (4, 9 - 11).

As a result of these considerations, it would be expected that surface effects during steam cracking would be apparent in the formation of gaseous, liquid and solid products. The present studies show that this is indeed the case.

EXPERIMENTAL

Coke formation has been studied in a conventional flow apparatus. A schematic diagram of the experimental apparatus is shown in Figure 1. Coke formation is measured on foils of different materials hanging from one arm of the microbalance (C.I. Mark 2B) in such a way that the foil is in the constant temperature zone of the reactor. The amount of coke deposited on the foils includes the deposition of coke formed in the gas phase as well as the coke formed on the surface.

The tubular reactor is made of stainless steel (Uddeholm Stainless 24, 18-2689) with an inside diameter of 22mm. The length of the reactor is 37 cm, with a constant temperature zone of ca. 16 cm (+ 3°C). Experiments have also been carried out in a tubular reactor made of quartz (i.e. quartz as a lining in the steel reactor). The inside diameter of the quartz reactor is 14.8 mm. The dimensions of the foil hanging in either reactor were usually ca. 8 mm x 28 mm and the weight about 0,3 gram if a steel foil was used.

All the experiments were carried out with steam and/or nitrogen as diluents. Steam was fed to the reactor by evaporating water into a stream of nitrogen. A stream of nitrogen is always main-

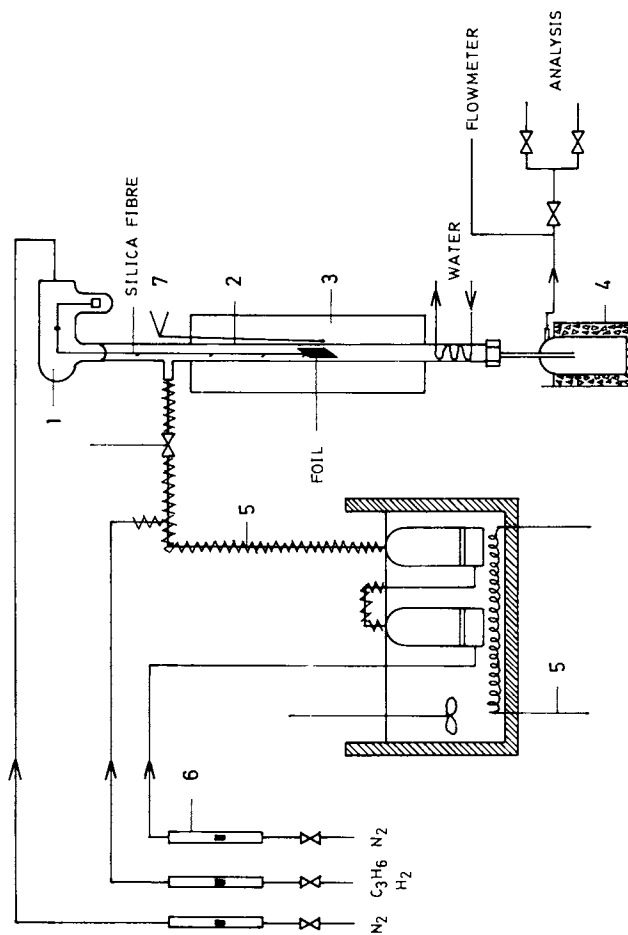


Figure 1. Experimental apparatus. Key: 1, microbalance; 2, reactor; 3, furnace; 4, water trap; 5, heater; 6, rotameter; and 7, thermocouple.

American Chemical
Society Library
1155 16th St. N. W.

tained through the microbalance in order to protect the balance against corrosive atmospheres. The exit gas from the reactor was quenched and the gas volume measured before complete gas analysis using two on-line gas chromatographs. The permanent gases (H_2 , N_2 , CO , CO_2) were separated on a 2 m column (1/4") packed with Porapak N (80/100 mesh), followed by a 3 m column (1/4") packed with 13X molecular sieve (30/50 mesh). Hydrocarbons were separated on a 3 m column (1/8") packed with squalane on Alumina H (100/120 mesh).

Two different pre-treatments of the foil and of the reactor surface have been used: either prereduction or preoxidation (with oxygen). During prereduction each foil was reduced for 18 h in flowing hydrogen at $770^\circ C$ and 1 h at the actual experimental temperature prior to the run. With steel foils it was impossible to oxidize the foil to constant weight and preoxidation involved heating in oxygen ($850^\circ C$) for various times as detailed in the text.

RESULTS

Experiments were carried out (a) in which the material of the reactor tube remained constant and the formation of coke was measured on foils of different materials and (b) in which the material of the reactor tube was varied and coke formation was measured on a foil of the same material. Both prereduction and preoxidation of the reactor system have been used as standard pretreatment in different cases.

Not surprisingly, the first geometry gave very similar results in all cases. Using the quartz reactor, coke formation was measured on foils fabricated from stainless steel, cobalt, molybdenum, copper and quartz. Typical exit gas compositions are shown in Figure 2 and rates of coke formation on the foils after prereduction are shown in Figure 3. The nature of the foil does not have any significant influence on the exit gas composition. On the other hand it is clear that the coke formation on fresh foils is dependent of the foil material. However, this initial variation in coke deposition on the foils is substantially decreased as the foils become more covered in coke. This coke originates at least in part in the gas phase and encapsulates the foil and breakaway metal particles (20). It is interesting to note that the higher initial rates were not observed on foils made of quartz or molybdenum: in fact, the rate for coke formation seems to increase somewhat as the reaction proceeds on these foils.

The effect of reactor material was studied using three different surfaces. These were quartz and oxidized and reduced stainless steel (Uddeholm 24 containing 17,2% Cr, 11,5% Ni, 2,7% Mo, 1,7% Mn, 0,5% Si and 66,4% Fe). Previous studies have revealed that the surface of the oxidized steel contains Fe and Ni oxides together with the Cr oxide, while the surface enrichment by Mn and Cr oxides is very pronounced during reduction of

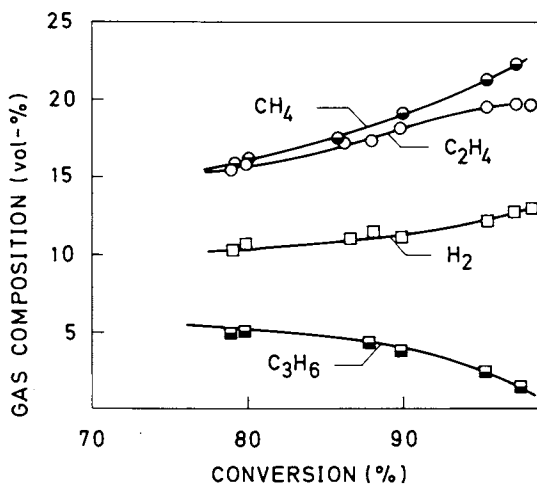


Figure 2. Exit gas composition from steam cracking of propane in quartz reactor with steel (Sandvik 15Re10) as the foil material after 10 min on stream. Conditions: temperature range, 800–870°C; feed gas composition, 29 mol% C₃H₈, 32% H₂O, and 39% N₂; and total feed rate, 0.42 L gas/min.

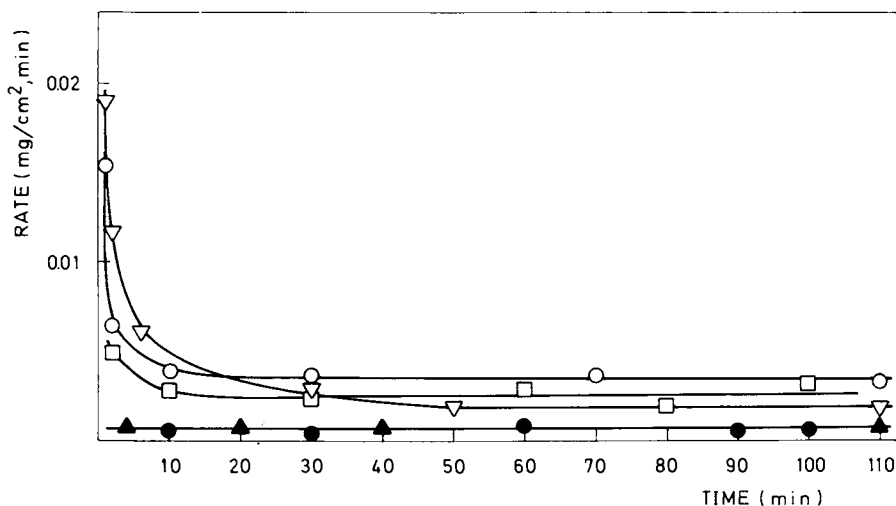


Figure 3. Coke formation during steam cracking of propane in the quartz reactor at 850°C on foils made from different materials. Key: ○, steel; ▽, Co; ▲, Mo; □, Cu; and ●, quartz. Conversion of C₃H₈ = 98%. Feed gas as in Figure 2.

the steel surface. (The content of Ni and Fe in the surface of the reduced steel is less than 0.3 wt-%) (20). Coke formation was measured from deposition on foils made from a steam cracker tube material (Sandvik 15Re10 containing 24,5% Cr, 20,5% Ni, 1,8% Mn and 52,5% Fe). Some experiments have also been performed with foils made of nickel. Typical exit gas compositions are shown in Figures 4 and 5. The amount of coke deposited on the foils are summarised in Figures 6, 7, 8 and 9.

It is seen that coke formation on the sample of foil is dependent on the material of the tubular reactor as is the product gas composition. With the steel reactor, preoxidation leads to a substantial increase in the coke formation on the steel foil (Figures 6 and 7). The effect of preoxidation is even more pronounced with Ni as the foil material (Figure 8). On the other hand, preoxidation does not lead to a high rate of coke formation on the steel foil if a quartz liner is used in the tubular reactor (Figure 9).

Gasification of the first coke deposit laid down on a new foil always resulted in higher rates for coke formation during subsequent runs (Figure 9). However, it has so far been impossible to establish a relationship between repeated coke formation/gasification and the rates for coke formation during the runs following the first gasification.

It was found that carbon oxides do not form in the quartz reactor whereas a large amount of carbon oxides was formed in the preoxidized steel reactor (Table I). The content of other products in the exit gas is also dependent of the reactor surface (Figures 2, 4 and 5). Increasing content of hydrogen was also observed when the same steel reactor was used for a large number of experimental runs with repeated coke formation/gasification. Similar effects have also been observed in a tubular reactor filled with pieces of the reactor material (Table II) during pyrolysis of ethane and ethylene. The oxidized surface did not effect the conversion of ethane very much, but the selectivity of ethylene formation was reduced from about 80% in the untreated reactor to about 15% when the surface was pretreated with oxygen.

DISCUSSION

The present studies have been concerned with the overall effect of surfaces on reactions occurring during steam cracking. The formation of gaseous and solid products has been related to the nature of the reactor surface. Steam cracking is, however, a high temperature pyrolysis reaction in which free radical intermediates play an important role. No attempt has been made to relate the experimental results to the nature and amount of free radicals present in the system.

Coke formation on the foils is found to be dependent not only on the nature of the foil but also on the material of the tubular reactor. Essentially, the studies involved three reactor surface

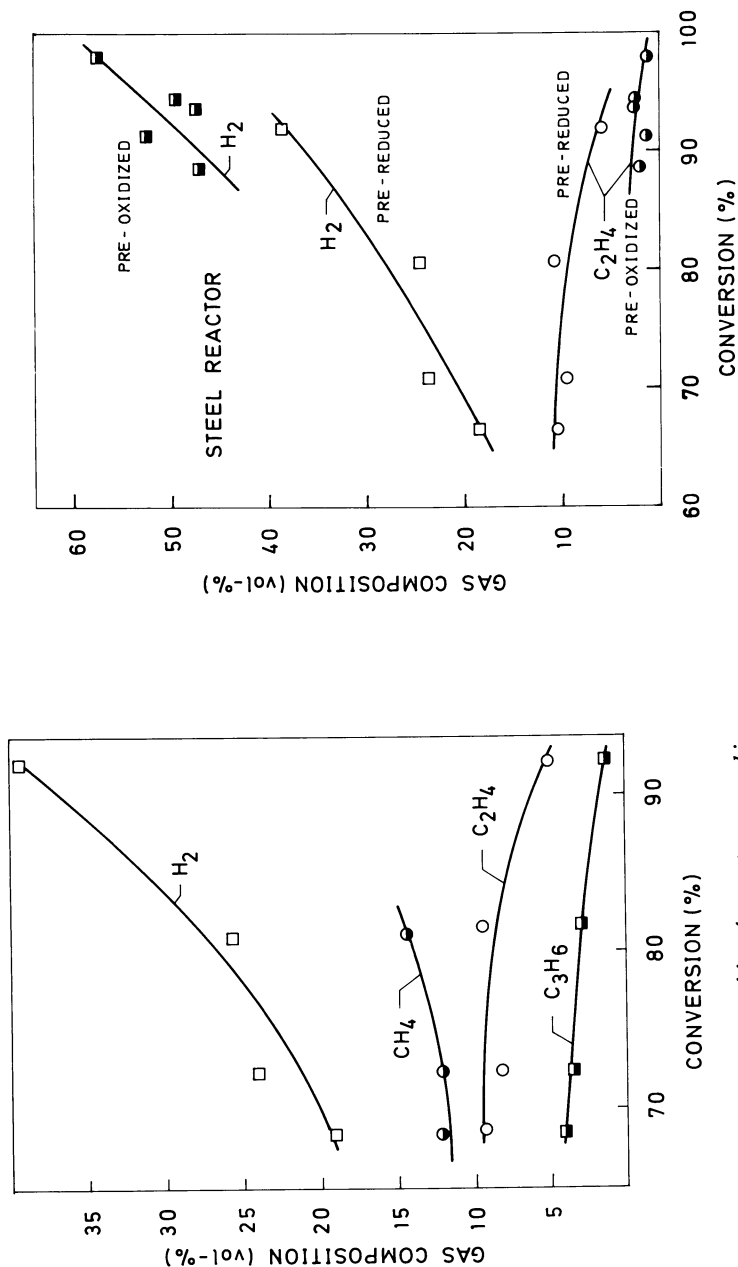


Figure 5. Exit gas composition from steam cracking of propane. Comparisons between prereduced and pre-oxidized systems. Conditions as in Figure 4.

Figure 4. Exit gas composition from steam cracking of propane in the prereduced steel reactor with steel (Sanavik 15Re10) as the foil material after 10 min on stream. Conditions: temperature range, 800–870°C; feed gas composition, 29 mol% C₃H₈, 32% H₂O, and 39% N₂; and total feed rate, 0.92 L/min.

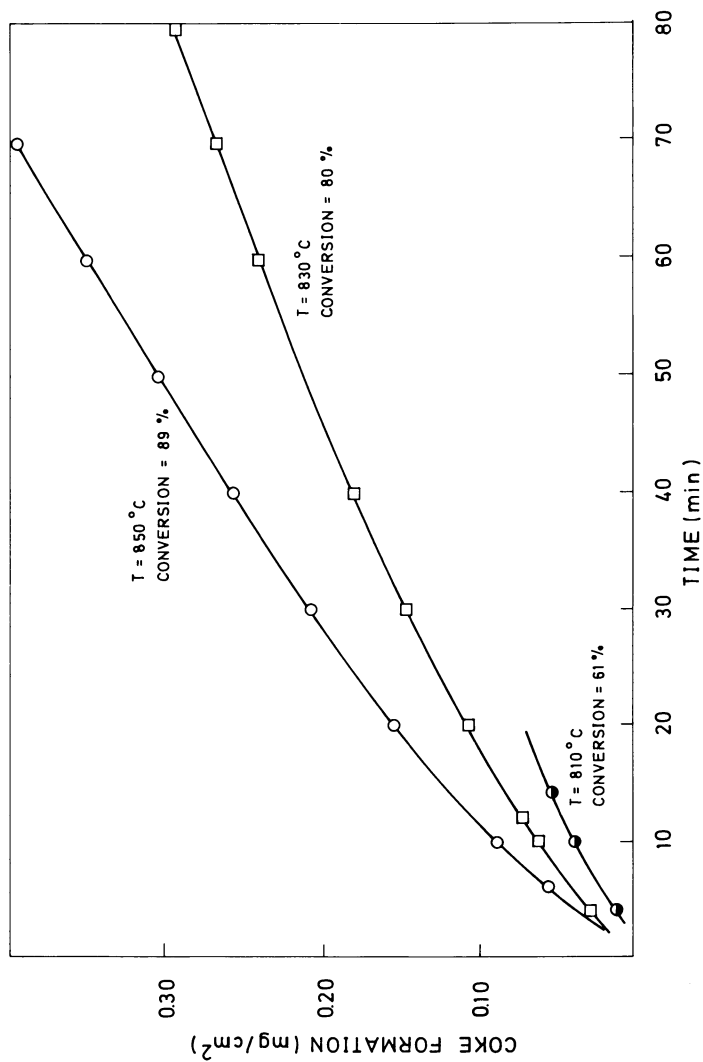


Figure. 6 Coke formation during steam cracking of propane on fresh foils (Sandvik 15Re10) in a prereduced steel reactor. Feed gas as in Figure 4.

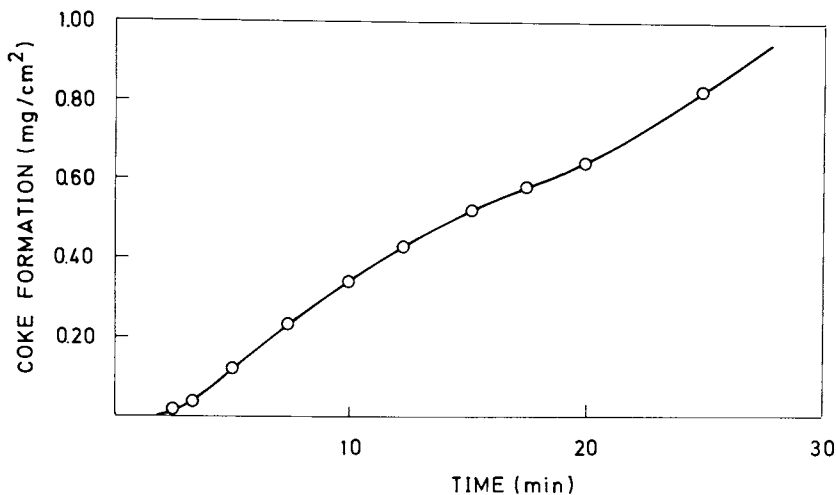


Figure 7. Coke formation during steam cracking of propane at 840°C on a steel foil (Sandvik 15Re10) in a preoxidized steel reactor. The reactor surface and the foil were preoxidized for 95 min using 46% O₂ in N₂ at 840°C. Conversion of C₃H₈:89%. Feed gas as in Figure 4.

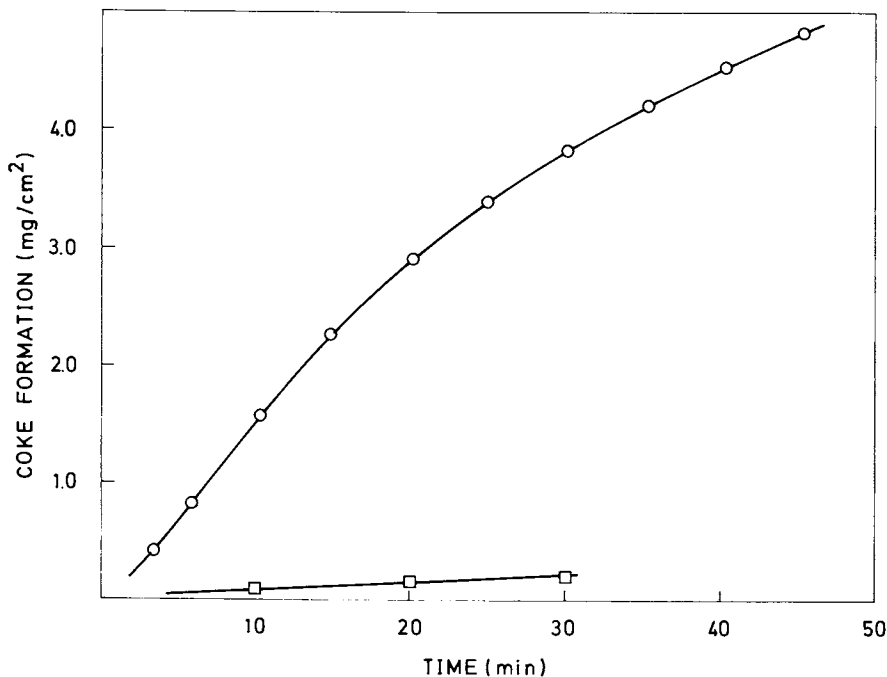


Figure 8. Coke formation during steam cracking of propane at 840°C on Ni-foils in the steel reactor. Key: ○, preoxidized; and □, prerduced. Conversion of C₃H₈:80%. Feed gas as in Figure 4.

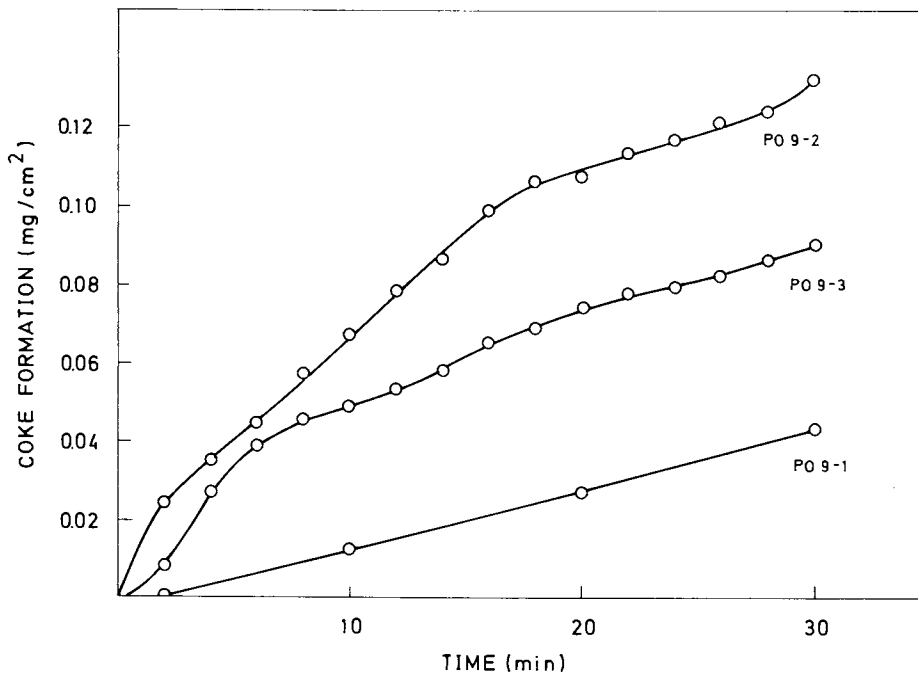


Figure 9. Coke formation during steam cracking of propane at 850°C on steel foils (Sandvik 15Re10) in a preoxidized quartz reactor.

The foil and the reactor were preoxidized for 155 min at 850°C and the coke deposit was burned out between each of the runs: PO 9-1, PO 9-2 and PO 9-3. Conversion of C_3H_8 : 98%. Feed gas as in Figure 2.

TABLE I.

Content of carbon oxides in the exit gas from steam cracking of propane in different reactors. Composition of the feed: 29 mol-% C_3H_8 , 32 mol-% H_2O and 39 mol-% N_2 . Inlet residence time = 8.2 sec. (= reactor volume/feed rate).

Reactor/ pretreatment	Conversion	Temperature	Exit gas, mol-%	
	C_3H_8 , %	°C	CO_2	CO
Steel reactor/ preoxidized	88.5	840	0.7	17.2
Quartz reactor/ preoxidized	96.7	855	-	-

TABLE II.

Effect of pretreatment of a steel reactor surface (Sandvik 15Re10) on the product gas composition during pyrolysis of ethane and ethylene at 750°C with a constant feed rate = 0.58 l/min. Dimensions of the reactor tube: length = 88 cm and inside diameter = 0.92 cm. The reactor tube was filled with pieces of the reactor material: 3.92 g or approximately 130 cm³.

Feed	Pretreatment	Exit gas composition, mol-%					Conversion %	Selectivity C ₂ H ₄ , %
		H ₂	CH ₄	C ₂ H ₆	C ₂ H ₄	C ₃ H ₆		
Ethane	New tube. ^a	13.1	0.52	74.1	12.1	0.06	14.4	81.1
Ethane	With O ₂ ^b	27.3	0.45	66.8	5.4	0.01	19.9	32.4
Ethylene	With O ₂ ^b	77.0	0.26	2.9	19.8	0.04	70.1	-
Ethylene	With H ₂ ^c	50.3	0.44	2.1	46.9	0.12	40.9	-
Ethylene	After 5 runs ^d	2.8	0.81	1.4	93.8	0.44	5.8	-

^a During the heating period the tube was exposed to an inert atmosphere (argon).

^b 0.2 l O₂/min in 15 min at 750°C. ^c 0.5 l H₂/min in 30 min at 750°C. ^d feed gas about 8 min. during each run, no gas supply between the runs.

compositions, and all of these gave significant differences in the gas and solid products (Table I and Figures 2, 5, 6, 7 and 9).

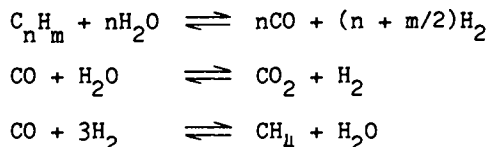
With a steel reactor it is shown that preoxidation of the foil and the reactor surface results in much higher coke formation on the foil compared with prereduction of the reactor system (Figures 6 and 7). This is not surprising since Fe and Ni present on the oxidized surface are known to be good catalysts for carbon formation (21). Prereduced foils, which contain mostly Cr and Mn on the surface, produce much less coke. In agreement with this, the coke deposit from the preoxidized foil surface contains Fe (characteristic of catalytic coke formation) whereas the deposit on the prereduced foils contains effectively no Fe (20).

Using the quartz liner, coke formation on the foils was substantially less and so were the difference between the coke formation of preoxidized and prereduced foils. Quartz has been found to be catalytically inert and any effect on steam-cracking of propane should not and does not reflect the chemical nature of the surface. Gaseous and solid products obtained in the quartz reactor are shown in Figures 2, 3 and 9. The gas phase product spectrum is typical of a quartz reactor (Figure 2) and is unaffected by the foil material. The initial rate of coke formation on the foil depends on the foil material, but the rate of coke formation on all foils appears to approach a value similar to that for coke formation on coke.

The results indicate that the effect of the reactor surface depends on the location in the reactor. At the reactor exit the tube material becomes covered in coke, and any differences due to the chemistry of the original surfaces would be expected to decrease with time on stream as seen by reference to Figure 3 and eventually disappear. However, due to the absence of coke formation over a length of reactor equivalent to the induction period (4, 19), the influence of the chemical nature of the reactor tube at the reactor inlet will persist.

However, it is the analyses of the gas phase products which is particularly interesting. It is clear from these experiments that carbon oxides are formed only on steel reactors (Table I), and this agrees with the findings of Dunkleman and Albright (12), who suggested that all carbon oxides result from gasification at a surface. In support of this, most carbon oxides are formed on pre-oxidized steels, which contain significant quantities of iron in the surface: both iron and iron oxides are known to be good gasification catalysts.

In addition, some of the formation of carbon oxides may be due to steam reforming reactions. The amount of hydrogen produced in the reaction was considerably higher over a pre-oxidized surface, while the amount of hydrocarbons was lower (Figures 2 and 5). It could well be that some of these effects are due to steam reforming reactions catalyzed by nickel exposed in the preoxidized surface. These reactions would lead to the effects observed:



with the production of hydrogen being favoured at the temperatures associated with steam cracking. Nickel and iron are known to be better catalysts for this reaction than chromium or manganese and these are better than quartz (22). As a result, the production of hydrogen should decrease and the amount of hydrocarbon should increase as the reaction is carried out over different surfaces in the following order: pre-oxidized alloy surface (Ni and Fe on the surface) > pre-reduced alloy surface (Cr and Mn on the surface) > quartz (no metals on the surface of the reactor). As seen in Figures 2 and 5 this effect has been observed experimentally.

The results show clearly the importance of the chemical nature of the actual surface in determining the product spectrum observed during steam cracking. The surface has an important bearing on both the solid and gaseous products of the reaction. It would be very interesting to establish the exact mechanism by which this occurs, but the free radical intermediates involved are not amenable to study using the present system.

Acknowledgments

The support of this work by the Royal Norwegian Council for Scientific and Industrial Research is gratefully acknowledged.

Literature Cited

1. Zdonik, S.B.; Green, E.J.; Hallee, C.P. "Manufacturing Etylene". Petroleum Publishing Corp. 1970. Tulsa, Oklahoma.
2. Goossens, A.G.; Dente, M.; Ranzi, E. Hydr.Proc. 1970. 57 (9), 227.
3. Bennett, M.J.; Price, J.B. "Behaviour In Simulated Cracker Environments of HK40 Steel, Silica and an ESC-Tube Coke". 14th Biennial American Carbon Conference Ext. Abstract Progr. 1979. 137-8.
4. Trimm, D.L. Catal. Rev. - Sci. Eng. 1977. 15 (2), 155.
5. Sundaram, K.M.; Froment, G.F. Chem. Eng. Sci. 1979. 34, 635.
6. Newsome, D.S.; Leftin, H.P. "Coking Rates in a Laboratory Pyrolysis Furnace". 72nd Annual AIChE Meeting. San Francisco. Nov. 25-29. 1979. Paper no 21d.
7. Albright, L.F.; Yu, Y.C.; Welther, K. "Coke Formation During Pyrolysis Operation". 85th National AIChE Meeting. June 4-8, Philadelphia. Paper no 15E.
8. Lahaye, J.; Badie, P.; Ducret, J. Carbon 1977. 15, 87.
9. Tsai, C.H.; Albright, L.F. "Surface Reactions Occurring

- During Pyrolysis of Light Paraffins". ACS Symp. Ser. 1976. 32, 274.
10. Crynes, B.L.; Albright, L.F. Ind. Eng. Chem. Process. Des. Dev. 1969. 8 (1), 25.
 11. Leathard, D.A.; Purnell, J.A. "Paraffin Pyrolysis". Annual Review Phys. Chem. 1970. 21, 197.
 12. Dunkleman, J.J.; Albright, L.F. "Surface Effects During Pyrolysis of Ethane in Tubular Flow Reactors". ACS Symp. Ser. 1976. 32, 241.
 13. Trimm, D.L.; Holmen, A.; Lindvåg, O.A. J. Chem. Tech. Biotechnol. 1981. 32, 241.
 14. Shah, Y.T.; Stuart, E.B.; Sheth, K.D. Ind. Eng. Chem., Process Des. Dev. 1976. 15 (4), 518.
 15. Laidler, K.J.; Sagert, N.H.; Wojciechowski, B.W. Proc. Roy. Soc. (London). 1962. 270A, 242.
 16. Tamai, Y.; Nishiyama, Y. Bull. J. Petr. Institute 1970. 12, 16.
 17. Volkan, A.R.; April, G.C. Ind. Eng. Chem., Process Des. Dev. 1977. 16 (4), 429.
 18. Albright, L.F. Ibid. 1978. 17 (3), 377.
 19. Trimm, D.L.; Turner, C.J. J. Chem. Tech. Biotechnol 1981. 31, 195.
 20. Holmen, A.; Trimm, D.L. "Coke Formation during Cracking of Hydrocarbons. Part II. In press.
 21. Lobo, L.S.; Trimm, D.L.; Figueiredo, J.L. Proc. 5th Int. Congr. Catal. 1973. 1125.
 22. Catalyst Handbook. Wolfe Scientific Texts (London). 1970.

RECEIVED June 28, 1982.

Oxidation of an Ethylene Steam Cracker Pyrolysis Tube Deposit in Water Vapor and Its Enhancement by Inorganic Catalysts

M. J. BENNETT and J. B. PRICE

Materials Development Division, AERE Harwell, Didcot, Oxon, OX11 0RA,
United Kingdom

Gasification of a carbonaceous deposit formed on a radiantly heated ethylene steam cracker pyrolysis tube, in water vapour, at 721-1056°C was chemically controlled. Oxidation rates were linear between 10-85% burn off and increased proportionally with water vapour partial pressure (38-362 mm Hg). The activation energy and pre-exponential factor were 57 Kcal mole⁻¹ and 3.6×10^9 mg cm⁻²min⁻¹ respectively. Gasification was catalysed by inorganic impurities entrained in the deposit and was promoted by hydrogen and butane.

Contamination of the deposit surface with Pb, Fe, Co and Ni (in the metallic state), Na, K, Li, Rb and Cs carbonates or oxides, and Ba and Sr oxides enhanced gasification, at 900°C, by up to a factor of 135. Catalysis derived from oxygen transfer mechanisms. A further nineteen elements had no significant influence.

A principal factor governing the operating cycle of ethylene steam crackers (ESC) is coke formation on the inside surfaces of the radiantly heated pyrolysis tubes. Steam is used as the carrier for the hydrocarbon feedstock as it is known empirically to minimise this coking. It is probable that the observed deposition is a net process representing the difference between formation and removal, primarily by thermal oxidation. A fundamental requirement of any detailed understanding of the overall processes involved, therefore, is knowledge of the oxidation behaviour of such deposits. Although several studies have been undertaken on various carbons considered to simulate ESC pyrolysis tube coke (e.g. (1)) no relevant information has been published for plant material. To provide these data, therefore, the oxidation behaviour of a coke formed on an ESC tube has now been examined in water vapour.

It is now well established (2-4) that the oxidation of carbon can be catalysed by certain metals and inorganic compounds; although information is less comprehensive for water vapour. As a consequence the effectiveness of a number of elements in promoting the oxidation of the radiant heater tube coke in this environment has been surveyed.

Experimental

The carbonaceous deposit was formed on the wall of a radiantly heated HK40 steel pyrolysis tube in an ethylene steam cracker from a naphtha hydrocarbon feedstock. It was derived from a region in which the temperature of the gas was 820-830°C, while that of the underlying tube wall was 920-930°C. The tube had been operated for 3 years on a cycle consisting of ~50 days cracking followed by decoking to burn out the carbonaceous deposits successively formed. The deposit examined was, therefore, that laid down during the final cracking operations. Its physical and chemical characteristics have been described (5).

The oxidation of randomly selected deposit samples, of approximate size 5 mm x 5 mm, was followed using a CI Electronics Mk 2 controlled atmosphere microbalance.

Argon, used both as the carrier gas for the oxidant, water vapour, and also as a purge gas was obtained from a liquid supply. It was purified by passage through BTS catalyst and magnesium perchlorate to remove oxygen and water vapour respectively. Water vapour was added at a prescribed partial pressure (p_{H_2O}), between 58-362 mm Hg, by passing the purified argon through a heated water saturator. Hydrogen, or any other gas required, was then added to the reaction gas, which at 1 atm pressure passed up over the sample suspended within an externally heated silica reaction vessel. Dry argon flowed continuously through the balance head and was exhausted, together with the exit gases from the reaction vessel, through a side arm located just above the furnace. This procedure protected the balance mechanism from water vapour and reaction products and also prevented condensation on the hangdown rods.

The experimental procedure was to bring the sample up to constant temperature (between 721-1056°C) in dry argon and then change to the reaction gas. Oxidation was followed by the continuous measurement of the loss in sample weight.

Surface contamination with inorganic salts was carried out by boiling deposit samples for 10 mins in either a 30wt.% or saturated salt solution, whichever was the lower concentration. After cooling in the solution the samples were removed and dried under an infra-red lamp at ~150°C. With certain salts (tin, bismuth and zirconium), which were unstable on boiling, the samples were soaked in the appropriate solution overnight and were air dried. Where possible, salts of organic acids were chosen as they decomposed in dry argon to the respective metal oxides at

temperatures below 500°C. Other salts (e.g. halides and sulphates) could have contaminated the deposit substrate with anions which could have affected the oxidation kinetics. The heat treatment of the sample was continued until constant sample weight was attained at the oxidation temperature before the reaction gas was admitted. The oxidation was then followed in an identical manner to that already described.

Results

In the kinetic plots (Figures 1-3, 5 and 6) the measurements of oxidation (i.e. the loss of sample weight) were normalised in terms of both the initial sample weight and the geometric surface area. The respective scales are given on the left and right hand sides of each figure.

Effect of Sample Containment and Gas Flow Rate. Two series of experiments established that, with the experimental procedures and conditions studied, gasification was controlled by chemical kinetics and not gas access. For experimental convenience the samples were contained within a silica crucible. To ensure that this would not impede gas movement either to or from the oxidising surface, the oxidation behaviour of a contained sample was compared with that of a sample freely suspended within the environment. At the highest temperature (1056°C), there was no significant difference over 70% burn off between either the kinetics or rates of oxidation of the samples in water vapour ($p_{\text{H}_2\text{O}} = 58 \text{ mm Hg}$). All subsequent specimens were exposed, therefore, within silica crucibles, except when the samples were contaminated with the alkali salts, where gold crucibles were used.

The second experimental parameter examined was the rate of gas supply to the specimen. Varying the argon carrier flow rate from 156 to 1000 $\text{cm}^3\text{min}^{-1}$ had no marked effect upon the oxidation behaviour of the deposit in water vapour at either 815°C (with $p_{\text{H}_2\text{O}} = 362 \text{ mm Hg}$) or 1050°C (with $p_{\text{H}_2\text{O}} = 58$ and 362 mm Hg) (Figure 1). In the majority of the later experiments the argon flow rate was maintained at 500 $\text{cm}^3\text{min}^{-1}$.

Effect of Deposit Structure. The deposit consisted of two layers with widely different concentrations of entrained inorganic impurities (5). The inner, thin, layer of filamentous material contained the bulk of the inorganic impurities analysed in the deposit; the principal constituents being 0.7 wt.% Fe, 0.1 wt.% Ni and 0.15 wt.% Cr. The corresponding levels in the outer, thicker pyrocarbon layer were considerably smaller, being 200 ppm Fe, 50 ppm Ni and 50 ppm Cr. Gas permeability through the deposit was low (5) so that only the outer deposit surface would have been oxidised in service, providing, of course, there were no radial cracks through the deposit.

To examine the effect of the inner layer, the oxidation of "as received" deposit was compared with that of material from which the inner layer had been removed by abrasion on silicon carbide papers,

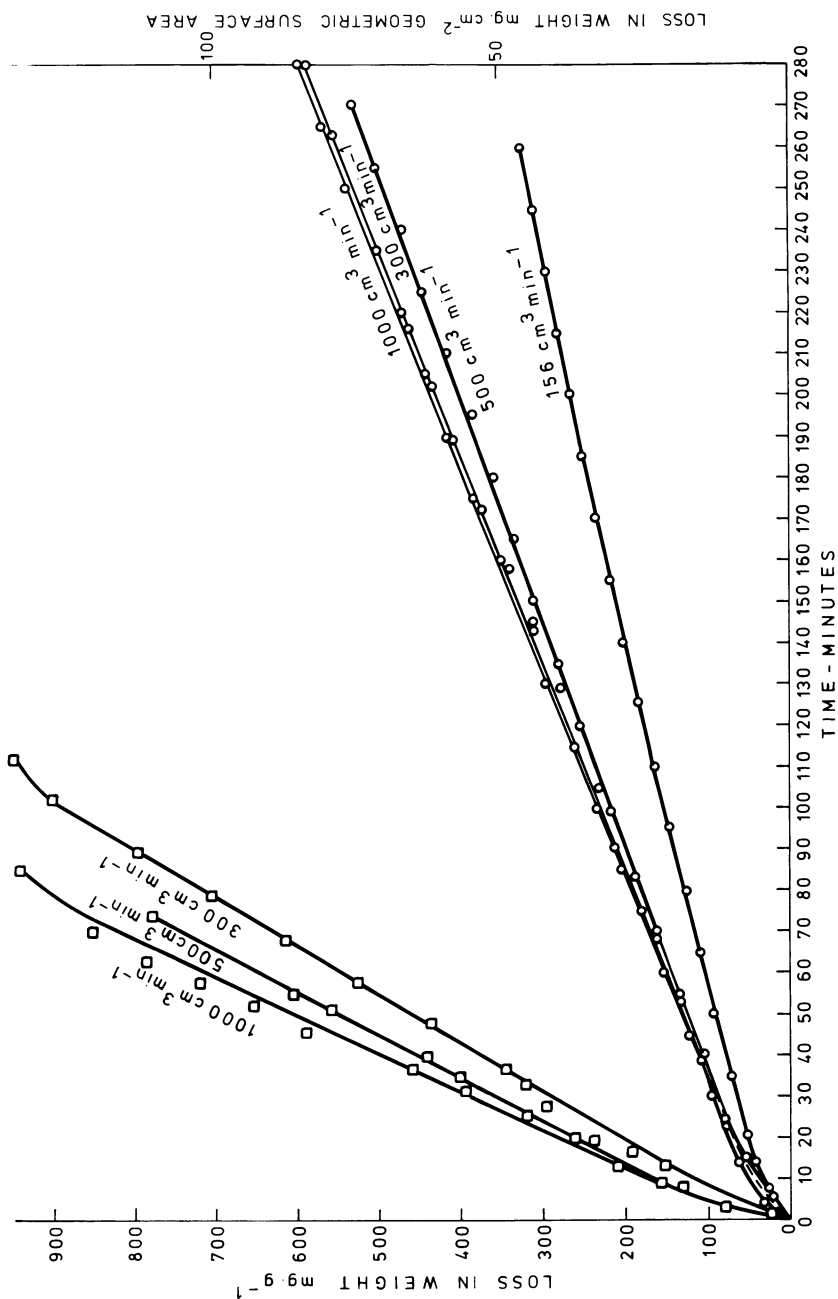


Figure 1. Effect of argon carrier flow rate upon the deposit oxidation by water vapor at 1056°C.
Key to water vapor partial pressure: ○, 58 mm Hg; and □, 362 mm Hg.

with a final abrasion in one experiment with 45 μm diamond. The exposure conditions covered the middle and upper temperatures (863 and 1056°C) and the minimum and maximum water vapour partial pressures (38 and 362 mm Hg) of the ranges studied. As shown in Figure 2 there was no marked effect of the abrasion. Although this was a somewhat arbitrary process and the inner layer had a variable thickness, the abrasion would have removed the bulk of the inner layer together with the associated inorganic impurities. Unless stated otherwise all other samples oxidised were of "as received" deposit.

Effect of Water Vapour Partial Pressure. The influence of water vapour partial pressure was examined at 815 and 1056°C. At the lower temperature one sample was oxidised at successively increasing partial pressures (100, 196 and 362 mm Hg respectively). On both occasions when $p_{\text{H}_2\text{O}}$ was increased so also did the reaction rate. If there was a simple power relationship between the oxidation rate and $p_{\text{H}_2\text{O}}$, i.e. rate $\propto (p_{\text{H}_2\text{O}})^n$, then n may be determined by comparison of the oxidation rates, r_1 and r_2 , at the instant of change of $p_{\text{H}_2\text{O}}$ from p_1 to p_2 and thus, also at the same extents of oxidation, from the expression,

$$n = \log \frac{r_2}{r_1} / \log \frac{p_2}{p_1}$$

Experimentally, for the increase in $p_{\text{H}_2\text{O}}$ from 100 to 196 mm Hg, and from 196 to 362 mm Hg, the oxidation rates were 1.3 and 2.7 mg/gh and 1.6 and 3.4 mg/gh respectively. The corresponding values derived for n were 1.1 and 1.2, suggesting that the rate was directly proportional to water vapour partial pressure.

At 1056°C a different, but complementary, procedure was used to investigate the effect of $p_{\text{H}_2\text{O}}$ on reaction rate. Separate deposit samples were oxidised in six different water vapour pressures between 38 and 362 mm Hg (Figure 3). The oxidation kinetics were all of a similar form, in that initially, the rate decreased with burn off up to 5-10% removal and then was essentially linear up to nearly 90% burn off before decreasing with greater attack. The last change was undoubtedly associated with the diminution of the sample size so that the proportionality relationship with the initial sample weight or surface area no longer applied. The mean reaction rates increased in direct proportion with $p_{\text{H}_2\text{O}}$ (Figure 4), as observed at 815°C.

Effect of Temperature. The oxidation of separate samples in 362 mm Hg water vapour pressure was examined at nine temperatures between 721 and 1056°C (Figures 5 and 6). At all temperatures, except at 959°C and possibly the lowest temperature 721°C, the oxidation kinetics already described applied. At 721°C oxidation was continued only up to \sim 10% burn off, so that the kinetics could

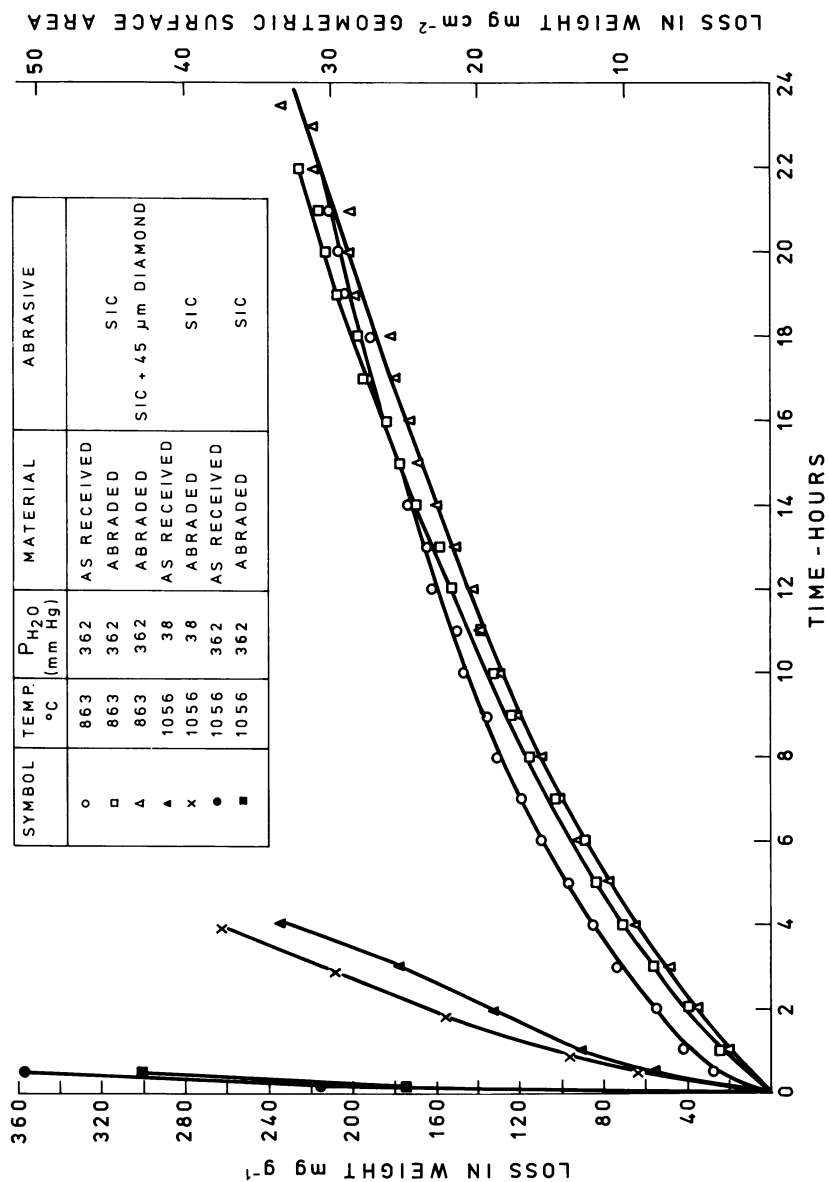


Figure 2. Effect of deposit structure on oxidation behavior.

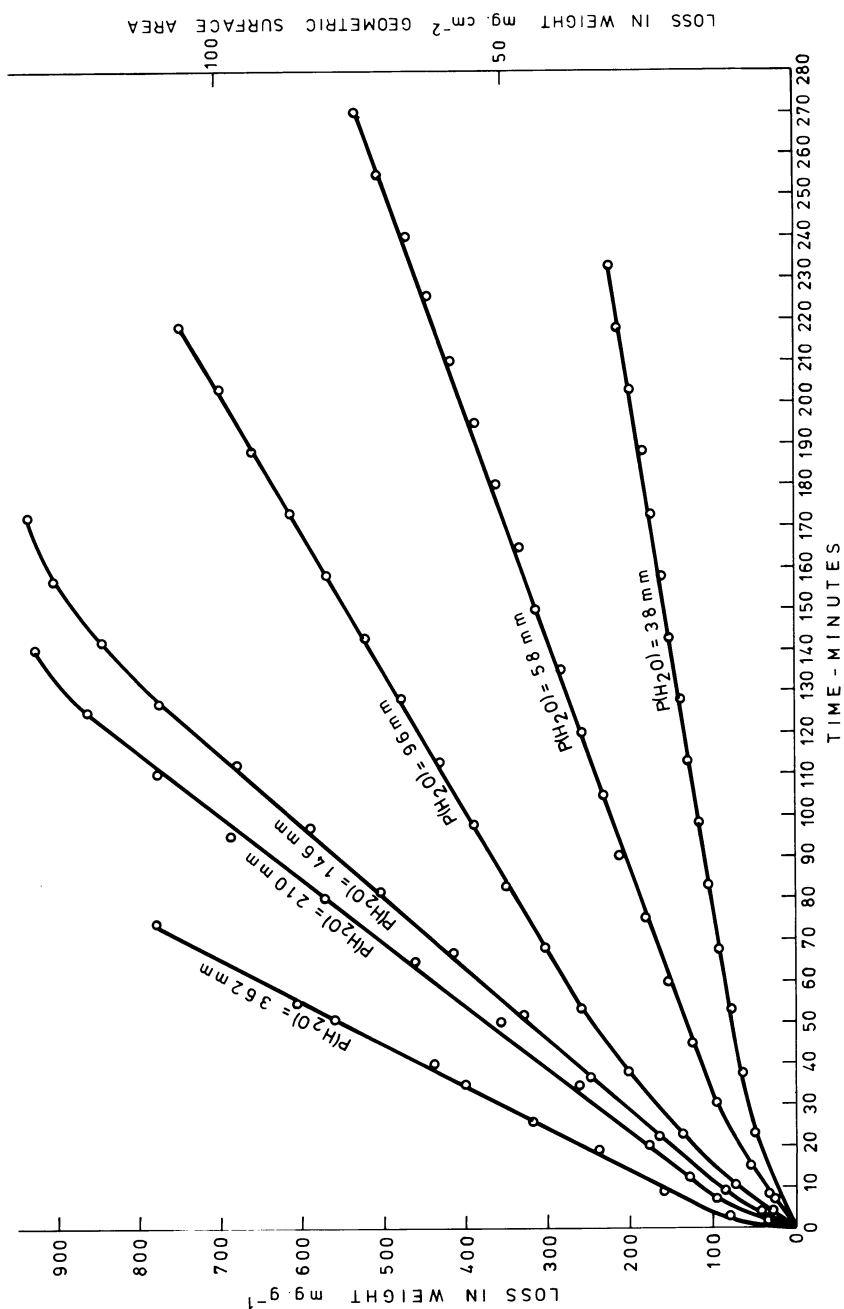


Figure 3. Effect of the water vapor partial pressure (P_{H_2O}) on deposit oxidation at 1056°C.

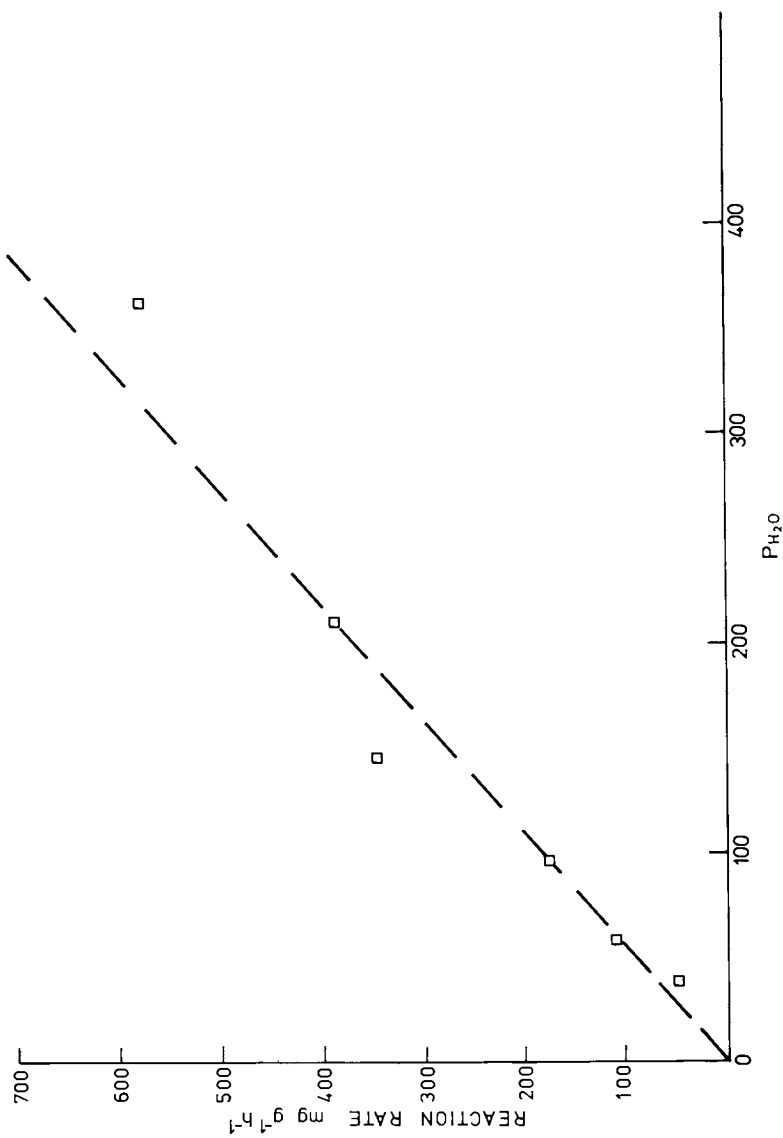


Figure 4. Effect of water partial pressure (P_{H_2O}) on the rates of deposit oxidation at 1056°C.

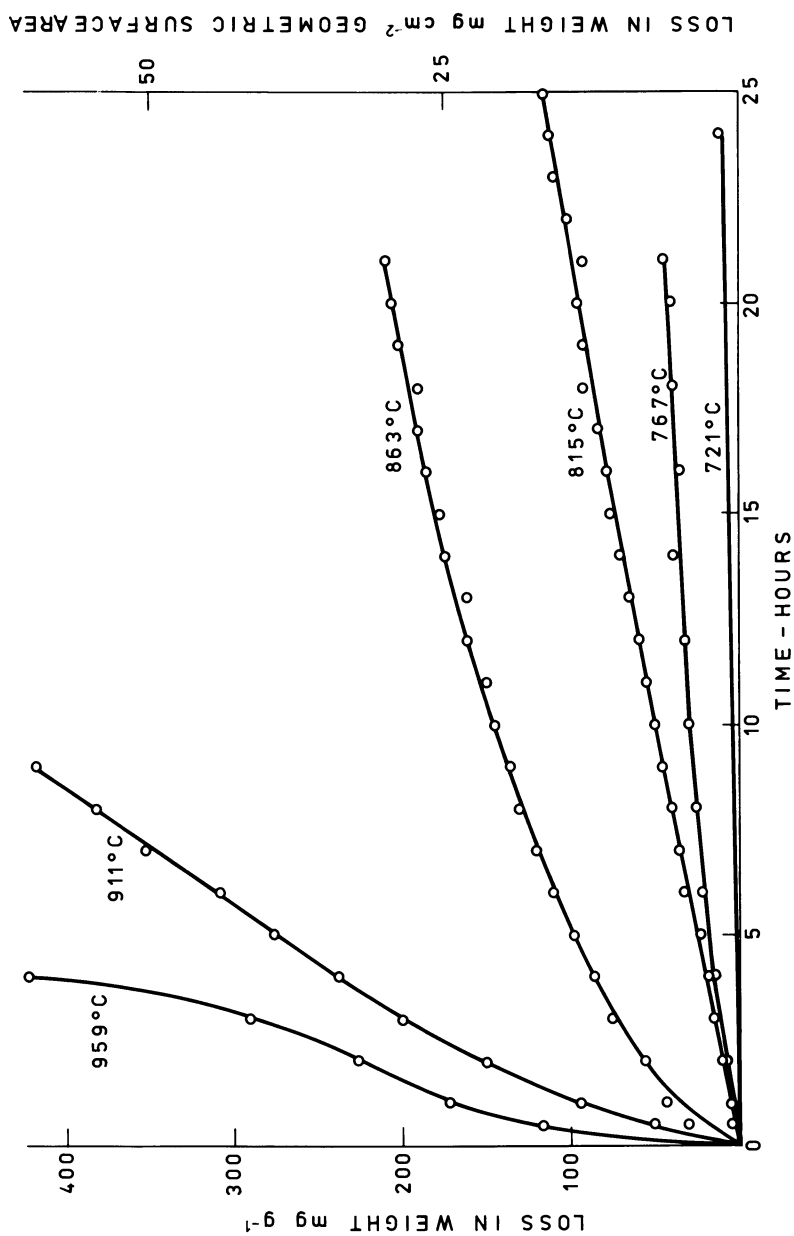


Figure 5. Deposit oxidation between 721-959°C in 362 mm Hg partial pressure water vapor.

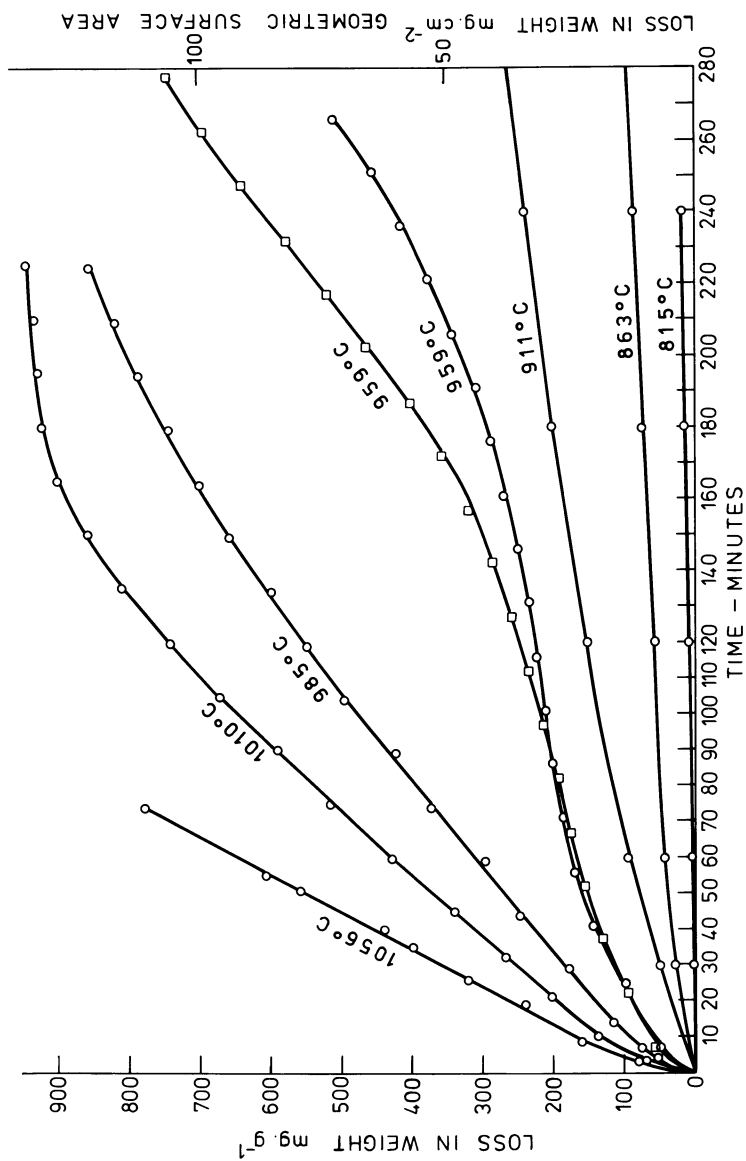


Figure 6. Deposit oxidation in 362 mm Hg partial pressure water vapor between 815-1056°C.

not be established with certainty. At 959°C the kinetics were different, in that the weight loss vs time curves were sigmoidal. Thus, after the initial period during which the oxidation rate decreased, it then gradually increased with time up to 80% burn off and finally decreased for the reasons already outlined. To examine the temperature dependence, average linear reaction rate constants were calculated at the end of the exposure, or 80% burn off, whichever was the greater. The resultant Arrhenius plot (Figure 7) gave values of the activation energy as 57 Kcal mole⁻¹ and of the pre-exponential factor as 3.6×10^9 mg cm⁻²min⁻¹.

Effect of Hydrogen. The influence of hydrogen additions to the environment was examined at 900 and 1056°C. With the experimental procedure employed, increasing p_{H_2} could only be accomplished by concurrently decreasing p_{H_2O} . At the lower temperature a deposit sample was oxidised initially in 362 mm Hg partial pressure water vapour and hydrogen was added stepwise at increasing partial pressures from 19.4 to 209 mm Hg (Figure 8). The water vapour partial pressures then decreased respectively from 354 to 262 mm Hg and the p_{H_2}/p_{H_2O} ratios ranged from 0.005 to 0.80. The initial hydrogen addition enhanced the rate of attack but its influence diminished with time. The pattern was repeated by successively smaller extents on each subsequent increase in p_{H_2} . The increased rates due to these hydrogen additions always exceeded, however, any reductions in rate resulting from the corresponding stepwise p_{H_2O} decrease. On removal of the hydrogen, which was accompanied by an increase in the water vapour partial pressure, the oxidation rate decreased but was accelerated again on the readmission of hydrogen.

At 1056°C the effect of hydrogen was examined on the oxidation behaviour of separate samples and in some experiments it was added continuously throughout the exposure (Figure 9). A hydrogen partial pressure of 19.4 mm Hg had no apparent influence upon the deposit oxidation in 353-362 mm Hg partial pressure water vapour. However, the reaction rates were extremely rapid, which could have masked any relatively small effect of hydrogen. At a lower p_{H_2O} (36.3-38.0 mm Hg) the addition of hydrogen, at a partial pressure of 34.5 mm Hg, either continuously throughout oxidation or after an initial period of oxidation in water vapour alone, enhanced the gasification rate considerably. Immediately the hydrogen addition was discontinued, the oxidation rate decreased to that for the p_{H_2O} alone. Hydrogen exerted a similar influence upon the oxidation behaviour of an abraded sample, as it had done upon that of the complete deposit.

Effect of Butane. The influence of butane additions upon the oxidation behaviour of abraded samples was examined at 793, 838 and 882°C. For the majority of the experiments, the p_{Butane}/p_{H_2O} ratio was changed by maintaining p_{Butane} and altering p_{H_2O} .

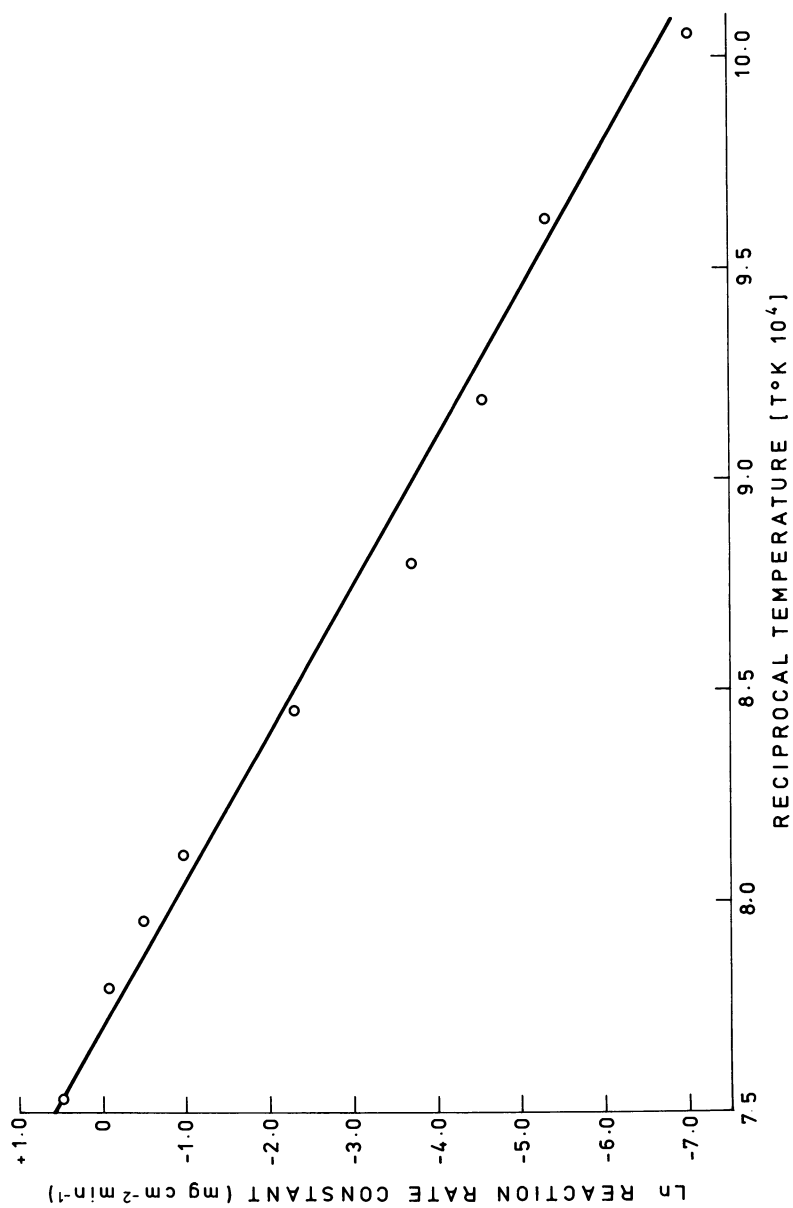


Figure 7. Arrhenius plot for the oxidation of the deposit in 362 mm Hg partial pressure water vapor.

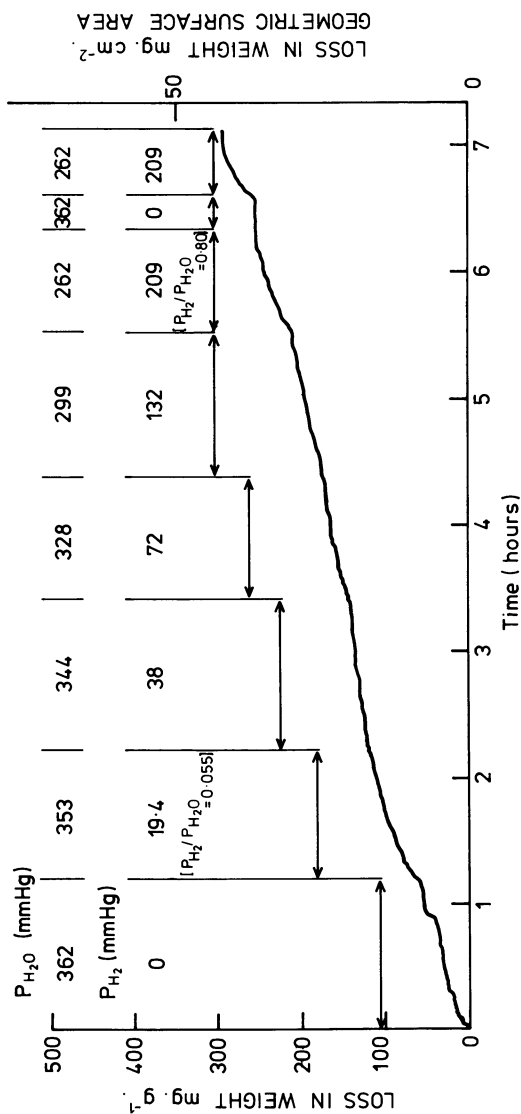


Figure 8. Effect of hydrogen upon deposit oxidation in water vapor at 900°C.

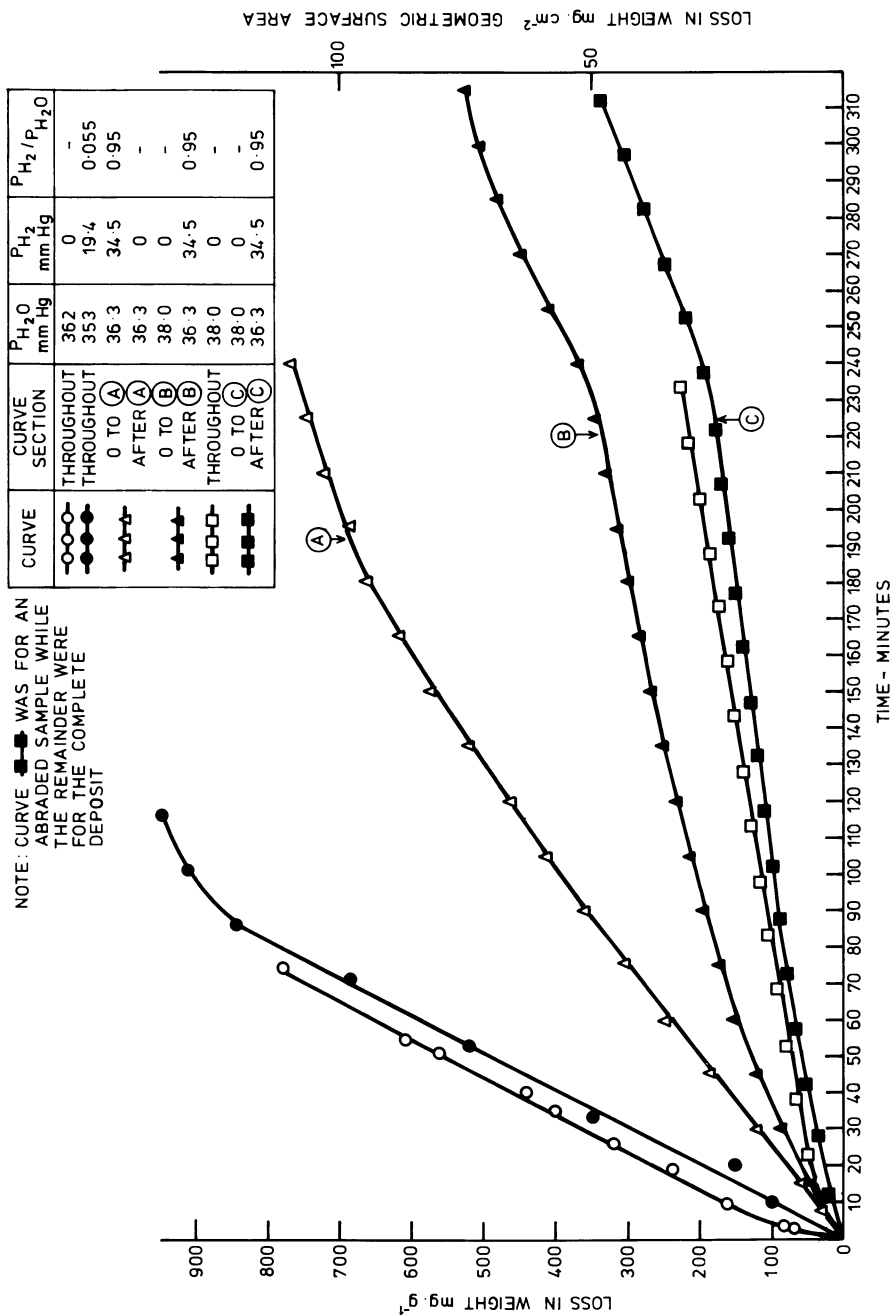


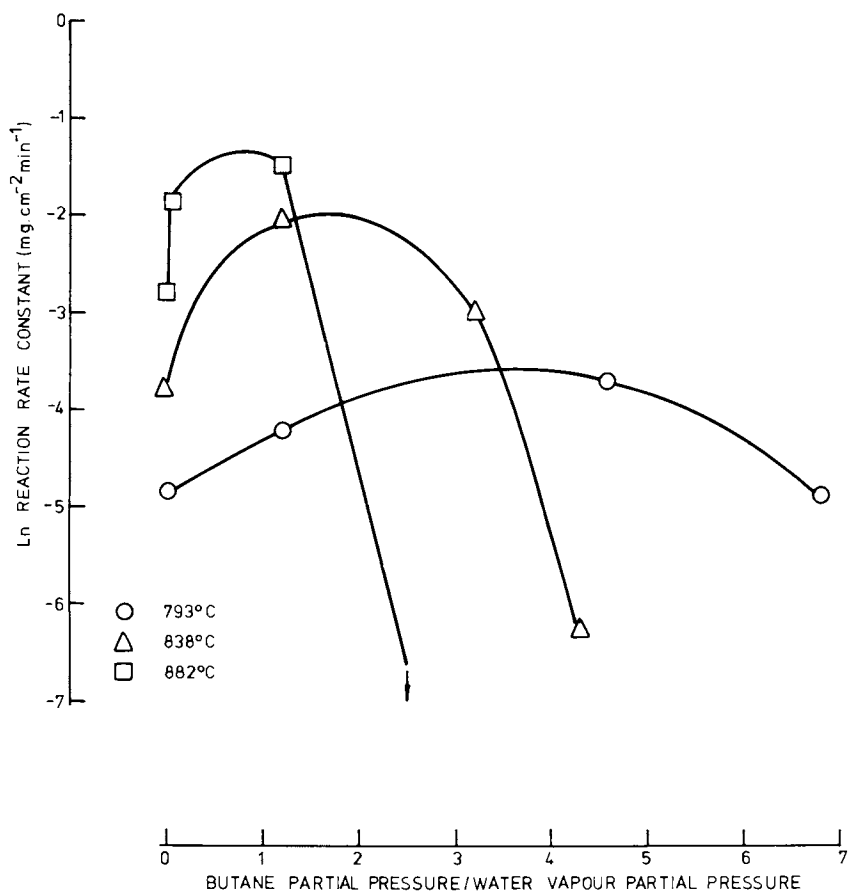
Figure 9. Effect of hydrogen upon deposit oxidation by water vapor at 1056°C.

The variation in reaction rate constant with $P_{\text{Butane}}/P_{\text{H}_2\text{O}}$ at each of the respective temperatures is shown in Figure 10. At each temperature with increasing $P_{\text{Butane}}/P_{\text{H}_2\text{O}}$ the reaction rate constant increased, went through a maximum and then decreased. The $P_{\text{Butane}}/P_{\text{H}_2\text{O}}$ ratio for the maximum decreased with increasing temperature. In interpreting these results it should be recalled that the basic experimental measurement was of sample weight change. The initial butane additions promoted the rate of sample weight loss due to oxidation, but with increasing $P_{\text{Butane}}/P_{\text{H}_2\text{O}}$ this was gradually exceeded by weight gain due to carbon deposition. SEM examination confirmed the occurrence of limited filamentary deposition on specimen surfaces exposed to $P_{\text{Butane}}/P_{\text{H}_2\text{O}} = 1.2$ at all three temperatures (6). The maximum influence of butane on oxidation at each temperature is given by the difference between the maximum reaction rate constant and that at $P_{\text{Butane}}/P_{\text{H}_2\text{O}} = 0.1$. On this basis the maximum factors by which the oxidation rate in a water vapour partial pressure of 316-345 mm Hg was increased by a butane partial pressure of 16-415 mm Hg at 793, 838 and 882°C were 3.5, 5.9 and 4.3 respectively.

Influence of Inorganic Contaminants. The effect of gross inorganic contamination of the ESC deposit surface was examined upon its oxidation, in water vapour, at 900°C. The influence of thirty-one elements, in either an oxidised or elemental condition, was studied. In the majority of the experiments, after an initial exposure to water vapour alone, hydrogen was added such that its partial pressure was increased stepwise over the subsequent exposure. During this period there was a corresponding decrease in $P_{\text{H}_2\text{O}}$. The ranges of P_{H_2} and $P_{\text{H}_2}/P_{\text{H}_2\text{O}}$ used were comparable to those whose influence had been examined already on the deposit oxidation, at the same temperature. Periodic control experiments (i.e. with untreated deposit samples) were carried out to establish that cross contamination had not arisen.

The inorganic contaminants could be divided into two groups, firstly, those which exerted, at most, a small influence and secondly, those which substantially enhanced gasification. Experimental data for the nineteen elements falling in the first group summarise the salt used in the surface treatment, the probable chemical state of the element during deposit oxidation, taking into account the $P_{\text{H}_2}/P_{\text{H}_2\text{O}}$ range covered and the number of atoms of the element per initial surface carbon site. The average oxidation rates for surfaces contaminated with boron, magnesium, aluminium, phosphorus, calcium, vanadium, chromium, manganese, iron (as oxide), copper, zinc, zirconium, molybdenum, silver, cadmium, tin, lanthanum, cerium and bismuth either fell within, or were up to 50% above the range of the values for untreated deposit (Table 1).

The experimental data for the eleven elements which catalysed the oxidation rate markedly, by factors up to 135, are summarised



RATIO $\frac{P(\text{BUTANE})}{P(\text{H}_2\text{O})}$	0	0.05	1.2	3.2	4.3	4.6	6.8
P(BUTANE) (mm Hg)	0	16	415	415	415	415	415
P(H ₂ O) (mm Hg)	345	337	345	129	96	90	61

Figure 10. Effect of the addition of butane upon the oxidation of the deposit.

Table I

Summary of conditions of experiments for elements having either no effect or possibly a slight influence upon ESC deposit oxidation in 262-362 mm Hg water vapour partial pressure at 900°C

Element	Salt	Probable chemical state at commencement of oxidation	No. of atoms of element per initial active carbon site	P_{H_2}/P_{H_2O} range (a)	Average reaction rate mg/gh (b)
Boron	boric acid	oxide	354	No H ₂ added	29
Magnesium	acetate	oxide	130	0.06-0.80	27
Aluminium	nitrate	oxide	14	0.06-0.80	30
Phosphorus	ammonium dihydrogen phosphate	oxide	242	0.06-0.80	28
Calcium	nitrate	oxide	90	0.06-0.80	38
Vanadium	ammonium vanadate	oxide	49	0.06-0.80	24
Chromium	nitrate	oxide	24	0.06-0.80	29
Manganese	acetate	oxide	39	0.06-0.80	46
Iron	citrate	oxide	72	0.06-0.80	32
Copper	acetate	metal	15	0.06-0.80	33
Zinc	acetate	oxide	69	0.06-0.80	16
Zirconium	nitrate	oxide	86	0.06-0.80	35
Molybdenum	ammonium molybdate	oxide	287	0.06-0.80	26
Silver	nitrate	metal	187	0.06-0.80	23
Cadmium	acetate	metal	65	0.06-0.80	22
Tin	nitrate	metal	39	0.06-0.80	35
Lanthanum	acetate	oxide	61	0.06-0.80	36
Cerium	nitrate	oxide	86	No H ₂ added	44
Bismuth	nitrate	metal	55	0.06-0.80	20

(a) Initially oxidation was in $P_{H_2O} = 362$ mm Hg. Subsequently, for $P_{H_2}/P_{H_2O} = 0.055$, $P_{H_2O} = 353$ mm Hg and $P_{H_2} = 19.4$ mm Hg, while for $P_{H_2}/P_{H_2O} = 0.80$, $P_{H_2O} = 262$ mm Hg and $P_{H_2} = 209$ mm Hg.

(b) For comparison the average reaction rates for seven separate untreated samples of deposit oxidised over the same P_{H_2O}/P_{H_2O} range, at 900°C, were 12, 15, 17, 21, 25, 27 and 30 mg/gh (Average = 21 mg/gh).

in Table 2, while the oxidation curves are shown in Figures 11-14. All the alkali metal oxides or carbonates were active (Figure 11) with their effectiveness decreasing with burn off. This has been indicated in Table 2 by separating the initial, high and the subsequent, slower, reaction rates, which, in general, were still greater than that of untreated deposit. On the assumption that the effectiveness of these elements was directly proportional to their surface concentration then the order of increasing activity of the salts of these elements was sodium comparable with potassium, lithium, caesium and rubidium. The alkaline earth oxides also enhanced oxidation, although to a smaller extent than the alkali metal carbonates or oxides. The results for calcium oxide have been discussed already, while the effects of barium and strontium oxides are shown in Figure 12. Again the effectiveness of these contaminants decreased with burn off, but even after 50% gasification they enhanced the oxidation rate by a factor between 2 and 4. Lead promoted deposited oxidation only after the introduction of hydrogen to the gas phase such that P_{H_2}/P_{H_2O} was 0.055 and it would have been present in the metallic state (Figure 12). Iron, present as an oxide, had no influence upon deposit oxidation (Figure 13). However, when the P_{H_2}/P_{H_2O} ratio was increased above that required (1.2) to ensure that the element was in the metallic state, it was extremely catalytic. Other transition metals, nickel and cobalt, also promoted gasification (Figure 14) with their activity being comparable to that of iron. Nickel was effective from the onset of the exposure to water vapour, as the hydrogen released by the oxidation was sufficient to ensure that the element was completely reduced. In contrast, cobalt oxide, formed by decomposition of the acetate with which the sample was treated, was only reduced to the elemental state on the addition of hydrogen to the gas phase such that P_{H_2}/P_{H_2O} exceeded that (0.04) at which the oxide was no longer thermodynamically stable.

Scanning Electron Microscopy. The surface topography of deposit samples oxidised at various temperatures and extents of oxidation were examined by scanning electron microscopy. To provide a basis for subsequent comparison, it was desirable to establish first the topography of the residual ash after complete combustion. That formed at 1056°C consisted of discrete fragments of varying size (Figure 15a) having a skeletal structure. After 21% burn off at 862°C the outer deposit surface (i.e. nearest the original gas interface) was criss-crossed with cracks (Figure 15b). The surface between the cracks was smooth with localised regions covered with iron rich debris (Figure 15c) with the smaller fragments being located particularly along the crack edges. Channelling had occurred at the sample edges, while the inner surface (i.e. nearest to the original tube interface) was covered with inorganic debris remaining from the oxidation of the inner deposit layer (Figure 15d). The structural features of the debris

Table II

Summary of the conditions for the experiments in which various elements enhanced the deposit oxidation in 362 mm Hg partial pressure water vapour at 900°C

Element	Salt	Probable chemical state at commencement of oxidation	No. of atoms of element per initial active carbon site	Initial reaction rate mg/gh	Burn off over which initial rate applied	Factor by which initial rate was enhanced	Subsequent reaction rate mg/gh	Burn off over which subsequent rate applied	Factor by which subsequent rate was enhanced
Lithium	acetate	oxide	145	440	0-10	21	30	25-30	1
Sodium	carbonate	carbonate	240	350	0-40	17	165	70-85	8
Sodium	carbonate	carbonate	215	435	0-40	21	185	60-75	9
Potassium	carbonate	carbonate	455	690	0-50	33	345	60-70	16
Rubidium	carbonate	carbonate	290	2830	0-20	135	65	75-85	3
Caesium	carbonate	carbonate	55	2700	0-10	130	55	45-55	2.5
Strontium	nitrate	oxide	65	100	0-20	5	40	40-50	2
Barium	nitrate	oxide	145	220	0-10	10	85	47-59	4
Lead	acetate	metal	20	125(A)	14-30	6			
Iron	citrate	metal	35	230(B)	15-60	11			
Cobalt	acetate	metal	25	440(A)	18-45	21	160	68-76	8
Nickel	acetate	metal	50	195	0-50	9	100	65-77	5

(A) Maximum rate in $P_{H_2O} = 353$ mm Hg, after $P_{H_2} = 19.4$ mm Hg added.

(B) Rate in $P_{H_2O} = 23.4$ mm Hg, after $P_{H_2} = 35.1$ mm Hg added.

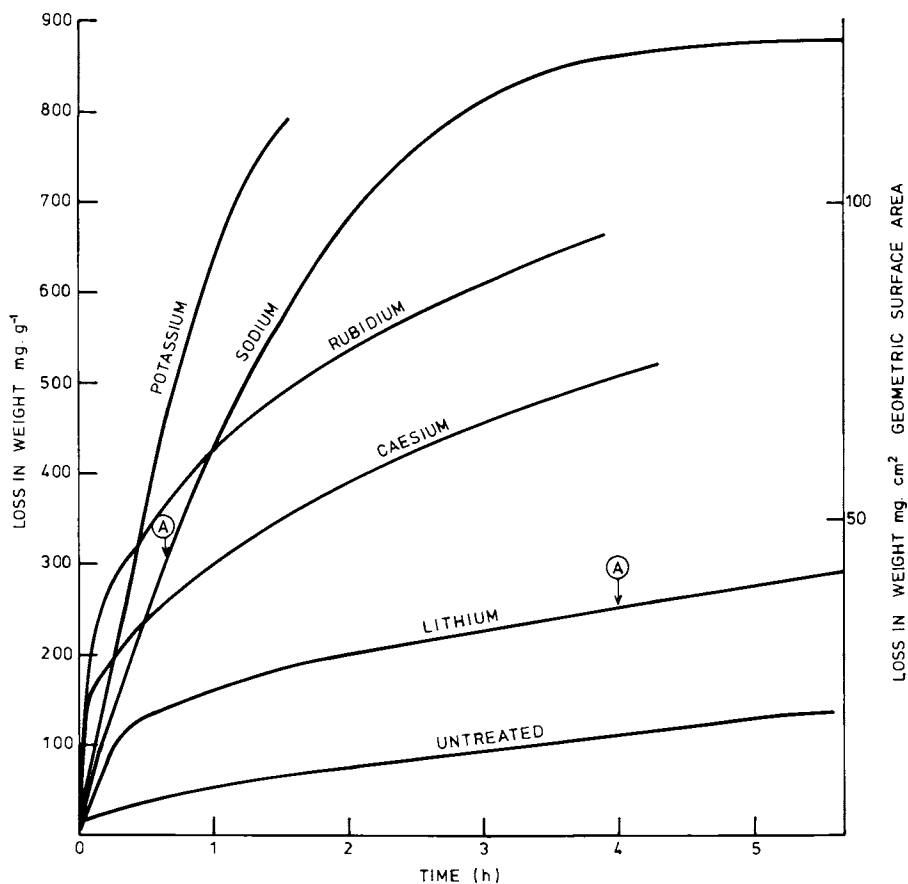


Figure 11. Effect of alkali metal salts upon the oxidation of the deposit in water vapor at 900°C. For all curves $P_{H_2O} = 362$ mm Hg except those after (A) when $P_{H_2} = 19.4$ mm Hg was added to $P_{H_2O} = 353$ mm Hg.

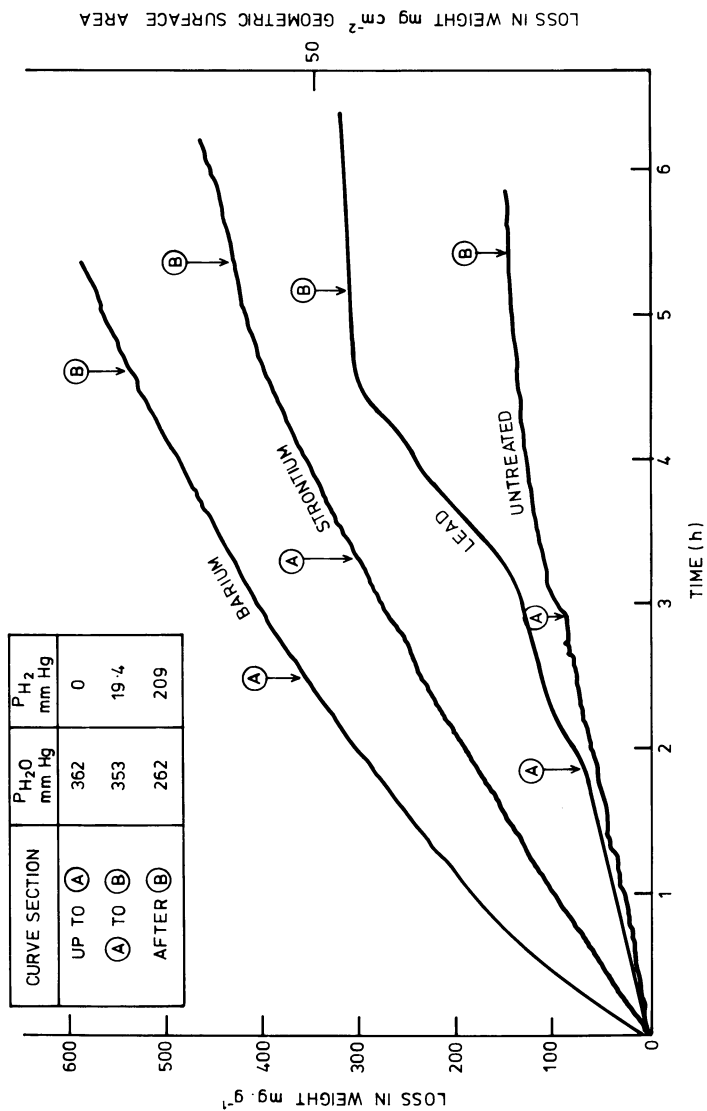


Figure 12. Effect of barium and strontium oxides and lead upon the oxidation of the deposit in water vapor at 900°C.

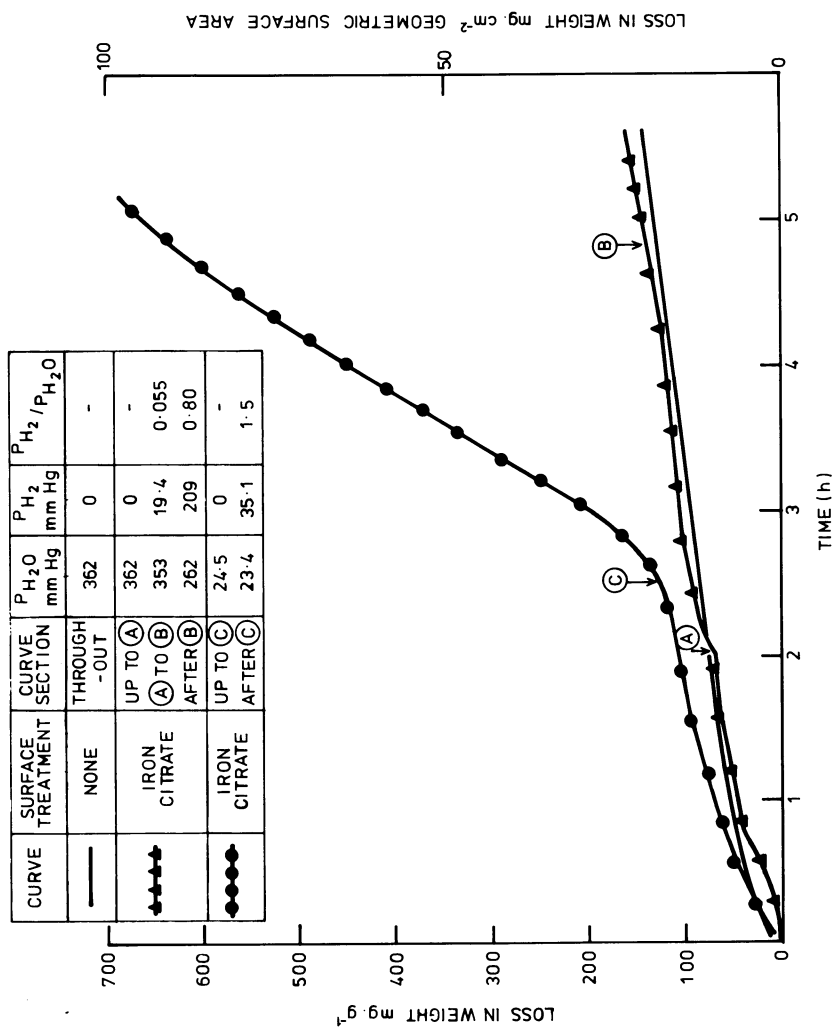


Figure 13. Effect of iron upon the oxidation of the deposit in water vapor at 900°C.

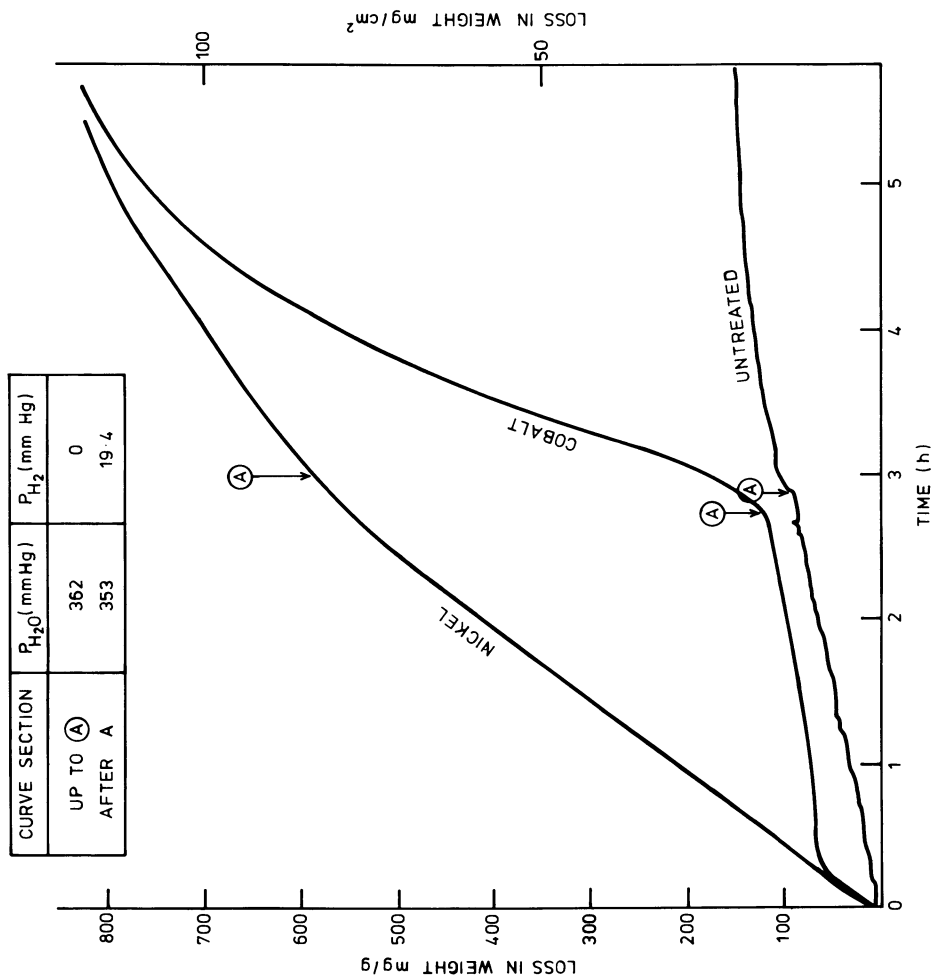


Figure 14. Effect of nickel and cobalt upon the oxidation of the deposit in water vapor at 900°C.

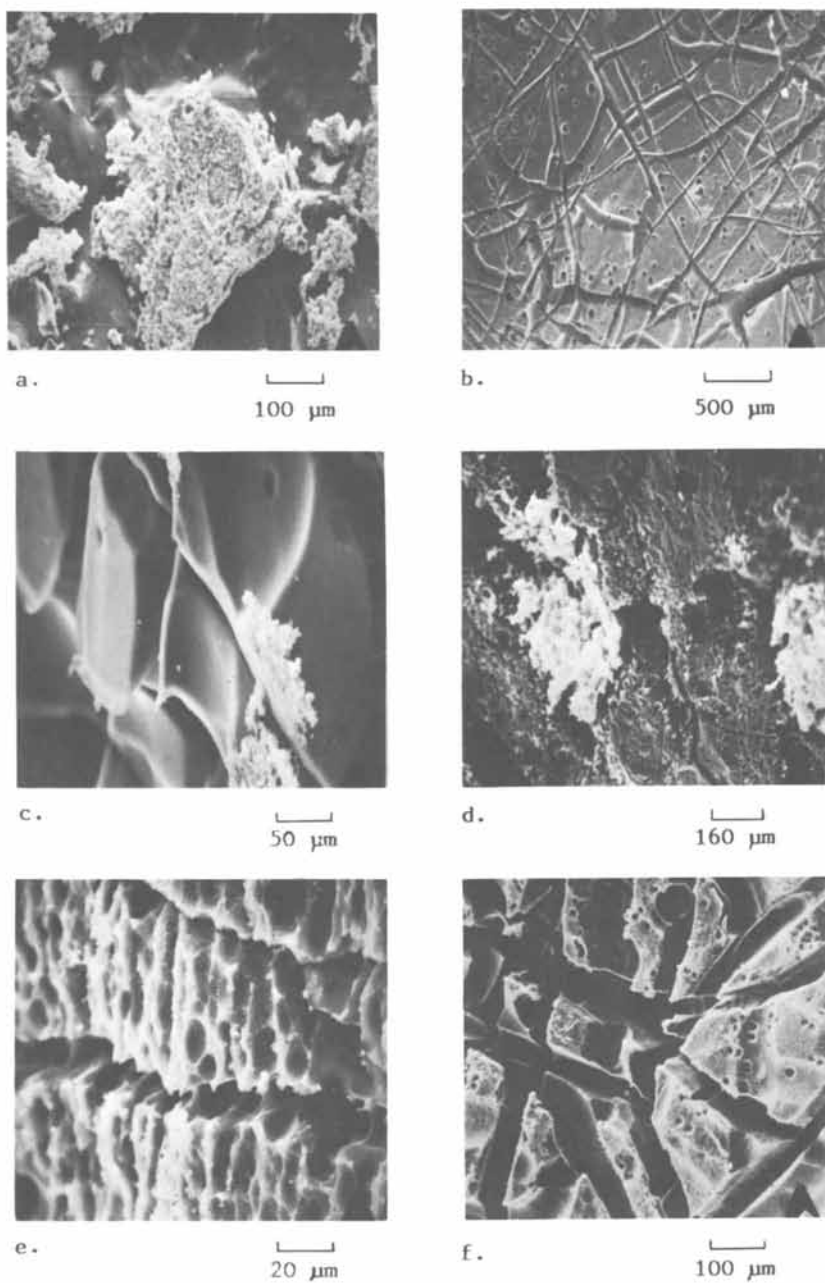


Figure 15. Surface topography of oxidized ESC deposits.

appeared to be similar to that of the ash. The underlying carbon surface had a honeycomb topography and was traversed by channels, while surface protrusions were often surmounted by small iron rich particles (Figure 15e). At 1056°C attack of the outer surface at a comparable burn off (18%) was characterised by pitting, in addition to deeper channelling. After 60% burn off the topography of the surfaces and edges were basically similar to that described, with a coarsening of the main features. The inorganic debris had spalled from the inner surface but again was still present as discrete particles surmounting deposit protrusions.

The surface topography of the respective deposit surfaces following oxidation enhanced by the various active contaminants was essentially similar to that described. The attack was characterised by channelling and pitting, which resulted in the formation of deeper channels in the case of the alkali metal oxides/carbonates, e.g. the effect of lithium oxide after 41% burn off is shown in Figure 15f.

Discussion

For the experimental conditions of temperature, water vapour partial pressure and gas flow rate examined the kinetics of gasification of the ESC deposit were consistent with previous observations for the carbon-water vapour reaction (7,8). The reaction was chemically controlled and the oxidation rate was linearly dependent upon water vapour partial pressure. The measured activation energy (57 Kcal mole⁻¹) was in the middle of the previously reported values (13.5 (1)-83 (9) Kcal mole⁻¹) for this reaction.

Many elements have been shown to catalyse carbon gasification by water vapour (2,3). The effectiveness of the majority of these elements, as well as others, in promoting the oxidation of this ESC deposit were examined. In agreement with previous observations on carbon, the three groups of elements which most actively catalysed ESC deposit oxidation were the transition metals (Fe, Co and Ni), the alkali metals (Na, K, Li, Rb and Cs) and the alkaline earths (Ca, Ba and Sr). The only apparent difference was that lead promoted oxidation of the ESC deposit but not graphite.

It seems to be widely accepted that oxygen transfer mechanisms are responsible primarily for the catalysed oxidation of carbon. These are based on the continuous cyclic variation of the oxidation state of the catalyst as it is oxidised by chemisorbed oxygen, from the dissociation of water vapour and then reduced by the underlying carbon, which in turn becomes gasified as carbon monoxide. The localised reaction of the catalyst particle with the carbon substrate results in particle motion and channelling of the surface.

For iron, cobalt and nickel the oxidation-reduction cycle was between metal and oxide, as gasification of the ESC deposit was catalysed only when the element could be present in the metallic

state. The critical parameter in determining the effectiveness of a transition metal would be its affinity for oxygen. Metals, such as copper and silver, having a lower reactivity for oxygen than iron, nickel and cobalt would form a less stable oxide and as a consequence could not have promoted the dissociation of water vapour. In contrast other metals with a higher oxygen affinity, such as chromium and manganese, formed a more stable oxide, which could not be reduced by reaction with the carbon substrate. Confirmation that chromium and manganese, when present initially in a metallic state, were not active catalysts was provided by the oxidation of deposit samples implanted with 10^{16} of the respective ions cm^{-2} . With this surface treatment technique the ions at $\sim 1\%$ concentration were incorporated into the surface to a maximum depth of 0.5 μm .

The observed catalytic effect of the alkali metal carbonates and oxides and the alkaline earth oxides upon the gasification of the ESC deposit in water vapour again most probably derived from successive oxidation and reduction processes. A possible cycle carbonate-metal-hydroxide could be feasible at this temperature, at least for sodium, potassium and lithium (3) and conceivably also for cesium and rubidium. For barium and strontium the cycle could be between a higher and a lower oxide. Calcium, in contrast to barium and strontium, does not form a peroxide by oxidation of calcium oxide and in any case this would not be stable above 200°C , which could explain why calcium oxide was not an active catalyst.

The ESC deposit contained appreciable levels of potential catalytic elements. These appeared to have promoted gasification, as the oxidation of the ESC coke was nearly five orders of magnitude greater than that of effectively pure graphite (SP-1), with an ash content of < 1 ppm (Table 3). Such a wide discrepancy would be less likely to be attributable to structural or textural differences. Also, metallic nickel dispersed in the SP-1 graphite at concentrations of 303 ppm and 1.4 wt.% increased its gasification rate by factors of 10^2 and 4×10^2 respectively. The corresponding oxidation rates of simulated carbonaceous deposits formed from cyclohexane decomposition were also considerably lower than that of the ESC coke (12). The factor of 3-4 higher gasification rate of the deposit formed on a steel rather than a carbon or silica substrate could possibly reflect the incorporation of potential catalytic metallic constituents during its formation. The 580 graphite was believed to simulate ESC coke (1) and in the event, its oxidation behaviour was comparable to that of the particular ESC coke examined. However, in view of the crucial dependence of gasification upon the extents and chemical state of entrained inorganic impurities and possibly also of the carbon structure, reliable oxidation data for plant deposits can be obtained only on such material. A corollary of this conclusion would be that there could be a significant variation between the oxidation behaviour of deposits from different plants and also of those formed from different feedstocks.

Table IIISpecific oxidation rates ($\mu\text{g m}^{-2}\text{min}^{-1} (\text{mm H}_2\text{O})^{-1}$ at 850°C

Carbon	Impurity content ^(a)	Oxidation rate	Reference
SP-1 graphite	Ash content 1 ppm	0.013	(10, 11)
Modified SP-1 graphite	330 ppm Ni	15	(10, 11)
Modified SP-1 graphite	1.4 wt.% Ni	50	(10, 11)
580 graphite	1500 ppm Fe, Ash content 1500 ppm	1000	(1)
Deposit on carbon (b)	N.D.	35	(12)
Deposit on quartz (b)	N.D.	44	(12)
Deposit on steel (b)	N.D.	156	(12)
ESC plant coke	Outer layer - 200 ppm Fe, 50 ppm Ni	880	This work

N.D. - not determined.

(a) Transition metals and other elements known to catalyse gasification.

(b) Deposit formed from cyclohexane and oxidised at 860°C.

The ESC coke examined consisted of two layers. Removal of the thinner, inner, deposit layer and associated inorganic impurity content did not appear to have any marked influence on the oxidation behaviour. This would suggest that the oxidation of the main bulk of the deposit (i.e. the outer pyrocarbon layer) was catalysed by impurities entrained within the layer. As far as could be ascertained these impurities were distributed randomly (5). There was no evidence of a concentration gradient for any element across this layer from the interface with the inner deposit layer.

Consistent with the dominant role of entrained catalytic elements within the ESC coke, hydrogen additions to the oxidant promoted gasification by activating catalyst formation. This outweighed the expected retardation by hydrogen of the carbon-water vapour reaction, as a result of it being a product of both the primary oxidation ($C + H_2O \rightleftharpoons CO + H_2$) and accompanying water gas shift ($CO + H_2O \rightleftharpoons CO_2 + H_2$) reactions. Butane (or its decomposition products) also enhanced the ESC coke gasification, again most probably by activating potential catalysts. The extent of the influence of butane would seem to exceed that of hydrogen and be continuous, whereas in some circumstances that of hydrogen was transitory.

Carbonaceous deposition during steam cracking is the net result of steady state formation and removal processes. If the measured oxidation rates in water vapour did represent the removal of the deposit in situ, then this would be an extremely rapid process over the temperature range at which deposition on radiantly heated process tubes is most significant. Thus, 1 mm thickness of deposit would be oxidised by 362 mm Hg water partial pressure in 300 h at 800°C, 33 h at 900°C and 5 h at 1000°C. If a hydrocarbon, or its decomposition products, enhanced the oxidation rate these times could be decreased. Coke removal by thermal oxidation cannot be ignored, therefore, although its extent would depend on specific plant operating conditions.

Conclusions

- (1) Oxidation of an ESC pyrolysis tube coke in water vapour, at 721-1056°C, followed linear kinetics between 10-85% burn off. The rate increased linearly with water vapour partial pressure (38-362 mm Hg). The activation energy for oxidation was 57 Kcal mole⁻¹ and the pre-exponential factor was 3.6×10^9 mg cm⁻²min⁻¹.
- (2) Gasification was catalysed by inorganic impurities, particularly iron and nickel, entrained in the coke and was promoted by butane and hydrogen.
- (3) Contamination of the coke surface with Pb, Fe, Co and Ni (in the metallic state), Na, K, Li, Rb and Cs carbonates or oxides and Ba and Sr oxides enhanced gasification at 900°C,

by up to a factor of 135. This catalysis probably derived from oxygen transfer mechanisms. A further eighteen elements (B, Mg, Al, P, Ca, V, Cr, Mn, Cu, Zn, Zr, Mo, Ag, Cd, Sn, La, Ce and Bi) either in the oxidised or elemental state had no significant influence.

Acknowledgements

This programme was sponsored by the Chemicals and Minerals Requirements Board, Department of Trade and Industry.

We are grateful to Dr. L.C. Dick, Dr. B. Estruch, and R.D. Smith (ICI Ltd.) for supplying the plant coke and also for the opportunity for detailed discussions with them and their colleagues. Likewise we also acknowledge helpful discussions with Dr. J.J. McCarroll and colleagues of the BP Research Centre. We wish to thank Dr. J.E. Antill for his guidance throughout the course of the programme.

Literature Cited

1. Reide, B.E.; Hanesian, D. Ind. Eng. Chem. Process. Des. Develop. 1975, 14, 10.
2. McKee, D.W., "Chemistry and Physics of Carbon"; Walker Jr., P.L.; Thower, P.A. Eds; M. Dekker New York, 1981, 16, 1.
3. McKee, D.W. Carbon 1979, 17 419.
4. Otto, K.; Bartosiewicz, L.; Shelef, M. Carbon 1979, 17, 351.
5. Bennett, M.J.; Price, J.B. J. Mater. Sci. 1981, 16, 170.
6. Bennett, M.J.; Price, J.B. Unpublished results.
7. Ergun, S; Menster, M. "Chemistry and Physics of Carbon"; Walker Jr., P.L. Ed.; M. Dekker: New York, 1965, 1, 203.
8. Thomas, J.M. Carbon 1970, 8, 413.
9. Long, F.J.; Sykes, K.W. J. Chim. Phys. 1950, 47, 361.
10. Otto, K.; Shelef, M. Carbon 1977, 15, 317.
11. Otto, K.; Shelef, M. Sixth Int. Congress on Catalysis, London, 12-16 July 1976, Preprint B.47.
12. Lahaye, J.; Badie, P. Carbon 1979, 17, 181.

RECEIVED June 28, 1982.

Effect of Hydrogen on the Iron- and Nickel-Catalyzed Formation of Carbon from Benzene

ALBERTO I. LACAVA, E. DANIEL FERNANDEZ-RAONE, LESLIE L. ISAACS, and MARITZA CARABALLO

The City College of the City University of New York, Clean Fuels Institute,
Department of Chemical Engineering, New York, NY 10031

The kinetics of carbon deposition from benzene over nickel and iron foils was studied at temperatures ranging from 500 to 650°C in atmospheres of hydrogen and mixtures of hydrogen and nitrogen, using a microbalance tubular flow reactor. Carbon deposition proceeds at a constant rate over both metals. The dependence of the rate on the partial pressure of hydrogen can be approximated by a power law kinetics. It is apparently third order over nickel and first order over iron. This behavior can be explained by a mechanism in which the benzene adsorbed on the surface is hydrogenated to produce intermediates. These intermediates in turn decompose to form carbon atoms which dissolve and diffuse into the metal to produce carbon filaments. Scanning Electron Microscope (S.E.M.) studies of the deposits showed the presence of these carbon filaments on both metal surfaces.

The phenomenon of carbon formation on the surface of a catalytic material is a reason for catalyst deactivation. Also, coking on surfaces of process equipment exposed to streams of gases containing hydrocarbons has been studied since carbon deposits can reduce heat transfer efficiencies, increase pressure drops, and even produce plugging in narrow tubes or valves.

0097-6156/82/0202-0089\$06.00/0
© 1982 American Chemical Society

Basic studies have concentrated on the mechanism of carbon formation and the kinetics of the process. Two approaches have been used which complement each other. Microbalance techniques (1,2,3) using pure metal foils have served to establish the overall kinetics of the process and the effect of the operational variables on the kinetics. Electron microscopy studies, especially experiments performed under controlled-atmosphere condition, have allowed an insight into the microscopic mechanism for the growth of carbon deposits (4,5,6).

For basic kinetic studies pure metal foils have been preferred (2,6,7,8) to supported catalysts since with the foils, metal-support interactions, mass transfer limitations and pore blockage problems are practically eliminated.

Among the different types of carbonaceous deposits on metal surfaces, carbon filaments have been reported by many authors. These filamentous growths can be explained by the following mechanism: gaseous hydrocarbon molecules are adsorbed on the metal surface where after a series of reactions carbon atoms are produced. These carbon atoms in turn dissolve into the bulk metal. Metal crystals are pushed out of the surface by the growing accumulation of atomic carbon and are carried with or within the filament. This allows for the surface reaction to propagate, although the amount of carbon produced in this way would be more than enough to cover all the available active sites. This is the commonly accepted mechanism for the production of carbon filaments. What has yet to be clarified is how and where the migrating carbon atoms are formed, and what factors are affecting this formation.

The question of where the carbon atoms are formed has to be answered separately for each particular hydrocarbon-metal reaction because the adsorption mechanism is specific to the individual metal. Once the carbon atoms are produced they dissolve in the metal and migrate to preferential regions. These regions are thought to be the grain boundaries where the carbon atoms are trapped and accumulated displacing metal crystallites from the grain surfaces (9,10). Similarity of the crystallite sizes of the original metal foils

and crystallites contained in the carbon filaments support these conclusions (11).

The question of how coke precursors are formed has been a matter of controversy, and a general mechanism explaining the formation has not yet been developed. This is due to the many different ways in which hydrocarbons adsorb and react on metal surfaces under similar conditions. In spite of this, some common features do exist. Among them is the fact that the presence of hydrogen affects the carbon deposition.

Few studies of carbon formation from aromatic hydrocarbons are reported in the literature (7, 12). Most of the studies have been performed with acetylene, olefins and paraffins (1, 6). The order of dependence of the reaction on hydrogen partial pressure is not unique.

Previous results from studies on the deposition from benzene (12) and other hydrocarbons (13) in the absence of hydrogen indicate that the reaction terminates after a fixed amount of carbon has been incorporated into the metal foil. Not surprisingly, the amount of carbon uptake by nickel foils corresponds to the solubility of carbon in nickel.

In this paper it is shown that the growth of carbon deposits can be maintained for long periods of time in the presence of hydrogen. The effect of hydrogen on the kinetics of carbon formation from benzene in hydrogen has been studied in experiments using nickel and iron foils. The results are presented below.

Experimental

The principles of flow microbalance reactors were described in a previous paper (3). The present experiments were performed in the equipment shown in Figure 1.

The reactor was a quartz tube, 4.25 cm i.d. and 80 cm long, held at the desired temperature within a tubular furnace. The sample foil was suspended by a quartz fiber from one of the arms of an Ainsworth microbalance and the weight of the foils, as functions of time, was monitored with a recorder.

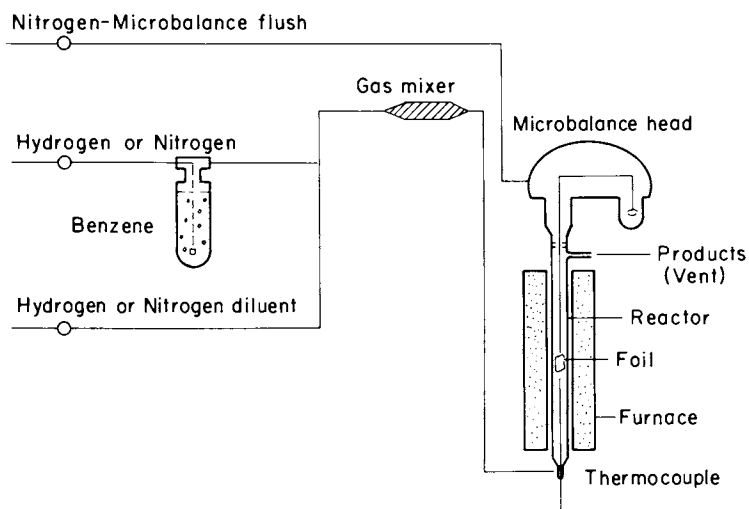


Figure 1. Schematic of flow microbalance reactor.

The metal sheets were obtained from United Mineral and Chemical Company with stated purity of 99.9%. The metal foils were cut into 1 x 4 inch rectangular pieces and gases used were of the highest available purity (Matheson). The morphology of the deposits were studied with an X-ray Diffractometer and a Cambridge SH Scanning Electron Microscope.

Results

Figure 2 shows the effect of temperature and benzene concentration on the kinetics of carbon deposition on a nickel foil. The temperature behavior follows a pattern that has been previously observed in the catalytic carbon formation from non-aromatic hydrocarbons (1,2). There are three regions in the Arrhenius plot. At low temperatures, the rate increases with increasing temperature and, thus, a negative slope-line is obtained in the Arrhenius plot. This low temperature region is denoted as Region I.

At intermediate temperatures, Region II, the data indicates an apparent negative activation energy, or a decrease in the rate with increasing temperature. At high temperatures, the non-catalytic carbon formation mechanism starts to be of significance and there is another region, Region III, of apparent positive activation energy. In Figure 2, the dotted lines represent Region III. This region was obtained from data of carbon deposition from benzene-hydrogen mixtures under conditions of homogeneous reaction (14). The temperature dependence of the rate of carbon deposition is similar to that reported by Lobo (15) for the deposition from propylene-hydrogen and 1-butene-hydrogen mixtures. In all cases, as temperature is increased, the overall rate of carbon deposition shifts from being catalytically controlled to being controlled by the homogeneous reaction in the gas phase. Region I shows a definite variation of the reaction rate with benzene concentration. The change corresponds to a first order effect.

Figure 3 shows the effect of temperature and benzene concentration of the rates of carbon formation over iron foils. The overall behavior is similar to that of nickel foils, although the changes with tem-

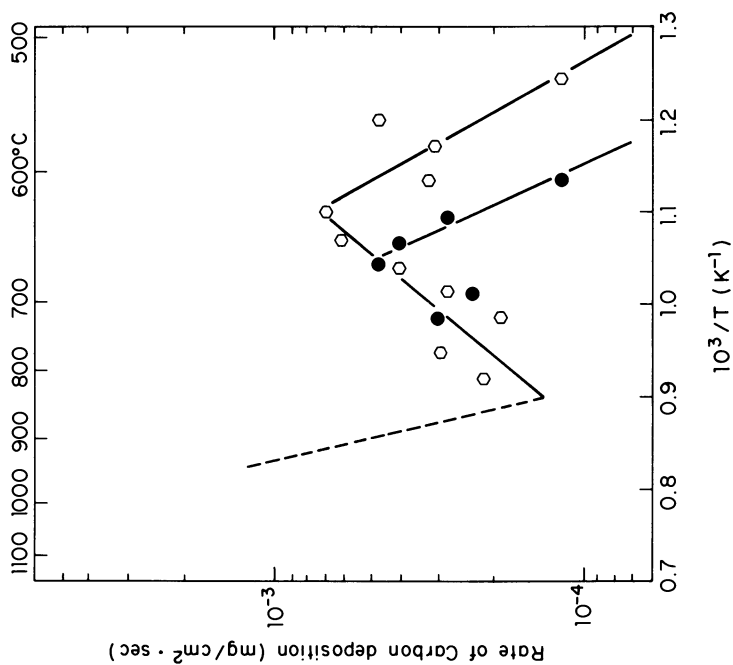


Figure 3. Arrhenius plot for the rate of carbon deposition from benzene onto iron foils (total pressure = 1 atm). Key is the same as in Figure 2.

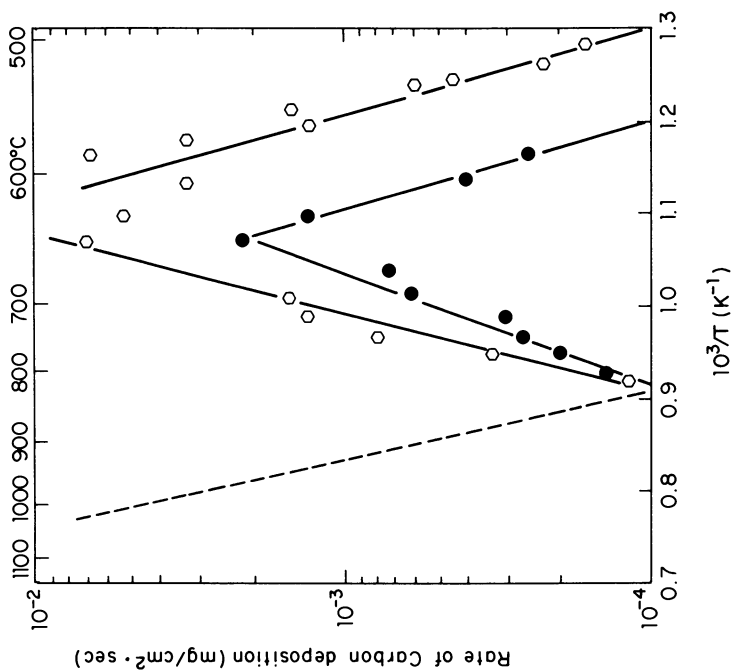


Figure 2. Arrhenius plot for the rate of carbon deposition from benzene onto nickel foils (total pressure = 1 atm). Key to P_{benzene} : ○, 0.132 atm; ◐, 0.091 atm. Key to P_{benzene} : ●, 0.091 atm.

perature are less marked in this case. All the results shown in Figures 2 and 3 were obtained using mixtures of hydrogen and benzene without using an inert diluent gas. Thus, it is difficult to observe the effect of hydrogen on the carbon formation rate. Another set of experiments was performed adding a diluent gas, nitrogen, to the gas stream. The total pressure of benzene was kept constant, but the relative amounts of hydrogen and nitrogen in the gas stream were varied. The results are shown in Figure 4. The effect of hydrogen on the rate of carbon formation on the nickel foils is very marked, resulting in a rate increase of two orders of magnitude. The effect is less pronounced with iron foils; the rate increase is only five fold with hydrogen addition.

Figure 5 shows the rate of carbon formation as a function of the gas flow rate in the reactor as measured by the volumetric residence time. The rate of the catalytic carbon formation, as expected, is nearly independent of the gas residence time in the experimental range of this investigation.

Scanning Electron Microscope observations of the deposit structure showed similarities in the morphology both for nickel and iron foils. Figure 6 shows the structure on a nickel foil. Carbon has been formed in a filament-like structure, similar to what has been observed previously in deposits from other hydrocarbons (4,5). The same type of structure is observed on the iron foils (see Figure 7).

In Figure 8, the X-ray Diffraction patterns of a carbon deposit over nickel and the pure nickel substrate are compared. A broad, low intensity peak corresponding to the graphite plane (002) appears in the region of 26° (2θ) indicating the presence of a few small graphite crystallites, but the bulk of the deposit appears to be amorphous carbon. All the lines corresponding to nickel appear in the carbon deposit pattern, indicating the presence of nickel crystallites in the deposit. However, the relative intensities of the lines is different from the pattern obtained with the pure substrate. This may indicate the preferential deposition of carbon on different nickel crystallographic planes.

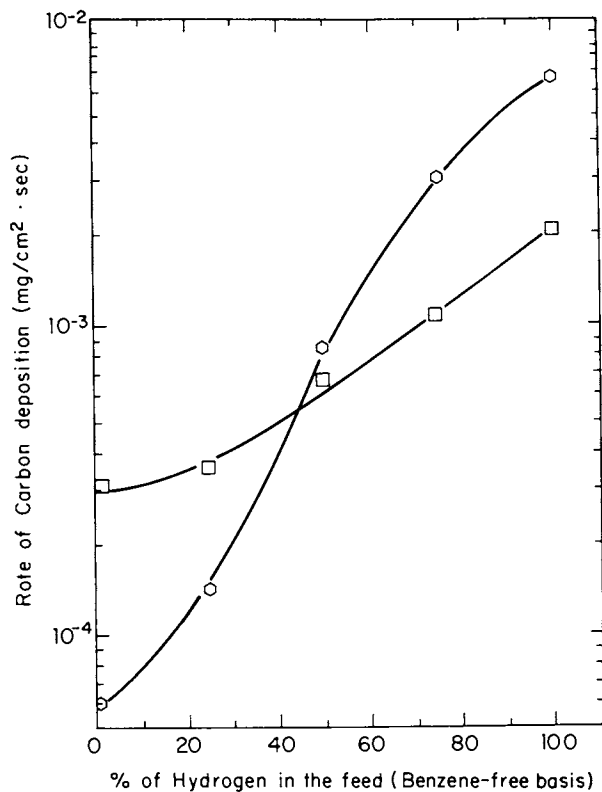


Figure 4. Effect of hydrogen on the rate of carbon deposition from benzene onto nickel (650°C) and iron (625°C). Nitrogen used as carrier (total pressure = 1 atm). Key: ○, Ni foils; and □, Fe foils.

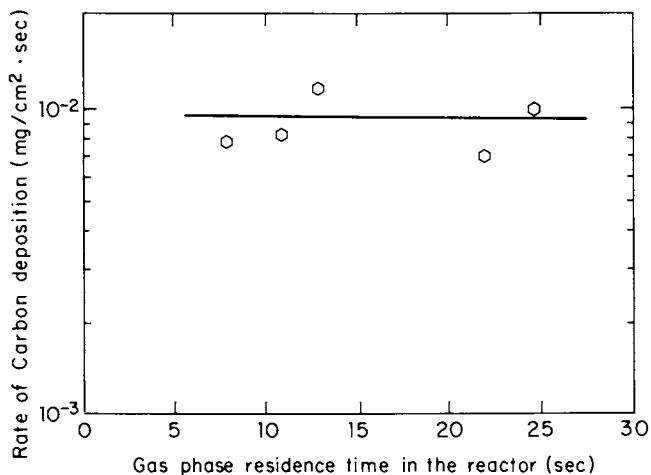


Figure 5. Effect of the gas residence time on the rate of carbon deposition at 650°C.

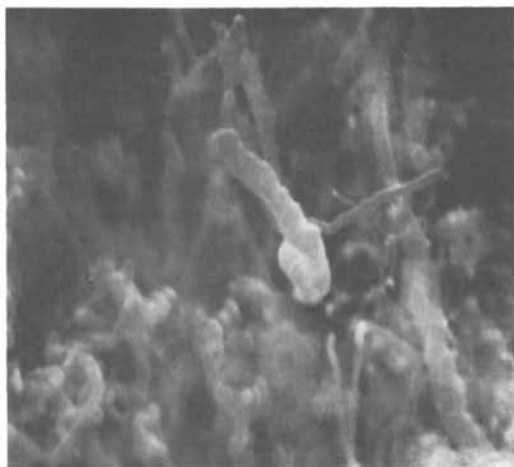


Figure 6. SEM photograph of carbon deposited on a nickel foil showing filament growth. Magnification is 9,350 \times .

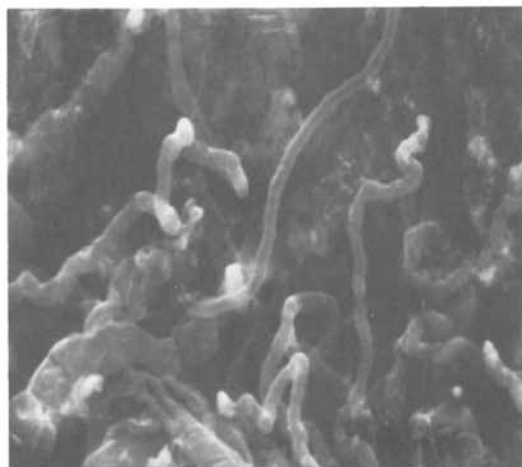


Figure 7. SEM photograph of carbon deposited on an iron foil showing filamentary growth. Magnification is 9,350 \times .

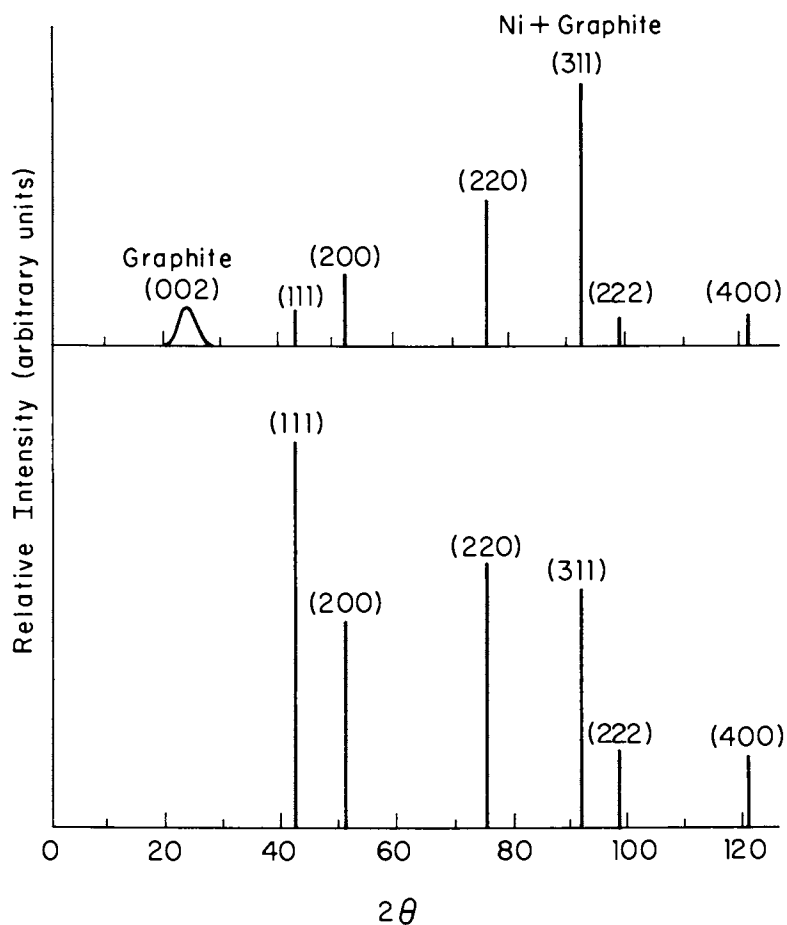


Figure 8. X-Ray diffraction patterns of carbon deposited on a nickel foil. Key: top, after deposition; and bottom, before deposition (clean foil).

Discussion

Carbon formation from different hydrocarbons over metals has been studied by several workers. The presence of carbon filaments on the surface of the metal, containing metal crystals, has been reported under conditions similar to those of these experiments.

Scanning Electron Microscope (S.E.M.) studies of the iron and nickel foils, after carbon deposition, showed the presence of filamentous growth of carbon on both metallic surfaces, as was expected. This is in agreement with the steady-state rate of carbon deposition observed for both iron and nickel foils. If filaments containing metal crystallites were not formed, the reaction would have to stop at a certain point because of deactivation and poisoning of the metal surface by the deposited carbon.

X-ray diffraction studies suggest that carbon is formed on all faces of a nickel crystal, but preferentially on the (111) planes. Relative intensity of the diffraction patterns associated with each plane on the surface was measured before and after reaction. Lower intensity would have to be expected as the amount of nickel diffracting had been reduced to those crystallites present in the carbon deposit from the original nickel foil. In this case similar reduction in the intensity of the diffracted peaks should be expected for all planes diffracting the X-rays. It can be seen from Figure 8 that the reduction in the (111) diffracted peak is above the average. Similar preferential segregation of carbon on nickel (111) planes (arising from internal migration) has been observed by Auger spectroscopy. This seems to correlate with the way in which benzene adsorbs on different planes of nickel crystals (16). The (111) planes have the most favorable structure for benzene chemisorption because of the similarities between dimension and shape of benzene molecules and (111) plane (Figure 9).

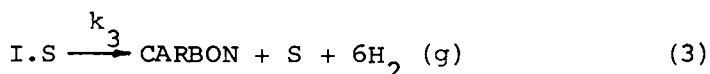
Models have been proposed in the literature to explain the growth of carbon filaments. The models postulate that the parent hydrocarbon adsorbs on the surface of a crystallite and undergoes dehydrogenation reactions to form atomic carbon. Filaments grow on the back of the crystallites by the addition of the carbon that diffuses, as was explained before.

The effect of hydrogen on the rate of filament growth, and therefore carbon deposition, is still open to discussion. If carbon deposits are formed through a dehydrogenation reaction, the effect of increasing hydrogen partial pressure should be to decrease the rate of carbon formation. The opposite effect was observed for these experiments since the rate of carbon deposition increased with the third power of the hydrogen partial pressure for nickel foils and with the first power of hydrogen partial pressure for the iron foils (Figure 10). This seems to suggest that even though a dehydrogenation reaction has to be present in order to produce atomic carbon, this is not the rate-controlling step.

The proposed kinetic models described below try to take into account this particular effect of hydrogen on the overall deposition rate.

Mechanism of Carbon Formation on Nickel

In the case of nickel foils, it is assumed that benzene adsorbs reversibly on the metal, followed by hydrogenolysis of the ring which leads to coke intermediates. The intermediates will then decompose rapidly to carbon atoms which will undergo the aforementioned dissolution and diffusion processes through the crystal:



The solution of the equations of the above model gives the following rate expression:

$$r_C = k_3 C_{I.S} = \frac{k_3 K_1 K_2 C_T P_B P_{H_2}^3}{1 + K_1 P_B + K_1 K_2 P_B P_{H_2}^3}$$

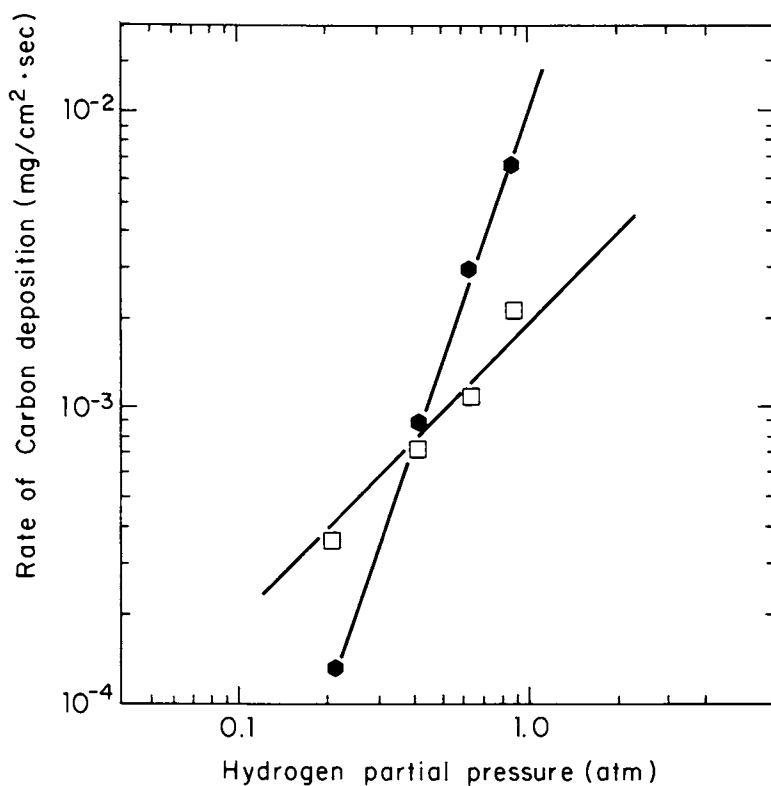
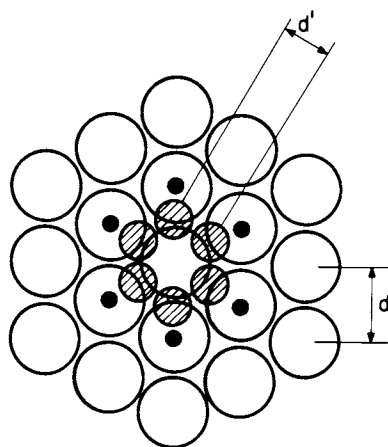


Figure 10. Apparent reaction order with respect to hydrogen for carbon deposition rate at constant temperature, constant pressure (1 atm), constant benzene partial pressure on nickel foils ($T = 650^{\circ}\text{C}$, $P_B = 0.132\text{ atm}$) and iron foils ($T = 625^{\circ}\text{C}$, $P_B = 0.132\text{ atm}$). Key: \bullet , Ni foils; and \square , Fe foils.

The parameters of the above model were estimated using a non-linear regression computer program. The parameters obtained are:

$$K_1 P_B + K_1 K_2 P_B^3 P_{H_2}^3 \ll 1 \quad (\text{negligible})$$

$$k_3 K_1 K_2 C_T = 1.2 \times 10^6 \times \text{EXP} (-31,200/RT)$$

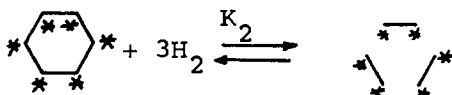
(mg cm⁻² sec⁻¹ atm⁻⁴)

From equation (3), the total activation of energy of the process should be:

$$E_T = E_3 + \Delta H_1 + \Delta H_2 = 31,200 \text{ cal/g mole} \quad (4)$$

The value of the activation energy can be justified if the individual activation energies and heats of reaction can be estimated or known. For the reaction of adsorption of benzene, literature values range from -30Kcal/mole (at zero coverage)¹⁷ to -6 Kcal/gmole (18). A value close to -6 Kcal/gmole may be expected under the experimental conditions reported here, where coverage is not zero.

Reaction 2 is assumed to be as follows:



and the "intermediate" I is assumed to be three adsorbed ethylene groups. The heat of reaction can be estimated from thermochemical data, and is found to be in the order of -10 Kcal/gmole.

In reaction (3), the adsorbed ethylene groups rapidly decompose to atomic carbon through a series of hydrogenolysis and dehydrogenation reactions to yield individual carbon atoms on the surface. This atomic carbon diffuses through the metal crystallite probably driven by a temperature gradient and forms a carbon deposit on the opposite face of the crystal (15).

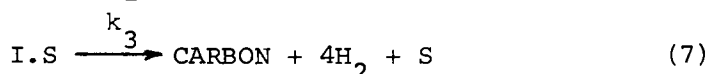
Work published by Lobo et al. (15) reports that the steps of reaction(3) (carbon formation from ethylene) are controlled by the diffusion of carbon through the metal crystallite. This process is known to have an activation energy of 35 Kcal/gmole.

With the above assumptions, the total activation energy calculated from equation (4) should be about 19 Kcal/gmole. The discrepancy can be attributed to inaccuracies in the estimation of the heat of reaction (1) and (2). This order of magnitude analysis indicates that the model can roughly account for the third order dependence on hydrogen pressure and first order dependence on benzene pressure.

The fitting of the model with the parameters to the experimental results is shown in Figure 11.

Mechanism of Carbon Formation on Iron

In the case of iron foils, the adsorbed benzene molecule is assumed to be attacked by hydrogen in steps of comparable rate to produce the coke intermediates. As in the case of nickel, intermediates decompose to atomic carbon which diffuses through the metal crystal:



The rate expression obtained from the above model is:

$$r_C = k_3 I.S = \frac{k_3 K_1 K_2 C_T P_B P_{H_2}}{1 + K_1 P_B + K_1 K_2 P_B P_{H_2}} \quad (8)$$

and the parameters obtained by non-linear regression are:

$$k_3 K_1 K_2 C_T = 2.9 \times 10^3 \times \text{EXP} (-23,400/RT)$$

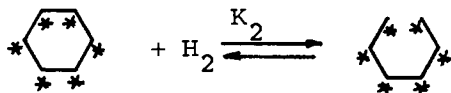
$$K_1 P_B + K_1 K_2 P_B P_{H_2} \ll 1 \quad (\text{negligible})$$

For this case also:

$$E_T = (E_6 + \Delta H_4 + \Delta H_5) = 23,400 \text{ cal/gmole}$$

No information was available on the heats of adsorption of benzene on iron, and no thermochemical data were found to estimate this value.

Reaction (6) can be assumed to proceed as follows:



since a single hydrogenolysis step would explain the first order dependence of the rate on the pressure of hydrogen.

Reaction (7) is assumed to be a series of hydrogenolysis and dehydrogenation reactions that would yield atomic carbon in the surface. This atomic carbon would then diffuse through the metal and deposit carbon on the opposite face of the crystallite. The activation energy of diffusion of carbon on iron is of the order of 13 Kcal/gmole, but in this case there is no evidence with regards to which is the limiting mechanism. Any of the surface reaction steps involved in reaction (7) could be controlling for the kinetics of this reaction, and would yield a higher activation energy than diffusion.

Assuming heats of adsorption in the order 0 to -6 Kcal/gmole, a heat of reaction of -3.8 Kcal/gmole for reaction (6) (estimated from bond energies) and activation energies for reaction (6) from 13 Kcal/gmole (diffusion controlling) to 40 Kcal/gmole (typical activation energy for a surface reaction), would yield an estimated total activation energy between 9 and 30 Kcal/gmole. The value of 23,400 cal/gmole is well within these expected limits.

These estimates tend to indicate that the model proposed would yield roughly the right activation energy. It also explains the first order dependency of the rate on both the partial pressure of benzene and hydrogen.

Figure 12 compares the model-predicted rates with the experimental results. As in the case of nickel, the standard deviation between model and experiments is of the same order of magnitude as the standard deviation of the experiments.

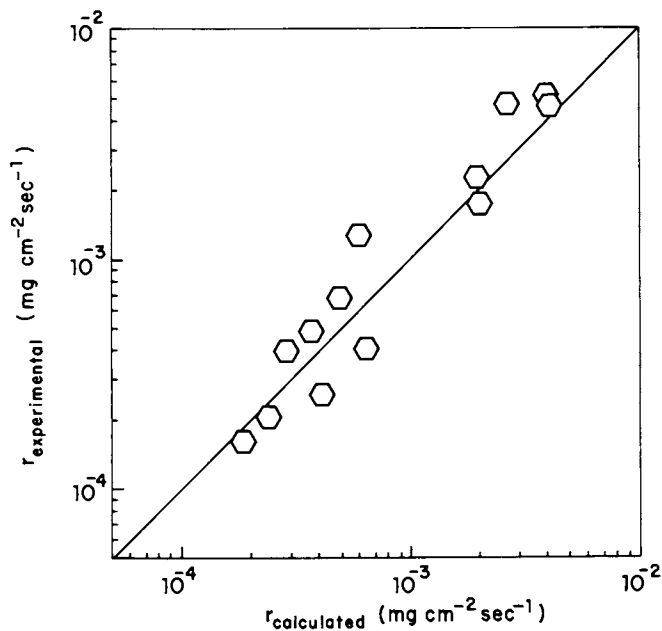


Figure 11. Comparison of carbon formation rates for nickel foils from proposed model and from experiments.

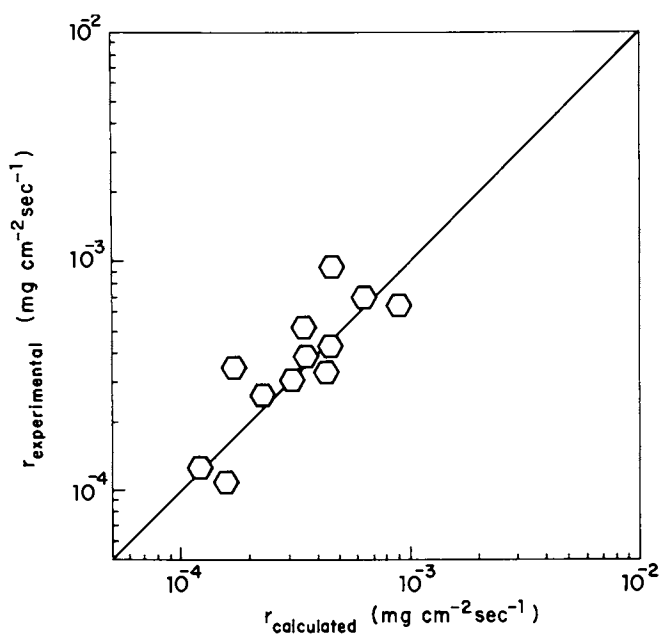


Figure 12. Comparison of carbon formation rates for iron foils from proposed model and from experiments.

Conclusions

We propose mechanisms for carbon formation in the presence of hydrogen on nickel and iron surfaces. Benzene is assumed to adsorb on the metal surface and to be hydrogenated to intermediates. These intermediates decompose to form atomic carbon which migrates through a metal crystallite to form carbon filaments.

The differences between the rates of carbon deposition on nickel and iron foils can be explained by the proposed mechanisms. In the case of nickel foils, the adsorbed benzene is hydrogenated to intermediates that look like adsorbed ethylene groups. The rate determining step is the decomposition of these intermediates to carbon and hydrogen. In the case of iron foils, the hydrogenation of the adsorbed benzene ring leads to a different intermediate (reaction (7)) in which the overall rate is again controlled by the decomposition of the intermediate to carbon and hydrogen.

Nomenclature

B	:	Benzene molecule
P_i	:	Partial pressure of ith component (atm)
C_i	:	Concentration of ith species
K_i	:	Equilibrium constant for ith reaction
k	:	Kinetic constant of the limiting step
S	:	Active site
B.S	:	Benzene adsorbed on active site
I.S	:	Intermediate species for coke formation
C_T	:	Total concentration of active site
r_C	:	Rate of carbon formation ($\text{mg cm}^{-2}\text{sec}^{-1}$)

Literature Cited

1. Bernardo, C.A.; Ph.D. Thesis, University of London (1977).
2. Lobo, L.S.; Ph.D. Thesis, University of London, 1971.
3. LaCava, A.I.; Trimm, D.L.; Turner, C.E.; Thermo-
chimica Acta 1978, 24, 273.
4. Baker, R.T.K.; Waite, R.J., J. of Cat. 1975, 37, 101.
5. Baker, R.; Barber, M.; Harris, P.; Feates, F.; Waite, R., J. of Cat. 1972, 26, 51.
6. Nishiyama, J.; Tamai, Y., J. of Cat. 1976, 45, 1.
7. Tamai, Y.; Nishiyama, J.; Takahashi, M., Carbon 1969, 7, 209.
8. Tamai, Y.; Nishiyama, J.; Takahashi, M., Carbon 1968, 6, 593.
9. Figueredo, J.; Ph.D. Thesis, University of London, 1975.
10. Kishimoto, S.; Sotani, N.; Niirui, K.; Urata, T., B. of the Chem. Soc. of Japan, 1978, 51, 1887.
11. Nishiyama, J.; Tamai, J., J. of Cat. 1974, 33, 98.
12. Tomita, A.; Yoshida, K.; Nishiyama, Y.; Tamai, Y., Carbon 1972, 10, 601.
13. Trimm, D., Catal. Rev. - Sci. Eng. 1977, 16 (2), 155.
14. LaCava, A.I.; Fernandez-Raone, E.D.; Caraballo, M., A.C.S. Symposium Series 1981, New York.
15. Lobo, L.S.; Trimm, D.L., J. of Cat. 1973, 29, 15.
16. Bertolini, J.C.; Dalmau-Imelik, G.; Rousseau, J., Surf. Sc. 1977, 67, 478.
17. Yu, Y.F.; Chessick, J.J.; Zettlemyer, A., J. Phys. Chem. 1959, 63, 1626.
18. Marangozis, J.K.; Mantzouranis, B.G.; Sophos, A. N., Ind. Eng. Chem. Prod. Res. Dev. 1979, 18, 61.

RECEIVED June 28, 1982.

Mechanism of Surface Carbon Formation During the Pyrolysis of Benzene in the Presence of Hydrogen

ALBERTO I. LACAVAL, E. DANIEL FERNANDEZ-RAONE, and
MARITZA CARABALLO

The City College of the City University of New York, The Clean Fuels Institute,
Department of Chemical Engineering, New York, NY 10031

The mechanism of carbon formation on polycrystalline Cu foils was studied for the pyrolysis of benzene in the presence of hydrogen. The study was carried out on a microbalance tubular flow reactor at temperatures ranging from 800 to 1050°C. The rate of surface carbon deposition was constant after an initial period during which no appreciable deposition was observed. The dependence of the rate on the partial pressure of hydrogen seems to follow a negative order, while it is linear with respect to benzene initial partial pressure. The temperature dependence of the rate was found to follow an Arrhenius behavior with activation energy close to 50 kcal/mole. These effects can be explained by means of a mechanism proposed in this paper which postulates that benzene molecules decompose to form free radicals; the free radicals in turn react among themselves to product macromolecules or react with hydrogen to become inactive. The macromolecules, after saturation is reached, will condense into droplets. The droplets will grow by further addition of macromolecules and collide with the metallic surface where they deposit.

0097-6156/82/0202-0109\$06.00/0

© 1982 American Chemical Society

During the gas-phase thermal decomposition of hydrocarbons, a carbonaceous material appears deposited on the surface that encloses the reacting environment. This deposit can give rise to operational difficulties in hydrocarbon processing equipment, such as increased pressure drops, plugging of pipes and valves and decreasing heat transfer efficiencies.

The mechanism under which this surface carbon is formed on non-catalytical surfaces is not very well understood yet. Several theories have been proposed from the observation of carbon formation on surfaces and in the gas phase under different conditions (1). From this study it can be concluded that a unique mechanism that explains the formation of carbon deposits on catalytically inert surfaces does not seem to exist. The answer has to be looked for each particular case as different operating conditions (pressure, temperature, reactants) produce different, if any, carbon deposits.

One of the proposed theories applied successfully to the formation of gas-phase carbon from benzene is the droplet condensation mechanism. This "condensation theory", revised recently by Lahaye et al. (2), explains the formation of soot aerosols during benzene pyrolysis. The authors obtained an excellent agreement between the theory and experimental results.

The theory assumes the following steps in the formation of carbon deposits:

a) Formation of "macromolecules" (large polycyclic aromatic compounds) from benzene, through a set of polymerization reactions.

b) The macromolecules concentration increases along the reactor, until it reaches the saturation point.

c) When the saturation point is reached (after a residence time t^*) nucleation and formation of droplets occur.

d) After nucleation, further macromolecules formed contribute to the growth of the droplets.

This theory is shown here to be relevant to the work described as the conditions used in (2) are close to those of the experiments reported in this paper. The present research is an attempt to elucidate the mechanism of surface carbon deposition from benzene in hydrogen at atmospheric pressure and in the temperature range 800 to 1050°C.

Experimental

Cu foils were selected as inert surfaces for these experiments since they do not present significant catalytic activity (3). The rate of surface carbon formation on pure Cu polycrystalline foils was measured with the aid of a microbalance tubular flow reactor. The principles of this equipment were described in a previous paper (4).

The reactor was a quartz tube, 4.25 cm i.d. and 80 cm long, held at the desired temperature within a tubular furnace. The sample foil was suspended by quartz fibers from one of the arms of an Ainsworth RV microbalance and the weight of the foils, as function of time, was monitored with a recorder.

The metal sheets were obtained from United Mineral and Chemical Company with 99.9% purity. Metal samples were cut into 1 x 4 inch rectangular pieces and gases used were of the highest available purity (Matheson).

The Cu sheets, after being washed in acetone, were reduced "in situ" with hydrogen at the reaction temperature of each run. The rate of carbon formation was measured as a function of temperature, benzene and hydrogen partial pressures, and gas phase reactor residence time.

The morphology and nature of the deposits were studied with a Cambridge SH Scanning Electron Microscope.

Results

Figure 1 shows the effect of temperature on the rate of carbon deposition. The rate was found to

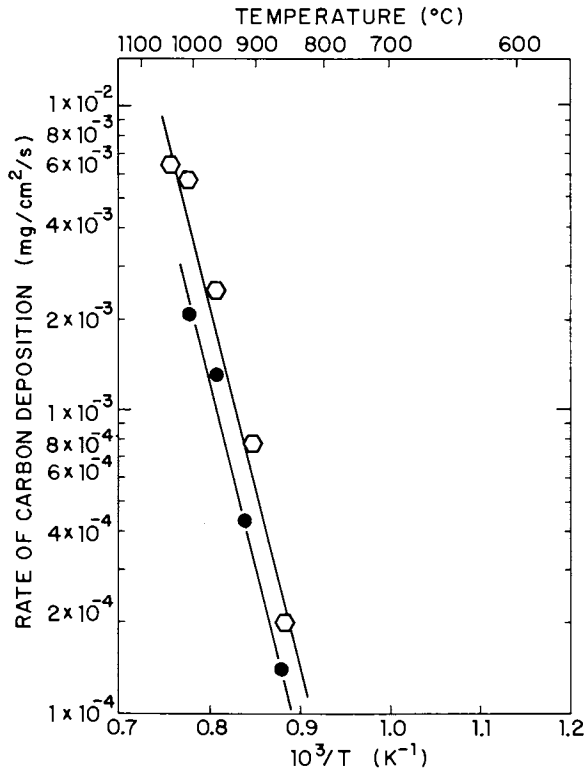


Figure 1. Temperature effect on the carbon formation rate on copper foils. Key to $P_{benzene}$: ○, 0.132 atm; and ●, 0.043 atm.

follow an apparent Arrhenius behavior in the range 800-1050°C, with an activation energy close to 50 kcal/mole.

Figure 2 shows the dependence of the rate of carbon deposition with initial hydrogen partial pressure. The rate depends on the hydrogen partial pressure with a negative order, i.e., the rate of deposition decreases with increased hydrogen pressure. The dependence of the rate on the initial benzene partial pressure is first order as revealed by the data on Figure 1. For fixed temperatures, benzene and hydrogen partial pressures, there is a critical gas phase residence time (t^*) below which no appreciable deposition occurs. Above the critical residence time t^* , deposition occurs and its rate increases linearly with gas residence time. This is depicted in Figure 3.

Scanning Electron Microscopy observations showed the deposit to be an aggregate of particles (Figure 4) that tend to coalesce in larger "drops" that attach to the surface of the foil (Figure 5). X-ray diffraction shows the deposit is amorphous in nature.

Discussion

Scanning Electron Microscope observations of the morphology of the deposit suggest the following mechanism for the "drop" formation:

a) Macromolecules are formed in the gas phase as a consequence of homogeneous reactions. The macromolecules so formed condense into droplets or particles by means of a physical or chemical process.

b) These particles, in a plastic state, diffuse and collide with the metallic surface, depositing on it.

The "condensation theory" presented by Lahaye et al. can account for part of the experimental facts. The model presented below is an extension of that theory. It also includes assumptions on how hydrogen partial pressure and gas phase reactor residence time affect the rate of deposition.

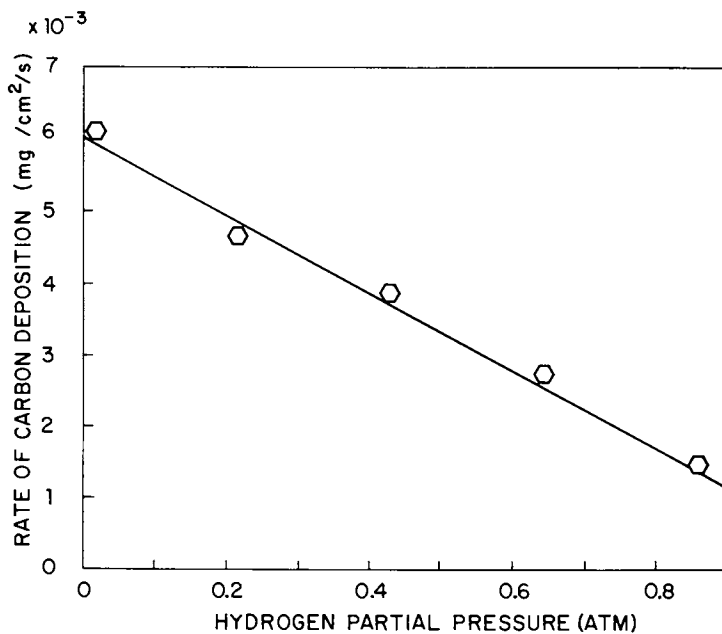


Figure 2. Effect of hydrogen partial pressure on the rate of carbon deposition on copper foils. Conditions: T , 950°C; P_{B_0} , 0.132 atm; and t , 22 s.

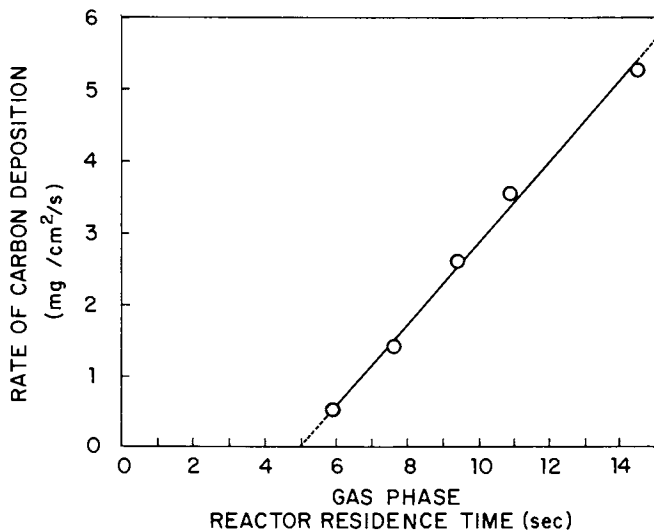


Figure 3. Effect of the gas residence time on the rate of carbon deposition at 1000°C. Conditions: P_{B_0} , 0.132 atm; and P_H , 0.868 atm.

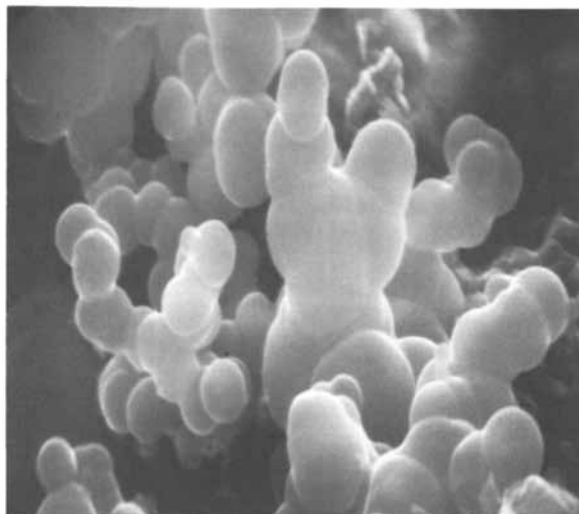


Figure 4. SEM photograph of carbon deposited on Cu foil. Magnification is 9,350 \times .

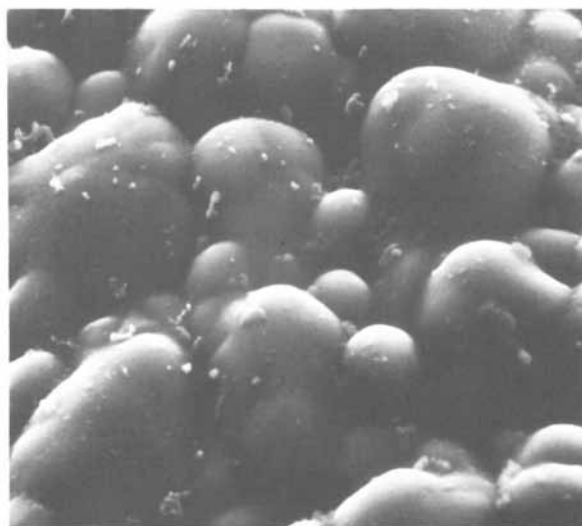


Figure 5. SEM photograph of carbon deposited on Cu foil. Magnification is 1,870 \times .

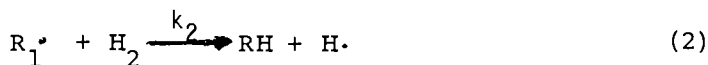
Model for Carbon Deposition in Droplets StateGas Phase Reactions

(1) Radical generation (benzene decomposition)



At the high temperatures of the experiments benzene is assumed to decompose into free radicals and one or more hydrogen atoms.

(2) Radicals capping with hydrogen



The free radicals can react with hydrogen to become inactive or react among themselves to give reaction 3.

(3) Formation of polymolecules or intermediates



n free radicals react to give a polymolecule (macromolecule).

Benzene Concentration Along the Reactor

The benzene concentration changes along the reactor as radicals and macromolecules are formed. In order to calculate this change, the following analysis was performed. Assume after Hou and Palmer (5) that benzene decomposes in the gas phase as a first order reaction:

$$\frac{dC_B}{dt} = -k_1 C_B \quad (4)$$

with initial condition $C_B = C_{B_0}$ at $t = 0$.

By integration of (4)

$$C_B = C_{B_0} e^{-k_1 t} \quad (5)$$

The hydrogen partial pressure is assumed to remain constant along the reactor because of the high hydrogen to benzene ratio and the low hydrogen production.

Concentration of Intermediate Along the Reactor

The intermediate concentration can be obtained by applying the stationary state hypothesis of free radicals to reactions (1), (2) and (3).

$$\frac{dI}{dt} = \frac{(1/n) P_{Bo}}{1 + (k_2/k_3) P_H} \quad (6)$$

with initial condition $I=0$ at $t=0$. Integration of above equation gives:

$$I = \frac{(1/n) P_{Bo}}{1 + (k_2/k_3) P_H} [1 - e^{-k_1 t}] \quad (7)$$

From (7), the time needed to reach saturation (t^*) can be easily obtained:

$$I^* = \frac{(1/n) P_{Bo}}{1 + (k_2/k_3) P_H} [1 - e^{-k_1 t^*}] \quad (8)$$

I^* represents the minimum concentration of intermediates necessary to begin condensation. When I^* is reached, nucleation and formation of droplets occur. Any other macromolecule formed after t^* will contribute to the droplets' growth. The droplets' concentration after nucleation will then be:

$$[c] = (I - I^*) M_{wI} \quad (9)$$

or

$$[c] = \frac{(1/n) M_{wI} P_{Bo} (e^{-k_1 t^*} - e^{-k_1 t})}{1 + (k_2/k_3) P_H} \quad (10)$$

For small values of $k_1 t$ the exponentials can be linearized to give:

$$[c] = \frac{78 k_1 (t-t^*) P_{Bo}}{1 + (k_2/k_3) P_H} \quad (11)$$

Also

$$\frac{1}{1 + (k_2/k_3) P_H} \approx 1 - (k_2/k_3) P_H$$

Now, calling $k_2/k_3 = b$

$$[c] = 78 k_1 (t-t^*) P_{Bo} [1 - bP_H] \quad (12)$$

It is assumed at this point that droplets deposit on the metallic surface by Brownian motion (i.e., diffusion). This assumption allows for the evaluation of the rate of deposition as follows:

$$R_{CD} = k_C [c]$$

$$R_{CD} = 78 k_c k_1 (t-t^*) \cdot P_{Bo} \cdot (1 - bP_H) \quad (13)$$

Temperature Dependence of b and t*

The temperature dependence of the term b can be predicted if values for the activation energies of reactions (2) and (3) (E_2 and E_3) are known.

Capping of hydrogen with similar free radicals has an activation energy of 2-8 kcal/gmol (6). An activation energy as low as 2 kcal/gmol can be expected for reaction (2). Reaction (3) has an activation energy close to 0 being that it is a termination reaction. Therefore, the dependence of b with temperature can be neglected under the present conditions.

The temperature dependence of t^* can be obtained by the following analysis:

The partial pressure of intermediate polymolecules required to condense at equilibrium is given by:

$$I_e = I_e^o \exp\left(-\frac{\Delta H_v}{RT}\right) \quad (14)$$

Assume the supersaturation pressure difference to be small, then

$$I^* \approx I_e^o \exp\left(-\frac{\Delta H_v}{RT}\right) \quad (15)$$

From (8), (15) and linearizing the exponential for small values of $k_1 t^*$

$$t^* = \frac{I_e^0}{k_{10} \exp\left(-\frac{(E_1 - \Delta H_V)}{RT}\right) (1/n) P_{Bo} (1 - bP_H)} \quad (16)$$

E_1 has a value of approximately 52 Kcal/gmol (5). ΔH_V can be estimated to be around 25 kcal/gmol. This value corresponds to a boiling point temperature of macromolecules of 1200°K-1300°K.

t^* will then decrease with temperature following an exponential decay where $(E_1 - \Delta H_V)$ is predicted to be ~27 kcal/gmol.

The rate of carbon deposition is then:

$$R_{CD} = 78 k_c k_1 (t - t^*) \cdot P_{Bo} \cdot (1 - bP_H) \quad (17)$$

where t^* is obtained from (16).

Equation (17) represents very closely the experimental behavior of carbon deposition on Cu polycrystalline foils from mixtures of benzene and hydrogen since:

- (i) the rate of deposition decreases linearly with hydrogen partial pressure (Figure 2);
- (ii) the rate grows linearly with residence time starting from an initial value of t^* (Figure 3);
- (iii) the rate follows an Arrhenius expression with temperature. The effect of temperature on t^* and b is masked by the much stronger temperature of $k_c k_1$;
- (iv) the rate is proportional to the initial concentration of benzene.

The value of the parameters in (12) was obtained by a nonlinear regression method using the Gauss-Newton Algorithm. Those values are:

$$78 k_c k_1 = 0.5 \times 10^7 e^{-\frac{53,000}{RT}} \text{ (cal/gmol)}$$

$$b = 0.87$$

$$\frac{nI^o}{k_{10}} = 0.22 \times 10^{-5}$$

$$E_1 - \Delta H_V = 24,000 \text{ cal/gmol}$$

Conclusions

A model based on the condensation theory was developed to explain the dependence of the rate of carbon deposition on the hydrogen and benzene partial pressure, on the gas phase residence time and on the temperature. The effect of hydrogen was explained assuming that it reacts with the free radicals that form the macromolecules of the condensation theory, decreasing the rate of production of carbon-forming intermediates.

The effect of initial benzene partial pressure was accounted for, assuming benzene undergoes a first order decomposition reaction to free radicals at any place in the reactor.

The dependence on the residence time was obtained from the assumptions involved in the condensation theory and by further linearization of the resulting equation for short residence times. The model presents a good agreement with the experimental results.

Nomenclature

B	:	Benzene molecule
[c]	:	Concentration of droplets (mg C/VOLUME)
C _B	:	Molar concentration of benzene
C _{BO}	:	Initial molar concentration of benzene
H ₂	:	Hydrogen molecule
I*	:	Macromolecule concentration at saturation
k _C	:	Mass transfer coefficient
k _i	:	Kinetic constant of ith reaction (sec ⁻¹)

- M_{WI} : Molecular weight of intermediate (assumed to be n molecular weight of benzene, i.e., $78n$).
- n : Number of free radicals in a macro-molecule
- P_B : Partial pressure of benzene
- P_{BO} : Initial benzene partial pressure
- P_H : Hydrogen partial pressure
- R_1 : Free radical
- t^* : Time needed to reach saturation

Literature Cited

1. Palmer, H.; Cullis, C.F., "Chemistry and Physics of Carbon," Dekker, New York, 1965; p. 266.
2. Lahaye, J.; Prado, G.; Donnet, J.B., Carbon 1974, 12, 27.
3. Lobo, L.S., Ph.D. Thesis, London University, London, 1971.
4. LaCava, A.I.; Trimm, D.L.; Turner, C.E., Thermo-chimica Acta 1978, 24, 273-280.
5. Hou, K.C.; Palmer, H., J. Phys. Chem. 1965, 69, 863.
6. LaCava, A.I., M.Sc. Thesis, London University, London, 1973.

RECEIVED July 9, 1982.

Formation and Removal of Coke Deposited on Stainless Steel and Vycor Surfaces from Acetylene and Ethylene

JAMES C. MAREK and LYLE F. ALBRIGHT

Purdue University, School of Chemical Engineering, West Lafayette, IN 47907

Small but significant amounts of coke are unfortunately always formed when hydrocarbons are pyrolyzed to produce ethylene and other valuable by-products and when 1,2-dichloroethane is dehydrochlorinated to produce vinyl chloride. Carbon deposition in pyrolysis tubes is always accompanied by the following deleterious effects including reduced yields of desired products, down-time for decoking, increased resistance to heat transfer, and reduced tube creep rupture strength from carburization and the accompanying metal segregation. These effects all contribute to increased operating expenses, and significant advantages would result if coking could be reduced or eliminated.

Albright, McConnell and Welther (1) obtained valuable new information by comparing the morphologies of coke formed on stainless steels from acetylene, ethylene, butadiene, and propylene. Acetylene is a highly reactive precursor for the production of coke, and it is present whenever large amounts of ethylene are present in pyrolysis units. Using a scanning electron microscope equipped with EDAX to analyze for metals, they concluded that coke formed on Incoloy 800 surfaces often contained highly dispersed metal particles of nickel, chromium, and especially iron. These metal particles had apparently been extracted from the Incoloy 800 surfaces in a manner similar to a mechanism postulated by Baker and associates (2,3,4) and Trimm and associates (5,6,7) who used surfaces of pure iron, nickel, etc. This mechanism explains the simultaneous formation of metal-catalyzed filamentous coke and corrosion, perhaps along with erosion, of the metal surface. Particularly noteworthy is the finding reported by Albright et al. (1), and Graff and Albright (8), that for aluminized (or Alonized) Incoloy 800 surfaces filamentous coke was not observed and iron, nickel, and chromium were not detected in the coke.

0097-6156/82/0202-0123\$08.00/0

© 1982 American Chemical Society

Coke is produced by both homogeneous gas-phase reactions and heterogeneous metal-catalyzed reactions. Similar mechanisms for coke production which incorporate both homogeneous and heterogeneous coke formation have been proposed by Lahaye et al. (9), and Graff and Albright (8). These mechanisms, while useful, raise more questions than they answer. Additional information has been obtained in this investigation to clarify the interactions between coke produced via homogeneous and heterogeneous reactions. Information concerning coke formation on surfaces previously subjected to one coking/decoking cycle is also presented. Other variables investigated include the effect of temperature, partial pressure of coke precursor, and geometrical relationship between the solid surface and the gas for solid surfaces of Incoloy 800, aluminized Incoloy 800, and Vycor glass.

EXPERIMENTAL DETAILS

The apparatus and operating procedures were similar to those used by Albright, McConnell, and Welther (1). Metal alloy coupons (received from Alon Processing, Inc., Tarentum, PA) were approximately 1.9 x 0.5 x 0.2 cm.; the coupons were first rinsed with acetone, then dried, and next weighed to ± 0.0001 g. using a Mettler model H10 balance. These coupons were then inserted into 2.5 cm. lengths of 0.64 cm. I.D. Vycor glass tubing. The tubing containing the samples were next placed inside a Vycor glass reactor tube (2.2 cm. I.D. and 85 cm. long) that was positioned horizontally in an electrical furnace which could be controlled at any desired temperature in the 500 to 900°C range. For most experiments, Incoloy 800 and aluminized Incoloy 800 coupons were positioned side by side at identical process conditions near the furnace midpoint; several runs were also performed with coupons upstream or downstream of the furnace midpoint. Acetylene, ethylene, helium, and oxygen flows were metered as desired to the inlet of the Vycor reactor. For decoking, some helium or helium-oxygen mixtures were saturated with steam at any desired temperature between 25 and 100°C by bubbling the gases through a heated flask containing water. Residence times of the gases in the constant temperature section of the Vycor reactor were from 7 to 16 seconds.

The coupons, after removal from the Vycor reactor, were cooled in an inert atmosphere and then weighed. Coupon surfaces were analyzed using a Jeolco JSM-U3 scanning electron microscope and photographs

were taken at magnifications varying from 60 to 20,000. The metal content of the coupon surfaces or bulk coke was determined using an EDAX model 9100 energy dispersive analyzer that collects data up to a sample depth of approximately one micron.

RESULTS

Preliminary Analyses of Metal Surfaces: As shown in Figure 1A, the untreated Incoloy 800 surfaces were unpolished and exhibited numerous heterogeneities. Iron-rich areas or particles were scattered randomly over about 5% of the surface. EDAX indicated that the approximate surface composition (in weight percent) of 51% iron, 18% chromium, and 31% nickel differed slightly from the bulk composition which was 47% iron, 23% chromium, and 30% nickel. Helium, steam, or oxygen treatment at 900°C resulted in some chromium-rich spikes which protruded from a roughened Incoloy 800 surface (Figure 1C). After heating in helium for 3 hours, the surface analyzed 30% iron, 55% chromium, 14% nickel, and 1% titanium, indicating a significant enrichment in chromium and titanium. Graff and Albright (8) had earlier reported similar findings.

Untreated aluminized (or Alonized) Incoloy 800 surfaces, as shown in Figure 1B, were smooth and exhibited distinct grain boundaries which appeared as a network of irregular chicken wire. About 80-90% of the aluminized surface was highly enriched in aluminum, except for some heterogeneous areas which were pitted and contained much less aluminum. Aluminum chunks were observed both in these pitted areas and scattered over the remainder of the surface. The average surface composition was 45% aluminum, 28% iron, 9% chromium, and 18% nickel. EDAX analyses for cross sections of aluminized coupons indicated aluminum was diffused approximately 150-300 microns into the Incoloy 800 base metal; relative aluminum weight concentrations were still generally greater than 5% to these depths. Little or no roughening or composition change was observed for aluminized Incoloy 800 surfaces after heating at 900°C. As shown in Figure 1D, however, the grain boundaries exhibited a smeared appearance in comparison to those on an untreated coupon.

Coking Results: Temperature, precursor type, precursor partial pressure, and run duration all significantly affected the amount of coke for Incoloy 800 and aluminized Incoloy 800 coupons and Vycor glass. The

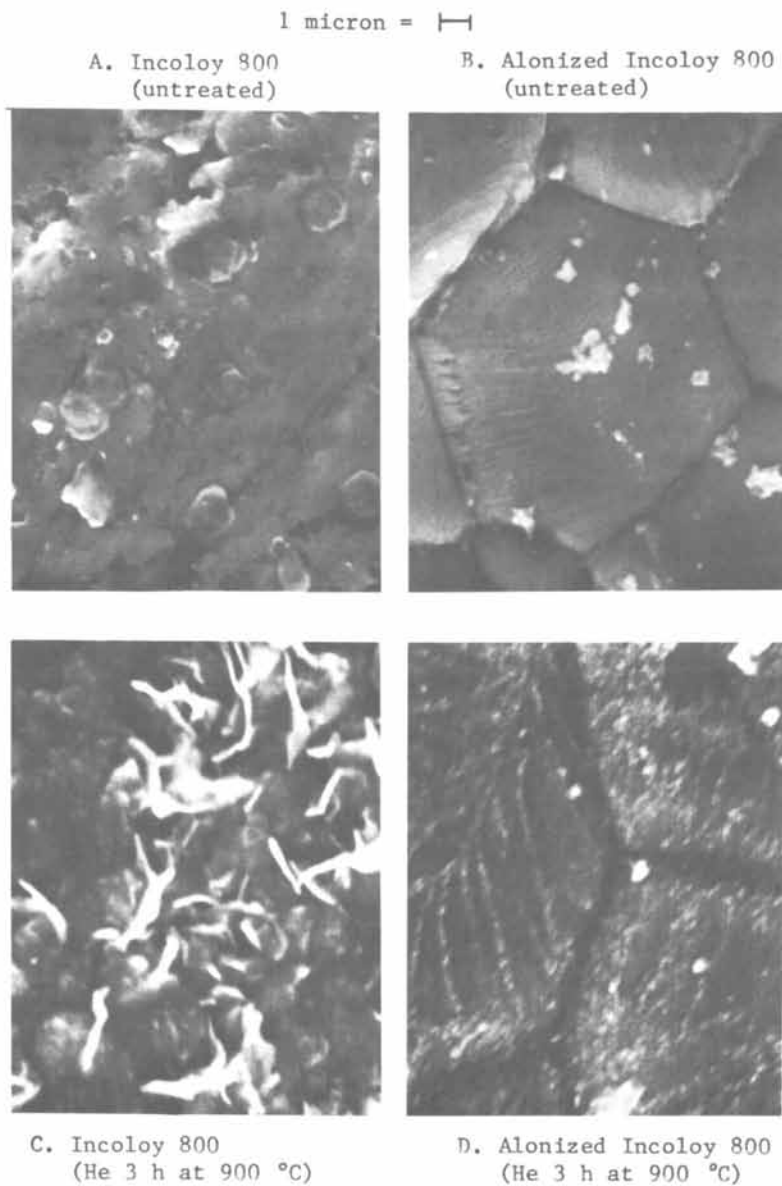


Figure 1. Untreated and helium treated alloy coupons.

quantitative results obtained in eleven runs of this investigation confirm the earlier more qualitative findings of other investigators (4,9). The combined rates of coke production and of collection on the surface are reported in the remainder of this paper as the rate of coke formation. This rate increased with increasing temperature and partial pressure (Table 1). For identical operating conditions, the amount of coke formed from 0.05 atm. acetylene was in all cases greater than or equal to the amount deposited from 0.1 atm. ethylene (Table 1). Since the rate of coke formation increases as confirmed in this investigation with increased partial pressure of the hydrocarbon, more coke is formed from acetylene than from ethylene based on similar hydrocarbon concentrations. The net amount of coke deposited on the coupons increased as the run progressed, but the rate of coke formation decreased with time for both Incoloy 800 and aluminized Incoloy 800 surfaces as will be discussed later.

Several types of coke were noted during the course of the present investigation. Filamentous cokes (including needles, ribbons, coiled filaments, braided diameter filaments, and straight, constant diameter filaments) were most predominant (but not exclusively present) on Incoloy 800 surfaces for runs at low temperatures (500 to 700°C), at low partial pressures (0.05 and 0.1 atm.), and short durations (\leq 1 hour). For example, coke structures formed on Incoloy 800 surfaces from 0.1 atm. ethylene ranged from needle-like filamentous deposits at 500°C (Figure 2A), and filaments at 700°C (Figure 2C), to aggregated chunks of globular coke which also contained braided diameter and coiled filaments, ribbons, and cylindrical coke at 800°C (Figure 3B), and stubby, cylindrical coke imbedded in and protruding from a matrix of globular coke (Figures 4A,4C) at 900°C. Raising the ethylene partial pressure to 0.5 atm. and increasing the run time from 0.33 to 1.0 hours at 900°C resulted in a massive spherical-globular coke deposit (Figure 4E and Table 1). Similarly, at 700°C a factor of ten increase in the ethylene partial pressure from 0.1 to 1.0 atm. concomitant with a 25% increase in run length led to a coke surface covered with globular deposits (Figure 5A).

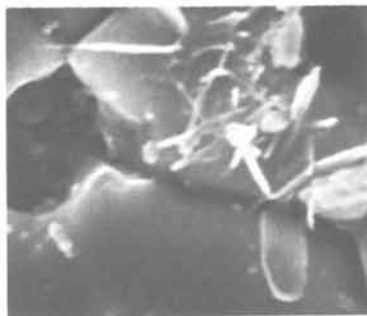
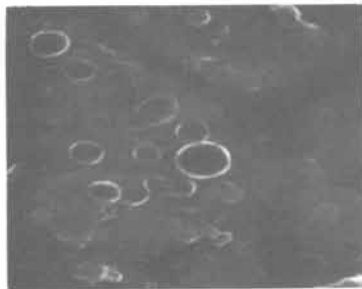
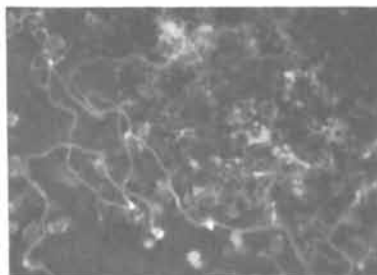
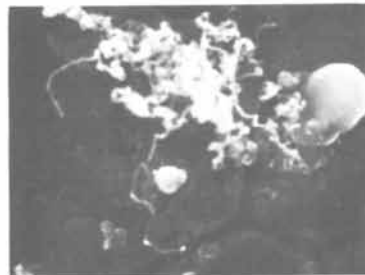
The orders of the rate of coke formation at 700 and 900°C were estimated from the measured buildup of coke on the metal coupons relative to the inlet ethylene partial pressure by the following equation:

$$\text{rate} = k(C)^n$$

TABLE I. Coking of Fresh Coupons

P Hydrocarbon in Feed*, Atm.	T, °C	Time of Run, Hours	Average Rate of Coking g coke/cm ² hr x 10 ⁴	Furnace Tube Position-Remarks	
				INCLOY 800	ALUMINIZED
<u>ETHYLENE</u>					
0.1	500	16	0.12	0.02	Midstream
0.1	700	10	0.28	0.03	Midstream
1.0	700	8	2.34	0.14	Upstream
1.0	700	8	5.76	0.08	Downstream
0.1	800	8	3.14 (G)	0.21 (H)	Midstream
0.1	800	8	3.61 (E)	0.56 (F)	Midstream-repeatedly withdrawn from tube (see Figure 9)
<u>ACETYLENE</u>					
0.1	900	0.33	3.40 (C)	1.90 (D)	Midstream
0.5	900	1	48.9 (A)	39.7 (B)	Midstream
<u>ACETYLENE</u>					
0.05	500	8	0.14	0.04	Upstream
0.05	700	16	1.04	0.09	Midstream
0.05	800	8	3.30	-	Upstream, top of pair
0.05	800	8	2.53	-	Upstream, bottom of pair
0.05	800	8	3.73 (I)	1.79 (K)	Midstream, singles
0.05	800	8	4.03 (J)	-	Midstream, top of pair
0.05	800	8	3.20	-	Midstream, bottom of pair
0.05	800	8	3.79	-	Downstream, top of pair
0.05	800	8	3.07	-	Downstream, bottom of pair

*Helium comprises remainder of feedstream (total pressure 1 atm.).
Letters allow coupon's history to be traced.

1 micron = A. Incoloy 800
(500 °C, 16 h)B. Alonized Incoloy 800
(500 °C, 16 h)C. Incoloy 800
(700 °C, 10 h)D. Alonized Incoloy 800
(700 °C, 10 h)E. Incoloy 800
(700 °C, 10 h,
O₂ pretreatment)F. Alonized Incoloy 800
(700 °C, 10 h,
O₂ pretreatment)Figure 2. 10% C₂H₄ at 500°C and 700°C.

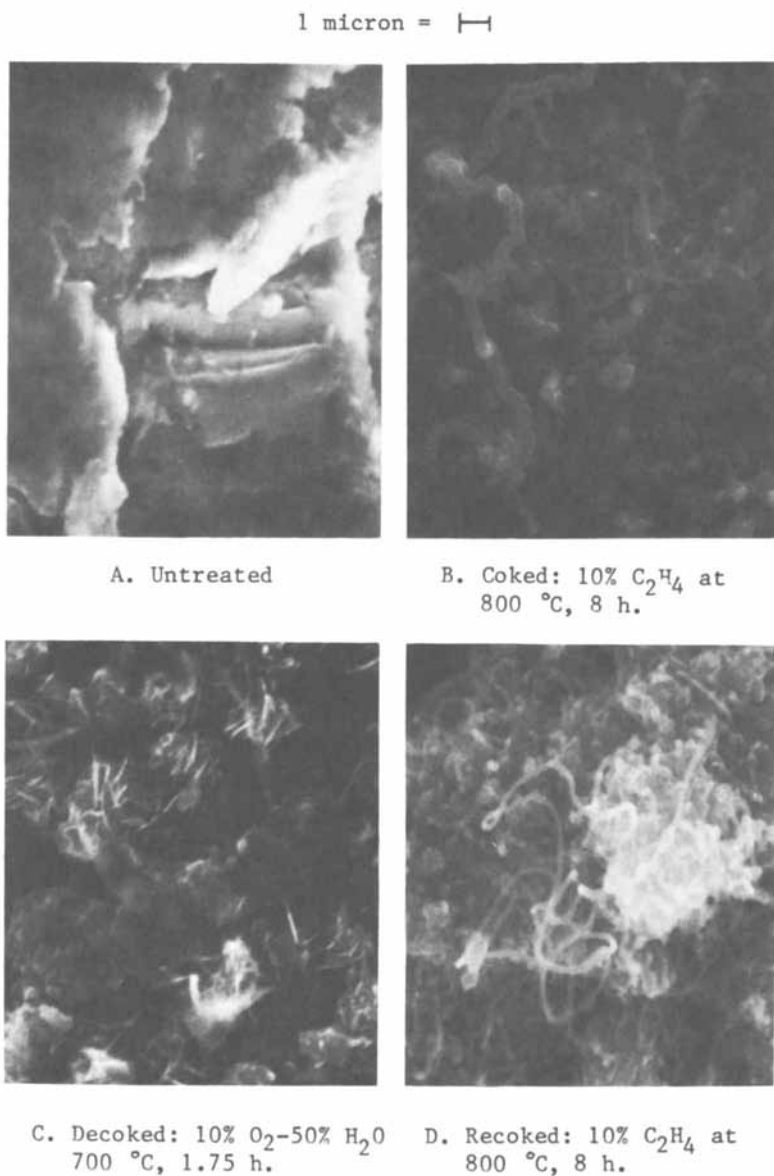


Figure 3. Coked and decoked Incoloy 800 surfaces.

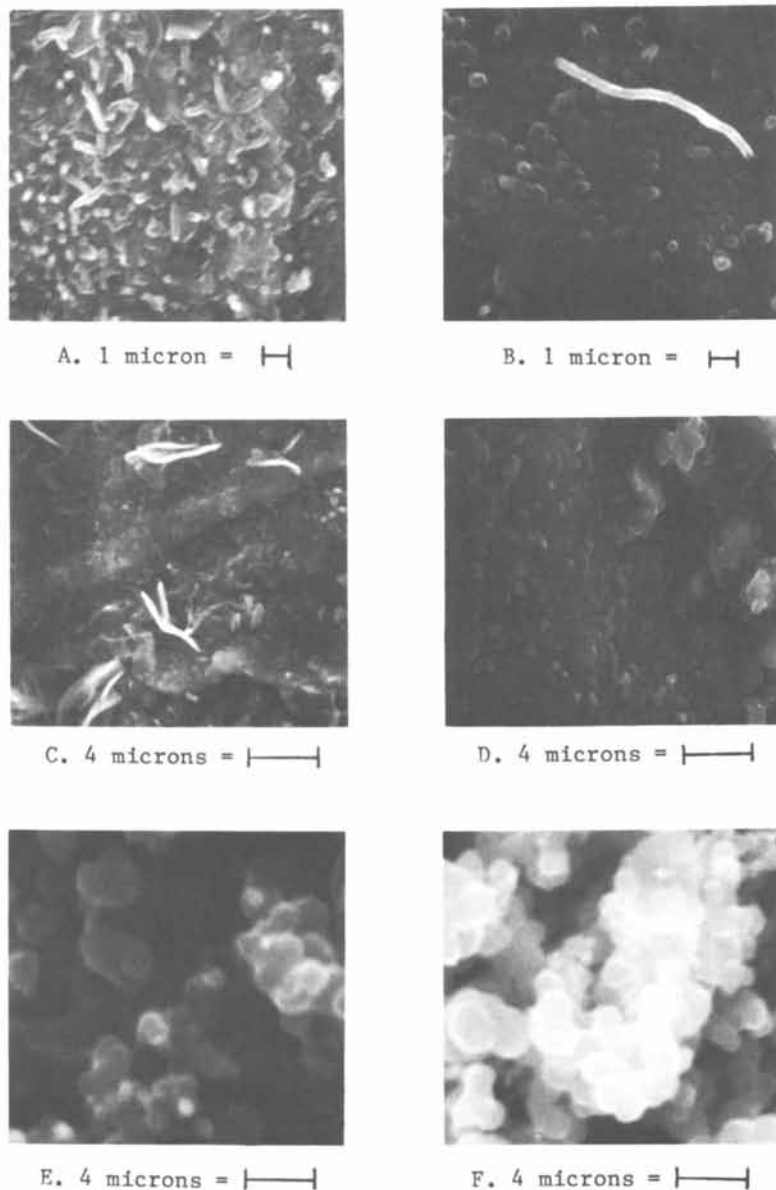


Figure 4. 10% and 50% C_2H_4 at $900^\circ C$. Key: A and C, Incoloy 800, 10% C_2H_4 , 0.33 h; B and D, alonized Incoloy 800, 10% C_2H_4 , 0.33 h; E, Incoloy 800, 50% C_2H_4 , 1 h; and F, alonized Incoloy 800, 50% C_2H_4 , 1 h.

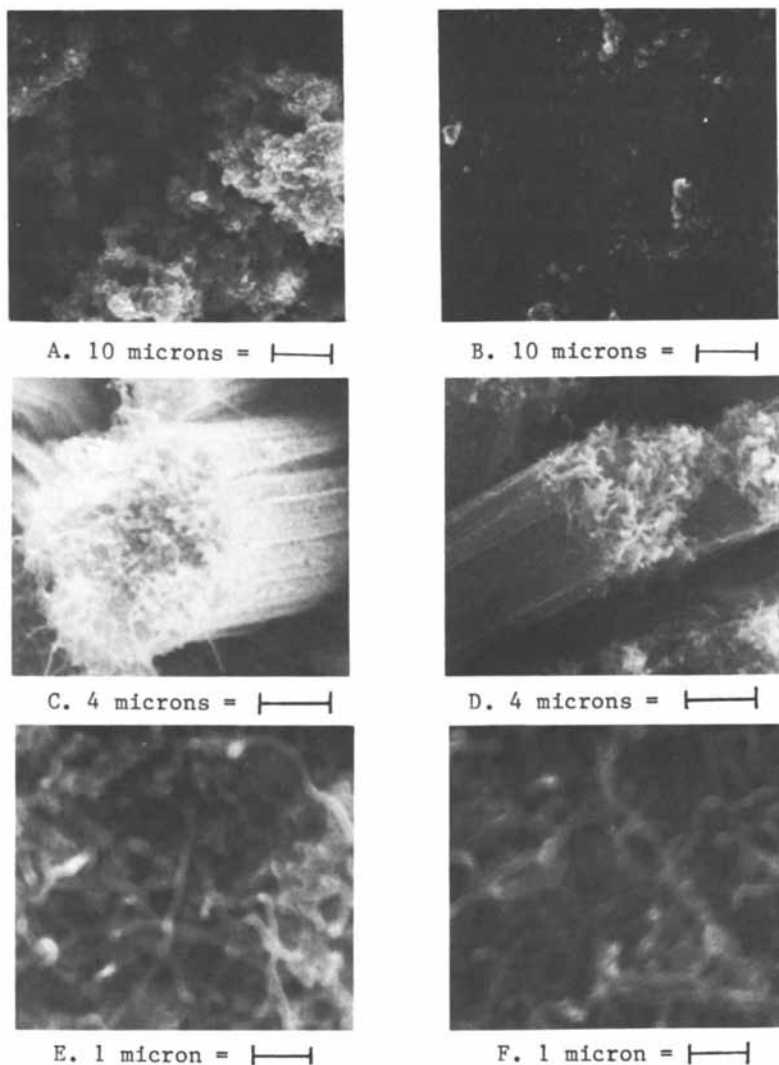


Figure 5. 100% C₂H₄ at 700°C for 8 h. Key: A, Incoloy 800, panoramic view; B, alonized Incoloy 800, panoramic view; C, round columns on Incoloy 800 surfaces; D, other columns on Incoloy 800 surfaces; E, face of round column; and F, area of Incoloy 800 surface near base of round column.

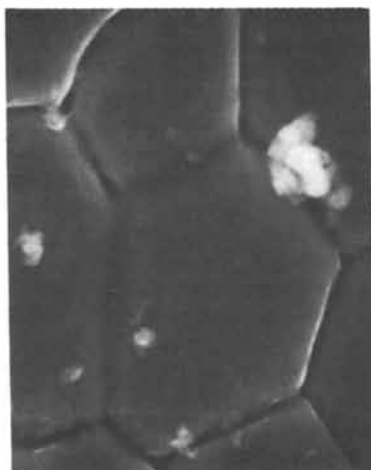
where

- k = constant of proportionality
- C = inlet ethylene partial pressure
- n = order of rate of coke formation

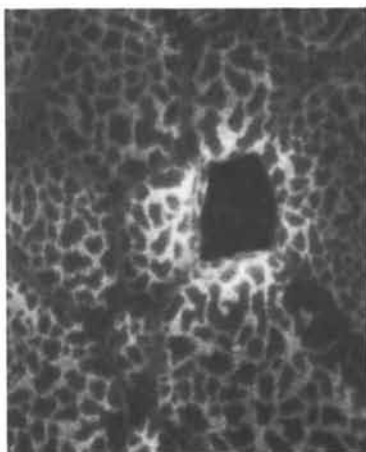
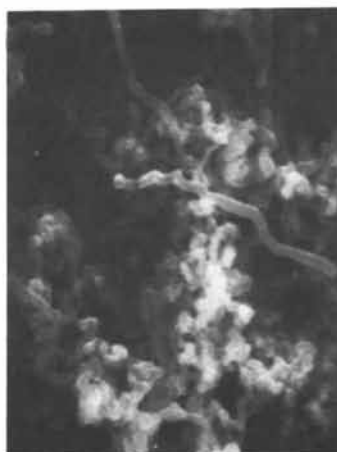
At 900°C, the order was slightly less than 2 for both aluminized and Incoloy 800 samples. At 700°C, the order estimated for Incoloy 800 coupons was approximately 1.0, while aluminized samples exhibited orders closer to 0.5.

Comparison of Surfaces: The character of the surface (i.e. material of construction) had major effects on both the amount and structure of the coke deposit, as indicated in Figures 2 through 8. Comparisons of the coke deposited on aluminized Incoloy 800, Incoloy 800, and Vycor glass surfaces subjected to identical process conditions support three findings. First, the average rate of coking calculated from the weight gain of the samples indicated that significantly more coke (often by a factor of five or greater) always formed on the Incoloy 800 coupons. Coking data obtained for samples subjected to 800°C with a 0.1 atm. ethylene feed and repeatedly withdrawn from the furnace tube for weighing showed that differences in coking rates for Incoloy 800 and aluminized Incoloy 800 samples on a relative basis (i.e. $\frac{\text{rate}_{\text{Incoloy}}}{\text{rate}_{\text{Aluminized}}}$) were greatest at short run lengths. The amounts of coke deposited on these coupons (reported as grams $\text{cm}^{-2} \times 10^4$) are depicted in Figure 9 as a function of time. The rate of coke formation for the Incoloy 800 coupon, determined as the slope of the top curve, decreased with time up to at least 8 hours. The small weight changes of the aluminized Incoloy 800 coupon especially during the early stages of the run were close to the observed precision of the balance, which complicates the interpretation.

Less coke was formed or deposited on Vycor glass in this same run than on either type of metal coupon. A silver or gray mirror-like coke generally covered 18-38 cm. of the Vycor furnace tube and the entire lengths of the 2.5 cm. Vycor sample tubes containing the metal coupons. Visual observations indicated that more coke was present on the Incoloy 800 and aluminized Incoloy 800 coupons after 0.5 hours. A perhaps more important finding is that no coke whatsoever was observed and no weight increase was detected after 0.5 hours when an empty Vycor sample tube was inserted in the furnace tube. Based on weight measurements of the empty sample tube after 8 hours operation, the rate of

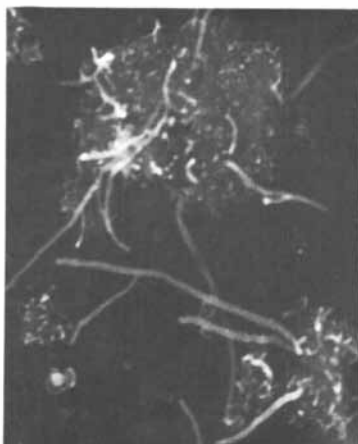
1 micron = 

A. Untreated

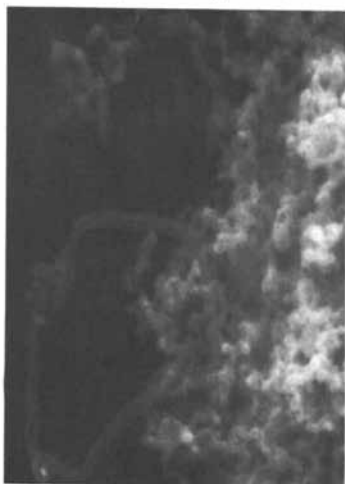
B. Coked: 10% C₂H₄
at 800 °C, 8 h.C. Decoked: 10% O₂-50% H₂O
at 700 °C, 1 h.D. Recoked: 10% C₂H₄ at
800 °C, 8 h.*Figure 6. Coked and recoked alonized surfaces.*

1 micron = 

A. Incoloy 800
(500 °C, 8 h)



B. Alonized Incoloy 800
(500 °C, 8 h)



C. Incoloy 800
(700 °C, 16 h)



D. Alonized Incoloy 800
(700 °C, 16 h)

Figure 7. 5% C_2H_2 at 500°C and 700°C.

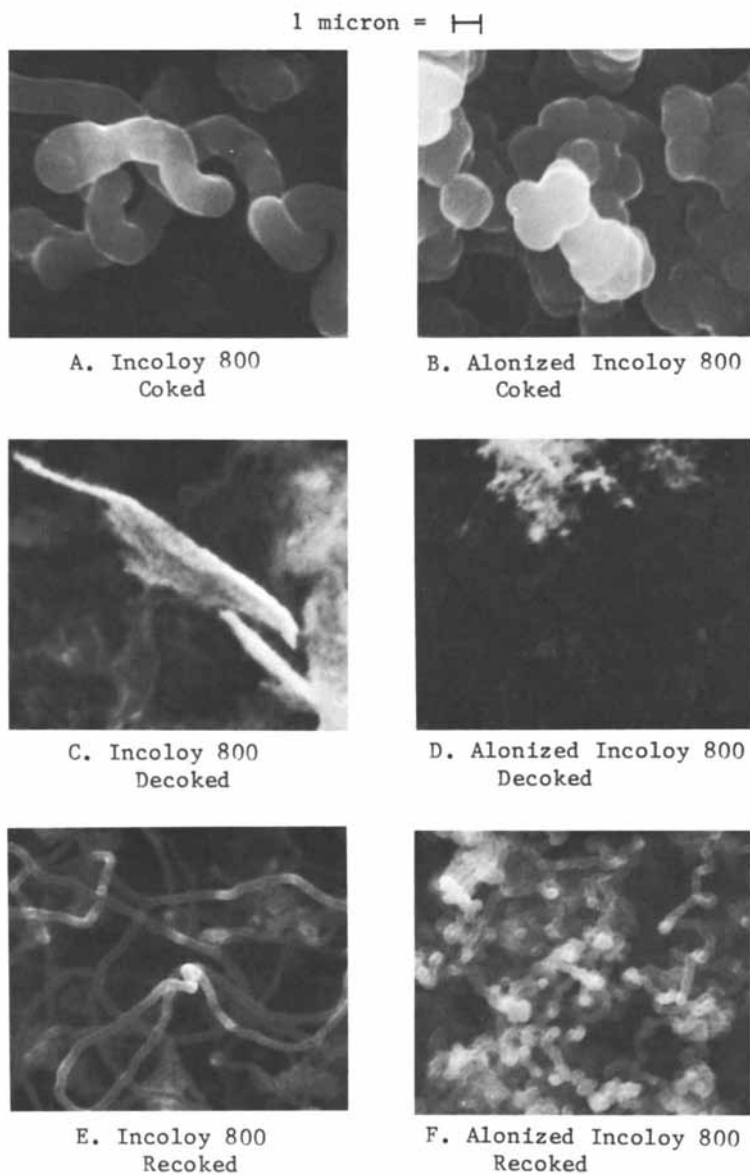


Figure 8. Coked and decoked Incoloy 800 and alonized Incoloy 800 surfaces. Key: A and B, 5% C_2H_2 , 800°C, 8 h; C and D, 10% O_2 -50% H_2O , 700°C, 1 h; and E and F, 5% C_2H_2 , 800°C, 8 h.

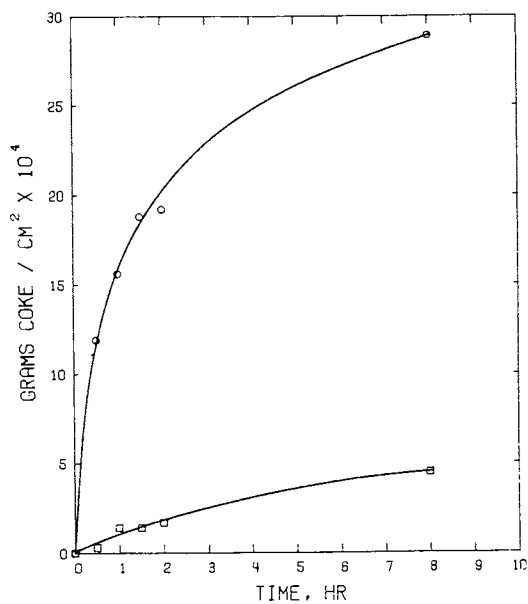


Figure 9. Coke deposition vs. time (10% C_2H_4 , at $800^\circ C$). Key: \circ , Incoloy 800; and \square , alonized Incoloy 800.

formation on the Vycor glass surface was estimated to be only 20% of that on the aluminized Incoloy 800 coupon.

A second finding is that the morphology of the coke deposited on aluminized Incoloy 800 and Incoloy 800 surfaces often was quite different. As depicted in Figures 2B, 2D, 2F, 4D, 4F, 5B, 6B, and 8B, the predominant structure of the coke observed on aluminized surfaces tended to be either a film of tar or a globular coke deposit. Filamentous coke was found on numerous Incoloy 800 samples (Figures 2A, 2C, 2E, 3B, 5C-5F, 7A, and 7C) whereas filamentous coke was detected at most in only small amounts on the aluminized surfaces of only three runs (Figures 2F, 7B, and 7D). Third, EDAX analyses indicated appreciable metal, generally mainly iron and nickel, in the coke formed on (or brushed off) the Incoloy 800 surfaces; analyses of coke deposited on aluminized Incoloy 800 coupons in the same runs indicated trace amounts of aluminum but no detectable iron, nickel, or chromium.

Surface heterogeneities described earlier often were important relative to coke formed or deposited on aluminized Incoloy 800 surfaces. Figures 5B, 6B, and 10B show globular and cylindrical coke which resulted preferentially in the pitted areas of aluminized surfaces in several runs. Filamentous coke formed at 700°C on an aluminized Incoloy 800 coupon subjected to a 0.05 atm. acetylene feed is depicted in Figure 7D; every filament observed was in or near a pitted area but interestingly not every pitted area contained filaments.

Heterogeneities and edge phenomena significantly affected the amount and type of coke formed at 700°C on an Incoloy 800 coupon contacted with 1.0 atm. ethylene. Most of the surface exhibited clusters of large, aggregated globular coke (Figure 5A). Between clusters, coiled filaments and smaller spherical-globular deposits were observed at higher magnifications. One notable exception, however, occurred near an edge of the coupon where the columns of coke depicted in Figures 5C and 5D were formed. Based on visual observations, this region of the coupon was not as heavily coked as the remainder of the coupon surface. Filament coke was detected on the column faces (Figure 5F). EDAX analysis of columns indicated they were formed in areas that were probably richer in iron and titanium than the surrounding metal surface.

Geometrical Effects: For coke deposition on metal samples, the orientation of the coupon face relative to



A. Bottom Face, INCOLOY 800

10 microns = 

B. Bottom Face, ALONIZED

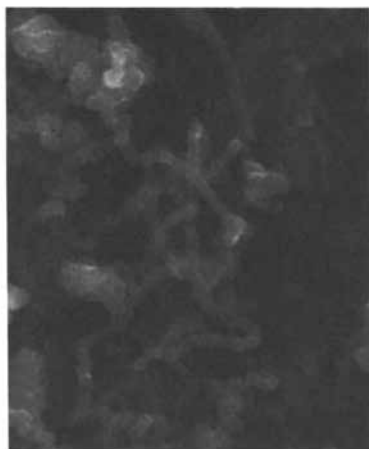
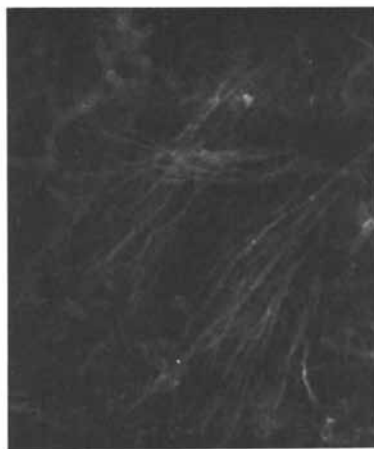
10 microns = C. Top Face, Top INCOLOY
800 Coupon4 microns = D. Top Face, Bottom INCOLOY
800 Coupon4 microns = 

Figure 10. Top-bottom geometrical effects. Key: A and B, 50% C_2H_4 , 900°C, 1 h; and C and D, 5% C_2H_2 , 800°C, 8 h.

the gas flowing over it had a significant effect on both the amount and structure of coke formed for runs at 800°C and 900°C. Comparison of Figure 10A vs 4E and Figure 10B vs 4F reveal major differences which occurred in the morphology of coke deposited on the top and bottom surfaces of both the Incoloy 800 and aluminized coupons. A dense layer of spherical-globular coke covered the top surfaces of both coupons (4E and 4F). The bottom surface of the Incoloy 800 coupon, on the other hand, exhibited numerous short cylindrical or "spaghetti" coke, intermixed with larger amorphous deposits (Figure 10A). The bottom surface of the aluminized Incoloy 800 coupon exhibited a thin layer of amorphous and globular coke deposits. The grain boundaries of the aluminized surface were clearly visible through the coke, indicating that less coke was present on the bottom than on the top. Numerous "weed patches" consisting of clusters of cylindrical coke (Figure 10B) were scattered randomly over the aluminized surface.

End effects were likely important for Incoloy 800 coupons. Relatively coke-free surface metal, enriched in both chromium and titanium, was visible at the upstream and/or downstream ends of several Incoloy 800 coupons subjected to 0.05 atm. acetylene at 800°C. Numerous small craters, or holes, were observed on the metal. A few isolated filaments protruded from the surface, and sparse amounts of globular coke were also detected at the ends. The bulk of the coke deposit, which consisted of filaments intermixed with larger amounts of globular coke (Figure 8A), occurred near the midsection of the coupon. A matrix of smooth and rather solid carbon was visible at the metal to coke transition region; the smooth matrix lay under the globular coke.

To further clarify the role of geometrical effects, the following experiment was performed. Three layered pairs of Incoloy 800 coupons, each pair consisting of one coupon atop a second, were placed in three separate 2.5 cm. lengths of Vycor tubing. One pair was positioned near the furnace midpoint, and the other two pairs were positioned 5 cm. upstream and 3 cm. downstream of the midpoint, respectively. Coke was deposited from 0.05 atm. acetylene at 800°C. Upon completion of the 8 hour run, all three coupon pairs had to be pried apart to separate them. More coke remained on the top coupons than on the bottom coupons (Table 1) for each pair. The top surfaces of all three top coupons exhibited similar types of coke; each was covered with a dense layer of spherical-

globular coke intermixed with relatively few filaments and amorphous chunks (Figure 10C). The bottom surfaces of all six coupons exhibited regions containing thin needle-like filaments, constant diameter filaments, and only small amounts of globular coke. The globular coke appeared to be entrapped by the filaments. The top surfaces of the bottom coupons exhibited both of these deposit characteristics; regions that had not been covered by the coupon had deposits similar to those on the top surfaces of the top coupons. Other regions (Figure 10D) that had been covered by the top coupons indicated coke coverage similar to that of the bottom surfaces of the coupons.

In the region of the Vycor reactor tube where mirror-like coke formed, more coke was observed on the bottom of the tube than on the top during runs at 700 and 800°C employing 0.05 atm. acetylene feeds. The coke at the bottom of the tube was a light gray powder. In addition, more coke was frequently observed on the top exterior regions and the bottom interior regions of the Vycor tubing used to hold the coupons. For example, after a 1 hour run a dark, powdery coke was detected on the top exterior of the Vycor tubing, which elsewhere was lightly smoked in appearance.

Results were also obtained at various axial furnace positions. Considerable more coke formed at 800°C from 0.05 atm. acetylene on layered and paired Incoloy 800 coupons at the midstream and downstream positions than at the upstream position. In a run employing ethylene, Incoloy 800 and aluminized coupons were positioned side by side in separate Vycor tubes both 4 cm. upstream and 4 cm. downstream of the furnace midpoint. For the Incoloy 800 coupons, about twice as much coke was formed at the downstream position (see Table 1). But, the reverse was true for the aluminized coupons.

Removal of Coke Deposits: Decoking rates for Incoloy 800 coupons, as shown in Table II, were approximately 1.3-4.0 times those of aluminized Incoloy 800 coupons subjected to identical conditions in both the initial coking and subsequent decoking runs. Caution must be exercised, however, in comparing the decoking rates of the two types of coupons since considerable less coke was present on the aluminized samples and since the decoking rates decreased significantly with increasing extent of burn-off.

The rate of decoking was significantly greater when oxygen was present in the oxidizing gas as

TABLE II. Decoking of Coupons at 700°C

Coupon Type	Feed* % O ₂	% H ₂ O	Run Duration, Hours	Average Decoking Rate (g coke removed) cm ² hr x 10 ⁴	% burn-off at run end
REMOVAL OF COKE DEPOSITED FROM ETHYLENE AT 900°C					
Incoloy 800, A	0	70	24	0.77	38
Aluminized, B	0	70	24	0.59	36
A	trace	100	105	2.88	100
B	trace	100	105	2.19	90
B	trace	100	3	0.61	97
Incoloy, C	100	0	0.42	>5.4	100
Aluminized, D	100	0	0.42	>3.1	100
REMOVAL OF COKE DEPOSITED FROM ETHYLENE AT 800°C					
Incoloy, E	10	50	1.75	14.1	100
Aluminized, F	10	50	1	4.81	100
Incoloy, G	0	50	2.25	1.08	11
Aluminized, H	0	50	2.25	0.3	<33
Incoloy, G	0	50	21.75	0.22	33
REMOVAL OF COKE DEPOSITED FROM ACETYLENE AT 800°C					
Incoloy 800, I	10	50	1	29.0	100
Incoloy 800, T	10	50	0.60	53.4	100
Aluminized, K	10	50	1	14.0	100

* Helium comprises remainder of feedstream (total pressure 1 atm.)
Letters allow coupon's history to be traced.

illustrated by decoking results for two Incoloy 800 coupons initially coked at 800°C with 0.1 atm. ethylene. Decoking with a 50% He-50% steam mixture for 24 hours removed only 30-40% of the coke deposit, but a 10% O₂-40% He-50% steam mixture resulted in a complete burn-off in 1.75 hours. The effects of a coking/decoking sequence on the morphology of the resulting surfaces were significantly different for Incoloy 800 and aluminized Incoloy 800 coupons. As shown in both Figures 3C and 8C, the decoked Incoloy 800 surfaces were much rougher than the untreated Incoloy 800 coupons shown in Figures 1A and 3A. Iron-rich spikes and iron-enriched areas (formed presumably via spalling) were frequently detected on decoked Incoloy 800 surfaces. While the overall surface compositions were still generally chromium-rich, these iron-rich spikes and regions indicate some segregation of the metals on Incoloy 800 surfaces. An especially dramatic example of surface alteration was noted for an Incoloy 800 coupon decoked with a 10% O₂-40% He-50% steam mixture. Three distinct regions were visible as seen by the naked eye - the upstream exhibited an orange rust powder, the middle was dark gray, and the downstream end was silver-gray in appearance. EDAX analysis of the top surface indicated that both ends, and especially the upstream end, were covered with flakes of iron oxide (see Figure 3C); the middle region was, however, chromium rich and contained some spikes richer in iron than the surrounding metal surface. These alterations in surface properties resulted in significant changes in the coking phenomena upon recoking, as will be discussed in detail later.

A coking/decoking sequence for aluminized Incoloy 800 coupons had little effect on the character of the surface (Figures 1B and 6A vs. Figures 6C and 8D). The aluminized coupons, after decoking, typically appeared to the naked eye as either a shiny silver or blue tinted color. Alternating light and dark spots were often detected on the aluminized Incoloy 800 surfaces under the SEM; in some cases these spots were so numerous they gave the aluminized surface a leopard-skin appearance (see Figure 6C). No differences in metal composition could be detected between the light and dark spots based on EDAX analyses. These spots are thought to be the result of varying degrees of oxidation or perhaps different alloy spinels on the aluminized surface.

Coke Formation on Used Surfaces and After Coking/Decoking Sequences: Coke deposition at 700°C from 0.1 atm. ethylene was investigated using Incoloy 800 and aluminized Incoloy 800 coupons which were first treated with oxygen at 700°C for 8 hours. As a result of the pretreatment, apparently activated areas of Incoloy 800 surface formed; patches of coke larger in size and present in greater amounts than the coke on the surrounding surface were detected on this Incoloy 800 coupon. These areas were scattered randomly over the Incoloy 800 surface. As depicted in Figure 2E, the filament and cylindrical coke in these patches were more plentiful and larger than the coke resulting on an Incoloy 800 surface subjected to the same coking conditions without an oxygen pretreatment (Figure 2C). Only a few activated areas containing filament coke were present on the aluminized Incoloy 800 surface as a result of the oxygen prior to coke deposition (Figure 2F); the predominant coke deposited on the aluminized coupon was globular coke.

Incoloy 800 and aluminized Incoloy 800 coupons were initially coked at 800°C with 0.1 atm. ethylene, next decoked at 700°C using a 10% O₂-40% He-50% steam mixture, and were then recoked at the same conditions as used for the initial coking. The amounts of coke formed in the recoking run were approximately 3.8 and 1.5 times the amounts formed in the initial coking run on the Incoloy 800 and aluminized Incoloy 800 coupons, respectively. For the Incoloy 800 coupon, more coke was detected at the upstream and downstream ends of the coupon, which were iron-rich after decoking as explained earlier. The coke present at the ends consisted of irregularly shaped clumps of globular coke which contained both constant diameter and coiled filaments (Figure 3D). Iron was present in the filaments. The middle area of this coupon exhibited much less coke; filament and globular coke as well as the chromium-rich surface metal were all detected. For the aluminized Incoloy 800 coupon, globular coke deposits were predominant as indicated in Figure 6D. Small amounts of filament coke were also intermixed with the globular coke deposit. The amount of coke formed on the surface was relatively small, and the discolored regions reported earlier could still be seen to some extent.

In a second recoking run at 800°C, used Incoloy 800 and aluminized Incoloy 800 surfaces were positioned side by side near the furnace midpoint and subjected to 0.05 atm. acetylene. Two additional coupons were included; a second used Incoloy 800 coupon was placed beside a new Incoloy 800 coupon at a position that was 5 cm. upstream of the furnace midpoint. About 27% more coke formed on this second used coupon than on the new coupon beside it, as indicated in Table III. Analogously, the amount of coke deposited on the aluminized Incoloy 800 coupon in the recoking was 67% greater than the amount deposited in the initial coking run. However, the amount of coke formed on the used Incoloy 800 coupon near the midpoint was 17% less than the amount formed in the initial coking run.

Several significant differences were found for coke structures formed on new and used coupons in the runs employing acetylene. Profuse filament growth was observed on both used Incoloy 800 coupons after recoking, and as shown in Figure 8E, relatively smaller amounts of globular coke were detected trapped in the filaments. The coke deposited on the fresh Incoloy 800 coupon was similar to that shown in Figure 8A. Coke-free metal was observed on perhaps 20-30% of the aluminized Incoloy 800 coupon after recoking. Elsewhere on the aluminized surface, patches of globular coke were predominant although some filament coke was intermixed with the globular deposits (Figure 8F). The filament coke was not observed on the aluminized surface after the initial coking run (Figure 8B).

Observations near the edges of several recoked Incoloy 800 coupons indicated that the structure of the coke deposit varied considerably with depth as the coke:metal interface was approached. The innermost layer, i.e., the layer in contact with the coupon surface, was observed to be a matrix of smooth and rather solid carbon. The outermost layer, however, consisted of the profuse filament growth which was described earlier from two-dimensional observations. This filamentous growth occurred in the region between the carbon matrix and the reacting gas phase.

DISCUSSION

Considerable more information has been obtained relative to coke formation and collection on stainless

TABLE III. Coking of Coupons with Various Past Histories

Hydrocarbon in Feed*, Atm.	T, °C	Time of Run, Hours	Average Rate of Coking g coke/cm ² hr x 10 ⁴	Remarks
<u>ETHYLENE</u>				
0.1	700	10	0.28	Fresh coupons
0.1	700	10	0.01	Coupons first oxidized with O ₂ 8 hours
0.1	800	8	3.61(E)	Initial coking
0.1	800	8	13.8(E)	Recoking
<u>ACETYLENE</u>				
0.05	800	8	3.73(I)	Initial coking, midstream
			4.03(J)	Midstream, top of pair
0.05	800	8	3.09(I)	Recoking, midstream
			4.61(J)	Recoking, upstream
			3.63	Fresh coupon, upstream

* Helium comprises remainder of feedstream (total pressure 1 atm).
Letters allow coupon's history to be traced.

steel surfaces and relative to decoking. Clearly some coke is formed catalytically on the surfaces with the subsequent corrosion of the surface as metal particles are extracted into the coke. Second, some coke or coke precursors such as tar droplets are formed in the gas phase and part of this coke or precursors then collect at the surface whereas the remainder exhausts with the main body of product gases. The collection of the coke or precursors formed in the gas phase obviously depends on several factors, but it seems obvious that filamentous coke and roughened surfaces promote collection of the gas-phase coke on the surface. The filamentous coke formed by catalytic surface reactions acts as a filtering medium for the tar droplets for example.

Surface corrosion can often be quite severe with stainless steels during coking-decoking sequences. There is first relative rapid diffusion of at least chromium and titanium to the surface. Second, catalytic coke formation acts to remove iron and nickel from the surface, which will be lost and likely exhausted from the reactor coil during burnoff or when portions of the filamentous coke are fragmented because of a variety of reasons including the rapid flow rates such as experienced in commercial pyrolysis coils. Third, carburization of the surface metals leads to a breakup of the integrity of the surface. Fourth, the surface oxidation or sulfidation of the surface metals occurs frequently in most pyrolysis coils because of the presence of steam, oxygen, hydrogen sulfide, or other sulfur-containing gases. The metal oxides and sulfides are eventually destroyed; the net result is, however, initial roughening of the surface but with time there will be a gradual spalling and loss of metal from the surface. Rougher surfaces probably in general result in increased formation of surface-catalyzed cokes (such as filamentous coke) and in more effective collection of gas-phase cokes or coke precursors on the surface.

The present results support the general conclusion by Baker and Chludzinski (10) that certain surfaces can minimize coke formation on the surface. In the present case, aluminized stainless steels as prepared by Alon Processing, Inc. retained their surface characteristics over at least two coking sequences. It is known in addition that a tube prepared by Alon Processing was used successfully in an ethylene coil for at least a year and that appreciable aluminum was still present on the surface at the

American Chemical
Society Library

1155 16th St. N. W.

end of that time. Baker and Chludzinski (10), however, reported that aluminum oxide fragmented and rapidly spalled off their aluminum-coated stainless steel; they did not report though their method of treating the metal surface to get a coating.

Clearly geometrical factors relative to coke collection on metal surfaces have an important effect on coke formation. There is obviously a need to obtain more information relative to the flow patterns at or near the surface and surface roughness (and composition). Indirectly these factors would certainly affect the wettability of the surface with coke or coke precursors.

ACKNOWLEDGEMENT

Acknowledgment is made to the donors of the Petroleum Research Fund, administered by the American Chemical Society, for partial support of the research. Alon Processing, Inc. of Tarentum, PA also provided support.

LITERATURE CITED

1. Albright, L.F.; McConnell, C.F.; Welther, K., "Thermal Hydrocarbon Chemistry"; Advances in Chemistry Series No. 183, Chapter 10, A.G. Oblad, H.G. Davis, and T.E. Eddinger, Ed., American Chemical Society: Washington, D.C., 1979.
2. Baker, R.T.K.; Barber, M.A.; Harris, P.S.; Feates, F.S.; Waite, R.J., J. Catalysis (1972), 26, 51-62.
3. Baker, R.T.K.; Harris, P.S., "Chemistry and Physics of Carbon", Vol. 14, Chapter 2, P.L. Walker and P.A. Thrower, Ed., Marcel Dekker, Inc.: New York, 1978.
4. Baker, R.T.K.; Harris, P.S.; Thomas, R.B.; Waite, R.J., J. Catalysis (1973), 30, 86-95.
5. Lobo, L.S.; Trimm, D.L., J. Catalysis (1973), 29, 15-19.
6. Lobo, L.S.; Trimm, D.L.; Figueiredo, J.L., Proc. 5th Int. Cong. Cat. (1973), 1125-1137.

7. Trimm, D.L., Catal. Rev. - Sci. Eng. (1977), 16(2), 155-189
8. Graff, M.J.; Albright, L.F., Carbon (1982), in press.
9. Lahaye, J.; Badie, P.; Ducret, J., Carbon (1977), 15, 87-93.
10. Baker, R.T.K.; Chludzinski, J.J., J. Catalysis (1980), 64, 464-478.

RECEIVED July 7, 1982.

Surface Phenomena During Pyrolysis: The Effects of Treatments with Various Inorganic Gases

JAMES C. MAREK and LYLE F. ALBRIGHT

Purdue University, School of Chemical Engineering, West Lafayette, IN 47907

Build-ups of coke in the coils of a pyrolysis furnace and in the transfer line exchanger necessitate shut-down of the unit for decoking purposes generally every one to six months. Many factors affect the rates of coke formation and collection on the surfaces of the coils and the transfer line exchangers, including the composition and roughness of the metal surfaces. For example, significantly less coke results on aluminized surfaces (1,2) and on silica-rich or silicon-rich surfaces (3). Furthermore, more coke is normally formed on stainless steel surfaces that have been coked and decoked once as compared to new surfaces (2).

Metal oxides on the inner surfaces of stainless steel coils are known to affect the formation of coke in pyrolysis units. Such oxides are formed by reactions with steam used as diluent in hydrocarbon feedstocks and with steam-air mixtures used for decoking the coils. The amount of oxygen or steam that reacts to produce metal oxides increases by a factor of perhaps 4-5 during the first few oxidation-reduction sequences (4). When a reactor with an oxidized surface is contacted at pyrolysis temperatures with hydrogen sulfide, the surface is sulfided and both water and sulfur dioxide are emitted as gaseous products (4). Nickel sulfides are known to be liquids at pyrolysis temperatures, and may be separated from the inner surfaces. Clearly oxidation, reduction, and sulfiding of the surface roughens it significantly.

Castle and Durbin (5) used x-ray photoelectron spectroscopy (XPS) to investigate the surface composition of 9% nickel and 12% chromium stainless steels that were subjected to oxidizing atmospheres at 500°C. Fe_3O_4 was predominant in the surface layer and a Cr_2O_3

0097-6156/82/0202-0151\$06.00/0

© 1982 American Chemical Society

layer was present just beneath the base of the magnetite film. Bittner et al. (6) investigated steam oxidation of simulated Incoloy 800 surfaces at 600°C. They found that the initial iron oxide layer present on the surface spalls off leaving a film rich in chromium oxides that is quite stable. Rather limited information is however available relative to coke formation on oxidized or reduced stainless steels. For instance, alloy composition appears to be of considerable importance in determining the amount and structure of coke deposits formed at 500 or 700°C from acetone-CO₂ mixtures (5,7).

The objective of the present investigation was to investigate systematically the effects of treating or contacting Incoloy 800 and aluminized Incoloy 800 steels with various inorganic gases and to determine how these treatments subsequently affect coking. In addition, comparisons were made between the original, unpolished metal surfaces and ones that were mechanically polished and smoothed.

Experimental Details

The apparatus was similar to the one used by Albright, McConnell, and Welther (8). The metal alloy coupons (supplied by Alon Processing, Inc., Tarentum, PA) were approximately 1.9 x 0.5 x 0.2 cm. Some coupons were conventional Incoloy 800 and others were aluminized by their proprietary process. These latter coupons are often referred to as alonized coupons. Select coupons were polished using 200 through 600 grit silicon carbide, 5 μm diamond, and finally 0.05 μm alumina polishing wheels. Residue from the polishing operations was removed by immersing the coupons in an ultrasonic cleaner. In every case, polished coupons prepared in this manner exhibited mirror-like surfaces. Both polished and unpolished coupons were rinsed in carbon tetrachloride, dried, and weighed to ±0.0001 g with a Mettler model H10 balance; they were then inserted into separate 2.5 cm. lengths of 0.64 cm. I.D. Vycor glass tubing.

The tubing containing the coupon samples were placed inside a Vycor glass tube (2.2 cm. I.D. and 85 cm. long) that was positioned horizontally in an electrical furnace controlled at either 700 or 900°C. For inorganic gas treatments, Incoloy 800 and polished Incoloy 800 coupons were positioned side by side 4.5 cm. upstream of the reactor midpoint; polished and unpolished aluminized Incoloy 800 coupons were likewise positioned side by side except 2.0 cm. upstream

of the midpoint. Helium, oxygen, and hydrogen sulfide flows were metered as desired to the inlet of the Vycor glass tube. Steam treatments were performed by saturating helium with steam; the gas was bubbled through a flask of water heated to 87°C to produce a 60% steam-40% helium mixture. For coking experiments, Incoloy 800 and polished Incoloy 800 coupons were positioned 3.8 cm. upstream of the reactor midpoint while polished and unpolished aluminized Incoloy 800 coupons were positioned at the reactor midpoint. A 5% mixture of acetylene in helium was then metered to the inlet of the Vycor tube.

The coupons, after removal from the Vycor reactor, were first cooled in an inert atmosphere and then weighed. Coupon surfaces were analyzed using a Jeolco JSM-U3 scanning electron microscope (resolution 300 Å) and micrographs were taken at magnifications ranging in general from 1,000 to 10,000. The metal content of the coupon surfaces was determined quantitatively using an EDAX model 9100 energy dispersive analyzer and EDAX supplied computer software.

Experimental Results

Surface Morphology of Metal Coupons: Surface morphology changed significantly especially for Incoloy 800 coupons after contacting them at 700° or 900°C with either helium, 60% steam in helium, oxygen, or hydrogen sulfide for four hours. In many cases various portions of a coupon were changed to different extents; the results are therefore an average of the changes in surface morphology. Figures 1 through 4 show pictures taken with the scanning electron microscope before and after the four treatments at 700°C of the Incoloy 800, polished Incoloy 800, aluminized (or alonized) Incoloy 800, and polished aluminized Incoloy 800 coupons, respectively.

The relative effect of these treatments on morphology was in the following order:



Helium is probably essentially inert although the helium used did contain trace amounts of oxygen. Changes in the morphology during helium treatments are believed to be caused by the high temperatures. Figure 1B shows an Incoloy 800 surface after helium treatment at 700°C; it is slightly rougher than the untreated Incoloy 800 surface shown in Figure 1A. Helium treatment of polished Incoloy 800 resulted in grains of metal outlined by a network of channels, as

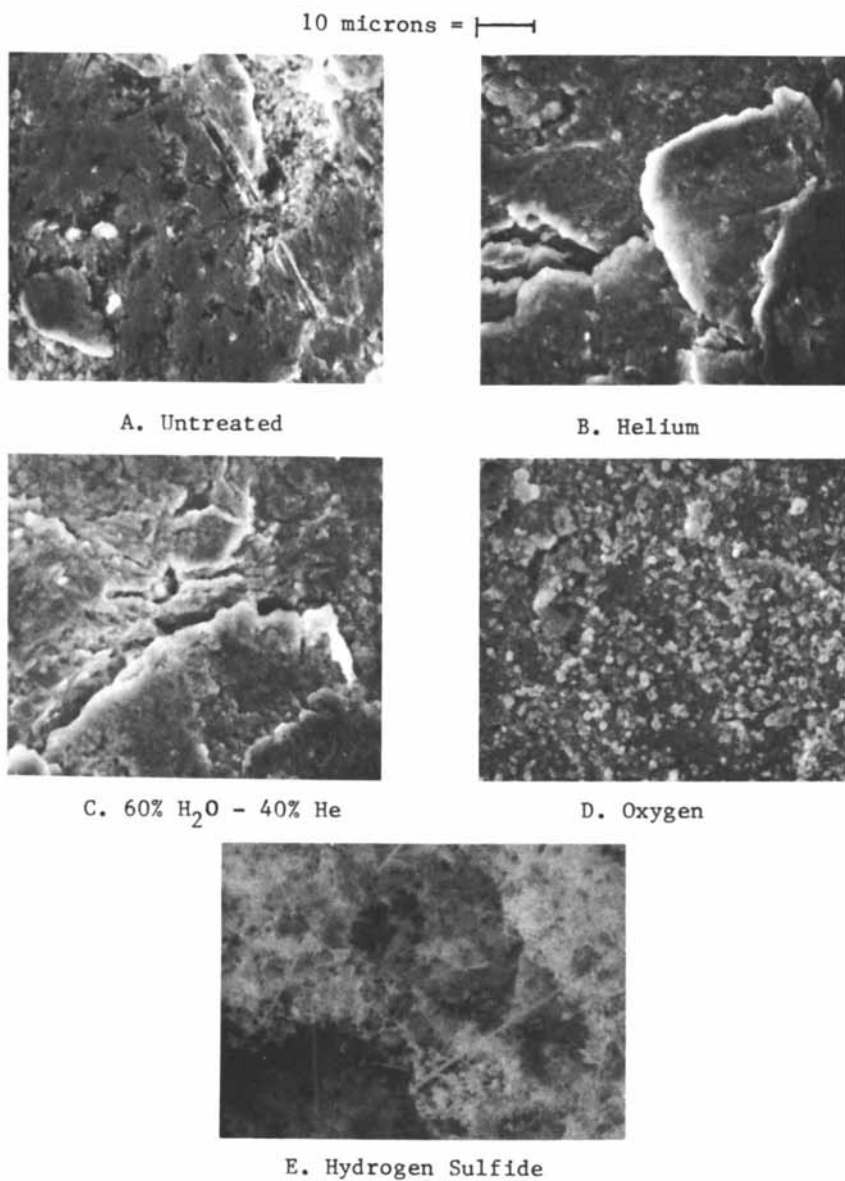


Figure 1. Gaseous treatments of Incoloy 800 at 700°C for 4 h.

shown in Figure 2B. Roughness increased relative to untreated polished Incoloy 800 (Figure 2A) but the surface was clearly smoother than untreated or helium treated unpolished Incoloy 800 surfaces.

Treatments of Incoloy 800 coupons with steam or oxygen were at conditions which result in the formation of metal oxides on the surface (4,6). As a result, the surfaces were much rougher, as shown in Figure 1; some areas had a fused particle appearance (Figure 1D) while other areas exhibited spikes. Less pronounced visual changes occurred in all cases for the polished Incoloy 800 coupons. As shown in Figures 2C and 2D, the surfaces were still generally smooth except perhaps where scratches had not been completely smoothed before treatment.

Treatments of aluminized (or alonized) Incoloy 800 coupons with helium, oxygen, or steam at 700°C in general resulted in only rather small changes in appearance, as shown in both Figures 3 and 4 for the unpolished and the polished coupons, respectively. The findings with the polished aluminized coupons must however be considered less reliable. The objective had been to remove only the outer layer that in places was almost pure aluminum and polish until the depth was reached at which aluminum had alloyed with the Incoloy 800. For some coupons, too much or perhaps too little metal was removed, such as for the rough portion of the steam-treated coupon shown in Figure 4C.

Hydrogen sulfide treatment had significant effects on the morphology of all coupons tested at 700°C. Exposure of Incoloy 800 to hydrogen sulfide resulted in a layer of sulfide scale covered with dendrites (or filaments) of metal sulfides, as shown in Figure 1E. The outer sulfide scale flaked off the base metal of the polished Incoloy 800 sample, resulting in the rough surface depicted in Figure 2E. Sulfide dendrites were formed in small amounts on aluminized Incoloy 800 and polished aluminized Incoloy 800 surfaces, as shown in Figures 3E and 4E. In general, the morphology of the various coupons changed in the following relative order with the various treatments:

Incoloy 800 > polished Incoloy 800 > aluminized Incoloy 800 > polished aluminized Incoloy 800

Oxidizing treatments of Incoloy 800 and polished Incoloy 800 coupons at 900°C resulted in larger changes in surface morphology, as shown in Figure 5. The surfaces were substantially rougher in appearance than after exposures to steam or oxygen at 700°C; a fused particle appearance was again observed. In some

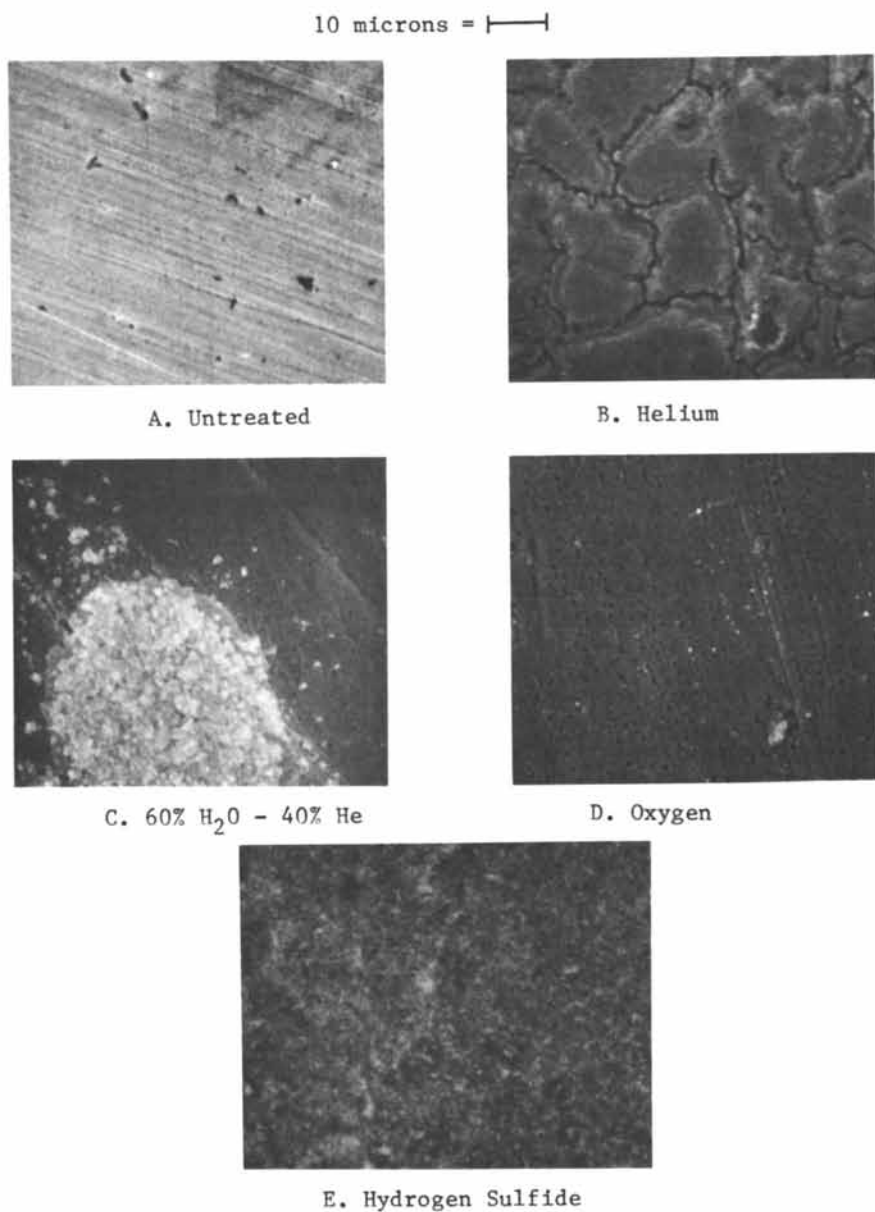


Figure 2. Gaseous treatments of polished Incoloy 800 at 700°C for 4 h.

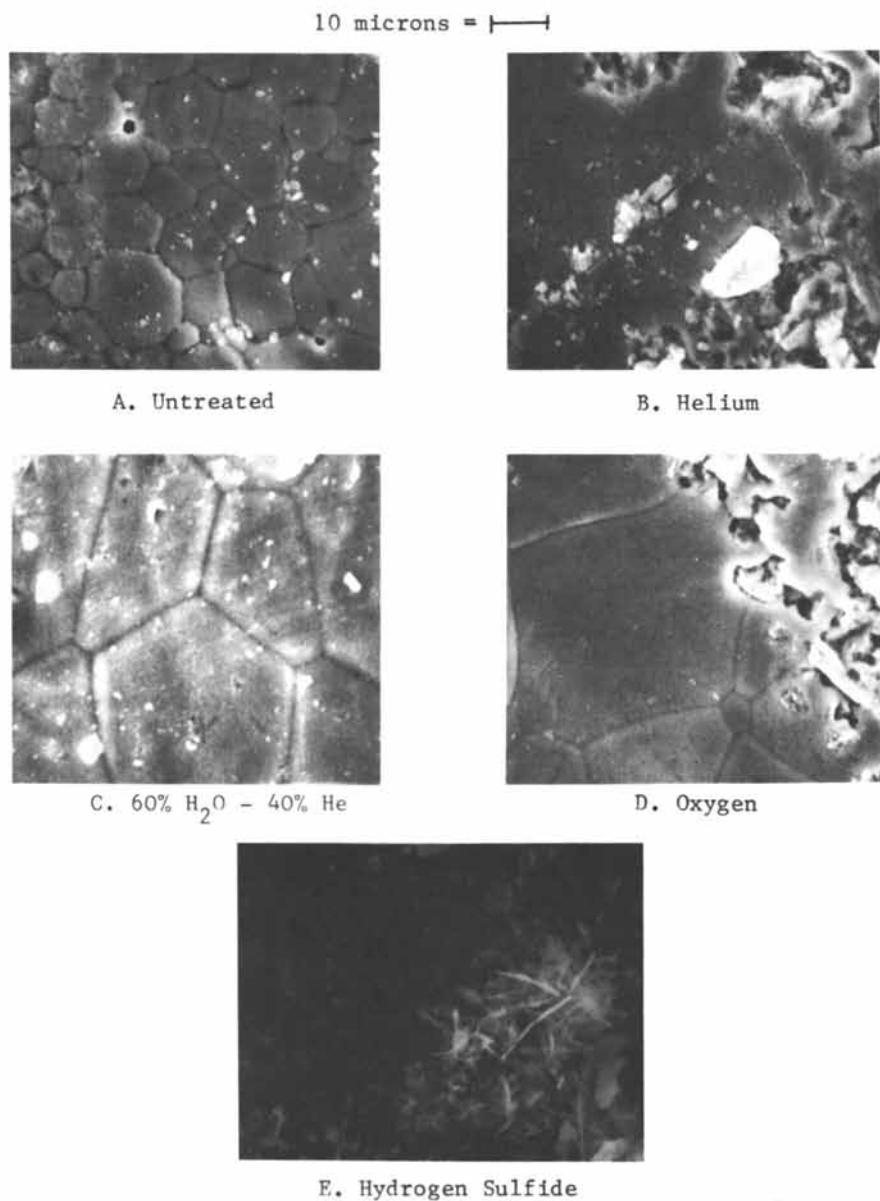


Figure 3. Gaseous treatments of alonized Incoloy 800 at 700°C for 4 h.

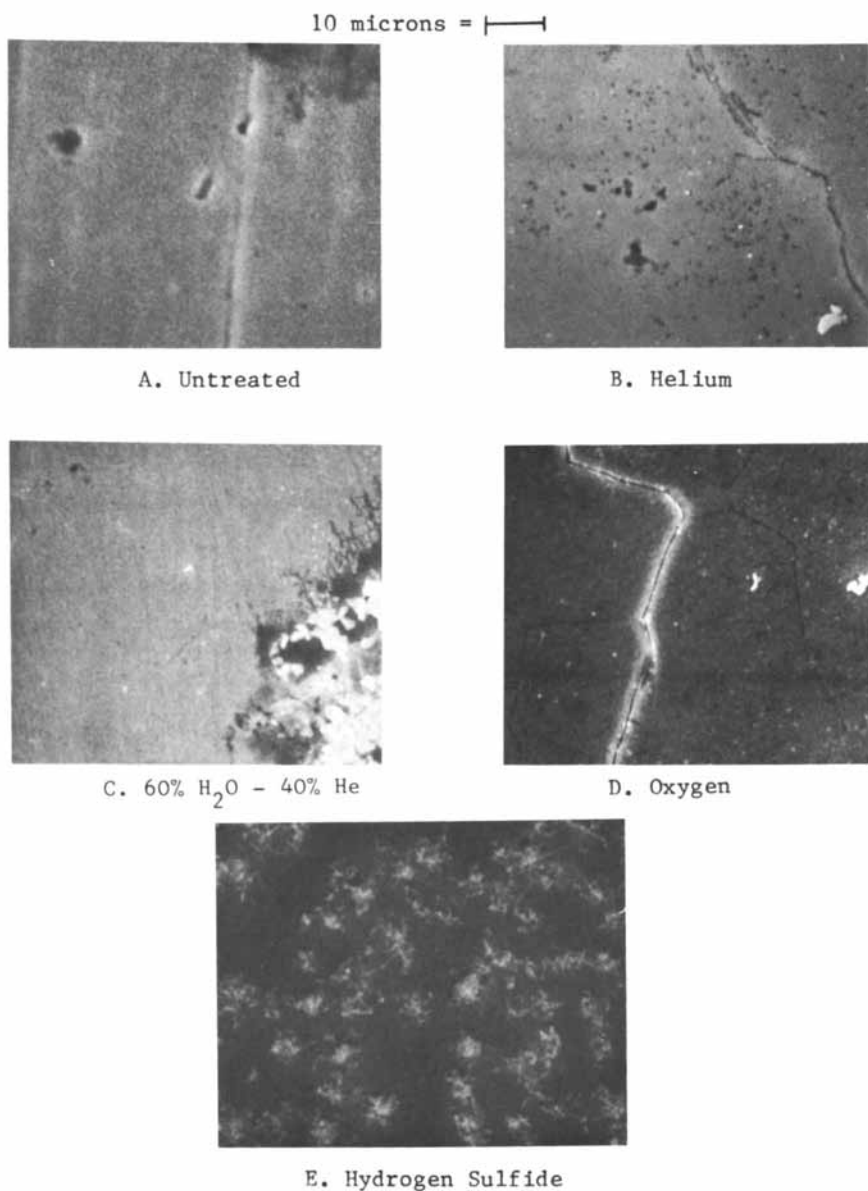


Figure 4. Gaseous treatments of polished alonized Incoloy 800 at 700°C for 4 h.

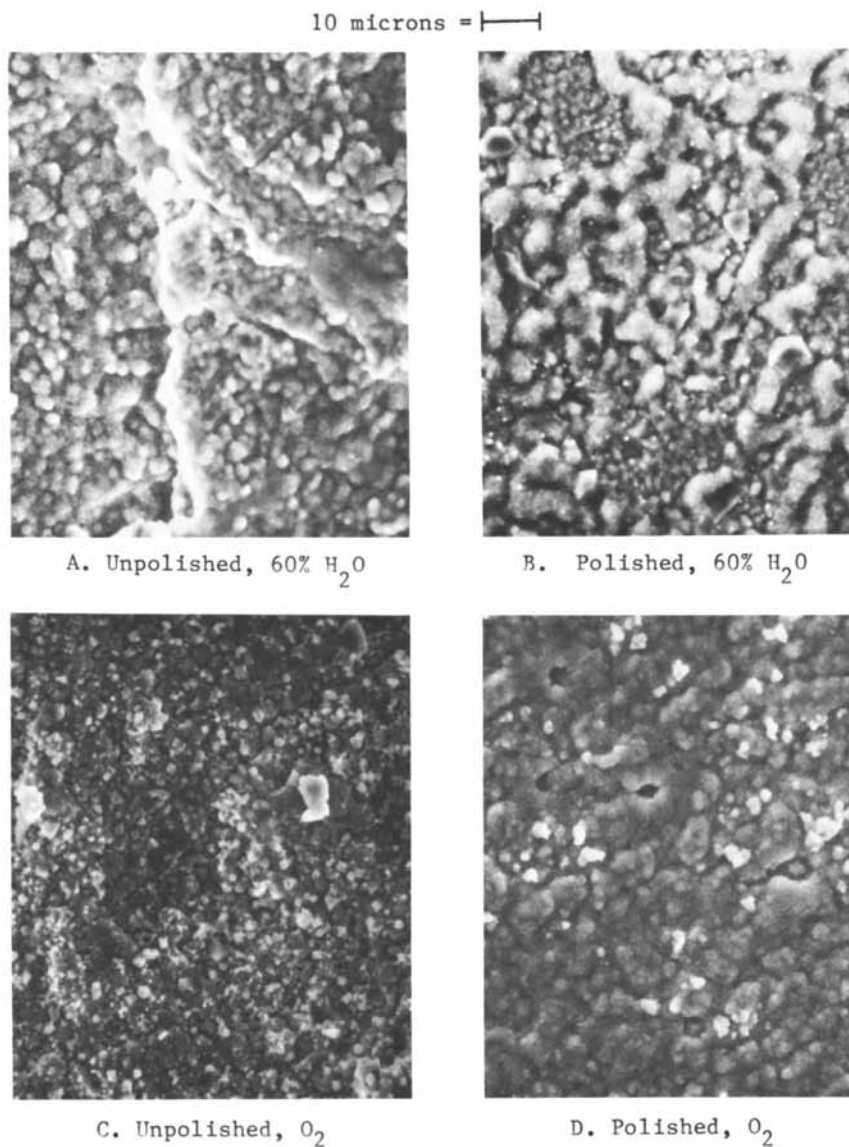


Figure 5. Gaseous treatments of Incoloy 800 surfaces at 900°C for 4 h.

cases, structures resembling octahedrons or tetrahedrons were observed at high magnifications.

Aluminized Incoloy 800 and polished aluminized Incoloy 800 coupons were generally less affected than Incoloy 800 coupons by treatments with oxygen or steam at 900°C, as shown in Figure 6. Rough, cracked, or even spalled areas were formed to a small extent at this temperature on the aluminized Incoloy 800 and polished aluminized Incoloy 800 surfaces. However, major portions of the surfaces were relatively unchanged.

Surface Compositions of Metal Coupons: Surface compositions of the Incoloy 800 and aluminized Incoloy 800 coupons after exposure to the inorganic gases for four hours at 700°C and 900°C are presented in Tables I and II. Analyses for the surfaces of the starting coupons are included for comparison. Polishing of both the Incoloy 800 and aluminized Incoloy 800 coupons resulted in major differences in the surface composition. The analysis reported in Table I for the polished Incoloy 800 surface is in excellent agreement with the nominal composition (20.6% Cr, 46% Fe, and 31.9% Ni) reported for Incoloy 800 (?). Incoloy 800 coupons as received had more iron on the surface; particles that were essentially almost pure iron were noted on all unpolished coupons tested. Aluminized Incoloy 800 coupons as received had regions of almost pure aluminum (or alumina) on the surface. The polished aluminized coupons indicated almost 40% aluminum; on an aluminum-free basis the chromium content was slightly lower compared to that for polished Incoloy 800.

The compositions of Incoloy 800 and polished Incoloy 800 surfaces after exposures to helium, steam, and oxygen at 700°C were slightly richer in chromium and titanium and slightly depleted in nickel, relative to untreated Incoloy 800. No significant changes in surface composition, within the limits of experimental error, were detected at 700°C for polished and unpolished aluminized Incoloy 800 samples exposed to identical conditions (see Table II). A slight decrease in aluminum from 39.6 wt% to approximately 35% was observed for the polished aluminized Incoloy 800 samples. This difference may be, in part at least, a result of variations in the thickness of the aluminum-rich layer for polished samples.

In contrast to the findings at 700°C, major differences in surface composition were found after exposure of Incoloy 800 and polished Incoloy 800

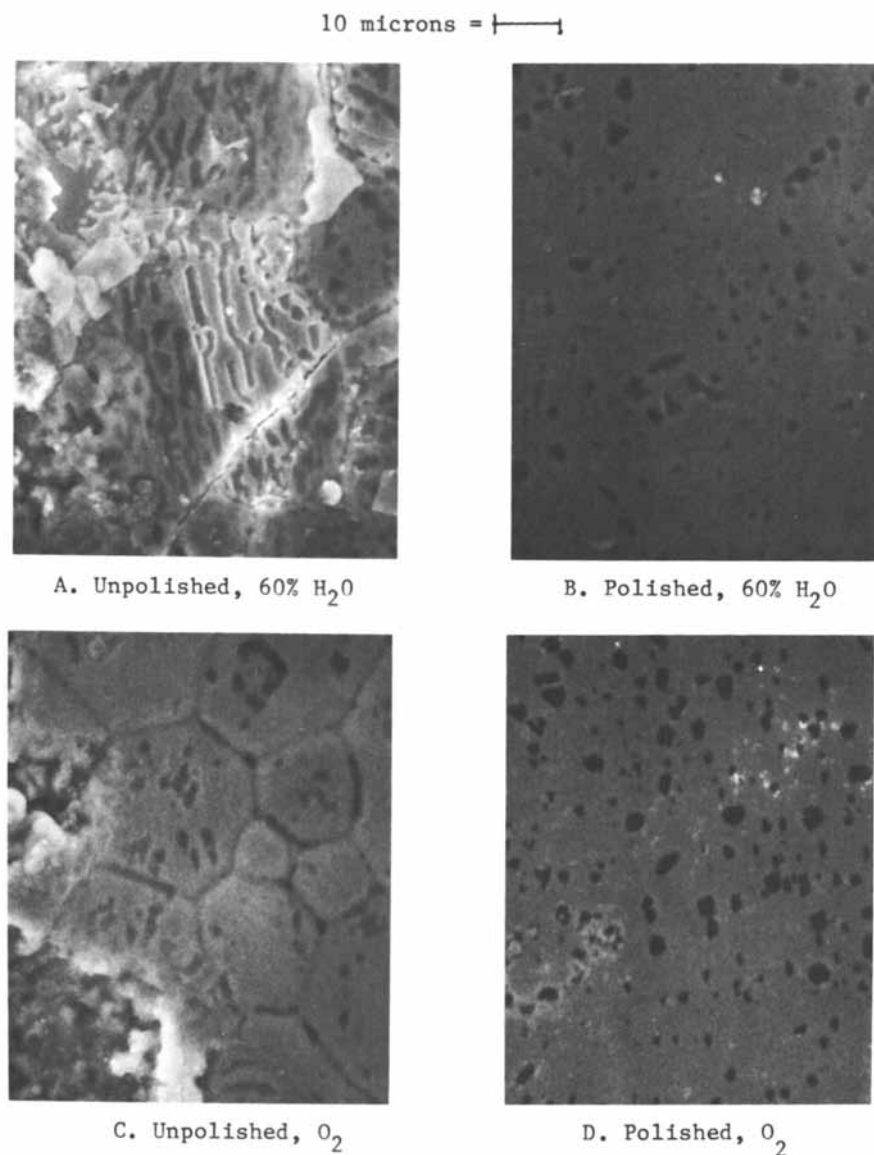


Figure 6. Gaseous treatments of alonized Incoloy 800 surfaces at 900°C for 4 h.

TABLE I: Compositions (wt.%) of Polished and Unpolished Incoloy 800 Samples after 4-Hour Exposures

Treatment	Incoloy 800				Polished Incoloy 800					
	%Ti	%Cr	%Fe	%Ni	%S	%Ti	%Cr	%Fe	%Ni	%S
None	-	18.0	49.0	33.0	-	-	20.2	46.7	33.3	-
He, 700°C	-	24.1	46.4	29.5	-	-	23.7	47.1	29.2	-
H ₂ O, 700 °C	0.4	20.8	49.5	29.3	-	1.0	22.6	47.1	29.2	-
O ₂ , 700°C	-	37.7	43.4	18.9	-	-	23.8	45.8	30.4	-
H ₂ S, 700°C	-	1.4*	45.7*	52.8*	29.5	0.8*	2.3*	60.0*	36.9*	28.9
H ₂ O, 900°C	2.5	54.9	28.1	14.5	-	3.0	66.9	19.2	10.9	-
O ₂ , 900°C	2.0	62.8	26.5	8.8	-	3.2	69.9	16.8	10.0	-

*Sulfur-free basis

TABLE II: Compositions (wt.%) of Polished and Unpolished Aluminized Incoloy 800 Samples after 4-Hour Exposures

Treatment	Aluminized Incoloy 800					Polished Aluminized Incoloy 800						
	%Al	%Ti	%Cr	%Fe	%Ni	%S	%Al	%Ti	%Cr	%Fe	%Ni	%S
None	45.1	-	9.2	27.5	18.1	-	39.6	-	9.3	29.1	22.0	-
He, 700°C	45.3	0.3	6.6	29.1	18.7	-	35.3	0.4	10.0	32.2	22.0	-
H ₂ O, 700°C	42.3	0.2	8.7	29.7	19.2	-	34.6	0.3	8.9	34.1	22.0	-
O ₂ , 700°C	45.7	0.2	8.0	28.0	18.1	-	35.6	0.4	9.7	33.5	20.8	-
H ₂ S, 700°C	45.5*	-	9.2*	27.5*	17.7*	22.7	41.8*	-	9.6*	29.1*	19.5*	19.7
H ₂ O, 900°C	52.4	0.4	7.3	24.3	15.6	-	52.5	0.6	7.0	23.8	16.2	-
O ₂ , 900°C	56.8	0.2	7.2	22.0	13.9	-	54.1	0.3	7.7	22.8	15.2	-

*Sulfur-free basis

samples to steam or oxygen at 900°C, e.g. the chromium and titanium content increased from about 18-20 and 0 wt.% to 55-70 and 2.5-3.0 wt.%, respectively. Exposure of aluminized samples to oxygen or steam at 900°C resulted in a detectable increase in the aluminum content with a final value of about 52-57 wt.% for both unpolished and polished coupons. This increase in the aluminum content was primarily at the expense of iron and nickel.

An appreciable amount of sulfur (probably as metal sulfides) was incorporated in the surface of all coupons exposed to hydrogen sulfide at 700°C, as shown in Tables I and II. For Incoloy 800 coupons, there was a very large decrease in the chromium content at the surface. On a sulfur-free basis, the iron content increased greatly for polished Incoloy 800 but the nickel content increased for the regular Incoloy 800 coupon. For aluminized Incoloy 800 coupons, there was little change in the metal content on a sulfur-free basis as a result of hydrogen sulfide treatments, as shown in Table II.

The metal coupons increased in weight as a result of the treatments with inorganic gases. With oxygen and steam, metal oxides were formed on the surfaces. The rate of weight increase with oxygen was in the range of $0.3-0.6 \times 10^{-4}$ g/cm²/hr and with steam was perhaps slightly less; the precision of the data are not sufficient, however, to differentiate between the weight increases at 700 or 900°C, for Incoloy 800 or aluminized Incoloy 800, or for unpolished or polished surfaces. Weight gains of aluminized and polished aluminized Incoloy 800 coupons because of treatment with hydrogen sulfide were similar to those with oxygen. The rate of weight increase with hydrogen sulfide was much greater (approximately 31×10^{-4} g/cm²/hr) in the case of Incoloy 800 and polished Incoloy 800 coupons. The metal sulfides spalled off the polished Incoloy 800 coupon quite readily; part of the sulfides and metal surface were lost when the coupon was removed from the balance after weighing.

Coke Deposits on Coupons: The amount and characteristics of the coke formed on coupons contacted with a mixture of 5% acetylene and 95% helium at 900°C varied significantly depending on the pretreatment of the coupons, as indicated by Table III and Figures 7 through 10. Although the coke deposits were generally rather rough and over relatively short distances were quite heterogeneous in appearance, panoramic views at magnifications of about 1000 often indicated similar

TABLE III: Rates of Coking for Pretreated Surfaces Exposed to 5% Acetylene at 900°C for 1 hour

Pretreatment for 4 hours	Coking Rate $\times 10^4$, grams/cm ² /hr			
	Incoloy 800 Regular	Incoloy 800 Polished	Alonized Incoloy 800 Regular	Alonized Incoloy 800 Polished
None	6.4	2.7	3.1	2.2
H ₂ O, 700°C	7.0	3.9	2.7	2.3
H ₂ O, 900°C	11.8	1.6*	2.9	2.5
O ₂ , 700°C	19.1	12.6	-	-
O ₂ , 900°C	9.8	19.7	2.4	2.4
H ₂ S, 700°C	-	(Sulfided surface) flaked	14.8	7.5
Coked, 900°C; Decoked, 700°C with O ₂ -H ₂ O-He	15.4	19.0	(NO evidence of sulfide flaking)	-
Coked, 900°C; Decoked, 700°C with O ₂ -H ₂ O-He; H ₂ S, 700°C, 2 hrs.	45.1	95.0	-	-

*Based on SEM observations this surface was more uniformly covered than either the regular or polished alonized Incoloy 800 surfaces. There were apparently uncovered areas on the latter two surfaces.

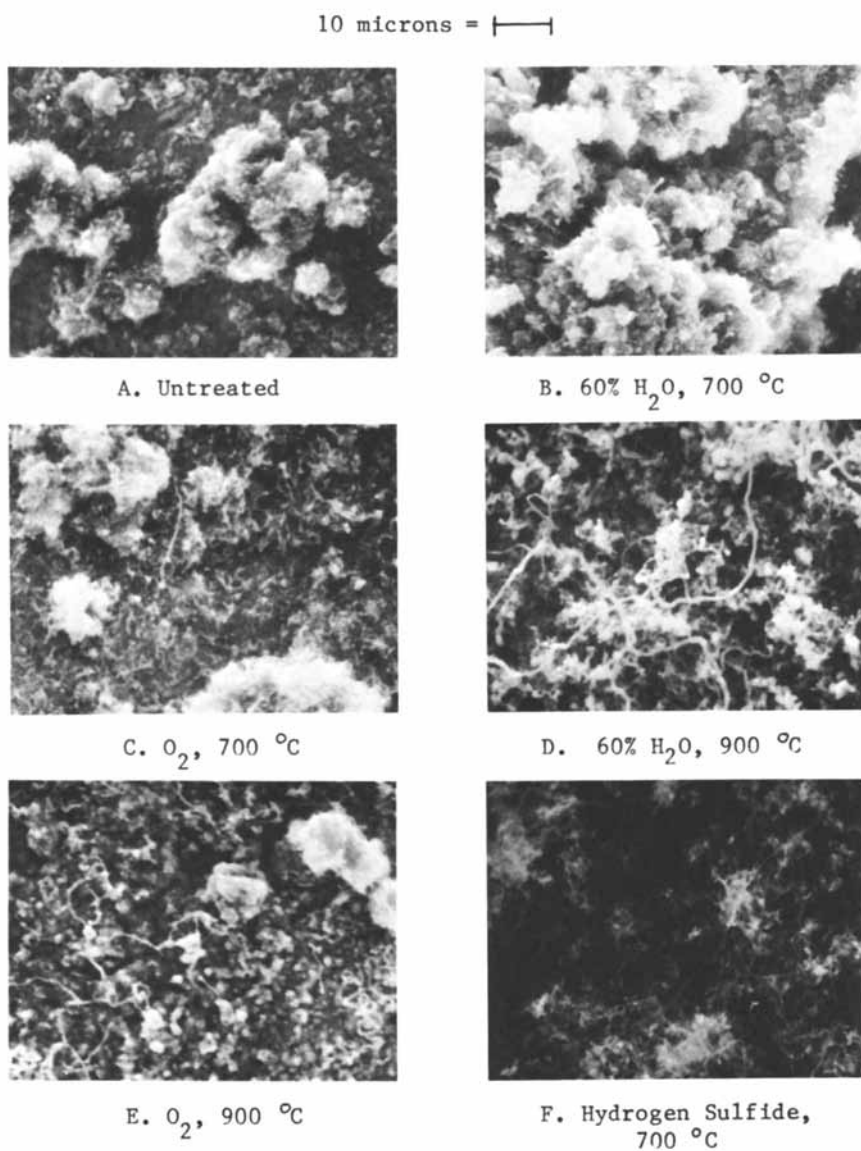


Figure 7. Coke deposited on various Incoloy 800 surfaces. Conditions: 5% C₂H₂; 900°C for 1 h.

characteristics and what appeared to be rather uniform coke thickness. The polished Incoloy 800 coupon pretreated with oxygen at 900°C was a definite exception however; on this coupon, coke deposits appeared especially thick near the edges of coupon, but less coke seemed to be present in the central regions of both the top and bottom flat surfaces. The reasons for such variations in coke thickness are not known.

The rates of coke formation on the different coupons, as reported in Table III, were calculated using the weight increase of the coupon while it was contacted with the acetylene-helium mixture. The basic assumption made was that the weight of coke deposited on each coupon was equal to the weight increase. The coupons had to be handled carefully so that no coke or metal oxides flaked off during handling. The small weight increase of the coupon caused by the formation of metal oxides or metal sulfides on the surface because of the pretreatments was ignored; it was assumed that the oxides and sulfides were reduced back to metals while the coke formed. The rates of coking, as listed in Table III, are obviously average rates --- averages for the one hour runs and averages relative to the entire surface of the coupon.

Figure 7 shows the coke formed on the various unpolished Incoloy 800 coupons. In all cases mixtures of filament and globular coke resulted on the Incoloy 800 surfaces; certain areas exhibited relatively large clusters of globular coke from which filament coke protruded.

For polished Incoloy 800 coupons (see Figure 8), a mixture of filament and globular coke formed on the oxygen-treated surfaces. Filament coke was, however, not detected on either untreated or steam treated coupons. The coupon treated with steam at 700°C was covered rather uniformly with globular coke. The coupon treated with steam at 900°C exhibited a rippled layer of coalesced globular coke.

Four of the five comparisons made with Incoloy 800 coupons that were either untreated, steam treated, or oxygen treated indicated that more coke formed on unpolished coupons as compared to polished coupons (see Table III). The single exception was the coupon on which most of the coke formed on the edges whereas the flat and polished surfaces were relatively free of coke. It seems safe to conclude therefore that less coke formed in all cases on the polished flat surfaces as compared to the unpolished surfaces.

In an effort to minimize the problem of spalling of metal sulfides from Incoloy 800 surfaces contacted

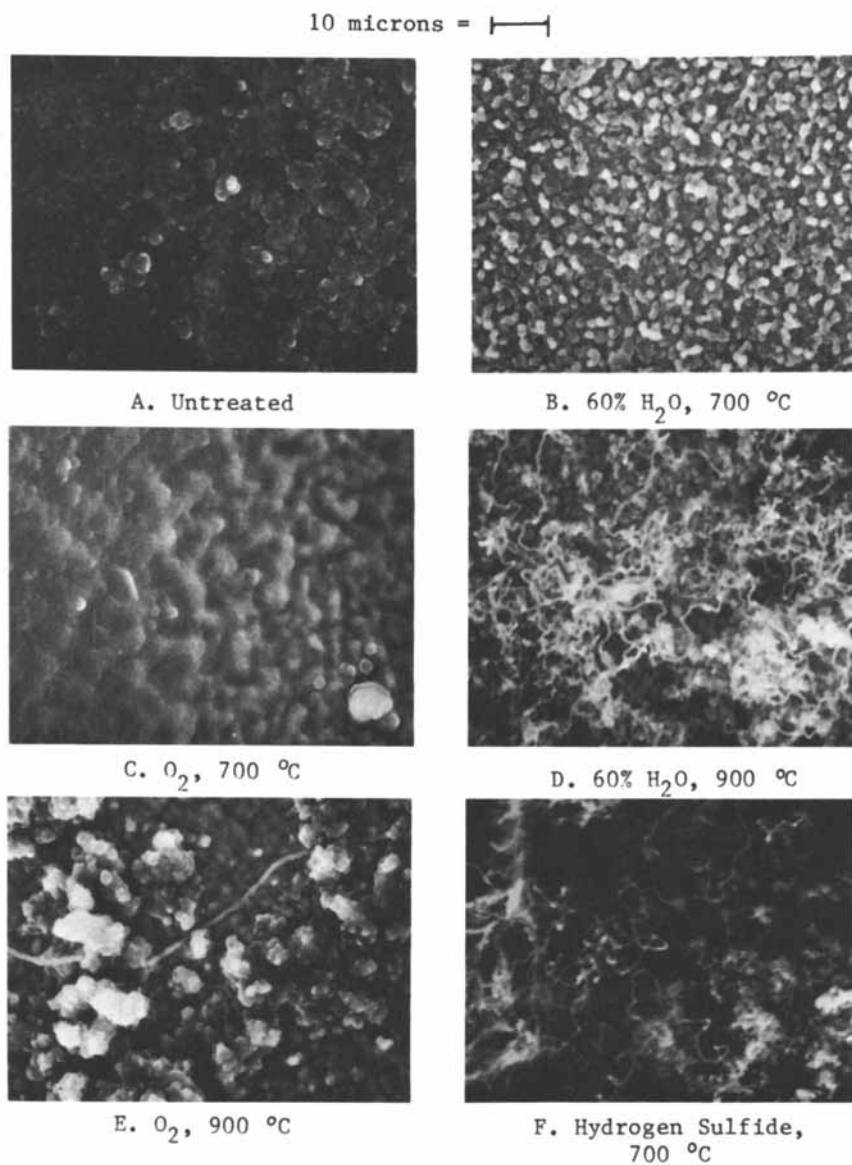


Figure 8. Coke deposited on various polished Incoloy 800 surfaces. Conditions: 5% C₂H₂; 900°C for 1 h.

with hydrogen sulfide, the following procedure was employed to compare polished and unpolished Incoloy 800 coupons. Two polished and two unpolished Incoloy 800 coupons were first contacted with 5% acetylene for one hour at 900°C; each coupon was then decoked with a mixture of 10% oxygen, 50% steam, and the remainder helium. Next, one polished and one unpolished coupon were contacted with hydrogen sulfide for two hours at 700°C; finally, all four coupons were then contacted with a 5% acetylene stream at 900°C for one hour. Sulfiding of the coupons resulted in a major increase (by a factor of 3 to 5) in the rate of coking. On the polished and unpolished coupons that had been sulfided, the filament coke formed was of relatively large diameter and contained iron and nickel.

In what is considered a key finding of this investigation, significant filamentous coke also formed on the surface of the Vycor tubes holding the sulfided coupons. This coke was found to contain both iron and nickel which had obviously been transferred from the Incoloy 800 coupons. Possibly the iron and nickel sulfides originally present on the coupons were liquefied or even volatilized and then transported to the Vycor surfaces where they catalyzed the growth of coke filaments.

For aluminized Incoloy 800 coupons that had been untreated, steam treated, or oxygen treated, the amount, metal content, and general appearance of the coke deposited on each coupon were similar, as indicated by SEM pictures in Figures 9 and 10, by EDAX analyses, and by the rates of coking. Coking rates listed in Table III indicated that polishing the aluminized coupons perhaps slightly decreased the amount of coke. In all cases, globular coke was present on a layer of amorphous coke. As shown in Figures 9 and 10, a few coke filaments were scattered on some of the surfaces. In the case of the untreated aluminized Incoloy 800 coupon, the filaments were clustered at or near pitted areas on the surface; less aluminum was detected by EDAX in these pitted areas. For steam-treated and oxygen-treated coupons which had not been polished, globular coke was collected to some extent in the pitted areas. Polishing the coupons usually tended to remove sufficient surface so that the pitted areas were no longer detectable, as shown in Figure 10.

Much more coke formed on aluminized surfaces that had been sulfided than on any other aluminized surface (see Table III). An appreciable number of coke filaments formed on both the polished and unpolished

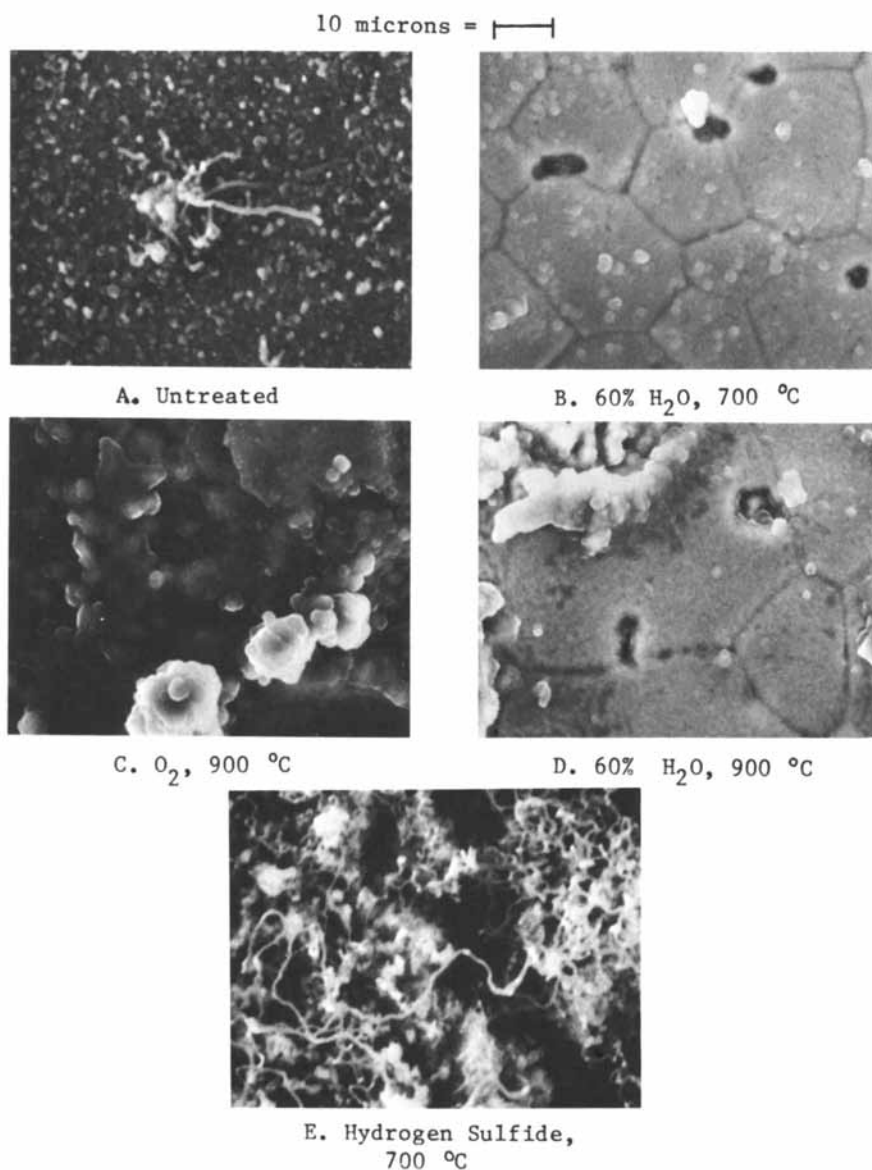


Figure 9. Coke deposited on various alonized Incoloy 800 surfaces. Conditions: 5% C₂H₂; 900°C for 1 h.

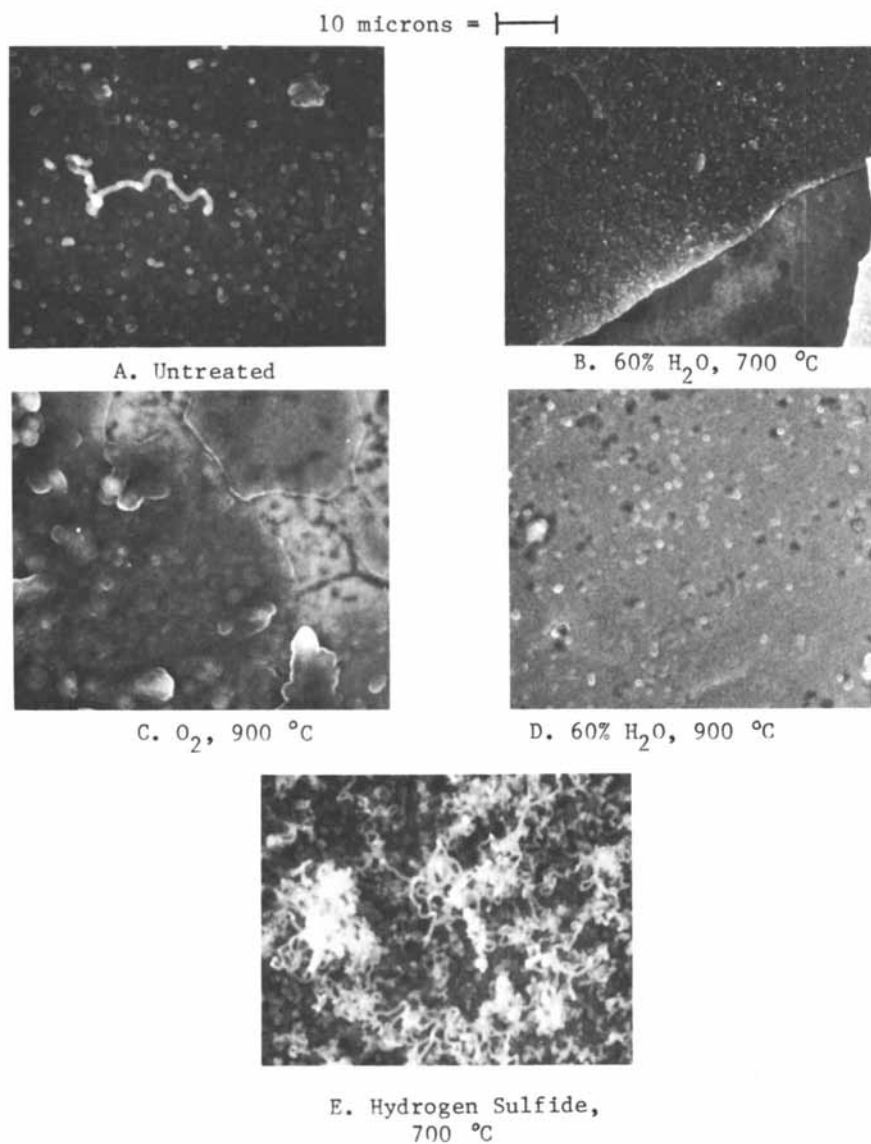


Figure 10. Coke deposited on various polished alonized Incoloy 800 surfaces. Conditions: 5% C₂H₂, 900°C for 1 h.

coupons, as shown in Figures 9E and 10E. These filaments probably contain iron and nickel; EDAX analyses were inconclusive because dense growths of filaments were not detected. The polished aluminized coupon had a significantly lower rate of coking than the unpolished coupon.

For unpolished coupons, all comparisons shown in Table III indicate that less coke formed on aluminized Incoloy 800 coupons as compared to Incoloy 800 coupons. Some caution must be exercised in interpreting the results since the Incoloy 800 coupons were positioned about 2.5 cm. upstream of the aluminized coupons in the flow path of the gases. Small differences in coking rates have been shown to result when coupons of the same alloy composition are positioned about 4 cm. apart in the furnace (2). However, the comparisons between Incoloy 800 and aluminized Incoloy 800 coupons found here are similar to those reported earlier (1,8). For polished coupons, three of the four comparisons indicate that less coke formed on the aluminized coupons as compared to the Incoloy 800 coupons. The lowest rate of coking apparently occurred, however, on the polished Incoloy 800 coupon that had been steam treated at 900°C. The coke on this coupon appeared to rather uniformly cover the surface, although the thickness of the coke layer was not determined. The comparably treated aluminized coupon appeared under the SEM to have areas that were coke free. No explanation can currently be given for these perhaps significant findings.

Discussion of Results

The results of this investigation greatly clarify several factors that affect coking in pyrolysis coils and transfer line exchangers. In particular, the role of the surface is better defined since significant differences in results were obtained when directly comparing Incoloy 800 versus aluminized Incoloy 800 and polished versus unpolished surfaces.

Increased roughness and major changes in surface roughness have been known for a considerable time to occur as a pyrolysis coil is used. The present results clearly indicate that significant changes occur within just four hours because of surface reactions with steam, oxygen, or especially hydrogen sulfide in the 700 to 900°C range. Even heating for four hours at 900°C caused major changes in the surface morphology of Incoloy 800. Although not specifically investigated, repeated oxidation-reduction sequences

such as occur during pyrolysis would severely roughen the surfaces. Such sequences occur as steam or oxygen (during burnoffs) oxidize the surfaces or as hydrocarbons react with the metal oxides to form carbon oxides, steam, and reduced metals (4). In units in which sulfur-containing gases are in the feedstream, sulfiding-desulfiding sequences also occur resulting in severe roughening of the metal surfaces. As indicated here, major differences occur in the ability of the surfaces to resist this roughening depending on their surface composition and roughness.

The present results also clarify some of the methods by which chromium, nickel, and iron are lost from the surface. For chromium, diffusion to the surface was clearly shown to be rapid at temperatures of 900°C or higher (as is prevalent in commercial units), and the chromium at the surface would then be oxidized with either steam or oxygen. A variety of surface reactions such as reduction, sulfiding, or coking would act to eventually spall off the chromia or other chromium compounds. In commercial units, the rapidly flowing gases would fluidize and move many of these compounds along the coil length.

Nickel and iron are certainly removed from the surface by at least three mechanisms. First, both elements are incorporated in certain cokes by catalytic reactions (10); filamentous coke is one such coke. The filaments are probably broken to some extent by the high velocity gases in commercial pyrolysis coils. Furthermore, oxidation reactions with steam (during pyrolysis runs or during burnouts) or with oxygen (during burnouts) act to free particles of finely divided iron and nickel oxides or other compounds. Second, spalling of the iron and nickel oxides or sulfides from the roughened surface certainly accounts for some losses. Third, some nickel and iron compounds (probably sulfides) are entrained in the gas stream or vaporized at temperatures of 900°C or higher. This latter means of transfer may be of considerable importance for transport of both nickel and iron to the transfer line exchanger where they are imbedded in the coke that collects there.

The results of this investigation help clarify why machining is beneficial relative to coke formation; rough areas on the surface act as excellent collection sites for coke or tar droplets formed in the gas phase. Such tar droplets eventually become globular coke. Smoother surfaces hence minimize such collection or surface deposits. In addition, smoothing or polishing of both Incoloy 800 and aluminized

Incoloy 800 surfaces acts to produce surfaces with more desirable compositions; these new surfaces are more resistant to oxidizing, sulfiding, or surface coking reactions. Of interest, Gregg and Leach (11) had found that less coke was formed on electropolished nickel surfaces as compared to unpolished nickel surfaces. In the case of the aluminized Incoloy 800, care must be taken not to remove too much of the surface since the aluminum has penetrated only short distances into the surface. The results of the present investigation imply that the method or degree of polishing is important. It is not clear why polished coupons in some cases collected considerable coke near the corners of the coupons.

Another advantage of aluminized Incoloy 800 surfaces is that diffusion of chromium and titanium to the surface is drastically decreased if not basically stopped. It seems clear that diffusion of aluminum in such alloys is however fairly rapid; as indicated by the present results. One would expect in commercial units however that all aluminum reaching the surface would quickly react with steam or oxygen to produce alumina.

The results of the present investigation strongly suggest that certain oxidized surfaces are highly beneficial on especially polished Incoloy 800 surfaces. For example, oxidation of the polished Incoloy 800 coupons with steam at 900°C resulted in a coupon that collected only a small amount of coke. Earlier Brown and Albright (12) also found that some highly oxidized surfaces were catalytically inert. It is thought that these desirable surfaces are rich in chromia and are probably quite impervious to diffusion of oxygen, steam, or hydrocarbons. There is clearly a need to obtain additional information clarifying the characteristics of this desired layer of surface oxides.

Further investigations now in progress will clarify further the key factors that affect the formation of catalytically-formed coke and the collection or deposition of gas-phase coke or tar droplets on solid surfaces.

Acknowledgment

Alon Processing, Inc. provided financial support to the present investigation.

Literature Cited

1. Graff, M. J.; Albright, L. F., Carbon (1982), in press.
2. Marek, J. C.; Albright, L. F., 182nd American Chemical Society National Meeting, New York, August, 1981; (Chapter 7, this book).
3. Baker, R. T. K.; Chludzinski, J. J., J. Catalysis (1980), 64, 464-478.
4. Tsai, C. H.; Albright, L. F., "Industrial and Laboratory Pyrolyses"; ACS Symposium Series No. 32, Chapter 16, L. F. Albright and B. L. Crynes, Ed., American Chemical Society: Washington, D. C., 1976.
5. Castle, J. E.; Durbin, M. J., Carbon (1975), 13, 23-31.
6. Bittner, H. F.; Bell, J. T.; Land, J. F., J. Electrochem. Soc. (1980), 127, 902-906.
7. Durbin, M. J.; Castle, J. E., Carbon (1976), 14, 27-33.
8. Albright, L. F.; McConnell, C. F.; Wether, K., "Thermal Hydrocarbon Chemistry"; Advances in Chemistry Series No. 183, Chapter 10, A. G. Oblad, H. G. Davis, and T. E. Eddinger, Ed., American Chemical Society: Washington, D. C., 1979.
9. Perry, R. H.; Chilton, C. H., Ed.; Chemical Engineers' Handbook", McGraw-Hill, Inc.: New York, 1973.
10. Baker, R. T. K.; Harris, P. S.; Thomas, R. B.; Waite, R. J., J. Catalysis (1973), 30, 86-95.
11. Gregg, S. J.; Leach, H. F., J. Catalysis (1966), 6, 308-313.
12. Brown, S. M.; Albright, L. F., "Industrial and Laboratory Pyrolyses"; ACS Symposium Series No. 32, Chapter 17, L. F. Albright and B. L. Crynes, Ed., American Chemical Society: Washington, D. C., 1976.

RECEIVED July 7, 1982.

Growth and Initiation Mechanism of Filamentous Coke

ALBERT SACCO, JR., and JOHN C. CAULMARE¹

Worcester Polytechnic Institute, Department of Chemical Engineering,
Worcester, MA 01609

Decomposition of carbon bearing gases over transition metals often results in the formation of filamentous materials ("carbon fibers"). These carbon fibers are uniform in width, usually between 500-1000 Å, come in the shape of flat ribbons, solid or hollow tubes, and some are even twisted. The formation of these filaments results in corrosion of the metallic phase.

An investigation was performed to try to ascertain the initiation and growth mechanism for fiber formation in a five component gas mixture (CO, CO₂, CH₄, H₂, H₂O) over iron. Phase diagrams were used to try to control the solid phase composition during reaction. An electrobalance was used to continuously monitor weight gain, and electron optics were used to examine the bulk metal and fiber structure(s). Preliminary results indicate that fiber formation only occurs when a carbide is thermodynamically favored. Also, the rate plotted as change in fractional weight gain per unit time goes through a maximum and then levels out at a constant rate. Possible reasons for this will be proposed and a mechanism hypothesized.

Transition metals exposed to carbon bearing gases at elevated temperatures often catalyze the formation of carbonaceous deposits. One of the more interesting carbon morphologies observed is frequently called "filamentous" carbon. This form of carbon consists of filaments or fibers. These filaments are generally cylindrical in shape and less than 1000 Å in diameter. Both solid (Hofer et al., (1)) and hollow (Oberlin et al., (2)) fibers have been observed as well as twisted or braided filaments (Boehm (3)). Most filaments have a small piece of metal, usually about the same diameter as the filament, embedded at some point along its length.

¹ Current address: EXXON Research and Engineering Company, Florhan Park, NJ 07932.

This metal crystal is believed to be the growth center (Baker et al., (4)). The recent results of Baker and Chludzinski (5) further support this contention. The penchant of this form of carbon for removing metal from the surface of a large piece of metal, or from a support material is the most interesting as well as damaging aspect of this type of deposit. Eventually, its formation results in the destruction of the parent metal matrix, or the removal of catalytic material from its support.

Many investigations have been performed to try to ascertain the growth mechanism of this form of carbon. An excellent review on work in this area is presented by Baker and Harris (6). However, none has resulted in a completely consistent mechanism that can explain the varied reported results. Surprisingly few investigations have attempted to study the initiation step, the way the growth crystal is extracted (extruded?) from the metal matrix or support initially. Also to the best of the authors' knowledge, no attempt has been made to control the surface phase(s) during reaction. This is of importance since phase(s) (e.g., carbides) can form during heating and cooling sequences. The objective of the present investigation is to try to understand the initiation step in fiber growth, and also to establish what iron metal phases catalyze filament growth.

Experimental

All experiments were performed on high purity (>99.99%) polycrystalline iron foils. Carbon was deposited from multicomponent mixtures of H_2 , H_2O , CH_4 , CO , and CO_2 at 900 K and 1 bar pressure. These reactant gases were delivered to the reactor at 20 cc/s (STP). The weight changes observed were attributed to carbon deposition or oxidation and monitored throughout the course of an experiment using an electrobalance-recorder unit. Figure 1 is a schematic of the experimental apparatus. Reactant gases were individually metered through Brook mass flow regulators. Their precise flow-rates were determined by measurement of their pressure drops through precision bore capillary tubes. They were then mixed by passage through a drying tube and fed dry or saturated with water to a fused quartz preheater-reactor. Saturation of the feed gas was accomplished by flow through a series of bubblers submerged in a thermostatically controlled water bath. Partial pressures of water from 0 to 0.34 bar were easily obtained. All feed and exit lines were wrapped with heating tapes and maintained at temperatures in excess of 363 K.

The reactor assembly consisted to two 38 mm diameter tubular sections: the reactor-preheater tube and the reactor-electrobalance interface section. The reactor-preheater tube is 0.66 m in length and is constructed of fused quartz. The lower portion of this tube is packed with fused quartz rings and is used as a feed gas preheater. A thermocouple is located in the reactor directly below the metal foil and a gas sampling port is positioned immediately

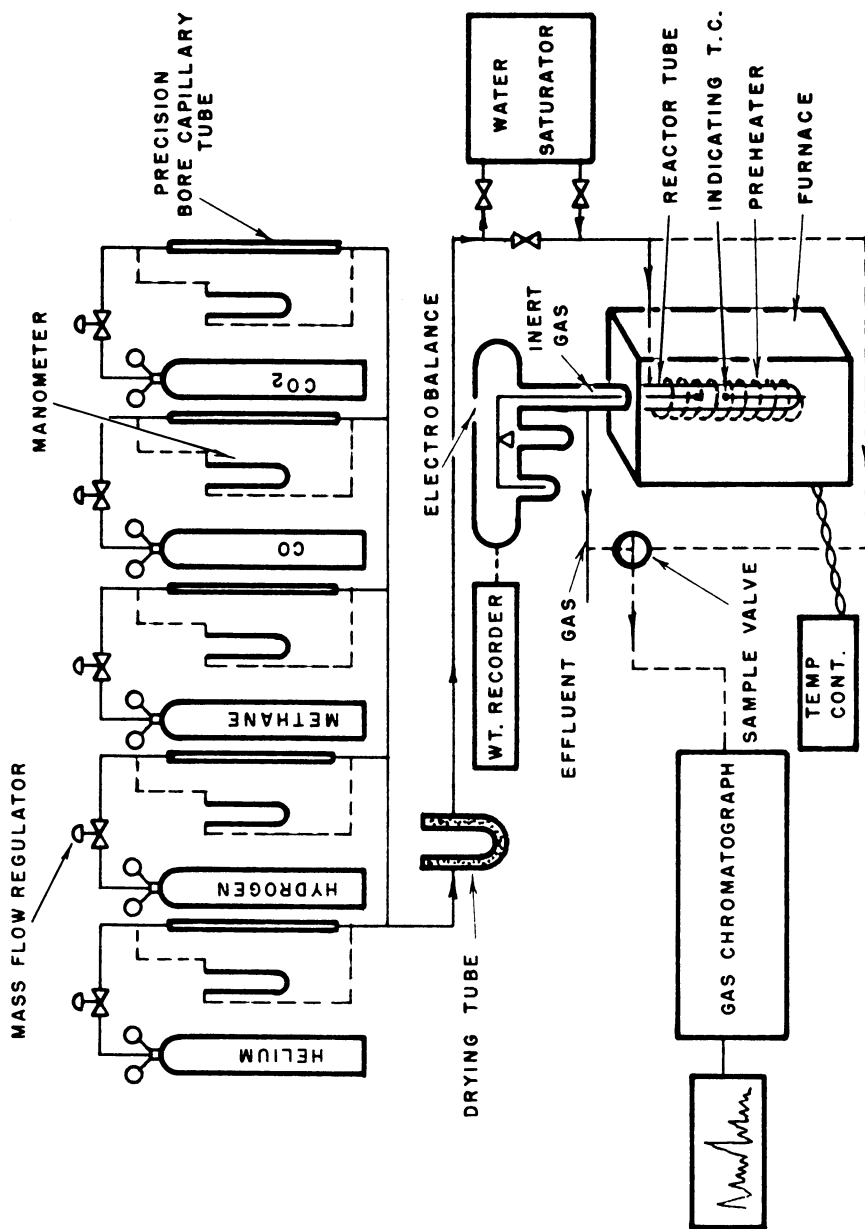


Figure 1. Experimental apparatus.

above the sample. The reactor effluent and the inert gas (helium), which is fed through the electrobalance to protect its mechanism, exit through lines located in the interface section. The reactor-preheater tube is housed within a tube furnace powered and controlled by a West SCR stepless proportional temperature controller. This system was capable of maintaining a 1 cm isothermal zone up to 1200 K. The entire reactor assembly and electrobalance were fixed on a specially designed frame (Figure 2). The frame allowed the electrobalance to perform at nearly maximum sensitivity.

Weight changes were monitored continuously using a Cahn 2000 electrobalance. A sensitivity of 10^{-6} grams was typical for the flow-reactor electrobalance system used in this investigation. Inlet and effluent gas streams were analyzed periodically using an on-line Sigma I (Perkin Elmer) gas chromatograph.

Method of Analysis

To determine which solid phases catalyze the formation of carbon filaments, phase diagrams were used. The usefulness of phase diagrams for this system has been demonstrated in the work of Sacco and Reid (7); and thus, only a brief description of their use will be given here. A phase diagram for the gas components of interest and the solid phases of interest is generated using available Gibbs-free energy data. Figure 3 represents the $\text{Fe}_3\text{C}-\text{Fe}_x\text{O}-\text{C}_{\text{gas}}$ (H_2 , H_2O , CH_4 , CO , CO_2) phase diagram at 900 K and 1 bar pressure. The apexes of the equilateral triangle represent atomic carbon, hydrogen and oxygen. Thus, any gas mixture composed of these elements can be plotted on this triangular surface. As examples, the locations of pure CO , CO_2 , H_2O , and CH_4 are shown in Figure 3. The curve which is concave downward represents the equilibria between alpha iron-wustite (Fe_xO) and gas. Any point located on this curve represents a gas mixture in equilibrium with alpha iron and wustite. As plotted if one is below this curve, such as in the region indicated by point X, iron oxide is the stable iron phase. That is, in this phase field the chemical potential driving force is such that reduced iron can not form. If one is above this curve, the iron-iron oxide-gas equilibria predicts reduced iron. However, when the alpha iron-cementite (Fe_3C)-gas equilibria is imposed on this system (dotted line) it is seen that any reduced iron formed will react with the gas phase to produce carbide (Fe_3C) in this region. Finally, the graphite-gas equilibria is superimposed on this diagram (solid line concave upwards). This curve represents the loci of possible gas mixtures in equilibrium with solid graphite at 900 K and under 1 bar pressure. If a gas mixture lies above this curve, then the chemical potential driving force is such that solid carbon should form. A gas mixture below this boundary will result in a driving force that favors solid carbon oxidation. This assumes that the solid surface present during reaction is a catalyst for carbon deposition or oxidation. For example, if we carefully carbide the surface

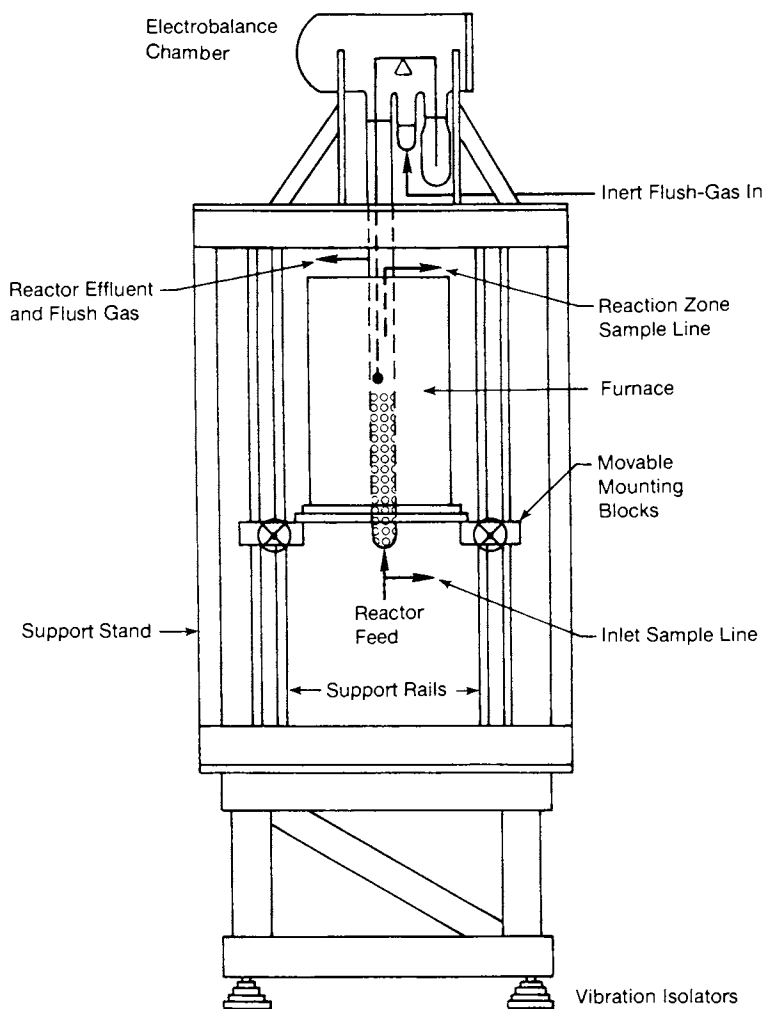


Figure 2. Reactor support assembly.

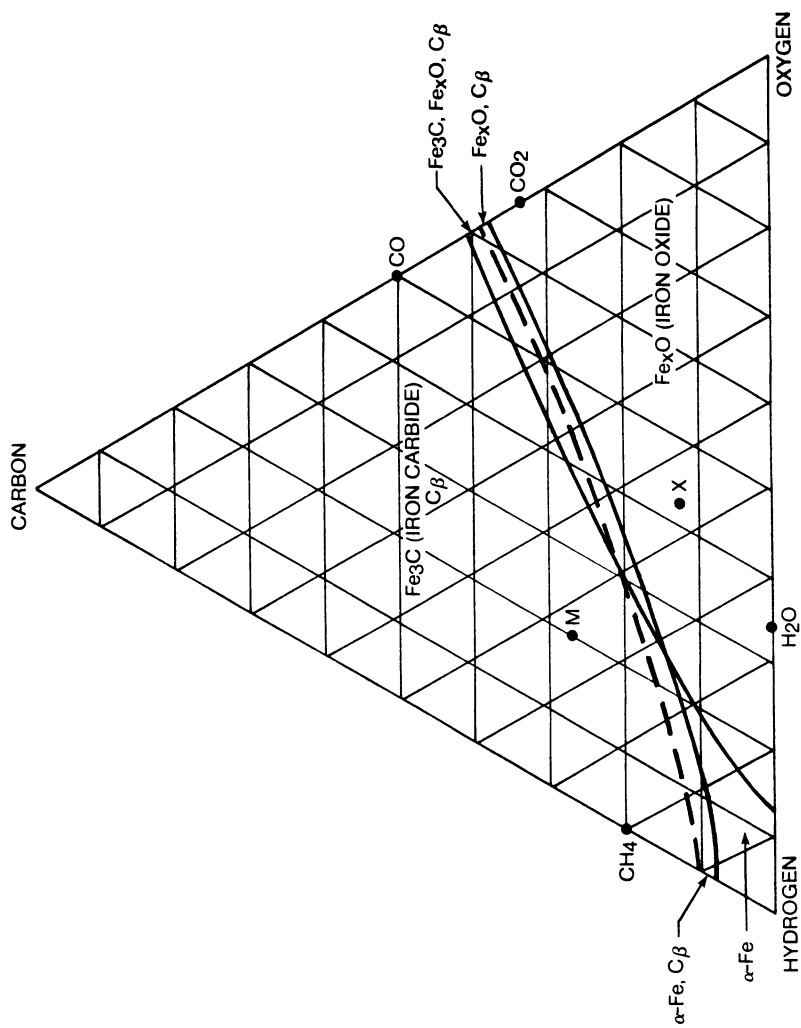


Figure 3. Iron-iron oxide-iron carbide-gas equilibria. Conditions: temperature, 900 K; and pressure, 1 Bar.

and then feed a gas mixture represented by point M carbon should form if cementite (Fe_3C) is a catalyst for carbon deposition. If Fe_3C is not a catalyst for carbon deposition, then there will not be a noticeable weight gain. In this manner one can control the surface phase and determine if it catalyzes fiber growth.

Procedures

In this work, a differential reactor was used to insure that the gas composition remains essentially unchanged and thus operation during an experiment remained in the phase field of interest. A computer program was used to calculate the gas phase compositions to be used for an experiment. Typically, a preweighted polycrystalline foil was placed in the reactor, heated in hydrogen to the desired reaction temperature, and the reactant gas mixture passed continuously over it. Inlet and exhaust gas samples were taken and analyzed every twenty minutes to insure that the gas composition remained constant. The mass of the foil was recorded throughout the run from start-up through the cooling sequence.

At the conclusion of an experiment, the reaction gases were vented and the reactor was allowed to cool down to room temperature within a flowing stream of helium. The time of cooling was not critical since experiments were only made at temperatures below the Eutectoid temperature (996 K), samples were held at reaction temperature for times in excess of 25 minutes, and cooling was slow (3-4 hrs). The Eutectoid temperature is the temperature at which a single solid phase begins to decompose into two other phases on cooling. The samples were removed from the reactor assembly and stored in a helium atmosphere to prevent oxidation. The samples were then examined using both an optical and scanning electron microscope.

Results and Discussion

Initially, a series of experiments were performed with a gas phase composition that maintained the solid surface in the reduced condition, while also maintaining a chemical potential driving force for carbon deposition. These experiments are identified by the open triangles on the C/H = 0.13 line in Figure 4. In Figure 4 an open triangle means that during the course of the experiment neither weight loss nor weight gain was detected. In these initial experiments, no weight change was detected up to as long as 140 minutes. After a sufficiently long period of neither weight gain or loss, usually between 30-60 minutes, the reactant gases were bypassed around the saturator.

This resulted in a dry gas stream at the same flow rate entering the reactor. In all cases a weight gain was observed immediately. These data are shown as the two darkened triangles

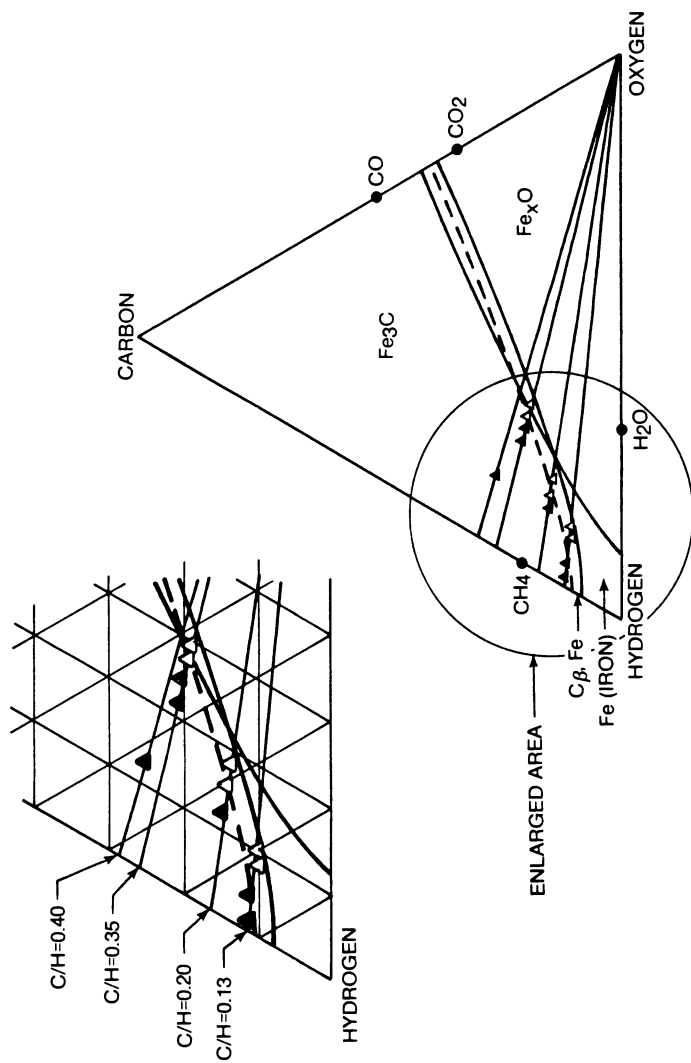


Figure 4. Evidence that cementite catalyzes carbon formation. Conditions the same as in Figure 3.
 Key: ▲, weight gain; and △, no weight gain or loss.

on the C/H line of 0.13. These dry gaseous mixtures are in the region where an iron carbide (Fe_3C) will form and suggests that carbon deposition may only occur when a carbide is present. To try to further substantiate this hypothesis, as well as to determine if water has an influence on the observed behavior, a series of experiments were performed at a C/H ratio of 0.40 in the carbide region. As indicated in Figure 4, weight gain was observed. The gas phase composition for these initial runs are presented in Table I. Also included in Figure 4 are data taken by Sacco and Reid (7) over a steel wool catalyst. Although more heavily alloyed (<99% iron) and porous in nature, the behaviour is the same; that is, carbon deposition only occurs in the region where a carbide (Fe_3C) is favored.

Using a JSM-U3 scanning electron microscope, the foils on which a weight gain was measured were examined. The surface was found to be covered with bundles of filamentous carbon. The fibers were cylindrical in shape and approximately $0.5 \mu\text{m}$ in diameter. All these fibers appeared to have a metallic crystal at their tip. However, the resolution was not fine enough to determine if the filaments were hollow or not. The foils were then polished and etched with 2-3% nital solution (nital is an etch consisting of nitric acid in methanol). The structure was pearlitic in nature, showing large carbide formations along grain boundaries.

The fact that the formation of cementite is apparently necessary before carbon will deposit (i.e., filaments will grow) is in agreement with the work of Tsao (8). Tsao ran pure carbon monoxide over reduced iron disks at 903 K. He then used Mossbauer spectroscopy to generate that data presented in Figure 5. As illustrated, iron carbide forms rapidly while free carbon appears to form only after sufficient quantities of carbide are present. These data, in agreement with the results illustrated in Figure 4, suggest that cementite (Fe_3C), not α -iron, is the catalyst for carbon deposition and therefore fiber growth.

Figure 6 is a plot of a fractional weight gain versus time for five different experiments run in the carbide region. As expected, the fractional weight gain increases at a given time as the CO concentration increases. Also, there appears to be an induction period followed by a period of constant weight gain. The slope of these curves were taken and plotted versus time in Figure 7. As indicated by the data in Figure 7, the rate of fractional weight gain appears to increase rapidly reaching a maximum then decreases slightly to a steady state value. This type of behavior was found for all experiments run in the carbide region.

It is tempting to suggest a kinetic mechanism for carbon deposition due to the apparent CO dependency; however, it must be remembered that the surface area is changing continuously in all these experiments. This is best illustrated in Figure 8. Under identical conditions for three separate experiments, the fractional weight gain as a function of time is shown to deviate from

Table I. Composition of All Preliminary Experiments

<u>Run No.</u>	<u>Mole Percent</u>						
	<u>H₂</u>	<u>CO</u>	<u>CH₄</u>	<u>CO₂</u>	<u>H₂O</u>	<u>C/H</u>	<u>O/H</u>
1	62.1	7.8	16.3	2.6	11.2	0.13	0.11
2	61.3	7.6	16.4	2.3	12.4	0.12	0.12
3	63.8	8.0	17.6	3.4	7.2	0.14	0.10
4	62.7	6.8	20.9	0.9	8.7	0.13	0.08
5	69.6	8.9	19.0	2.5	0.0	0.14	0.07
6	69.9	8.9	19.1	2.1	0.0	0.14	0.06
7	68.2	7.4	22.9	1.5	0.0	0.14	0.05
8	62.2	1.0	34.7	0.1	2.0	0.13	0.01
9	19.9	37.6	39.7	1.7	1.1	0.39	0.21
10	19.9	37.6	40.0	1.8	0.7	0.40	0.21
11	19.6	37.6	40.0	1.9	0.9	0.40	0.21
*12	65.0	2.7	30.2	0.2	1.9	0.13	0.02
*13	66.2	2.8	30.8	0.2	0.0	0.13	0.01

* Composition set using flow system not confirmed by gas chromatograph

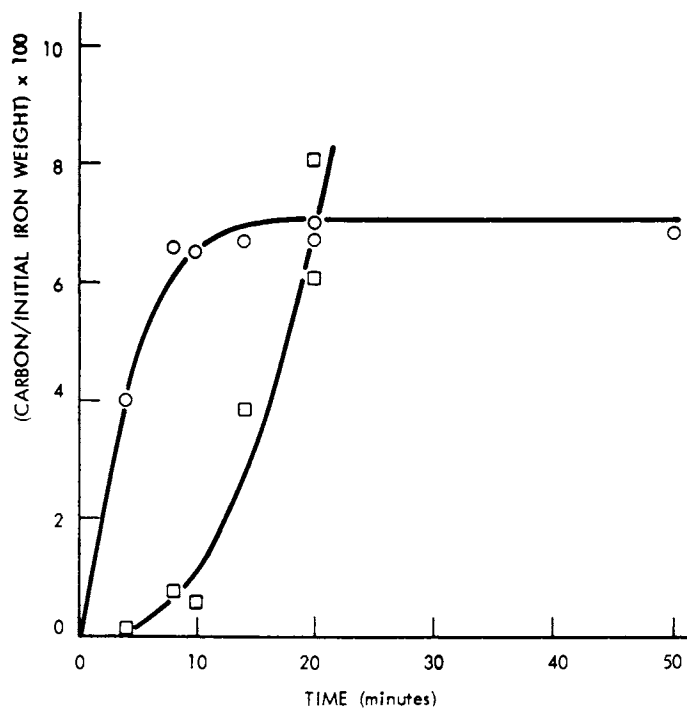


Figure 5. Carbon analysis of the disks reacted at 903 K ($G = 0.3$ L (STP)/min). Key: \circ , iron carbide; and \square , free carbon. (Reproduced, with permission, from Ref. 8).

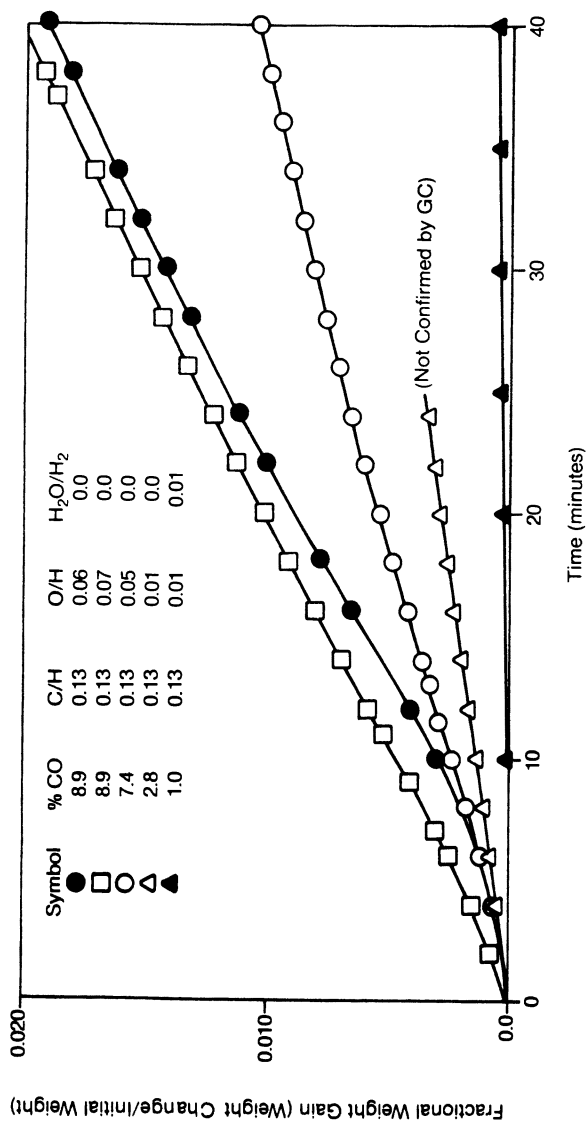


Figure 6. Fractional weight gain vs. time. Conditions: temperature, 900 K; and pressure, 1 Bar.

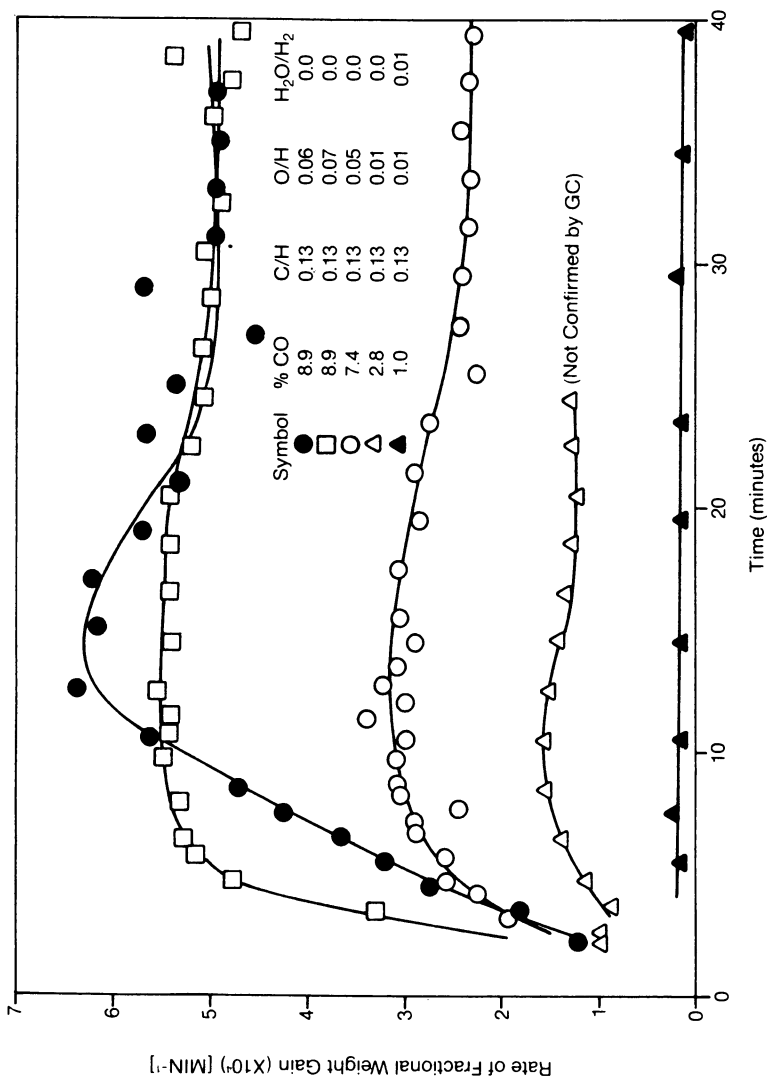


Figure 7. Rate of fractional weight gain vs. time. Conditions: temperature, 900 K; and pressure, 1 Bar.

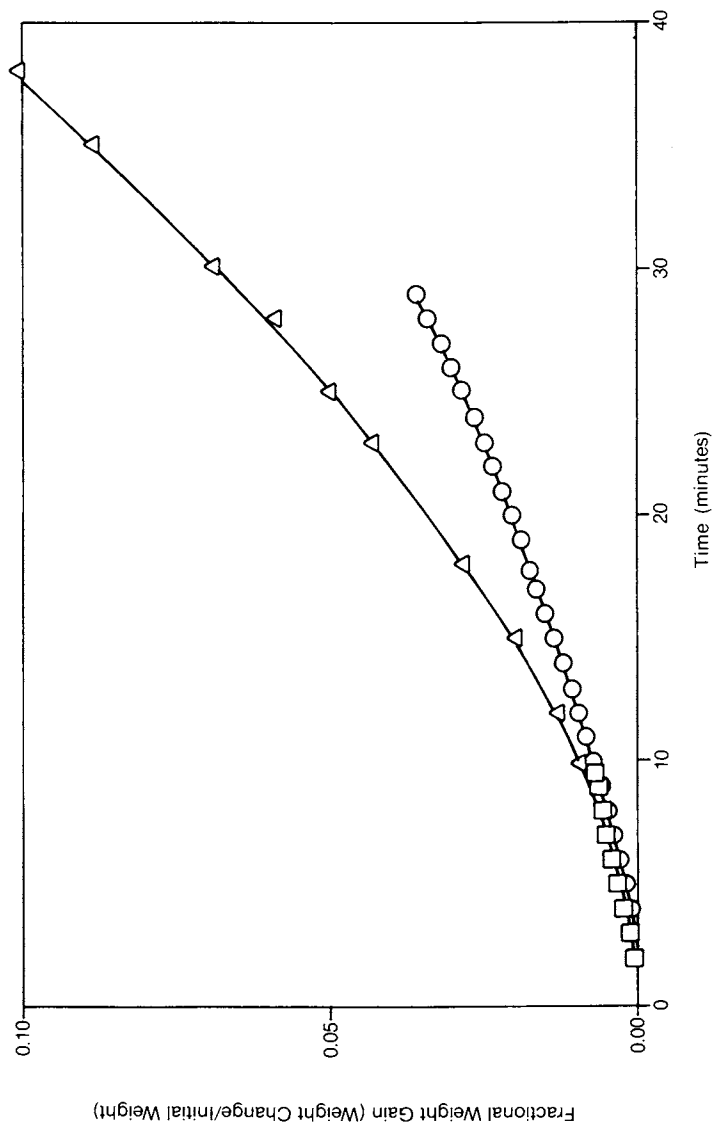


Figure 8. Fractional weight gain vs. time. Conditions: % CO, 37.5; C/H, 0.40; O/H, 0.22; and H_2O/H_2 , 0.03.

each other after 6-10 minutes. This behavior is due to the fact that initially the surface areas for the three foils are very nearly equal. After carbides form (first 6-10 minutes), fibers begin to form and the effective surface area increases. This increase is related to the number of fibers and the number of locations where fibers begin to grow. This behavior makes it very difficult to test any proposed kinetic mechanism.

Conclusions

These preliminary results suggest that cementite is probably a catalyst for carbon deposition and thereby filament growth. Also, the pearlitic structure found after the foils were etched indicates that carbon from the gas phase diffuses into the surface layer (no pearlitic structure was observed in the foils prior to reaction). Based on the preliminary results and the work of Tsao (8), it is felt that the shape of the curves in Figure 7 can be interpreted as cementite formation followed by an increasing carbon deposition rate as more and more carbide is formed. Carbides such as cementite will form at the more energy favorable dislocations such as grain boundaries and other areas of structural irregularities. These formations on surface irregularities (e.g., scratches, edges, grain boundaries) results in large growth areas which then break into smaller crystals which form the growth tips for filaments. The formation of these carbide growth crystals (with their concomitant area increase) is reflected in the rapid increase in rate of fractional weight gain. The steady state (constant rate) portion is believed to be due to fiber growth with a relatively fixed number of fibers.

Acknowledgement

The authors gratefully acknowledge the support and encouragement of the National Science Foundation through the Research Initiation Grant Program, Grant No. ENG 78-05579.

Literature Cited

1. Hofer, L.J.E.; Sterling, E.; and McCartney, J.T. "Structure of the Carbon Deposited from Carbon Monoxide on Iron, Cobalt, and Nickel"; J. Phys. Chem. 1955, 59, 1153.
2. Oberlin, A.; Endo, M.; and Koyama, T. "Filamentous Growth of Carbon through Benzene Decomposition"; J. Crystal Growth 1976, 32, 335.
3. Boehm, H.P. "Carbon from Carbon Monoxide Disproportionation on Nickel and Iron Catalysts: Morphological Studies and Possible Growth Mechanisms"; Carbon 1973, 11, 583.

4. Baker, R.T.K.; Harris, R.S.; Thomas, R.E.; and Waite, R.J. "Formation of Filamentous Carbon from Iron, Cobalt and Chromium Catalyzed Decomposition of Acetylene"; J. Catalysis 1973, 30, 86.
5. Baker, R.T.K.; Chludzinski, Jr., J.J. "Filamentous Carbon Growth on Nickel-Iron Surfaces: The Effect of Various Oxide Additives"; J. Catalysis 1980, 64, 464.
6. Baker, R.T.K.; Harris, R.S. "The Formation of Filamentous Carbon"; Chem. Physics Carbon 1978, 14, 83.
7. Sacco, Jr., A.; Reid, R.C. "Water Limitations in the C-H-O System over Iron"; AIChE J. 1979, 25, 839.
8. Tsao, T. "Kinetics of Dissociation of Carbon Monoxide on α -Fe"; Carnegie-Mellon University, Ph.D. 1974.

RECEIVED June 28, 1982.

The Characterization of Carbon Deposit Morphologies Using In Situ Scanning Electron Microscopy

A. M. BROWN and M. P. HILL

Central Electricity Research Laboratories, Surrey, United Kingdom

Carbon deposits have been grown on heated polycrystalline iron specimens in a gas reaction cell in a scanning electron microscope. The complete range of deposits formed from methane at temperatures between 620°C and 850°C have been surveyed, from the first appearance of solid carbon on the surface to the final structural breakdown of the metal. Four characteristic morphologies have been identified. There are indications that solution-precipitation processes are involved in the growth mechanisms in each case.

The importance of structural disorder in the metal is considered and the behaviour of well annealed material is compared to structurally less stable but clean metal surfaces. The processes that occur in the development of particulate deposits have been followed. Auger analysis of individual morphologies has highlighted particular problems in the analysis of carbon deposits after ion etching.

The implications of these observations to deposition on less well-defined metal surfaces and gases containing trace impurities is discussed.

The formation of carbon deposits is an undesirable feature of a number of industrial processes, for example on the fuel pins in nuclear reactors, on the catalysts and structural materials of reactors in petrochemical plant, and on furnace wall linings. A greater understanding of the mechanism of deposition is required in order to develop improved methods of control. Metal-carbon interactions are also important in the catalysis of carbon gasification for the manufacture of synthetic fuels.

The deposits formed on transition metals from hydrocarbons or carbon monoxide exhibit a variety of morphologies including graphitic laminar films, mound (monticular) growths, columnar, particulate, and numerous filamentary types of carbon, (1-4). The

0097-6156/82/0202-0193\$08.50/0

© 1982 American Chemical Society

observations suggest that several different chemical and/or physical processes occur both simultaneously and sequentially during the reaction. Although one particular morphology may have been identified as a product of several hydrocarbon-metal reactions, there have been few systematic studies of the growth mechanisms. However, considerable progress has been made in understanding the growth of filamentary carbon (4), using controlled atmosphere transmission electron microscopy which has demonstrated the value of in-situ observations (5). Transmission electron microscopy has the benefits of high resolution and the availability of electron diffraction, but is limited to the examination of small particles, thin foils, and products formed at the edges of specimens too thick for transmission of the electron beam. In order to study carbon deposition on bulk metals in-situ scanning electron microscopy is more suitable, offering the facilities of resolution down to $\sim 50 \text{ \AA}$, good depth of field, stereoscopic viewing of deposits, and the use of various micro-analytical techniques.

The metal most active in supporting carbon deposition is iron, closely followed by nickel, and is the one selected for this work. The iron-carbon system is complex because both graphite and iron carbides are possible reaction products. Below the Fe-C eutectoid temperature (721°C or 738°C) additional solid-state transformations are known leading to the structures found in ferritic steels, i.e. pearlite, martensite and bainite etc. Consequently, care must be taken over the temperature cycling experienced by the specimen to avoid introducing additional complications. In particular, cooling a specimen to ambient temperature for examination increases considerably the risk of modifying existing structures or introducing new precipitation products. Ambiguities arising from these sources are largely avoided by use of the in-situ SEM technique.

Several mechanisms of carbon deposition have been proposed (4, 6-8) including:

- (i) carbon dissolution, diffusion to suitable sites, followed by precipitation,
- (ii) formation of metal carbide on the surface followed by thermal decomposition,
- (iii) surface diffusion of carbon atoms or a C/H/metal organo-metallic type complex species,
- (iv) bulk carbon diffusion.

Under different experimental conditions one or other of these mechanisms may predominate. However, at the present time the growth mechanism for the majority of carbon structures is uncertain.

In carbon deposition on a bulk metal specimen, the carbon uptake follows a sigmoidal curve as a function of time typical of an autocatalytic reaction. Initially carbon dissolves in the metal until the saturation solubility has been exceeded. This step is observed as an incubation period. The initial solid product formed causes no disruption of the metal surface and the growth rate remains low. It starts to rise rapidly as particulate

material is extracted from the metal and becomes incorporated in the deposit, leading eventually to complete breakdown of the metal structure. Most of the carbon deposit is formed during this period as increasing amounts of active catalyst become available, and the greatest variety of deposit morphologies are observed. The reaction eventually slows down either by formation of inert products, e.g. Fe + CO (9) or by encapsulation of active metal particles in carbon(10).

In the work reported in this paper, the in-situ hot stage SEM technique has been used to examine the carbon deposits formed in the iron-methane reaction, with the objective of separating the different stages by identifying the characteristic morphologies. It is presented as a survey of the range of product morphologies starting with the carbon dissolution stage and ending with the complete structural breakdown of the experimental foil.

Experimental

The SEM used for the work is a specially adapted ultra-high vacuum field emission source instrument (V.G. Microscopes Ltd.). It has a gas reaction cell which surrounds the specimen whilst permitting most microscope stage movements. Reactions can be carried out at pressures up to ~ 50 Torr, but above ~ 0.2 Torr the electron gun chamber must be isolated and so continuous specimen observation is not possible. In the normal microscope mode the resolution is better than 50 \AA at specimen temperatures up to 800°C , but is reduced to $\sim 250 \text{ \AA}$ in the reaction cell because of a requirement to increase the probe current to achieve sufficient signal(11). The microscope is equipped with an energy dispersive X-ray analyser, a cylindrical mirror Auger analysers (CMA) and an argon ion gun. As indicated in Figure 1, the reaction cell must be opened to permit microanalysis and ion etching. Full operation of the microscope is available on the heated specimens and all the micrographs and analytical data presented were taken with the specimens at the appropriate reaction temperature.

The specimen is in the form of a $25 \mu\text{m}$ thick foil. Three mounting systems have been used:

- (i) an electrically heated plate,
- (ii) direct resistive heating,
- (iii) indirect electrical heating in which the foil is spot-welded to two D.C. heated conducting wires(11).

Methods (i) and (iii) give uniform temperatures, but the 'hot plate' is more susceptible to transfer of impurities. Method (ii) introduces steep temperature gradients between the centre and ends of the foil, but permits both carbon dissolution (in the centre) and carbon precipitation (in the cooler regions) to take place simultaneously. The carbon deposit structure is independent of the method used.

Quantification of Auger data can present problems on rough surfaces, for example, after ion etching. To minimise roughness

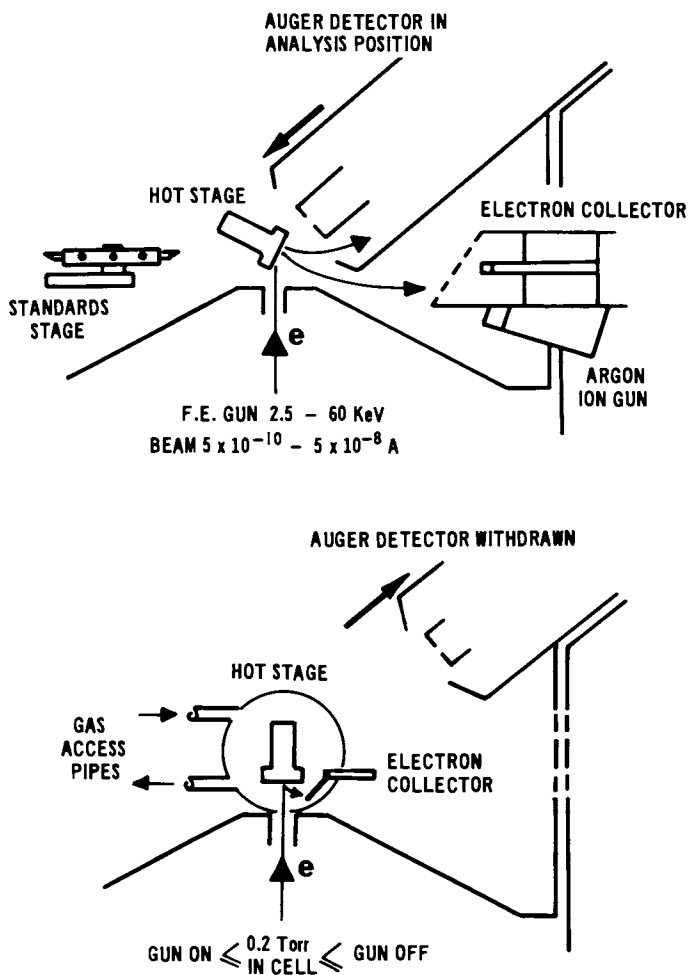


Figure 1. Modes of operation of the cerl field emission source SEM with environmental cell. Key: top, scanning electron microscopy, Auger electron spectroscopy, and argon ion etching; and bottom, gas reaction cell configuration.

effects, areas are chosen for analysis that are favourably oriented to the CMA. Ion etching introduces further difficulties. Sputtered material can be spread over the surface, and selective etching effects can influence the measured compositions. These effects will be discussed further in the results section. Estimates of the depth of material removed from the surface by ion etching are based on measurements of the height reduction of real features and are regarded as more accurate than values calculated from published sputter rates.

The experimental procedure can be understood by reference to the Fe-C phase diagram, Figure 2. The specimen is reacted with methane at temperatures of 750-850°C. Carbon dissolves in the metal until the saturation solubility has been exceeded at the γ -Fe/Fe₃C phase boundary, or alternatively the specimen is cooled to a temperature below the iron-carbon eutectoid (721°C or 738°C). The solid and dotted lines in Figure 2 indicate the alternative iron-Fe₃C and iron-graphite phase boundaries respectively. Either method produces similar reaction products but the isothermal experiment is preferably carried out at higher pressures, e.g. 50 Torr, to minimise run times.

Polycrystalline iron foil (99.999% quoted purity, ex-Johnson-Matthey) was used so that any specific activity of the grain boundary intersections at the surface would be apparent. The gas was B.O.C. Ltd. research grade, used without further purification.

Results

Surface Preparation. In the "as received" condition the metal foil is covered with an oxide layer and has extensive surface damage from the rolling process, Figure 3a. Ion etching is required to remove the cold-worked layer and the oxide, and it introduces characteristic etch structures dependent on ion beam incidence angle, crystal orientation and relative sputter yields of contaminants. The cone type features in the foreground of Figure 3b are often regarded as the principal ion etch structures, but our experience suggests that the stepped structures shown are equally probable. In Figure 3b a treatment of 10³ μ A-mins has removed ≈ 2 μ m of the surface. It is necessary to thermally anneal to remove the ion etch damage, Figure 3c and 3d. Several ion etching-thermal annealing cycles may be needed to remove impurities that segregate to the surface from the bulk metal, e.g. sulphur. Annealing at 850°C for at least 15 hours is required to produce a clean surface that would be thermally stable at the reaction temperature for long periods in the absence of reaction.

After the preparative treatment, the metal has recrystallised into a few large grains, but is rippled from the remains of former grain boundaries, Figure 4a. The grain boundary intersections at the surface are thermally grooved and exhibit a characteristic rounded profile, Figure 4b(12). The profile and step densities of

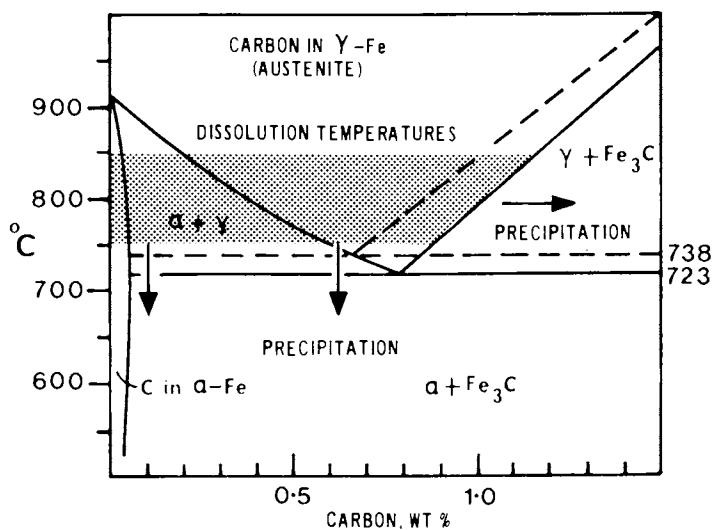


Figure 2. The iron-carbon phase diagram (part), with the dissolution and precipitation regions used in this work. Key: —, Fe-cementite; and ---, Fe-graphite.

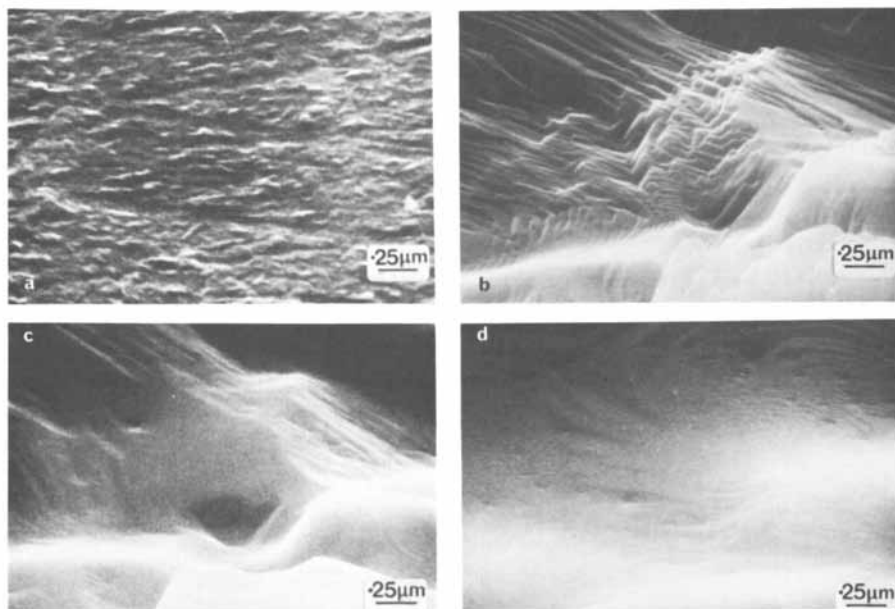


Figure 3. Surface preparation of the polycrystalline iron foil as received, with damage from cold work (a), ion etched, to remove $\sim 2 \mu\text{m}$ of metal (b) after annealing for 2 h at 500°C to remove etch structure (c), and development of step structure after further annealing for 3 h at 600°C (d).

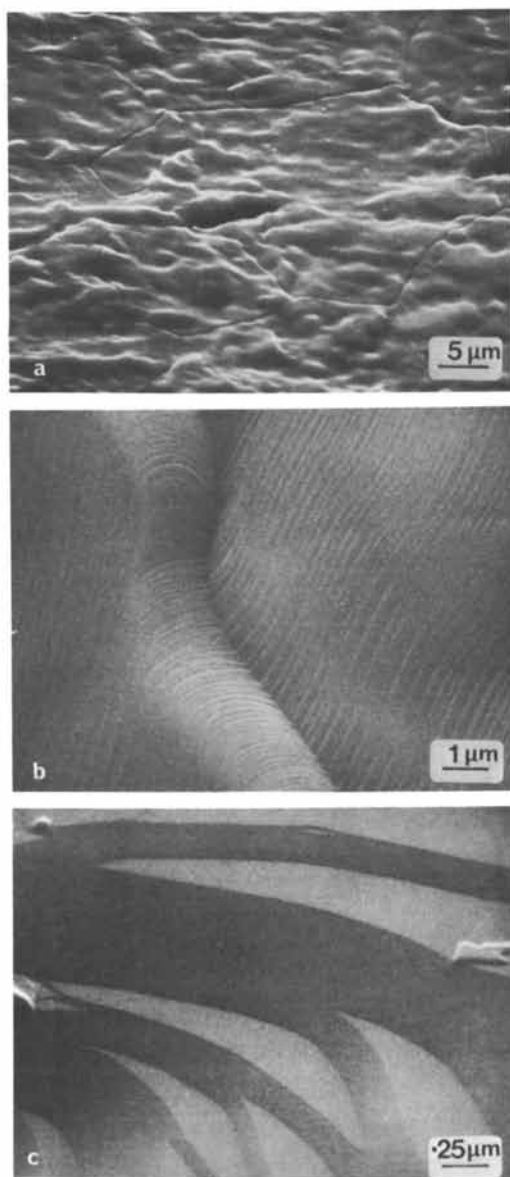


Figure 4. Structure of as prepared iron foil. Key: a, grain structure after high temperature annealing at 850°C; b, typical step structure at a thermal groove; and c, terrace structure developed at sites away from grain boundaries.

the grooves change on exposure to methane, before any carbon is deposited(13). Elsewhere on the surface terrace structures develop during annealing, at low temperatures, Figure 3d and after the final heat treatment (Figure 4c) with typical step heights of $\sim 0.2 \mu\text{m}$ and terrace widths of $\sim 0.4 \mu\text{m}$ in the latter case.

Carbon Precipitation and Re-solution. If carbon is dissolved in the iron foil at 750°C and then precipitated by cooling to 620°C , it forms rapidly on some grains whilst others remain unaffected, Figure 5a. The stepped structure is smoothed in the areas of heaviest precipitation (Area A, Figure 5a) leaving a laminar carbon layer with a 'polygonised' ridge structure that has been noted previously in this and other deposition systems (1, 2, 14, 15). Some intermediate zones are evident where the terrace width and step heights have increased; Area B Figure 5a. Step heights in the carbon free regions are typically $100\text{-}300 \text{ \AA}$ and $500\text{-}1500 \text{ \AA}$ in the intermediate zones.

The scanning Auger map for carbon, Figure 5c, confirms the absence of precipitation in the faceted regions of Figure 5b. Changes in the step structure occurring before a laminar carbon film appears (lower left in Figure 5b) are shown in the Auger map to be associated with carbon. Extended areas covered with the laminar carbon film, Figure 5a, are common but are not the only form of carbon precipitate. In some areas, mound-like growths develop, Figure 6. Structural changes continue for several hours after a precipitate has appeared. Carbon covered zones spread laterally into carbon free areas, Figure 7. Previous measurements showed that the lateral growth followed a $t^{\frac{1}{2}}$ power law, which for processes such as thermal grooving is indicative of mass transport rate control by surface diffusion(13).

If the carbon precipitates are re-dissolved by increasing the temperature above the Fe-C eutectoid, then recrystallization to form a new grain structure occurs, accompanied by faceting in most areas, Figure 8a,b,c. After another cooling induced precipitation at 620°C , the same field of view now has isolated mound type precipitates forming, Figure 8d,e, as indicated by the arrows. The original grain structure, as in Figure 8a, is not re-established. The overall tendency from repeated dissolution and precipitation cycles is to disorder the surface and produce particulate material (13).

Carbon Mound Growths. The dissolution-precipitation cycling experiments above suggest that the carbon mounds are associated with structural changes in the underlying metal. If these deposits are formed continuously in the deposition reaction, for example using the thermal migration method described in Section 2, considerable areas of the surface are covered with the precipitate but a limit to growth is reached with some of the metal surface still exposed. In Figure 9, the projected area of carbon mounds on the surface does not change with increased methane exposure,

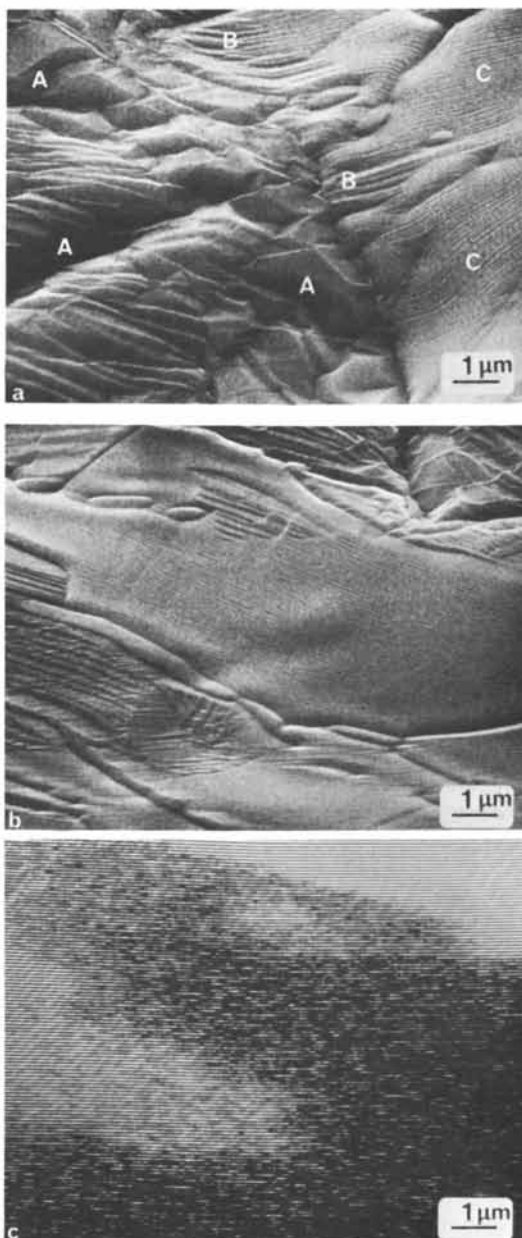


Figure 5. Iron foil after carbon precipitation at 620°C. Key: a, laminar carbon film, region A, and carbon free regions C; b, carbon precipitated regions, faceted carbon free regions, and intermediate stepped zone; and c, carbon Auger map of area in b, (KLL 271 eV).

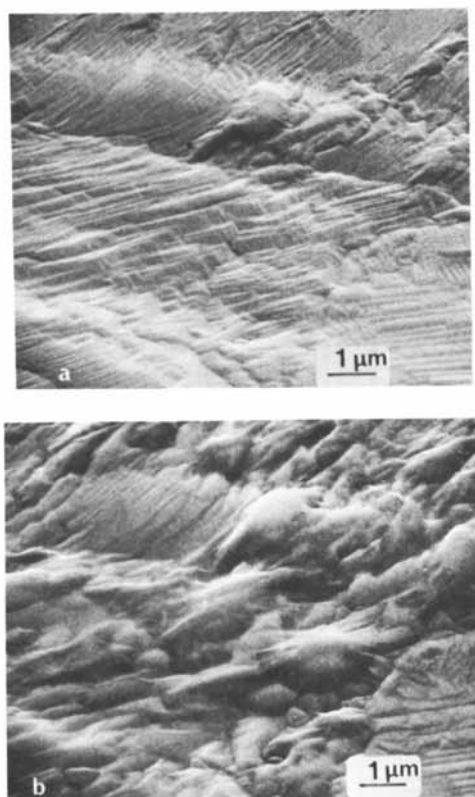


Figure 6. Mound-type carbon growths formed by precipitation at 620°C after prior methane exposure of 12 torr h at 750°C. Key: a, surface after 10 min; and b, same view after 1 h.

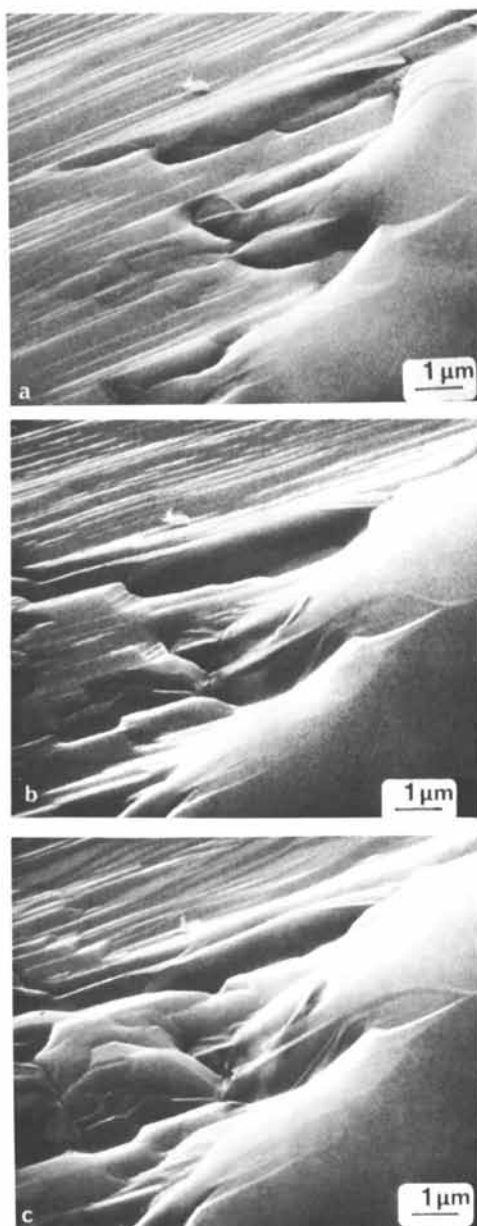


Figure 7. Lateral spreading of carbon precipitate zone into adjacent carbon-free area. Key to time after cooling to 600°C: a, 18 h; b, 44 h; and c, 136 h.

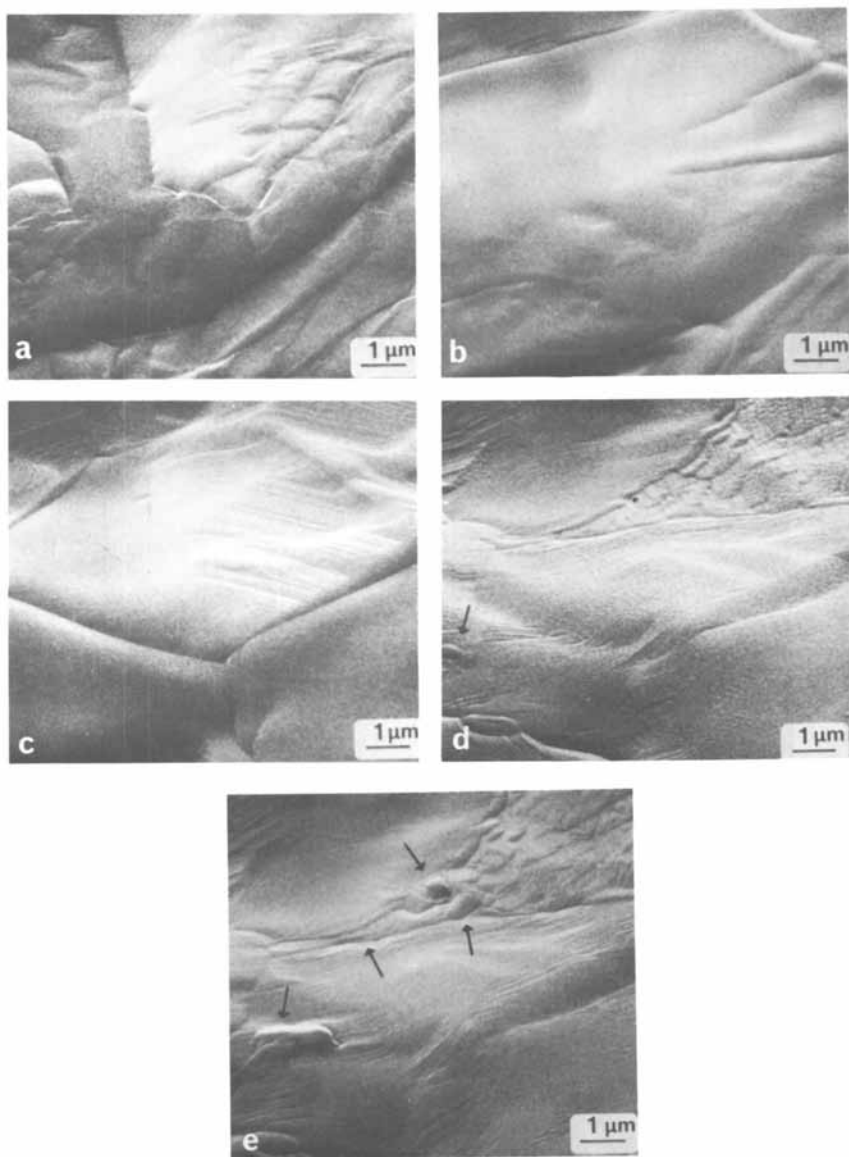


Figure 8. Carbon dissolution and reprecipitation. Key: a, as precipitated at 620°C; b, same site as (a) after dissolution at 750°C for 15 min; c, further dissolution 20 min at 750°C; d, same site after cooling for 15 min at 620°C; and e, precipitation product after 47 min at 620°C.

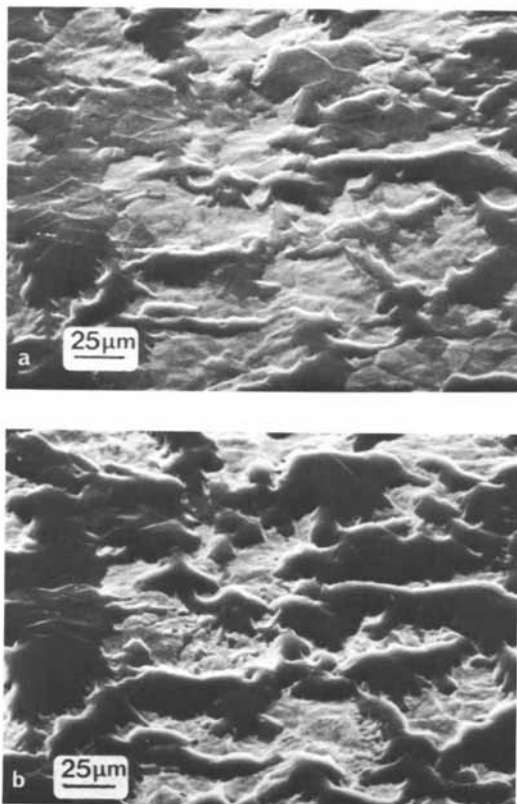


Figure 9. Typical mound carbon deposits formed at 720°C. Key: a, initial island areas of mounds; and b, same area after further methane exposure for 170 torr h with carbon dissolved at 800°C.

although the height of the mound features increases due to processes occurring in the substrate. The growth kinetics follow a direct logarithmic rate law

$$\Delta W = k \log(t + t_0) - k \log(t_i + t_0)$$

where ΔW = carbon uptake, t_i = induction period to deposition, t_0 is an arbitrary constant, and k is the rate constant. Such kinetics can be derived on the basis of a fixed number of surface sites or active area available for deposition, which decreases exponentially during the course of the reaction. The rate at any time t depends on the amount of active area remaining(16).

Under the argon ion beam (4 KeV), carbon etches more slowly than the surrounding metal, as expected from the relative sputter yields(17). The ridges that form the 'polygonised' pattern etch more rapidly than the surrounding carbon (Figure 10a) to leave channels in the surface, possibly because they present a more favourable orientation to the ion beam. Heavier etching (12325 $\mu\text{A}\cdot\text{mins}$) exposes the interface between the carbon cap and the substrate, Figure 10b. Auger spot and line scan analyses have been made on the substrate and side of the mound as exposed by ion etching, and on the mound top, Figure 11. The micrograph in Figure 11b is slightly defocussed to provide sufficient Auger signal(11). The light band in the middle of Figure 11b shows material in the side of the mound. There is no indication of a compositional discontinuity at the boundary between the carbon cap and its substrate. The carbon content is low (<10 At%) in the surrounding metal, but rises continuously in the substrate of the mound. At the interface the concentrations are Fe = 72 At%, C = 23 At%, which approximates to the cementite-Fe₃C composition. This apparent correlation should be treated with caution because there is no microscopic evidence of a separate phase immediately below the carbon zone and there is a continuous compositional variation both above and below the interface. The surface of an unetched mound has typical iron concentrations of 0-3 At%. In the mound of Figure 11, after removal of $\sim 0.25 \mu\text{m}$ of carbon, the iron content is ~ 28 At%. This value could be spuriously high if iron from the surrounding areas has contaminated the surface during ion etching. Iron contamination is more likely if bare metal is exposed between the carbon mounds by etching as in this case.

Particulate Development: Crystalline Particles. Particulate material is first detected in areas between the carbon mounds after lateral growth of the mounds has ceased, Figure 9b. Two types of particulate eventually develop, viz

- (i) crystalline deposits between the mounds, and
- (ii) agglomerates of smaller particles, possibly amorphous material, formed at isolated sites on the carbon layer, Figure 12.

The crystalline deposits have particle sizes typically in the size

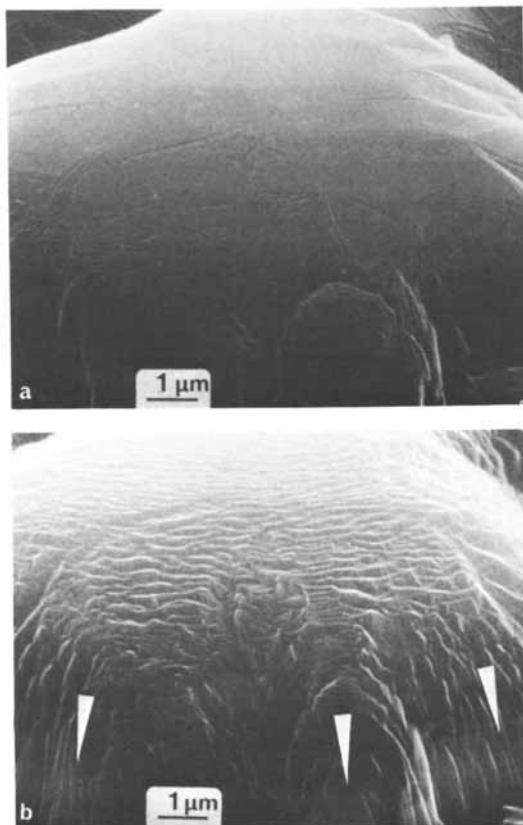


Figure 10. Structure of carbon mounds after ion etching. Conditions: a, 1,325 $\mu\text{A min}$; b, 12,325 $\mu\text{A min}$. White markers show position of interface.

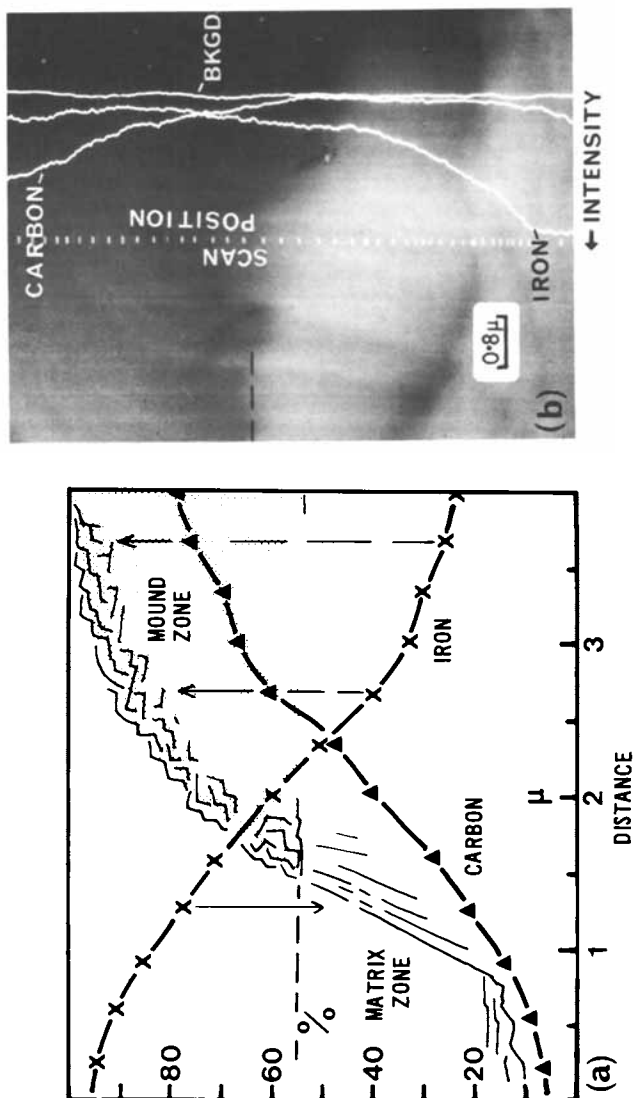


Figure 11. Carbon and iron concentration profiles on mound side exposed by ion etching.

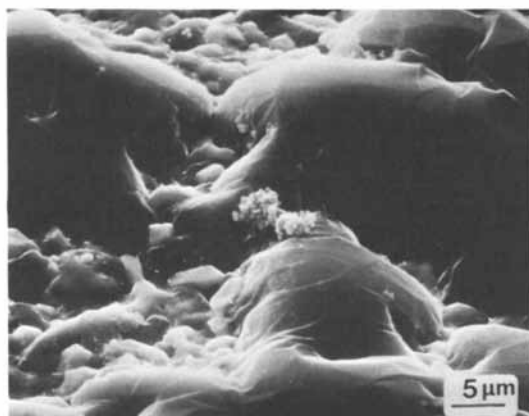


Figure 12. Initial development of particulates between the mound growths. Methane exposure 406 torr h at 800°C.

range 1 μm to 4 μm . Most have some angular facets, Figure 13a, and a few approach an equilibrium shape, Figure 13b. A number of different crystal habits have been observed including octahedral and cubic structures. In some areas the particles are observed to have penetrated the laminar carbon layer, Figure 13c.

Auger analysis of the crystalline particles, after ion etching to reveal structure, is given in Figure 14. Initially all areas reveal high carbon concentrations, e.g. >85%, but after light etching greatly increased iron levels (~ 50 At%) are detected on crystal A, Figure 14. With continued etching the carbon concentration increases again suggesting that the carbide is decomposed under the ion beam and the iron component is selectively removed. Region C, Figure 14, displays a high carbon content because it has been protected from the ion beam by the overlying material in region B. The composition of crystal A corresponds to a stoichiometry of FeC, the significance of which will be discussed later. The composition of an adjacent mound similar to those in Figure 12, shows the iron content increasing with the amount of ion etching. The analytical error quoted in Figure 14 refers to reproducibility, and does not indicate the magnitude of the possible ion beam effects discussed above. When the crystalline material is grown isothermally, rather than precipitated by cooling, considerable mobility of the surface layers is observed during the in-cell experiments at methane exposures in the range 600-2000 Torr.h at 750-800°C. The mobile material can develop into extended networks of deposit, Figure 15. However, the overall trend in the reaction is towards the formation of the isolated crystalline type of particulate deposit, Figures 13 and 14.

Energy dispersive X-ray analysis confirms that both types of particulate material contain iron, Figure 16. The absence of an Fe K α signal from the surrounding laminar carbon indicates that its layer thickness in this region is ~ 1 to 2 μm , in agreement with the value estimated from the etched mounds.

Particulate Development: 'Core' and 'Shell' Type Particles and Filamentary Deposits. These particles are identified by the strongly electron emitting 'core' surrounded by a 'shell' of lower emission, Figure 17a,b. The Fe K α X-ray map, Figure 17c, clearly shows the 'core' material to contain iron. Auger analysis of unetched clusters of the particles gives carbon contents for the shells of 91 to 96 At%, which is comparable to the laminar carbon films. Typical overall diameters are in the range 0.3 μm to 0.6 μm . 'Shell' thicknesses are estimated to be ~ 0.1 μm .

As deposition continues, the laminar carbon film on the mounds becomes covered with particulates and at the stage where the metal structure breaks down completely, the mounds are undetectable. Heavy deposition involves only the formation of particulates, Figure 18a. The surfaces of the particles appear to have active sites for the development of further particulate material.

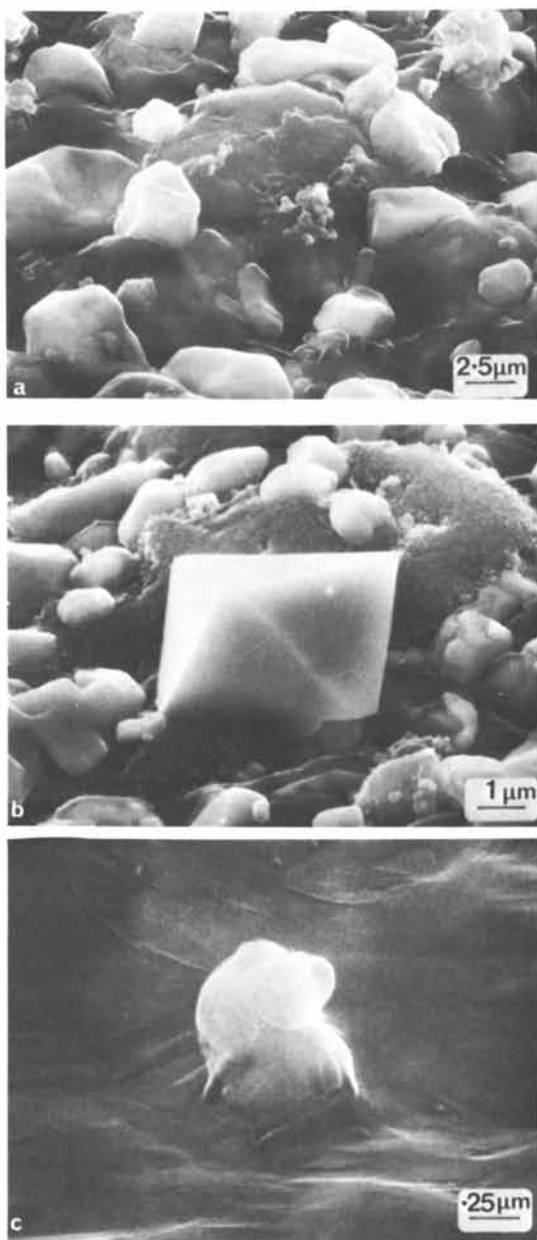
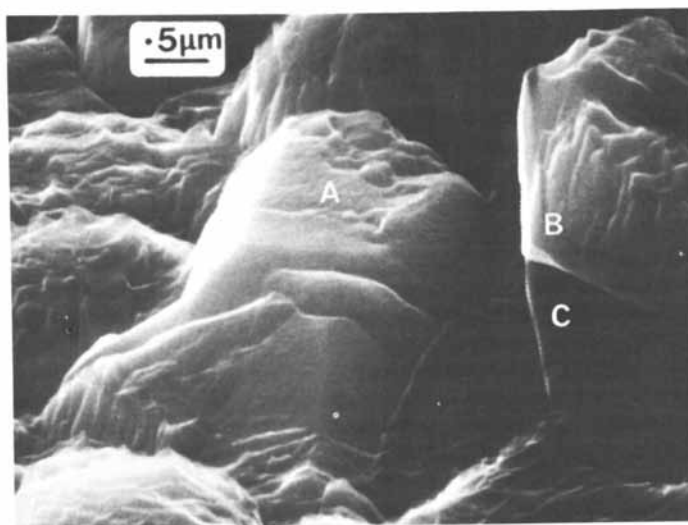


Figure 13. Typical particulate deposits. Key: a, larger crystalline particles, and agglomerations of smaller particles after 10,120 torr h methane; b, development of stable crystal habit; and c, particulate material breaking through laminar carbon film.



REGION	MEAN COMPOSITIONS	
	%C	%Fe
A (0.2 μm removed)	58	42
A (0.5 μm removed)	48	52
B	63	37
C	71	29
ADJACENT MOUND (not shown)		
0.02 μm removed	93	7
0.2 μm removed	89	11

all analyses $\pm 2\%$

AUGER ANALYSIS

Figure 14. Ion etched Fe/C crystals with Auger analysis of selected areas. Methane exposure 406 torr h at 800°C.

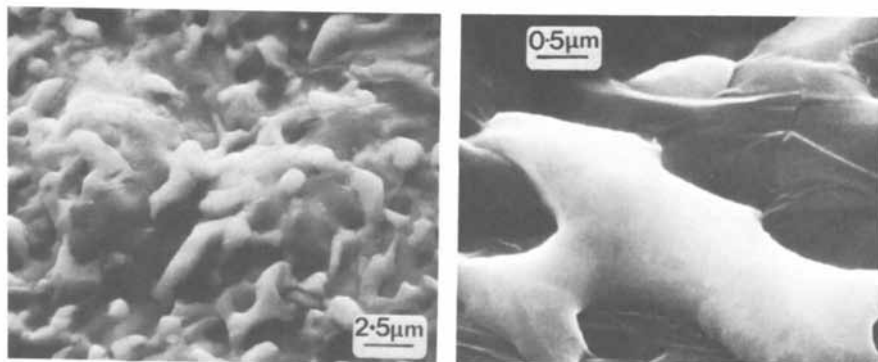


Figure 15. Coalescence of Fe/C crystals to form extended networks of deposit between the carbon mound growths. Methane exposure 900 torr h at 780°C.

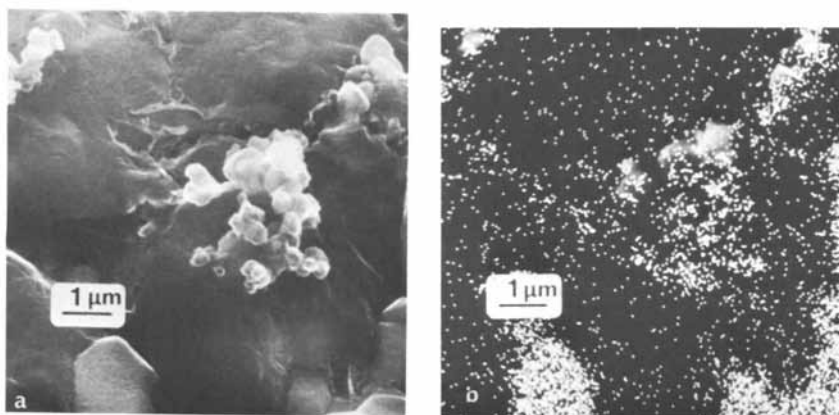


Figure 16. Two types of particulate deposit surrounded by a laminar carbon layer (left) and iron K_{α} X-ray map (primary beam energy = 10 KeV) (right).

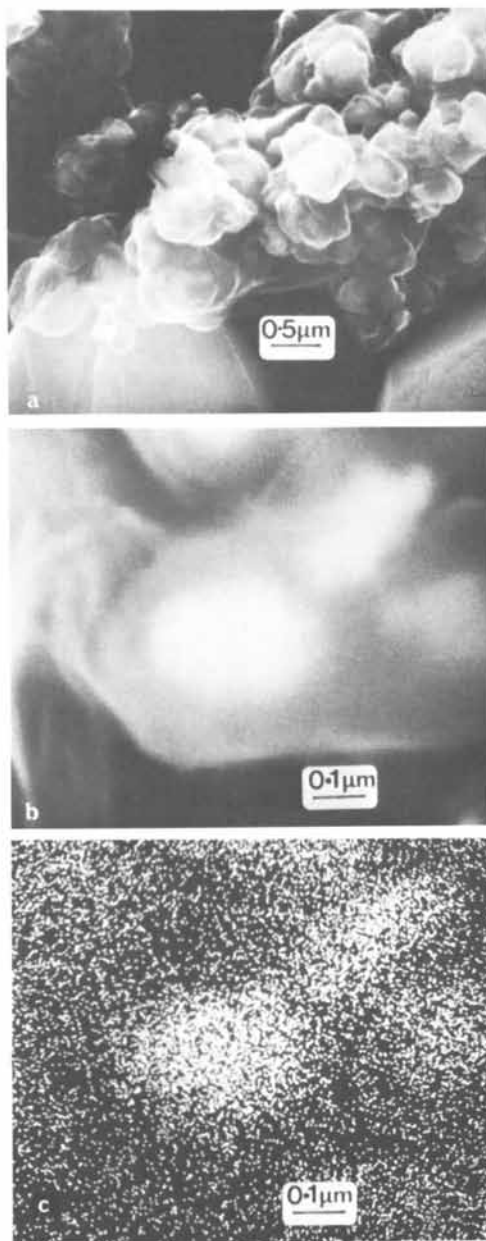


Figure 17. Core/shell type particles. Methane exposure 10,120 torr h at 780°C. Key: a, cluster of particles at a growth site; b, individual particle cores in a cluster; and c, iron K α X-ray map of area in b (primary beam energy = 10 KeV).

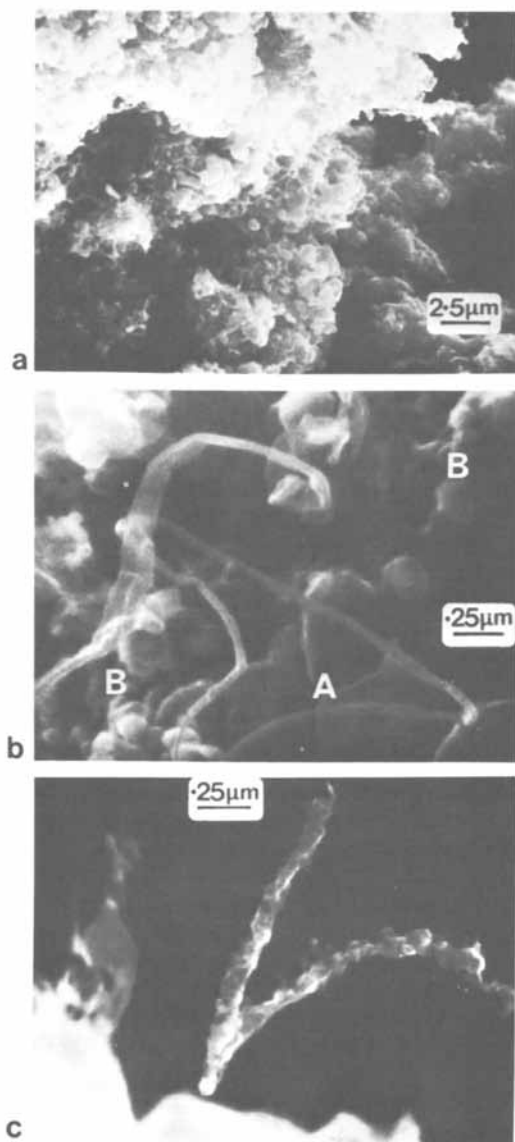


Figure 18. Particulate structure developed when the iron foil is reacted to the stage of structural breakdown (a), filaments and two types of Fe/C particulate material (A and B) (b), and filaments composed of small particles (c). Methane exposure 10,120 torr h at 780°C.

Only a limited amount of filamentary material is formed, Figure 18b and c. The filaments shown in Figure 18b are similar to those reported for other systems, e.g. Ni/C₂H₂, having single metal particles contained in the head(4). However, the majority of filaments were composed entirely of particulate material (Figure 18c) with iron distributed throughout the structure, Figure 19. In neither case was it possible to associate the filament growth site with a specific type of particle.

Discussion

The Influences of Metal Structure. The formation of a continuous laminar carbon film over extended areas of the surface appears to be a characteristic of precipitation on a well-annealed metal. Structural disorder may be introduced by successive dissolution-precipitation cycles, or may remain as the cold-worked zone on non-annealed material. In both cases, a greater proportion of the mound-type of deposit is expected, which has a carbon over-layer identical to the continuous laminar carbon layer.

Changes in the metal structure occur during a cooling induced precipitation because the metal transforms from the γ -(face centred cubic) to the α -(body centred cubic) iron lattice. Precipitation at 620°C, Figures 5 to 7, takes place at the onset temperature for recrystallization, i.e. $0.4 \times T_m$ (T_m = melting point). It is not surprising, therefore, that the metal undergoes a radical change in grain structure. Using the resistive heating techniques (method (ii), Section 2), the metal undergoes an α - γ transformation in the hot zone as carbon dissolves and the concentration rises above the α -phase boundary, Figure 2. Initially precipitation in the cold zone takes place in α -Fe, but it is likely that the high emissivity of the deposit produces some localised cooling, which would move the precipitation zone towards the hotter central region of the specimen as the reaction proceeds. Subsequent precipitation could be taking place in a zone that has undergone an $\alpha \rightarrow \gamma \rightarrow \alpha$ change, and the consequent disorder in the metal would contribute significantly to forming the mound-type deposits, Figures 9 and 12. A similar type of deposit was reported previously, although under conditions in which the specimen was cooled to ambient temperature prior to SEM examination, which may have introduced structural changes after the deposition experiment had finished(18).

The slower changes observed as a spreading of the island carbon zones may arise because the $\gamma \rightarrow \alpha$ transformation does not go to completion in all areas. The lateral spreading (Figure 7) could be associated with retained γ -Fe being slowly incorporated in the adjacent α -matrix with the rejection of more carbon to the surface.

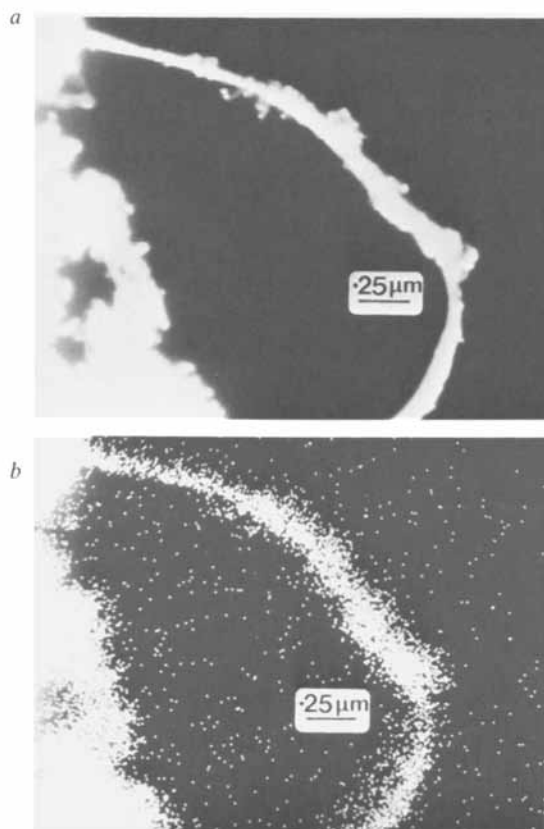


Figure 19. Filament composed of Fe/C particles (a), and iron K_{α} X-ray map (primary beam energy 20 KeV)(b).

The Development of Mound Growths. The mound carbon encapsulates the metal and prevents it from taking part in the reaction until particulate growth has caused substantial break-up of the bulk metal. Similar types of deposit have been reported in the Ni/C₂H₂ reaction at 990°C and Fe/CH₄ system at 1100°C(19). A reduction in reactivity caused by encapsulation was reported for the Fe/C₃H₆ deposition reaction(20)

The reasons for the limitation on the growth of mound deposits is not yet clear. The amount of carbon formed depends on the amount initially in solution in the metal(16). Precipitation can proceed according to the stable iron-graphite or the metastable iron-iron carbide phase diagrams (both are superimposed in Figure 2). It is proposed that the carbon film is not formed over the entire surface because carbide precipitates are nucleating within the metal in some areas and are competing for carbon in solution. Growth of the laminar carbon may be significant only during this carbide nucleation stage. Eventually, carbide crystal growth becomes sufficiently rapid from the available carbon in solution that the rate of growth of the laminar carbon on the mounds decreases.

A number of questions on the composition of the carbon mounds remain unanswered. It is not clear whether the carbon cap contains iron with the concentration increasing with depth from the surface, or whether the iron present (Figure 11) has been deposited by the sputtering process. The outer surface of the unetched deposit usually consists of 98-100 At% carbon. The composition of the material under the cap is also uncertain; the validity of the observed carbon profile requires confirmation.

The carbon layer composing the cap is strongly adherent. There is no evidence of spallation during ion etching as would be possible if there was an abrupt compositional change at the interface.

Particulate and Filamentary Growth. It is implicit in the mechanism proposed above for carbon mound growth, that the crystalline particulates are nucleated at active sites within the metal. The evidence that further growth causes the particles to be ejected through laminar carbon overlayer is given in Figure 13c. The mechanistic steps required for carbide particle growth are

solution
↓
diffusion to active sites
↓
nucleation
↓
precipitation

rather than a direct gas-phase attack at the metal surface.

Auger analysis of the crystalline deposit, Figure 14, suggests

that it is a carbide with the formula FeC . A carbide with this composition was reported to be formed in Fischer-Tropsch hydrocarbon synthesis(21), but later work claimed that the true stoichiometry was Fe_7C_3 (22). Firm conclusions on the composition will not be possible until the problems surrounding Auger measurements on ion etched surfaces have been resolved.

The 'core' and 'shell' type of particulates are similar to one of the deposit morphologies formed on an Fe-Ni alloy from CO at temperatures above 500°C where the 'core' consisted of a metal particle in the size range 0.09 to 0.2 μm , with a 'shell' thickness typically of 0.04 μm (23). The structure of the particles, i.e. a carbon layer on metal, is comparable to the laminar film on the metal, suggesting that the carbon in the shell has been precipitated. Free metal particles have not been observed on the iron foils that could serve as active centres for growth directly from the gas phase. Therefore, it must be concluded that a solution-precipitation process plays a part in determining the final morphology of the 'core'/'shell' particles, but further details of the mechanism of growth cannot be established at present.

The initial particulate deposits can act as a substrate for the development of further particulate material. In spite of this high activity, the fact that many particles are of a suitable size for incorporation into filaments, i.e. 0.01-1 μm , and the large quantity and high area of particles, very little filamentary carbon is formed. Previous reports have indicated that there is difficulty in forming filaments from methane(24). It has been suggested that filaments are formed only from higher hydrocarbon impurities in the methane(25). Trace quantities of higher hydrocarbons could be formed by a Fischer-Tropsch reaction using iron carbide in the deposit as a catalyst and hydrogen released from the CH_4 dissociation during deposition. Factors such as temperature, pressure, and residence time of methane over the deposit would be important in determining the quantities of hydrocarbons formed. The failure of pure methane to form filaments has been attributed to the decomposition being endothermic. In addition to thermodynamic reasons, kinetic factors may favour the encapsulation of active particles, particularly as in these experiments the conditions appear to be suitable for the formation of a carbon 'shell'. The fact that some filaments consist of an agglomeration of particles implies considerable mobility of Fe/C species. Some evidence for mobility is shown in Figure 15, where the crystalline deposits have coalesced into extended networks.

Application to Less Well-defined Surfaces and Reaction Conditions. In all practical situations where carbon deposition presents problems, the alloy surface is not in a condition comparable to that prepared for these experiments. A heavily cold-work layer will be present covered by an oxide film, which itself may have a complex composition and structure. The

main physical effect on deposition is to provide a more disordered surface which will inhibit formation of an extended laminar carbon film. The mound type of growth would be more common, and particulate material would become available at an earlier stage of the reaction. In the reducing environment, the oxide film will provide a source of metal particles. In industrial plant, a methane atmosphere is likely to yield filamentary deposits because of higher hydrocarbon impurities present. Trace oxidants in the gas stream would inhibit carbon encapsulation processes. Another effect of protective oxide films and of trace oxidants in the gas would be to reduce the rate of carbon dissolution(26), thus extending the initial induction period of the reaction. When the metal had become saturated in carbon, the same deposit growth processes would be expected, and particulate material would rapidly disrupt the oxide layer exposing the metal to further rapid attack.

Conclusions

The results of this in-situ SEM work suggest that solution-precipitation processes have some part in the development of four of the morphological types discussed, i.e. continuous laminar carbon films, mound growths, and two types of particulate material. Although a small amount of filamentary carbon was observed, it does not appear to be a major characteristic of the Fe-CH₄ reaction.

The next priority in future work should be to study the growth mechanisms of the particulate materials. Their development represents the most rapid deposition stage of the reaction and is the route by which metallic material is transferred to the deposit.

Auger microanalysis is potentially a valuable tool for establishing compositional variations in the deposits, but problems of making reliable measurements on ion etched surfaces needs resolving.

Acknowledgment

The work was carried out at the Central Electricity Research Laboratories and is published by permission of the Central Electricity Generating Board.

Literature Cited

1. Presland, A.E.B.; Walker, P.L. *Carbon* 1969, 7, 1
2. Brown, A.M.; Emsley, A.M.; Hill, M.P. "Gas Chemistry in Nuclear Reactors and Large Industrial Plant"; Dyer, A., Ed.; Heydon; London 1980, p.26
3. Baird, T. *Carbon* 1977, 15, 379

4. Baker, R.T.K.; Harris, P.S. "Chemistry and Physics of Carbon"; Walker, P.L. Jr.; Thrower, P.A.; Eds.; Dekker; New York; 1978, 14, 83
5. Baker, R.T.K. "Chemistry and Physics of Solid Surfaces"; Vanselow, R.; Tong, S.Y.; Eds.; C.R.C. Press; Cleveland, Ohio; 1979, p.293
6. Irvin, S.M.; Walker, P.L. Carbon 1967, 5, 399
7. Baird, T.; Fryer, J.R.; Grant, B. Carbon 1974, 12, 591
8. Bernardo, C.; Lobo, L.S. Carbon 1976, 14, 287
9. Walker, P.L. Jr.; Raksawski, J.F.; Imperial, G.R. J. Phys. Chem. 1959, 63, 140
10. Baker, R.T.K.; Barber, M.A.; Feates, F.S.; Harris, P.S.; Waite, R.J. J. Catalysis 1972, 26, 51
11. Brown, A.M.; Hill, M.P. "Electron Microscopy and Analysis"; Institute of Physics Conf. Series; 1980, 52, 379
12. Gjostein, N.A. "Metal Surfaces: Structure, Energetics and Kinetics"; American Society of Metals, Ohio; 1963, p.99
13. Brown, A.M.; Hill, M.P. Carbon 1981, 19, 51
14. Presland, A.E.B.; Roscoe, C.; Walker, P.L. Jr. Proc. 3rd Int. Conf. on Industrial Carbon and Graphite; Society of Chemical Industry, London; 1970
15. Blau, G.; Presland, A.E.B. Proc. 3rd Int. Conf. on Industrial Carbon and Graphite; Society of Chemical Industry, London; 1970
16. Emsley, A.M.; Hill, M.P. 14th Amer. Carbon Conf., Penn State Univ. 1979, p.131
17. Franks, J. Adv. in Electronics and Electron Physics; 1978, 47, 1
18. Robertson, S.D. Carbon 1972, 10, 221
19. Derbyshire, F.J.; Trimm, D.L. Proc. 4th Conf. on Industrial Carbon and Graphite, Society of Chemical Industry, London; 1974, paper 14
20. Cooper, B.J.; Trimm, D.L. Proc. 5th London Carbon and Graphite Conf., Society of Chemical Industry; 1978, 2, 768
21. Eckstrom, H.C.; Adcock, W.A. J. Amer. Chem. Soc. 1950, 72, 1042
22. Herbstein, F.H.; Snyman, J.A. Inorganic Chem. 1964, 3, 894
23. Audier, M.; Guinot, J.; Coulon, M.; Bonnetain, L. Carbon 1981, 19, 99
24. Baker, R.T.K.; Harris, P.S.; Henderson, J.; Thomas, R.B., Carbon 1975, 13, 17
25. Evans, E.L.; Thomas, J.M.; Thrower, P.A.; Walker, P.L. Jr. Carbon 1973, 11, 441
26. Emsley, A.M.; Hill, M.P. Carbon 1977, 15, 205

RECEIVED June 28, 1982.

Inhibition by Sulfur Poisoning of the Heterogeneous Decomposition of Acetone

M. J. BENNETT, G. H. CHAFFEY, B. L. MYATT, and D. R. V. SILVESTER

Materials Development Division, AERE Harwell, Didcot, Oxon, OX11 0RA,
United Kingdom

Inhibition by sulphur poisoning of carbon deposition from the heterogeneous decomposition of acetone on an oxidised 20% Cr/25% Ni/Nb stainless steel and representative scale constituents (Fe_3O_4 and Cr_2O_3) has been studied. Two procedures examined were prior sulphiding and the continuous addition of sulphur compounds (thiophene, H_2S , SO_2 and COS) to the gas phase. Deposition on Fe_3O_4 was reduced, and in certain circumstances prevented, as catalytic intermediate formation was inhibited either by the preferential adsorption of the additives poisoning surface sites or by oxide conversion to $\text{Fe}_1\text{-N}_\text{S}$. Sulphur poisoning did not inhibit acetone decomposition by Cr_2O_3 . The oxide behaviour reflected that of the oxidised 20/25/Nb steel. Sulphiding reduced deposition for a limited period until new catalytic intermediates were generated by the simultaneous oxidation of the steel. All the gaseous additives were effective by extents which increased with their partial pressure.

The coolant for the UK advanced gas-cooled power reactors is carbon dioxide containing minor controlled levels of carbon monoxide, methane and water vapour. Radiation-induced degradation of the carbon monoxide and methane can result in gas-phase precursors, which in turn can be decomposed catalytically to produce carbonaceous deposits on the oxidised 20% Cr-25% Ni niobium stabilised (20/25/Nb) austenitic stainless steel fuel cladding surfaces (1, 2). This deposit forms as flocculent aggregates of interwoven filaments, and iron and nickel are the principal metallic constituents of the catalysts involved. This type of deposition has been simulated out of reactor from the thermal degradation of acetone both on the 20/25/Nb steel and a range of oxides (such as Cr_2O_3 , Fe_3O_4 and other spinels) (3). These are the principal constituents of the scales formed on this steel

This chapter not subject to U.S. copyright.
Published 1982 American Chemical Society.

during oxidation in carbon dioxide over the temperature range of interest. Filamentary deposit growth on metals and alloys from hydrocarbon degradation has been studied extensively (4) with a common feature being the high catalytic activity of the transition elements. This is also one of the main types of carbonaceous deposit formed on ESC pyrolysis tubes during cracking operations (5).

Previous work (6) has indicated that carbon disulphide and other sulphur compounds (hydrogen sulphide, ethyl mercaptan, thioglycollic acid, allyl isothiocyanate and trithioacetaldehyde), at a 0.1% concentration, were effective gas phase poisons of the thermal decomposition of ketones on heated nickel-chromium heat resistant alloy reaction vessels. In addition, sulphur compounds prevented the deposition of carbon on iron and various steels by the Boudouard reaction from carbon monoxide (7). On this basis two approaches to reduce acetone decomposition by the 20/25/Nb steel, Fe_3O_4 and Cr_2O_3 have been examined. The first was pretreatment to form a sulphide surface layer, which could be less catalytically active. The second was to add a sulphur bearing compound continuously to the gas phase, which would be adsorbed on the active surface sites preferentially to acetone. The relative effectiveness has been compared of hydrogen sulphide, sulphur dioxide, carbonyl sulphide and the heterocyclic sulphur containing organic compound, thiophene. The latter was selected because for some reactions the relative toxicity of a number of poisons, each containing the same toxic atom, increased with the covering power of the respective molecules, i.e. with the complexity of the chain or ring attached to the toxic atom (8).

Experimental

Materials. The 20/25/Nb stainless steel specimens, with dimensions 2 cm x 1 cm, were cut from 250 μ m thick annealed strip with the analysis and grain size given in Table I. The specimen

TABLE I - Analysis and Grain Size of 20/25/Nb Stainless Steel

Wt.%					ppm		Grain size μ m
Cr	Ni	Mn	Nb	Si	C	S	
19.8	22.6	0.9	0.70	0.56	400	100	18 - 25

surfaces were abraded with 600 grit silicon carbide paper and then were oxidised, in carbon dioxide, for 1000 h, at either 600° or 700°C. The oxygen uptakes by the individual specimens are given in

Tables III and V. The Fe_3O_4 powder was a composite of three batches, prepared by the oxidation of Johnson-Matthey spectroscopic grade iron sponge in dry carbon dioxide, at $350^\circ\text{--}500^\circ\text{C}$, for 2000-3000 h. Analysis and X-ray diffraction (Table II) indicated the presence of some Fe_2O_3 , in addition to Fe_3O_4 . The Cr_2O_3 powder was a high purity grade ($>99.999\%$) supplied by Koch-Light Ltd. The surface areas of both oxides, also given in Table II, were determined by the BET method from the nitrogen adsorption measurements, at 78°K , using a Perkin-Elmer sorptometer.

TABLE II - Analyses and Surface Areas of Fe_3O_4 and Cr_2O_3

Oxide	Surface Area m^2/g	Analyses		
		Fe	C	S
Fe_3O_4	0.61	71.5%	1.0%	20 ppm
Cr_2O_3	43.8	50 ppm	100 ppm	20 ppm

The thiophene was supplied by Koch Light Ltd., while the other sulphur bearing gases (hydrogen sulphide, sulphur dioxide and carbonyl sulphide) were obtained from BOC (Special Gases) Ltd.

Experimental Procedure. As gold does not catalyse acetone decomposition. It was used to fabricate crucibles (1 cm diam., 1 cm high) for the containment of oxide specimens and as support wires for the 20/25/Nb specimens. The oxide sample weight used was 50 mg. The specimens were exposed in silica reaction vessels.

Acetone, at partial pressures of ~ 0.15 and 0.31 atm, was introduced into the carbon dioxide carrier gas by passage through a bubbler at 0°C and ambient temperature respectively. The carbon dioxide pressure was 1 atm and its flow rate was 200 cc/min. For the experiments in which thiophene was added to the gas, the bubbler was charged with a mixture of acetone and thiophene. Although the acetone partial pressure in the gas phase was maintained effectively constant, that of the thiophene was altered by changing the thiophene concentration in the bubbler. Hydrogen sulphide, sulphur dioxide and carbonyl sulphide were added to the carbon dioxide carrier gas prior to saturation with acetone. The partial pressures of the respective constituents, other than sulphur dioxide, both before and after the reaction vessel, were measured by gas chromatography. The respective sulphur dioxide concentrations were evaluated by gas analysis, involving absorption by hydrogen peroxide and subsequent sulphur determination by a Technicon autoanalyser. There was no marked depletion in any

Table III - The Effect of Sulphiding Upon Carbon Deposition from Acetone on Oxidised 20/25/Nb Stainless Steel

Oxidation by CO ₂ , 1000 h		H ₂ S treatment		1st exposure to (O ₂ + acetone (0.31 atm. pressure))			2nd exposure to (O ₂ + acetone (0.15 atm. pressure))				Sulphur remaining after exposure to CO ₂ + acetone mg/cm ²	
Temp. °C	Weight gain mg/cm ²	Exposure Conditions	Weight gain mg/cm ²	Temp. °C	Time h	Carbon uptake mg/cm ²	Deposition Reduction Factor (a)	Temp. °C	Time h	Weight gain mg/cm ² (b)		Deposition Reduction Factor (a)
700	0.095	24h, 20°C	N.M.	700	6	0.10	6-160	600	115	50.0	NIL	N.D.
600	0.801	1h, 600°C	0.113	600	7.5	0.18	4-270	600	28	2.08	NIL	0.120
700	0.096	1h, 600°C	0.010	700	7	0.03	20-560	600	115	0.13	10-375	0.018
									213	0.13		

N.M. = none measurable N.D. = not determined

(a) The ratio of the extents of deposition on oxidised and sulphided 20/25/Nb stainless steel for similar conditions. The former data are from reference (3).

(b) Accumulative values for successive exposures.

experiment of either acetone or a sulphur-bearing gas constituent across the reaction vessel. As a consequence only the inlet values are quoted in Tables III-VIII.

The deposition kinetics were determined, either discontinuously by weighing the specimens after intermittent exposure, or continuously by measuring the extension of a silica spring balance.

Results

Sulphiding. Oxidised 20/25/Nb stainless steel and Fe_3O_4 were sulphided by exposure to hydrogen sulphide, either for 24 h at room temperature or for 1 h at 600° - 625°C . The Cr_2O_3 , however, was only sulphided at the higher temperature. The respective sulphur uptakes are given in Tables III, IV and V. X-ray diffraction examination revealed that the more severe sulphiding at the higher temperature resulted in the partial formation of $\text{Fe}_{1-\text{N}}\text{S}$ and Cr_2S_3 from Fe_3O_4 and Cr_2O_3 respectively.

The extents of deposition on the sulphided 20/25/Nb stainless steel during 6-7.5 h exposure to carbon dioxide containing acetone (0.31 atm pressure) at 600° and 700°C are given in Table III. For similar exposure conditions these were lower by factors between 4 and 56 than those on oxidised 20/25/Nb stainless steel (3). However, during longer exposures of the sulphided steel to carbon dioxide containing 0.15 atm acetone, protection ceased on two out of the three specimens as comparable deposition occurred to that expected for the oxidised steel. Nevertheless, inhibition was still maintained on the third specimen. Loss of protection was not due to the removal of sulphur, as the amounts analysed after exposure to acetone were similar to the weight gains of sulphiding.

The sulphide layer on Fe_3O_4 dramatically reduced the extent of deposition at 600 and 700°C (Table IV). For comparable exposures at the lower temperature the factor by which deposition was reduced increased with the sulphur content of the Fe_3O_4 . This correlation could not be ascribed to any change in surface area, as that of the most completely sulphided Fe_3O_4 ($0.97 \text{ m}^2/\text{g}$) was similar to that of the original material ($0.61 \text{ m}^2/\text{g}$). As with the 20/25/Nb stainless steel, the sulphur contents of the sulphided Fe_3O_4 before and after exposure to the depositing gas were similar to within a factor of two.

The exposure of Cr_2O_3 to hydrogen sulphide resulted in its almost complete conversion to Cr_2S_3 with a corresponding reduction in surface area from 43.8 to $8 \text{ m}^2/\text{g}$. The kinetics of deposition on the sulphided material at 600°C were similar to those on Cr_2O_3 (Fig. 1) and whilst the extent of deposition was at least comparable, it could have been slightly increased (Table V).

Gas Phase Poisons. The effectiveness was examined of four sulphur compounds, thiophene, hydrogen sulphide, sulphur dioxide and carbonyl sulphide, as gas phase poisons.

TABLE IV - The Effect of Sulphiding by H₂S on Carbon
Deposition from Acetone on Fe₃O₄

H ₂ S treatment			Exposure to carbon dioxide containing acetone					
Temp °C	Time h	Sulphur content % (a)	Temp °C	Time h	Acetone pressure atm.	Carbon uptake % (a)	Deposition reduction factor (c)	Sulphur content after exposure % (a)
20	24	0.06	700	6	0.31	1.3	185	0.003
			600 (b)	115	0.15	378	40	
600	1	9.2	700	11.5	0.31	5.1	90	N.D.
600	1	10.3	600	8	0.31	62	250	6.7
				221 (b)	0.15	468	90	
600	1	38.4	600	266	0.15	3.5	9.4 x 10 ³	35.5

N.D. = Not determined

- (a) Expressed as a percentage of the original Fe₃O₄ sample weight. Value for complete conversion to FeS = 41.5.
- (b) Successive exposures.
- (c) The ratio of the extents of deposition on untreated control and sulphided Fe₃O₄ for comparable exposure conditions. The former data are from reference (3).

TABLE V - Influence of Sulphiding and the Continuous Addition of a Sulphur Compound to the Gas Phase upon the Interaction between Cr_2O_3 and Acetone at 600°C

Sulphur treatment/ gas phase additive	Partial pressure (atm)		Exposure duration h	Sulphur uptake (a)	Carbon uptake after 75h $\mu\text{g}/\text{cm}^2$ (b)	
	Sulphur additive	Acetone			With sulphur treatment	Without sulphur treatment
Sulphided by H_2S (1h, 600°C)	-	0.15	266	Decreased from 56.1 to 40.4 during exposure	0.99 (c)	0.39
Thiophene	8×10^{-4}	0.38	50	0.013	1.02	0.92
Thiophene	0.10	0.20	50	0.95	0.68	0.92
H_2S	8×10^{-6}	0.11	73	0.23	0.43	0.39
H_2S	6×10^{-4}	0.11	72	13.4	0.44 (c)	0.39
SO_2	4×10^{-3}	0.31	69	1.1	0.49	0.92

(a) Expressed as a percentage of the Cr_2O_3 weight; value for complete conversion to $\text{Cr}_2\text{S}_3 = 63.2\%$.

(b) Calculated from Cr_2O_3 surface area, except (c) calculated from sulphided Cr_2O_3 surface area.

TABLE VI - Influence of the Continuous Gas Phase Addition of a Sulphur Compound on the Decomposition of Acetone by 20/25/Nb Stainless Steel at 600°C

Weight gain during 1000h oxidation in CO ₂ at 600°C	Deposition exposure conditions				Sulphur uptake μg/cm ²	Carbon uptake mg/cm ²	Deposition reduction factor ^(a)
	Sulphur bearing additive	Partial pressure atm.	Acetone partial pressure atm.	Duration h			
0.157	Thiophene	1.5x10 ⁻⁴	0.19	17	4	14.0	1-6
0.077	Thiophene	6x10 ⁻²	0.15	48	6	0.02	45-7500
0.080	H ₂ S	2x10 ⁻⁶	0.09	4	N.D.	18.4	1-3
0.095	H ₂ S	2x10 ⁻⁵	0.11	72	15	0.13	6-1100
0.135	H ₂ S	3x10 ⁻⁵	0.14	50	≤5	0.24	3-470
0.055	H ₂ S	5x10 ⁻⁵	0.12	73	≤5	0.04	18-3400
0.085	H ₂ S	5x10 ⁻⁴	0.12	73	50	0.04	18-3400
0.125	SO ₂	8x10 ⁻⁶	0.10	75	≤5	1.15	1-12
0.105	SO ₂	4x10 ⁻⁵	0.12	75	5	0.65	1-210
0.070	SO ₂	4x10 ⁻³	0.31	71	2	0.06	13-2500
0.055	COS	0.3x10 ⁻⁶	0.07	75	8	0.25	3-550
0.160	COS	4x10 ⁻⁵	0.10	75	4	0.70	1-200

N.D. - Not determined

- (a) The ratio of the extents of deposition for similar exposure conditions without and with the addition of sulphur compounds to the gas phase. The former data are from reference (3).

TABLE VII - Influence of Continuous Addition of Thiophene to the Gas Phase upon Carbon Deposition from Acetone Decomposition on Fe_3O_4 at 600°C

Partial pressure (atm)		Exposure duration h	Sulphur uptake ^(a) ppm	Carbon uptake ^(a) %	Deposition reduction factor ^(b)
Thiophene	Acetone				
2×10^{-7}	0.28	2	N.D.	68	N11
10^{-5}	0.31	71	<125	3.5	5.7×10^4
4×10^{-5}	0.24	7	N.D.	N.M.	(c)
1.5×10^{-4}	0.19	4.25	< 50	N.M.	(c)
1.6×10^{-3}	0.32	7	100	N.M.	(c)
8.7×10^{-3}	0.28	7	125	N.M.	(c)
3.7×10^{-2}	0.13	5.75	3000	N.M.	(c)

N.D. - Not determined.

N.M. - Not measurable.

- (a) After exposure, expressed as a ratio of the Fe_3O_4 weight.
- (b) The ratio of the extents of deposition on Fe_3O_4 for similar exposure conditions without and with thiophene addition to the gas phase.
- (c) Not quantifiable as no deposition measured.

TABLE VIII - Influence of the Continuous Addition of Either Hydrogen Sulphide, Sulphur Dioxide or Carbonyl Sulphide to the Gas Phase upon Carbon Deposition from Acetone Decomposition on Fe_3O_4 at 600°C

Sulphur bearing gas phase additive	Partial pressure (atm)		Exposure duration	Sulphur uptake ^(a)	Carbon uptake ^(a) %	Deposition reduction factor ^(b)
	Sulphur additive	Acetone				
H_2S	3×10^{-6}	0.17	50	0.04	0.13	10^4
H_2S	2.5×10^{-5}	0.12	72	0.04	0.1	2×10^4
H_2S	5×10^{-4}	0.12	50	0.17	0.3	6×10^3
H_2S	1.7×10^{-3}	0.31	7	19.7	4.8	3×10^3
SO_2	8×10^{-6}	0.11	75	0.01	0.4	7×10^3
SO_2	9×10^{-5}	0.14	80	0.01	0.8	3×10^3
SO_2	4×10^{-3}	0.31	72	3.9	1.1	1.8×10^5
SO_2	4×10^{-3}	0.26	65	0.2	0.9	2×10^5
COS	0.25×10^{-6}	0.07	75	0.04	1.7	1.5×10^3
COS	4×10^{-5}	0.11	75	0.08	0.8	3.1×10^3

(a) After exposure, expressed as a percentage of the original Fe_3O_4 weight.

(b) The ratio of the extents of deposition for similar exposure conditions without and with the addition of a sulfur bearing compound to the gas phase.

(a) Thiophene. The 20/25/Nb stainless steel, preoxidised at 600°C, was exposed at 600°C to carbon dioxide containing 0.15-0.19 atm acetone and either 150 μ atm or 0.6 atm thiophene. Deposition was inhibited particularly by the exposure to the higher thiophene partial pressure, when it was reduced by a factor of 45-7500 (Table VI). This apparent influence of thiophene partial pressure cannot be attributed to sulphur pick-up by the 20/25/Nb stainless steel as these were comparable in the two experiments.

On exposure of Fe₃O₄ at 600°C to carbon dioxide containing 0.28 atm acetone the smallest thiophene partial pressure examined (0.19 μ atm) did not affect deposition (Table VII). However, with a thiophene pressure of between 10 μ atm and 0.04 atm maintained continuously, although Fe₃O₄ initially (< 1 h) lost weight, there was then no substantial weight change during ~ 6 h further exposure. The only exception was a small amount of deposition between 3-18 h exposure to the gas containing 10 μ atm thiophene but this was still a factor of 6×10^4 lower than that anticipated for the same exposure conditions in the absence of thiophene. As no further weight change occurred during the following 56 h exposure to this environment the results of the shorter term tests with higher thiophene partial pressures were unlikely to have been misleading due, for example, to an induction period. The carbon contents of the Fe₃O₄ exposed to 0.13-0.32 atm acetone containing thiophene partial pressures between 150 μ atm- 3.7×10^{-2} atm were analysed and were comparable to those of the original material (1.0%). Thus, the thiophene at these partial pressures had completely inhibited carbon deposition. The corresponding sulphur uptakes ranged between < 50-3000 ppm and for comparable exposure periods increased with the thiophene partial pressure. X-ray examination of exposed specimens indicated the presence of Fe₃O₄ only, whereas originally Fe₂O₃ was also present. Consequently, the small initial weight losses, equivalent to 1-2% of the original sample weight, were due to reduction of the higher oxide.

The effect of discontinuing the thiophene addition was examined at 600°C on Fe₃O₄ exposed initially to carbon dioxide containing 0.28-0.33 atm acetone and 8.7×10^{-3} atm thiophene. After 24 h subsequently in acetone alone the carbon content of the reaction product had increased to 46.7% of the original Fe₃O₄ sample weight. The extent of deposition was lower by a factor of 1.4×10^3 than that which would have been anticipated on Fe₃O₄. The low (100-125 ppm) sulphur uptake during the initial exposure to thiophene, was unlikely to have been the sole cause of this inhibition as it is not conceivable how it could have provided greater protection to acetone decomposition than the more extensive prior sulphiding (compare with Table IV).

With Cr₂O₃ the addition of thiophene, at pressures of either 1000 μ atm or 0.1 atm, did not influence either the kinetics or extent of acetone decomposition at 600°C (Fig. 1 and Table V). The sulphur uptakes for similar exposure conditions increased with thiophene partial pressure (Table V).

Symbol	Acetone Partial Pressure (atm)	Sulphur Poisoning Conditions
○	0.15	None
△	0.31	None
●	0.15	Sulphided
▲	0.38	Thiophene added (1000 μ atm pressure)
■	0.20	Thiophene added (0.10 atm pressure)
◆	0.31	SO ₂ added (4000 μ atm pressure)
×	0.11	H ₂ S added (120-570 μ atm pressure)

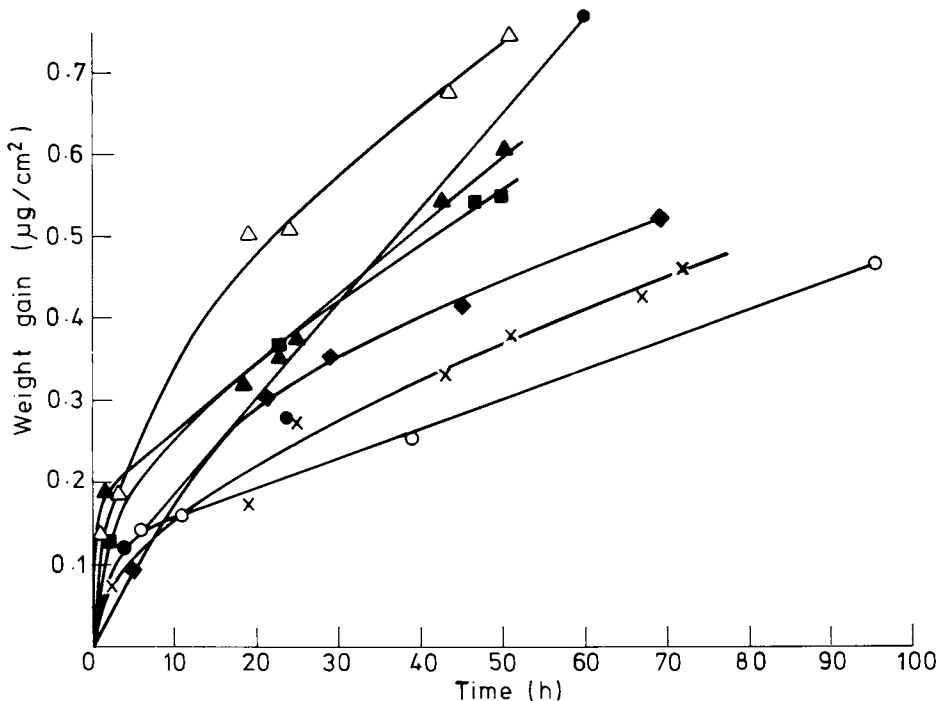


Figure 1. Influence of sulfur poisoning on the catalytic decomposition of acetone by Cr_2O_3 at $600^\circ C$.

(b) Hydrogen sulphide, sulphur dioxide and carbonyl sulphide. Reaction between the 20/25/Nb stainless steel and acetone was reduced increasingly with increasing hydrogen sulphide and sulphur dioxide partial pressures (Table VI), although in no case was it prevented. The sulphur compounds at the lowest partial pressures examined could have inhibited the reaction as the resulting carbon uptakes during these exposures were at the lower end of the scatter band of values for the 20/25/Nb stainless steel-acetone reaction under similar conditions. The effect of carbonyl sulphide was studied only at lower partial pressures and in this range it exerted a similar influence to the other additives.

The decomposition of acetone (0.07-0.17 atm pressure) by Fe_3O_4 at 600°C was inhibited markedly by the continuous addition to the gas phase of hydrogen sulphide, sulphur dioxide and carbonyl sulphide over the range of partial pressures examined (Table VIII). These were 2.2-1700 μatm for hydrogen sulphide, 5.0-3700 μatm for sulphur dioxide and $\leq 0.25-40 \mu\text{atm}$ for carbonyl sulphide. With increasing partial pressure the effectiveness of hydrogen sulphide decreased slightly, while that of sulphur dioxide increased by 100 fold. The observed initial decrease in specimen weight during these exposures, probably again arose from the reduction of the Fe_2O_3 present. In every case there was a measurable sulphur uptake, which was greatest for the Fe_3O_4 exposed to the highest hydrogen sulphide, sulphur dioxide and carbonyl sulphide partial pressures. There was always a small carbon uptake, which nevertheless was lower by factors between $3 \times 10^3-2 \times 10^5$ than would have been expected for the acetone- Fe_3O_4 reaction under the same conditions. Control experiments were carried out during each series of experiments with the various inhibitors and established that the effectiveness of the lower additive partial pressures was not attributable to any rig memory effect, e.g. desorption of sulphur compounds or degradation products from the reaction vessel surfaces.

Neither hydrogen sulphide (3.7-570 μatm pressure) nor sulphur dioxide (4000 μatm pressure) additions affected the kinetics or inhibited the extent of decomposition of acetone by Cr_2O_3 , at 600°C (Fig. 1 and Table V). The sulphur uptakes were 1.1% of the original Cr_2O_3 weight, except in the experiment with the highest hydrogen sulphide partial pressure, when it was 13.4%. Since the Cr_2O_3 surface area was decreased by sulphiding this was used to calculate the carbon uptake on this specimen. The value so obtained, normalised to 75 h, 0.44 $\mu\text{g}/\text{cm}^2$ was in close agreement with that (0.39 $\mu\text{g}/\text{cm}^2$) for Cr_2O_3 (Table V).

Discussion

Before considering the possible roles of sulphur, some of the essential features of acetone degradation on the two oxides and the 20/25/Nb stainless steel (3) need to be reiterated. Fe_3O_4 was

extremely active in promoting this reaction. Graphitic filaments were formed through which iron became finely distributed. X-ray diffraction indicated that this was present as Fe_3C and FeO , although neither necessarily was the active catalytic state. Both the threshold temperature ($\sim 550^\circ\text{C}$) and the induction period preceding reaction were associated with catalyst formation. The extent of reaction on chromia, in contrast, was extremely small and the amount of carbon formed was insufficient for detailed characterisation. Chromia was not affected chemically by the reaction with acetone, whose degradation was believed to have been catalysed by the oxide, with the primary adsorption site possibly being the chromic ion.

Oxidation of the 20/25/Nb stainless steel in carbon dioxide at $600\text{--}700^\circ\text{C}$ resulted in the formation of a scale consisting of Cr_2O_3 where the grain boundaries interacted with the surface and an (FeCrNi) spinel over the grains. Following an induction period, again attributed to catalyst formation and probably involving the reduction of the spinel, acetone was decomposed following pseudo-parabolic kinetics. The deposit produced was again filamentary in structure, with the main metallic constituent being iron, present as Fe_3C . The role of the oxide scale formed on the 20/25/Nb steel mirrored, therefore, the respective behaviour of Fe_3O_4 and Cr_2O_3 .

Two possible complementary mechanisms were responsible for the reduction, or in some circumstances complete inhibition, by sulphur of carbon deposition from acetone on Fe_3O_4 . The first was operative on material sulphided before exposure to acetone, and possibly also when high partial pressures of hydrogen sulphide and sulphur dioxide were added continuously to the gas phase, as this also resulted in appreciable $\text{Fe}_{1-\text{N}}\text{S}$ formation. In these instances reduced deposition could be attributed, at least partly, to a slower rate of formation of the reaction intermediary, e.g. iron carbides, on $\text{Fe}_{1-\text{N}}\text{S}$ as compared with Fe_3O_4 . Thiophene carbonyl sulphide, together with hydrogen sulphide and sulphur dioxide at lower partial pressures, inhibited deposition by a second mechanism. These compounds were adsorbed preferentially on the active surface sites to the exclusion of acetone and thereby, prevented the initial catalyst formation. That this was primarily a surface phenomenon is demonstrated by the sulphur uptakes which were extremely small. A value of 100 ppm represented $\sim 20\%$ coverage of the iron sites on the surface of Fe_3O_4 and therefore, the measured uptakes corresponded to surface coverages of this order extending up to the formation of a few monolayers of sulphide. Thiophene was slightly more effective in preventing deposition than the simpler sulphur compounds, possibly due to its larger molecular area blocking adjacent sites. The continuing inhibition of acetone decomposition was considerably greater than would have been obtained by the associated sulphidation alone. The extents of adsorption of the poison would be pressure dependent, so that it was not surprising that at low partial pressures

(e.g. 0.19 uatm thiophene) the surface coverage was insufficient to block critical adsorption sites.

With Cr_2O_3 , neither sulphiding nor sulphur-containing gas phase additives, which also sulphided the surface, inhibited acetone deposition. This reflected the different mechanism involved in carbon deposition on this oxide such that whether the surface anion was either oxygen or sulphur, did not affect either acetone adsorption or the subsequent decomposition of the adsorbed molecules.

The reaction between acetone and preoxidised 20/25/Nb stainless steel was catalysed primarily by iron. It would have been anticipated, therefore, as observed that it would have been inhibited also by sulphur poisoning. However, the influence of sulphur was not so marked as for Fe_3O_4 . The smaller amount of deposition on the steel catalysed by the chromium-containing oxides would not have been affected significantly by sulphur poisoning, as demonstrated for Cr_2O_3 . These reactions would account probably for the small carbon uptakes always observed, even when that principally responsible for deposition was inhibited. Sulphiding was effective initially as again this inhibited the formation of the catalytic intermediaries. The decreased protection on extended exposure to the carbon dioxide containing environment was not caused by sulphur removal. This resulted probably from outward iron diffusion from the underlying steel to form a surface oxide layer and the resulting generation of catalysts for acetone decomposition. High partial pressures of sulphur additives to the gas phase, as on Fe_3O_4 , again resulted in sulphide formation. However, lower partial pressures, which prevented deposition on Fe_3O_4 were not effective in poisoning the oxidised steel surface possibly because absorptive bonding was less strong on the mixed (FeCrNi) spinel than on Fe_3O_4 .

Conclusions

- (1) The heterogeneous decomposition of acetone by Fe_3O_4 , at 600 and 700°C resulting in carbon deposition, was reduced significantly, and in some instances prevented, by sulphur poisoning. Two procedures examined were prior sulphiding and the continuous addition to the gas phase of either thiophene, H_2S , SO_2 or COS . These inhibited the formation of the catalytic intermediates responsible for deposition either by preferential adsorption poisoning active surface sites or by oxide conversion to $\text{Fe}_{1-\text{N}}\text{S}$. Thiophene was the most effective additive as its larger molecular area than the simple sulphur compounds enhanced surface active site blockage.
- (2) Active decomposition on Cr_2O_3 at 600°C was not diminished either by prior sulphiding or sulphur bearing gaseous additives, which reflected the different reaction mechanism than with Fe_3O_4 .

- (3) The effectiveness of these procedures to inhibit acetone decomposition by an oxidised 20% Cr/25% Ni/niobium stabilised stainless steel, at the same temperatures, reflected the behaviour of the two oxides which were representative principal constituents of the scale on the steel. Prior sulphiding reduced deposition for a limited period until new catalytic intermediates were generated by the simultaneous oxidation of the steel by the carbon dioxide carrier gas. Deposition was decreased throughout the exposure by sulphur bearing gaseous additives, whose effectiveness increased with partial pressure.

Acknowledgements

We gratefully acknowledge the analytical work carried out by A. Parker, G.S. Spicer, A. Mead and D.J. Darke, and for detailed discussions with Dr. J.E. Antill.

Literature Cited

1. Campion, P.J., "Gas chemistry in nuclear reactors and large industrial plant"; Dyer A. Ed; Heyden, London, 1980, 53.
2. Bennett, M.J.; Faircloth, R.L.; Firth, R.J.; Houlton, M.R.; Norwood, K.S.; Prior, H.A. "Gas chemistry in nuclear reactors and large industrial plant"; Dyer A. Ed; Heyden, London, 1980, 81.
3. Bennett, M.J.; Chaffey, G.H.; Langford, A.J.; Silvester, D.R.V. UKAEA Report AERE-R7407; HMSO, London, 1973.
4. Baker, R.T.K.; Harris, P.S. "Chemistry and Physics of Carbon", Walker Jr., P.L.: Thrower, P.A. Eds; M. Dekker, New York, 1978, 14, 83.
5. Bennett, M.J.: Price, J.B. J. Mater. Sci. 1981, 16, 170.
6. British Patents 629,211 (1949); 698,121 (1953).
7. Karcher, W.; Glaude, P. Carbon, 1970, 9, 617.
8. Maxted, E.B. Advances in Catalysis, 1951, 3, 129.

RECEIVED June 28, 1982.

Influence of Total Pressure and Hydrogen:Hydrocarbon Ratio on Coke Formation over Naphtha-Reforming Catalyst

NORA S. FIGOLI, JORGE N. BELTRAMINI, AMADO F. BARRA,
ELOY E. MARTINELLI, MARIO R. SAD and JOSÉ M. PARERA

Instituto de Investigaciones en Catálisis y Petriquímica-INCAPE-Santiago del Estero
2654, 3000 Sante Fe, Argentina

The decreasing of the total pressure and of the hydrogen to naphtha ratio produces the increment of the coke formation over Pt/Al₂O₃. Critical values below which there is a great increment of the amount of coke and its degree of polymerization exist. For a given feed the catalyst deactivation is a function of the deposited coke obtained either by diminution of the pressure or of the hydrogen to naphtha ratio. A great carbon deposition -mainly on the metal- is observed during the first hours of operation, and later a slow deposition -mainly on the alumina- continues. When the soluble fraction of the coke is extracted with solvents, a C to H ratio 0.79 is obtained.

The objectives of the catalytic reforming of naphtha are to increase the naphtha octane number (petroleum refination) or to produce aromatic hydrocarbons (petrochemistry). Bifunctional catalysts that promote hydrocarbon dehydrogenation, isomerization, cracking and dehydrocyclization are used to accomplish such purposes. Together with these reactions, a carbon deposition which deactivates the catalyst takes place. This deactivation limits the industrial operation to a time which depends on the operational conditions. As this time may be very long, to study catalyst stability in laboratory, accelerated deactivation tests are required. The knowledge of the influence of operational conditions on coke deposition and on its nature, may help in the efforts to avoid its formation.

The influence of the total pressure and hydrogen to naphtha molar ratio on the amount and nature of the coke deposited on a monometallic bifunctional catalyst was studied by means of a standardized catalyst test.

0097-6156/82/0202-0239\$06.00/0
© 1982 American Chemical Society

Experimental

Catalyst. A Pt/Al₂O₃-Cl catalyst containing 0.375% Pt and 0.87% Cl was used. It was prepared impregnating with H₂PtCl₆ samples of CK 300 alumina from Ketjen following the method of Castro et al. (1). The support surface area was 200 m²/g and the catalyst had 90% metal dispersion.

Catalyst Tests. They were performed in a bench scale equipment that was described elsewhere (2). Octane number (RON) was taken as a measure of activity and liquid yield ($\eta_{C_5}^+$) as a measure of selectivity. These properties, the percentage of aromatics in the liquid (%Ar_L) and the percentage of C₁-C₃ were calculated from chromatographic analysis data, as previously described (2).

The adopted standard test (3) consisted in the operation of the catalyst at normal conditions (P = 30 atm; H₂:naphtha molar ratio = 8) during seven hours (period I). Then pressure and H₂:naphtha ratio were decreased during twenty hours (period II). Finally, pressure and H₂:naphtha ratio were returned to initial values for seven hours (period III). All the test was carried out at 515°C and WHSV = 6 h⁻¹.

An example of the test is shown in Figure 1. Two important types of values can be obtained that are useful for investigating catalyst deactivation by coke:

a) The differences between the values obtained during periods III and I: modification in RON (Δ RON), in $\eta_{C_5}^+$ ($\Delta\eta_{C_5}^+$), etc., due to the accelerated deposition of coke.

b) The slope of change of RON, $\eta_{C_5}^+$, etc. during period II produced by the continuous deposition of coke.

The coke content of the catalysts was measured by combustion-volumetry after the run. The differential thermal analysis (DTA) of the used catalysts was performed with an Aminco Thermoanalyzer using oxygen as dynamic gas. The soluble fraction of coke from used catalysts was extracted with solvents and the solutions were analyzed by several techniques in order to determine their nature.

Feed. Pure La Oxígeno hydrogen was used. It was previously purified by passage through a deoxygenating copper bed and dehydrated passing through a Molecular Sieves 4 A bed.

The naphtha had the following properties:

Density: 0.736 g/ml

Mean Molecular Weight: 109

Boiling point range: 65-147°C

RON: 59

Composition (weight %): Paraffins: 64.2

Naphthenics: 24.2

Aromatics: 11.6

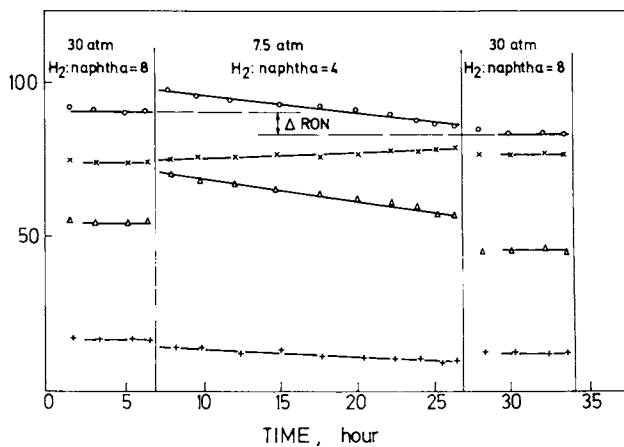


Figure 1. Diagram of a standard test, showing modifications of RON (○), ηC_5^+ (×), % Ar_L (△), and $C_1/C_1 + C_2 + C_3 \times 10^2$ (+). Conditions: temperature, $515^\circ C$, and $WHSV, 6 h^{-1}$.

Results

Influence of Pressure. In order to study the influence of total pressure on coke deposition, the operating pressure was varied between 2 and 20 atm in period II, keeping the other conditions previously described as standard. So, when referring to an experiment at 2 atm pressure, it is meant beginning at 30 atm and H₂:naphtha molar ratio 8 for seven hours, then decreased and maintained the pressure at 2 atm and H₂:naphtha molar ratio at 4 for twenty hours, and coming afterwards back to the initial conditions. The results are presented in Table I.

It may be observed that decreasing the pressure during period II, increments in the amount of coke deposited on the catalyst and in the negative differences ΔRON and $\Delta\%Ar_L$ between I and III are produced. Lower pressures produce lower increments in $\Delta\eta C_5^+$. Correlations between the carbon percentage on the catalysts, pressures and ΔRON were derived using the least square method. Linear, exponential, power law and semilog relationships were considered in all cases, taking that with the best correlation coefficient (r^2) as the most accurate one.

The best correlation obtained for the carbon percentage and pressure was:

$$\%C = 7.71 P^{-0.96} \quad r^2 = 0.95 \quad (1)$$

The amount of carbon deposited on the catalyst modified ΔRON according to:

$$\Delta\text{RON} = 2.50 e^{0.39 (\%C)} \quad r^2 = 0.97 \quad (2)$$

The relation between pressure during period II and ΔRON was:

$$\Delta\text{RON} = 11.76 e^{-0.98 P} \quad r^2 = 0.99 \quad (3)$$

The slope of decay of RON during II was higher when a lower pressure was used and its relationship was:

$$\text{Slope of RON} = -1.52 e^{-0.12 P} \quad r^2 = 0.99 \quad (4)$$

The differential thermal analysis of the different catalysts is shown in Figure 2. Two different combustion zones can be observed, which may be considered as produced by the combustion of substances of different nature: one zone from 123 to 369°C and the second one from 369 to 555°C. The first zone is not very well defined: different peaks can be seen and there is an increase of the zone when the pressure is decreased.

The second zone appears as more sensitive to the pressure change. The pressure decreasing produced a great increment of this zone and particularly of the peaks appearing at high combustion temperatures.

It is important to observe that modifications of pressure above 7.5 atm did not produce a very significative change in the amount and nature of the coke. But very important changes were produced when pressure was below 7.5 atm, being specially modified

Table I
Influence of Pressure on Catalyst Behavior During a Standard Test

Pressure (atm)	Carbon (%)	Slope during II					Difference (III - I)				
		RON	% Ar _L	C ₁ /C ₁ +C ₂ +C ₃ x10 ³	ΔRON	Δ% Ar _L	ΔrC ₅ ⁺	Δ(C ₁ /C ₁ +C ₂ +C ₃)			
2	4.00	-0.99	-1.6747	-7.0	-10.19	-13.60	1.63	-0.016			
5	2.34	-0.91	-1.0461	-2.5	-7.46	-8.28	1.94	-0.026			
7.5	0.81	-0.58	-0.7384	-1.9	-5.16	-6.81	3.00	-0.035			
10	0.66	-0.50	-0.6583	-1.8	-4.28	-5.50	3.14	-0.046			
15	0.60	-0.29	-0.3593	-1.5	-2.65	-2.32	4.70	-0.075			
20	0.54	-0.11	-0.0035	-1.3	-1.75	-1.65	8.13	-0.103			

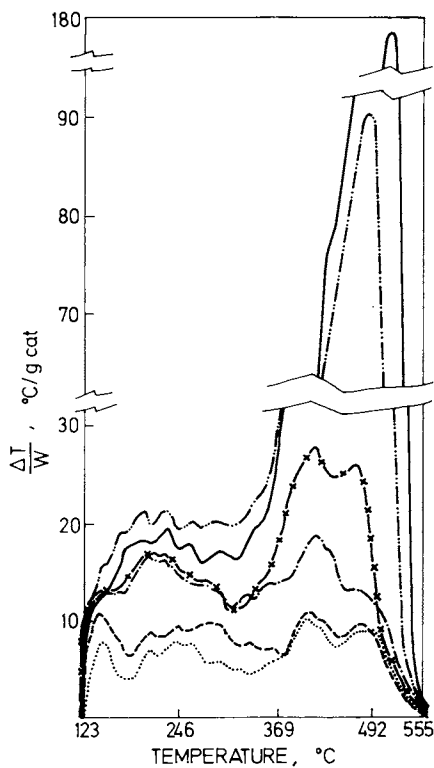


Figure 2. Differential thermal analysis of catalysts used under different pressures. Key to pressure (atm): $\cdot\cdot\cdot$, 20; ---, 15; $\cdot\cdot\cdot$, 10; $-\times-\times-$, 7.5; $-\cdot\cdot\cdot$, 5; and —, 2. Conditions: heating rate, 24 °C/min; and oxygen flow rate 60 cm³/min.

the amount of coke that burns at higher temperatures which is more stable and difficult to eliminate. The critical pressure value seems to be 7.5 atm, as it can be seen in Figure 3.

Influence of hydrogen-hydrocarbon ratio. Molar values from 8 to 2 and a pressure of 10 atm during period II were used, being the results presented in Table II. More severe conditions, as smaller hydrogen to naphtha ratios, meant more carbon deposition and higher slopes of decrease of RON and %Ar_L. Comparing the catalyst behavior before and after the severe period, it may be seen that when smaller the used ratios, higher was ΔRON as well as the Δ%Ar_L and a smaller increment in ΔηC₅⁺ was noticed.

As when pressure modifications were studied, correlations between %C, ΔRON and H₂:naphtha molar ratio, were derived:

$$\%C = 4.72 (H_2:naphtha)^{-1.28} \quad r^2 = 0.97 \quad (5)$$

$$\Delta RON = 3.05 e^{0.44 (\%C)} \quad r^2 = 0.97 \quad (6)$$

$$\Delta RON = 11.88 (H_2:HC)^{-0.67} \quad r^2 = 0.97 \quad (7)$$

$$\text{Slope of RON during II} = -1.18 e^{-0.21 (H_2:naphtha)} \quad r^2 = 0.99 \quad (8)$$

When the carbon nature was studied by differential thermal analysis, two zones appeared clearly distinctive, as shown in Figure 4. In the first zone there were little differences between the catalysts operated at different hydrogen to naphtha ratios, being greater the differences in the second. Smaller ratios increased the peaks of the second zone and also produced a further increase on the ones of higher combustion temperatures.

As when considering the effect of pressure, a critical value for hydrogen to naphtha ratio -approximately 3- may be pointed out, as shown in Figure 5.

Discussion

The amount and nature of coke deposited on the catalyst is affected by several factors, as the operational conditions (pressure, H₂:naphtha ratio, temperature and WHSV) and the catalyst nature, such as its chlorine content (4).

Studying the influence of total pressure and hydrogen to naphtha ratio, it was found that there are critical values that must be avoided during operation in order to prevent greater and more polymerized coke deposits, which make decrease the catalyst activity and modify its selectivity, as had been shown in Figures 3 and 5. If the data from DTA analysis is considered, it may be also noticed that when the carbon deposit is higher than 1%, there is a great increment of the peaks which corresponds to a more stable deposit.

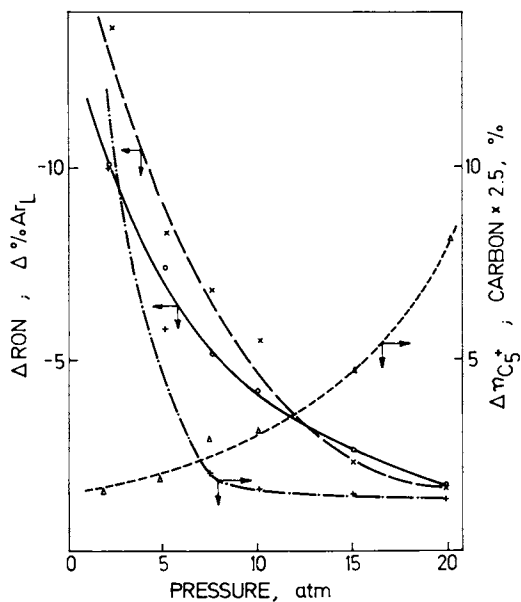


Figure 3. Modifications of ΔRON ($-o-$), $\Delta\% Ar_L$ ($-x-$), and $\Delta\eta_{C_5^+}$ ($--\Delta--$) and percentage of carbon on catalysts ($- \cdot - + - \cdot -$) used under different pressures during the standard test. Conditions: temperature, $515^\circ C$; and $WHSV$, $6 h^{-1}$.

Table II
Influence of Hydrogen:Naphtha Molar Ratio on
Catalyst Behavior During a Standard Test

H ₂ :naphtha molar ratio	Carbon (%)	Slope during II			Difference (III - I)			
		RON	% Ar _L	C ₁ /C ₁ +C ₂ +C ₃ x10 ³	ΔRON	Δ% Ar _L	Δ(C ₁ /C ₁ +C ₂ +C ₃)	
2	2.38	-0.84	-1.4359	-7.8	-8.31	-14.20	1.78	-0.018
3	1.00	-0.57	-0.8112	-6.0	-5.3	-6.70	2.50	-0.039
4	0.66	-0.50	-0.6583	-1.8	-4.28	-5.50	3.14	-0.046
8	0.38	-0.22	-0.4777	-1.2	-3.2	-4.93	5.40	-0.080

**American Chemical
Society Library**

1155 16th St. N. W.

Washington, D. C. 20036

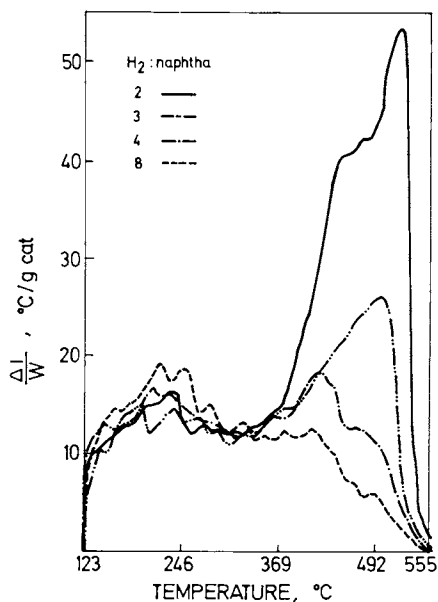


Figure 4. Differential thermal analysis of catalysts used under different H_2 :naphtha molar ratios. Conditions: heating rate, $24^\circ C/min$; and oxygen flow rate $60 cm^3/min$.

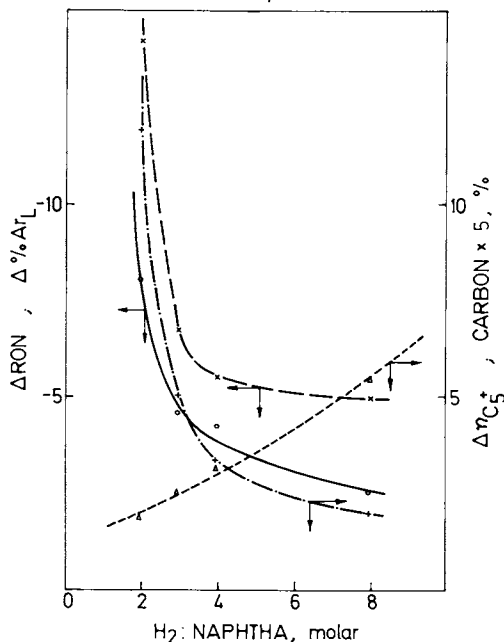


Figure 5. Modifications of ΔRON ($-o-$), $\Delta \% Ar_L$ ($-x-$), $\Delta \eta C_5$ ($--\Delta--$), and percentage of carbon on catalysts ($- \cdot - + - \cdot -$) used under different H_2 :naphtha molar ratios during the standard test. Conditions: temperature, $515^\circ C$; and $WHSV$, $6 h^{-1}$.

Considering that this catalyst is a bifunctional one, many authors have studied whether the carbon deposition is produced on the metallic or on the acidic function. Barbier et al. (5) studying coke formed from cyclohexane, found two peaks in their temperature programmed oxidation studies, which they stated belong to carbon deposited over the metallic and over the acidic function of the catalyst. We obtained similar results by DTA analysis. Using an Al_2O_3 catalyst with the same chlorine content than $\text{Pt}/\text{Al}_2\text{O}_3$ in the standard test, the thermogram showed only one peak, the one of the second zone, as shown in Figure 6. As the pure alumina had not metallic function, it can be supposed that the peaks of the first zone correspond to carbon deposited on the metallic function, whereas the peaks of the second zone, correspond to carbon deposited on the acidic function.

The values $C_1/C_1+C_2+C_3$ shown in Tables I and II can be considered as a way to compare hydrogenolysis and hydrocracking (or in other words metallic and acidic functions), because it is known that C_1 is formed through hydrogenolysis on the metallic function and C_2 and C_3 mainly through hydrocracking on the acidic function.

During coke accelerated deposition (period II) $C_1/C_1+C_2+C_3$ decreased (negative slope), being the decrease higher for more severe conditions, and the difference $\Delta(C_1/C_1+C_2+C_3)$ (between periods III and I) negative. This means that coke on the catalyst principally diminishes the hydrogenolysis that occurs on the metallic site. Looking back to Figures 2 and 4 it can be seen that for more severe conditions, the ratio between the first and the second zone is lower. If the first peak corresponds to coke on the metallic site, the lower value may be because the metallic component is almost completely covered and the severity increases the deactivation of the acid part C_2+C_3 producing then a smaller difference $\Delta(C_1/C_1+C_2+C_3)$. It must also be taken into account that the number of metallic sites is much lower than the number of acid sites (considering a catalyst with 0.37% Pt).

It has been shown that more severe conditions mainly increase the carbon of the second zone, which corresponds to the one on the acidic function. It can be considered that the effects of a higher severity may be assimilated with larger periods of operating time, as by DTA we have found the same kind of coke from accelerated deactivation tests and long time operation under normal conditions. Our results are consistent with Gates et al. (6): for long time deactivation, carbon is deposited on the acidic function of the catalyst.

The differences in RON (ΔRON), before and after the severe period is related to the percentage of carbon on the catalyst, independently if the severity was achieved changing pressure or H_2 :naphtha ratio. This is shown in Figure 7, where it may be seen that also the slope of deactivation during II is only related to the amount of carbon. The curves in Figure 7 do not go to the origin, showing that there is a very rapid initial coke deposition

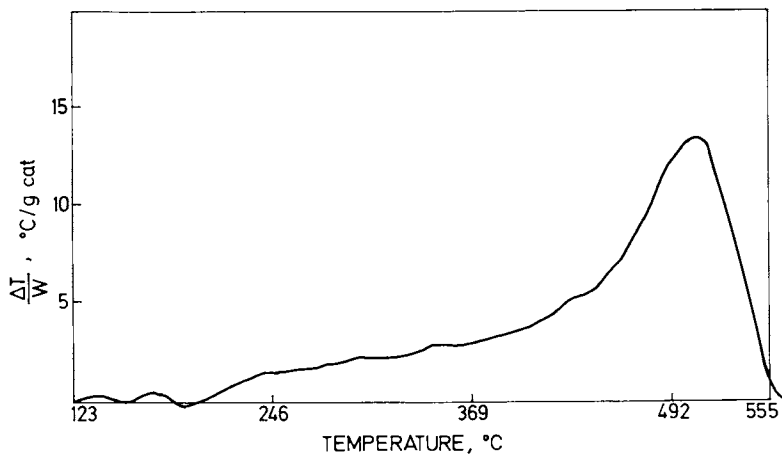


Figure 6. Differential thermal analysis of an alumina used during 30 h. Conditions: pressure, 30 atm; H_2 :naphtha molar ratio, 8; temperature, 515°C; and WHSV, 6 h^{-1} .

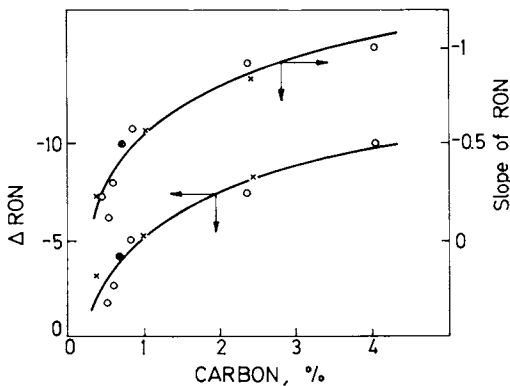


Figure 7. Influence of different amounts of carbon produced through modifications of pressure and H_2 :naphtha ratio of RON and on the slope of RON during Period II. Key: \circ , pressure; and \times , H_2 :naphtha ratio.

which amount is approximately 0.2-0.4%. This fact was checked studying the amount of carbon deposited under normal operational conditions as a function of time, as shown in Figure 8.

Coke deposition on Pt/Al₂O₃ is a very complicate phenomena. There is an initial rapid deposition that mainly affects the metallic function. That initial deposition produces a decreasing of the great initial hydrogenolytic activity. Tennison (7) also stated that the initial coke deposition is on the metal crystallites. Then the deposition is slower and at longer times or more severe conditions, the deposition of coke tends to occur on the acidic function, partly because the metallic function is almost completely covered, even it is not poisoned, as coke is not a poison for the reaction. It must be remembered that the catalyst has only 0.37% metal on a high surface area alumina. The coke increase its degree of stability with the severity of the operational conditions.

The nature of coke was studied by extraction of its soluble fraction with different solvents (benzene-methanol (8) and carbon tetrachloride) with a Soxhlet. After the evaporation of the solvent at room temperature, the extract was analyzed by ¹HNMR, IR and mass spectrometry. The soluble fraction of the coke is the less polymerized, and can be taken as containing the precursors that determine coke composition.

By ¹HNMR and applying the methods of Clutter et al. (9) and Herod et al. (10) the percentage of the different types of carbons, as well as the mean molecular weight and C/H ratio for a catalyst operated during a standard test (P = 10 atm, H₂:naphtha (molar) = 4 during II) were determined. The results are shown in Table III.

Table III
Percentage of Different Carbon Types, Mean Molecular
Weight and C/H of the Soluble Fraction of Coke from
a Catalyst Operated During a Standard Test

PM	alkylic carbon, %	naphthenic carbon, %	aromatic + olefinic carbons, %	C/H
227.1	38.5	21.6	39.9	0.79

The presence of the different carbon types was confirmed by IR analysis as has been also done by Bakulin et al. (11). In addition vibrations in the 560-970 cm⁻¹ region indicated the presence of condensed aromatics with alkylic substituents as shown by Eberly et al. (12).

The mass spectrometric analysis of the extracted coke showed components of molecular weights between 100 and 300.

Analyzing the results obtained through different techniques, of the coke soluble fraction, we can say that coke precursors are

molecules of an approximately molecular weight 220, including condensed aromatics or aromatics plus naphthenics joined by alkylic chains, with a general formula $C_{17}H_{22}$.

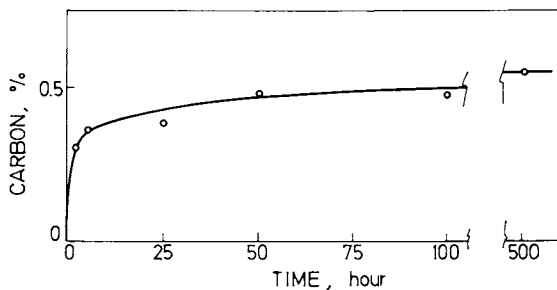


Figure 8. Percentage of carbon over a catalyst used during different periods of time. Conditions are the same as in Figure 6.

Literature Cited

1. Castro, A.A.; Scelza, O.A.; Benvenuto, E.R.; Baronetti, G.T.; Parera, J.M. 6th Iberoamerican Symposium on Catalysis, Rio de Janeiro, Brazil, 1978, Paper No. 55.
2. Sad, M.R.; Fígoli, N.S.; Beltramini, J.N.; Jablonski, E.L.; Lazzaroni, R.A.; Parera, J.M. *J. Chem. Tech. Biotechnol.* 1980, **30**, 374.
3. Fígoli, N.S.; Sad, M.R.; Beltramini, J.N.; Jablonski, E.L.; Parera, J.M. *Ind. Eng. Chem. Prod. Res. Dev.* 1980, **19**, 545.
4. Parera, J.M.; Fígoli, N.S.; Jablonski, E.L.; Sad, M.R.; Beltramini, J.N. "Catalyst Deactivation"; Delmon, B.; Froment, G.F. (eds.); Elsevier Publ. Co.: Amsterdam, 1980; p. 571.
5. Barbier, J.; Marecot, P.; Martin, N.; Ellassal, L.; Maurel, R. "Catalyst Deactivation"; Delmon, B., Froment, G.F. (eds.); Elsevier Publ. Co.: Amsterdam, 1980, p. 53.
6. Gates, B.C.; Katzer, J.R.; Schuit, G.C.A.; "Chemistry of Catalytic Processes"; McGraw-Hill: New York, 1979, p. 287.
7. Tennison, S.R. *Chem. in Brit.* 1981, **17** (11), 536.
8. Bodzek, D.; Marzek, A. *Fuel* 1981, **60**, 47.
9. Clutter, D.R.; Petrakis, L.; Stenger, R.L.; Jensen, R.K. *Anal. Chem.* 1972, **44** (8), 1395.
10. Herod, A.A.; Ladnev, W.R.; Snape, C.E. *Phil. Trans. R. Soc. Lond.* 1981, **A 300**, 3.
11. Bakulin, R.A.; Levinter, M.E.; Unger, F.G. *Neftekhimiya* 1978, **18** (1), 145.
12. Eberly, P.E.; Kimberlin, R.N.; Miller, W.H.; Drushel, H.V. *Ind. Eng. Chem. Proc. Des. and Dev.* 1966, **5**, 2.

RECEIVED June 28, 1982.

Reactivity of Surface Carbon on Nickel Catalysts: Temperature-Programmed Surface Reaction with Hydrogen and Water

J. G. McCARTY, P. Y. HOU, D. SHERIDAN, and H. WISE

SRI International, Menlo Park, CA 94025

The nature of the carbon deposits formed on an alumina-supported nickel catalyst have been characterized by their reactivity with H_2 and H_2O during temperature-programmed surface reaction (TPSR). Carbon deposits formed by exposure to hydrocarbons and carbon monoxide exhibit, depending primarily on the temperature during deposition, seven reactive carbon states during TPSR with 1-atm H_2 , including two very reactive states of chemisorbed carbon, a carbon film, nickel carbide, and two types of filamentary carbon. Filamentary carbon was identified by transmission and scanning electron microscopy, and Ni_3C was identified from x-ray diffraction measurements.

These results suggest that the deactivation of nickel catalysts is due to the accumulation of a carbonaceous film at low temperature, the rapid formation of filamentary carbon at moderate temperatures, and the formation of encapsulating carbon layers at very high temperature.

Carbon can exist on the metal surfaces of nickel catalysts in a variety of forms. Hydrocarbon exposure to nickel crystallites at elevated temperature (> 700 K) can rapidly produce a mass of long-growing carbon filaments (1, 2) as identified in numerous experiments analyzed by transmission electron microscopy (TEM). Yet very reactive forms of surface carbon can exist, since carbon atoms chemisorbed on nickel surfaces apparently play a central role in the mechanism of several nickel-catalyzed reactions, such as hydrocarbon synthesis, (3, 4, 5) hydrocarbon steam reforming, (6, 7) and hydrogenolysis (8).

In a previous study (9) we used temperature-programmed surface reaction (TPSR) with 1 atm hydrogen to determine the

0097-6156/82/0202-0253\$08.50/0
© 1982 American Chemical Society

reactivity of carbon deposited on alumina-supported nickel. In that study several forms of very reactive carbon were distinguished by their relative reactivity as determined by the temperature at maximum gasification rate with hydrogen. The two most reactive forms of surface carbon (α' , α) were attributed to chemisorbed carbon atoms followed in order of reactivity by the initial layers of nickel carbide (γ) and finally a layer of amorphous carbon (β). These carbon forms were deposited by exposure to both CO and C₂H₄ over a temperature range from 473 K to 750 K.

In recent work, supported by the Fossil Fuels Division of the U.S. Department of Energy, we have extended the range of exposure conditions for carbon deposition by CO and C₂H₄ decomposition on Ni/Al₂O₃ surfaces and more fully explored the nature of such deposits. The TPSR studies with 1 atm H₂ as reactant were also extended by studies with 0.03 atm H₂O in He diluent as the reactant gas. The bulk carbon deposits produced by CO or C₂H₄ exposure were also examined with x-ray diffraction and transmission and scanning electron microscopy so that the reactivity of each form of carbon was identified with its morphology.

Experimental Details

Microreactor System for TPSR. The reactivity of carbon deposits on reforming catalysts has been studied with a quartz microreactor system using the TPSR technique (Figure 1). A small bed (10 to 40 mg) of a powdered catalyst is placed on the porous fritted disk of a 1-cm³ quartz microreactor. The catalyst bed can be heated up to 1375 K by radiation and convection from a 12-mm by 25-mm coil of 0.81-mm-diameter Nichrome wire, which is suspended around the microreactor. The wire is electrically heated with a programmable DC power supply that is controlled by a custom-designed temperature programmer. A stream of dry N₂ purges air from contact with the heater wire to extend its lifetime and to cool the reactor. The catalyst bed can be cooled from 1375 K to below 500 K in less than one minute, and when a steady stream of nitrogen is passed through a Dewar flask of liquid nitrogen, the bed can be cooled to below 180 K. The programmer can heat the reactor at linear from 0.1 to 4 K s⁻¹. The catalyst bed temperature is measured with an unshielded 0.075-mm Chromel-Alumel or 0.25-mm Pt-10% Rh/Pt thermocouple that penetrates the bed. The thermocouple output is compensated for ambient temperature with an Omega MCJ reference junction. The thermal response time of the catalyst bed thermocouple system is about one second.

The TPSR experiments were conducted at one atmosphere pressure with a stream of helium or reactive gas mixtures flowing through the catalyst bed. High purity reactant gases, including hydrogen, carbon monoxide and light hydrocarbons, could be blended with a helium carrier before introduction into the reactor. We purified the helium carrier by passing it through a bed of copper turnings at 573 K and then through a liquid N₂ cooled molecular

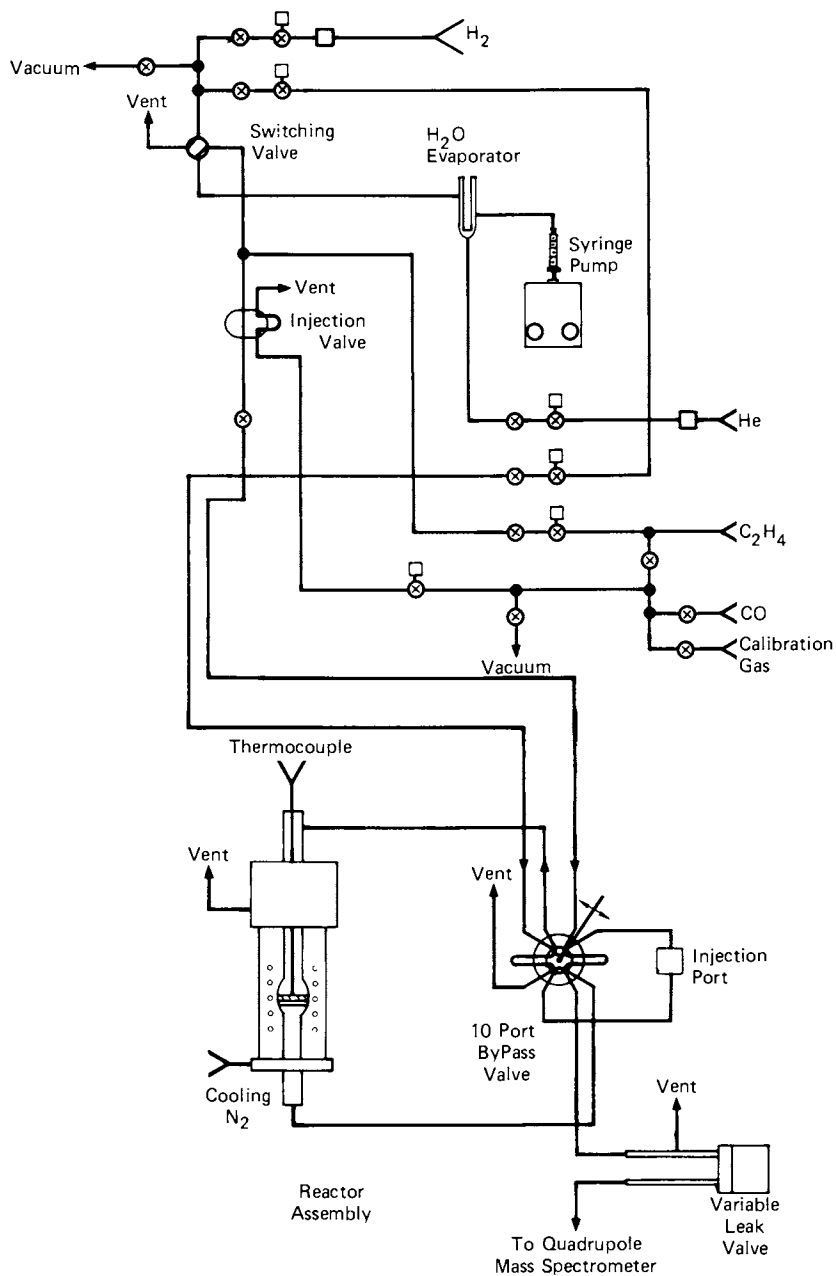


Figure 1. TPSR and pulsed flow system.

sieve trap. Hydrogen, initially 99.99% purity, was further purified by diffusion through a Ag/Pd alloy tube. The other reactant gas mixtures, 3.0-vol% CO in helium, 1.0-vol% C₂H₂ in helium were used as received from the supplier. Steam was generated at the desired rate by a special vaporizer fed by a syringe pump. Water was delivered through a syringe to a layer of glass thread wrapped around a glass cylinder located inside a larger concentric glass vessel. The feed rate of water was adjusted to attain the desired vaporization rate. A cartridge heater inside the cylinder provided the heat necessary for steady steam evaporation.

We continuously monitored the composition of the microreactor effluent gas with a quadrupole mass spectrometer (EAI Quad 300C) by sampling a small portion of the effluent gas stream with a variable leak valve (Granville Phillips). The pressure, indicated by a nude ionization gauge in the mass spectrometer chamber, was controlled at 9×10^{-7} torr with an automatic servo-controlled pressure controller (Granville Phillips). The mass spectrometer system was calibrated by injecting known amounts of pure gases into a He carrier stream. A conversion factor was obtained for each gas, giving quantitative expression of the TPSR rate data in terms of either concentration in the effluent gas or net reaction rate from the product of effluent concentration and carrier flow rate. In later experiments, 0.1-vol% argon was added (premixed) to the helium carrier as an internal standard for calibrating the mass spectrometer. The mass spectrometer could monitor up to eight individual ion mass peaks with an automatic mass peak selector (Vacuumetrics) and transmit the signal from selected mass fragments to recorders and an electronic integrator (Spectraphysics) or, more recently, to a laboratory microcomputer (Dual Systems). The mass spectrometer sensitivity during TPSR was about 30 ppm for H₂ and CO and 10 ppm for other gases. By carefully measuring the mass 32 peak, we kept the level of oxygen impurity in the pure H₂ and He carrier streams reaching the reactor always below 1 ppm and typically at 0.1 ppm.

TPSR Characterization of Deposited Carbon. In an experiment to analyze the TPSR characteristics of a carbon deposit, 15 to 35 mg of powdered (170/250 Tyler mesh) catalyst was placed on the porous disk of a quartz microreactor. Typically, a fresh sample of catalyst was reduced for 15 hr at 773 K in 1 atm flowing H₂ and a previously reduced catalyst was heated to 773 K for at least 1 hr before a TPSR experiment. Following reduction, the catalyst was flushed with pure He and cooled or heated to a predetermined carbon deposition temperature. Carbon was deposited by exposure to a stream of dilute hydrocarbon (typically 0.14-vol% C₂H₄) in helium using a special 10-port switching valve (Figure 1). Following carbon deposition, the catalyst was cooled to room temperature while the bed was flushed with pure He, and the He carrier (now in reactor by-pass mode) was replaced by the TPSR reactant gas stream (1-atm H₂ or 0.03-atm H₂O in He). After the

catalyst bed cooled to ambient temperature, the reactive gas was switched through the catalyst bed and temperature programming began.

During TPSR, the rate of gasification of the carbon deposit (as determined by continuous measurement of the effluent gas composition) was recorded as a function of time. The data are represented by the calculated gas production rate versus bed temperature as in conventional thermal analysis. TPSR analysis was performed for various conditions of exposure temperature, exposure duration, and exposure gas (CO, C₂H₄ or C₂H₂) for both 1-atm H₂ and 0.03-atm H₂O in He as the gasifying reactant.

Electron Microscopy. Some of the carbon produced on G-56H by C₂H₄ exposure has been associated with filamentary carbon growing from nickel crystallites through observations of deposited carbon using TEM and SEM. For TEM, samples were sandwiched between Formvar-coated 200-mesh nickel grids. Kodak electron image plates were exposed for 2 s at an accelerating voltage of 80,000 eV on a Philips 200 electron microscope. A magnification range of 3,000-200,000 diameters was used. For SEM, the samples were mounted in colloidal silver on microscope chucks and observed in the Cambridge Mark IIa SEM instrument. The magnification range was 100 to 50,000 diameters.

Catalysts. The nickel catalysts used in the TPSR studies G-56H and G-65, both were commercial (United Catalysts Incorporated) high metal-weight-loading catalysts with alumina supports. The 17-wt% Ni/Al₂O₃ catalyst (G-56H) had a relatively low metal surface area (4 m²/g Ni) but resisted sintering since it only lost 20% of its surface area after heating to 1273 K in 1 atm H₂. The 25-wt% Ni/Al₂O₃ (G-65) had a modest surface area (29 m²/g Ni) and contained some CaO (see Table I for a summary of the catalyst properties).

Table I
PROPERTIES OF NICKEL CATALYSTS

Catalyst	Support	Metal Loading	Total Surface Area (m ² /g cat)	Specific Metal* Area (m ² /g Ni)
G-56H/UCI	Al ₂ O ₃	17	-	4
G-65/UCI	Al ₂ O ₃ + CaAl ₂ O ₄	25	56	28

*The metal surface area was determined by adsorption of CO at 300 K presuming 1.1×10^{15} molecules CO/cm².

Results

Carbon Deposited on Nickel via C_2H_4 Exposure: TPSR with 1-atm H_2 . Carbon deposited on alumina-supported nickel (17 wt%) following ethylene exposure at various temperatures has a wide range of activity for reaction with H_2 (Figure 2). Different states of carbon are identified by maxima in the rate of CH_4 production. The temperature of the rate maximum (T_p) for a particular carbon state was generally found to be independent of both the amount of carbon in that state and the temperature of deposition. Thus T_p will be taken as characteristic of the reactive state of carbon^p in a deposit. Increasing the temperature of carbon depositions via C_2H_4 produced carbon states with higher T_p and hence lower reactivity with H_2 .

The TPSR (H_2) results did not differ significantly for either of the alumina-supported nickel catalysts as seen by T_p for the various carbon states (Table II). This was true for both TPSR (H_2) with 1-atm H_2 and TPSR (H_2O) with 0.03-atm H_2O in He.

Exposure of G-65 to aliquots of C_2H_4 in He at low temperature (573 K) produced several very reactive states of carbon. A small amount of the carbon deposit, i.e. the α' carbon state (9) with less than one monolayer coverage which is taken to be equal to the CO uptake at 300 K, had a peak temperature at 400 K and even had an observable CH_4 production rate at room temperature (300 K). The α' TPSR peak with H_2 was often obscured by a larger peak at 495 ± 20 K representing the α carbon state. Below 600 K the α state was populated up to about one monolayer before giving rise to another state (the γ carbon state) produced at very high C_2H_4 exposure (Figure 2).

Because the γ carbon state could be populated to an extent equivalent to 10 monolayers, it seems obvious that this state was a bulk state and was either bulk nickel carbide, Ni_3C , or some form of free carbon. Based on x-ray diffraction analysis, and the fact that this state was never populated at 773 K (Ni_3C is known to decompose above 600 K (10)), the γ carbon state was most likely Ni_3C . X-ray diffraction measurements of reduced 17-wt% Ni/Al_2O_3 always show metallic nickel lines even after deposition of large amounts of carbon at 773 K and higher temperatures. However, following long exposure to C_2H_4 at 573 K, the nickel x-ray diffraction lines showed a pronounced decrease in intensity. Diffraction lines for Ni_3C were not observed probably because most of the nickel crystallites were transformed into amorphous Ni_3C or crystallites of Ni_3C with small domain size (10).

Another form of carbon (the β carbon state) was also observed following the C_2H_4 exposure at 573 K to both the 25-wt% Ni/Al_2O_3 and 17-wt% Ni/Al_2O_3 catalysts. The β carbon state had a peak temperature that increased from 660 K at low coverage to 740 K at high coverage. The amount of carbon deposited into the β carbon state was observed not to exceed 4 monolayers. This state has not been positively identified, but its coverage is limited to a few

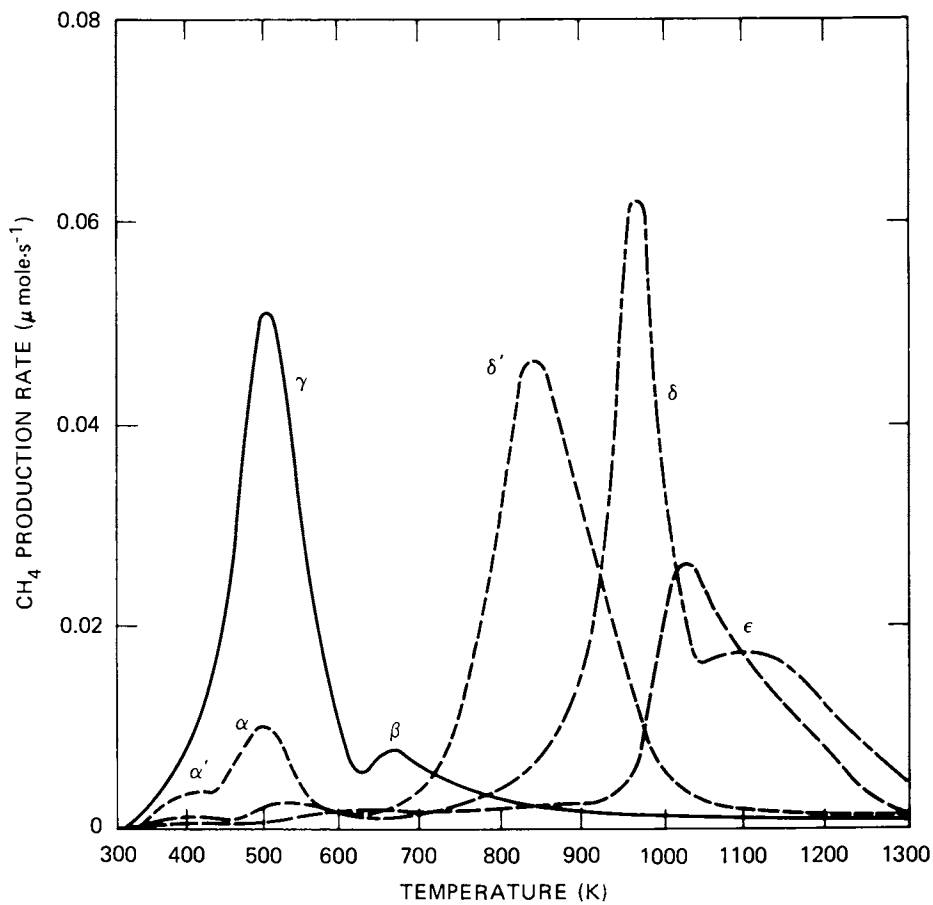


Figure 2. TPSR with hydrogen of carbon deposited on G-56H by exposure to ethylene. Key to carbon deposition temperature: —, 573 K; ---, 773 K; - · - · -, 1073 K; and - - - -, 1273 K.

Table II
TPSR CHARACTERIZATION OF CARBON DEPOSITED ON
NICKEL CATALYSTS FOLLOWING ETHYLENE EXPOSURE

Catalyst	Deposition Temperature (K)	Product/ Reactant Gas	Temperature (K) at Maximum Rate					Carbon	
			α'	α	β	δ'	δ		ϵ
G-65	573	CH ₄ /H ₂	400	480	685	-	-	1105	-
	773	CH ₄ /H ₂	395	505	625	850	-	1115	-
	573	CO ₂ /H ₂ O	-	-	630	865	-	-	1210
	773	CO ₂ /H ₂ O	-	-	575	830	-	-	1295
	773	CO ₂ /O ₂	-	-	-	-	895	-	1215
G-56H	573	CH ₄ /H ₂	-	505	655	-	-	-	-
	773	CH ₄ /H ₂	395	505	-	815	-	-	-
	873	CH ₄ /H ₂	-	510	-	835	950	1090	-
	973	CH ₄ /H ₂	385	510	-	850	955	1160	-
	1073	CH ₄ /H ₂	400	515	-	-	965	1130	-
	1273	CH ₄ /H ₂	-	525	-	-	1005	1150	-
	773	CO ₂ /H ₂ O	-	-	-	855	-	-	1220
	873	CO ₂ /H ₂ O	-	-	-	855	985	-	1255
	973	CO ₂ /H ₂ O	-	-	-	860	-	-	1280
	1073	CO ₂ /H ₂ O	-	-	-	860	945	-	-
	1273	CO ₂ /H ₂ O	-	-	-	830	935	1115	1280
1073	CO/H ₂ O	-	-	-	850	950	1070	-	
1273	CO/H ₂ O	-	-	-	815	925	1095	1265	

* δ' and δ states not resolved.

monolayers, and this makes it likely to be an amorphous carbon film (possibly with some hydrogen present (11)). The β carbon state is not populated at 873 K and higher temperature (see Table III, for 17-wt% Ni/Al₂O₃).

A number of less reactive forms of carbon are produced following C₂H₄ exposure to the Ni/Al₂O₃ catalysts at 773 K and higher temperature. At 773 K, (Figure 2) C₂H₄ exposure produces a bulk form of carbon (the δ' carbon state) with T_p at 875 ± 20 K. At 873 K two forms of carbon are produced (Figures 3 and 4) on the 17-wt% Ni catalyst following steady exposure to a stream of 1.0-vol% C₂H₄ in helium. One form is the δ' carbon state; the other form with T_p at 960 ± 15 K (also a bulk form) is the δ carbon state. Following C₂H₄ exposure at 973 K the δ' carbon state appears as a shoulder on the much larger peak representing the gasification of the δ carbon state (Figure 4) and at 1073 K this state is no longer present (Figures 4 and 5).

Both the δ' and δ states are identified with filamentous carbon by electron microscopy. Transmission electron micrographs of G-56H, after a relatively long exposure (10 min) to 0.1-atm C₂H₄ at 875 K, show the extensive formation of filamentous carbon (Figures 6a through 6e). The micrographs show a wide distribution of filament diameters from 70 Å to 1000 Å, with approximately bimodal distribution centered at 100 Å and 800 Å. The TEM micrographs are very similar to the classic carbon filament pictures published by Baker and Harris (1) and others (2), (12-19). The filaments appear to have narrow hollow interiors with low density (more transparent) cores and denser (less transparent) outer shells, and often have a very dense particle (presumably a nickel crystallite) at their tips (Figure 6b). The SEM results showed the entire catalyst particles are completely coated with a thick mat of carbon filaments (Figures 6c through 6e).

The electron micrographs of the 17-wt% Ni catalyst (G-56H) after 100-s exposure to 0.004-atm C₂H₄ at 1073 K are similar to the results obtained at 875 K, except that the extent of carbon formation at 1073 K was substantially less: ~ 3% weight gain versus > 50% weight gain at 875 K. The rate of filament growth was faster at 873 K than at 1073 K, and the average filament length was much longer at the lower temperature. Again, large (800 Å) and small (100 Å) carbon filaments were produced; however, many metal particles appeared to be completely encapsulated by carbon films.

At 1273 K, 1073 K, and 873 K (with > 100-s exposure) C₂H₄ exposure produces yet another form of carbon (ϵ carbon state) with very low characteristic reactivity with hydrogen (Figure 2). The peak temperature of the ϵ carbon state was about 1120 K, although the TPSR (H₂) peak produced by this state varied some ± 40 K and was often difficult to resolve from the peak produced by the δ carbon state.

A unique feature of the CH₄ production during TPSR with 1-atm H₂ at temperatures above 1100 K in general, and for the peak

Table III
 POPULATION OF TFSR STATES FOR CARBON DEPOSITED ON AN
 ALUMINA-SUPPORTED NICKEL CATALYST (G-56H)
 FOLLOWING ETHYLENE EXPOSURE

State	Identification	CH ₄ /H ₂ TFSR T _p (K) *	C ₂ H ₄ Exposure Temperature (K)			
			573	773	873	1073
α'	Chemisorbed carbon	410 ± 15	x	x	x	x
α	Chemisorbed carbon	480 ± 25	x	x	x	x
γ	Nickel carbide	550 [†]	x			
β	Beta carbon film	660 ± 30 [†]	x			
δ'	Filamentous carbon (TEM, SEM)	875 ± 20		x		
δ	Encapsulating carbon (TEM)	960 ± 15		x	x	x
ε	Platelet (?) carbon	1120 ± 20 ^{†,‡}		x	x	x

* Peak temperature (T_p) for heating rate = 0.9 K/s. The TFSR product is CH₄, the reactant is H₂.

[†] Increases with increasing coverage; T_p for low coverage limit.

[‡] Equilibrium limited for TFSR with H₂.

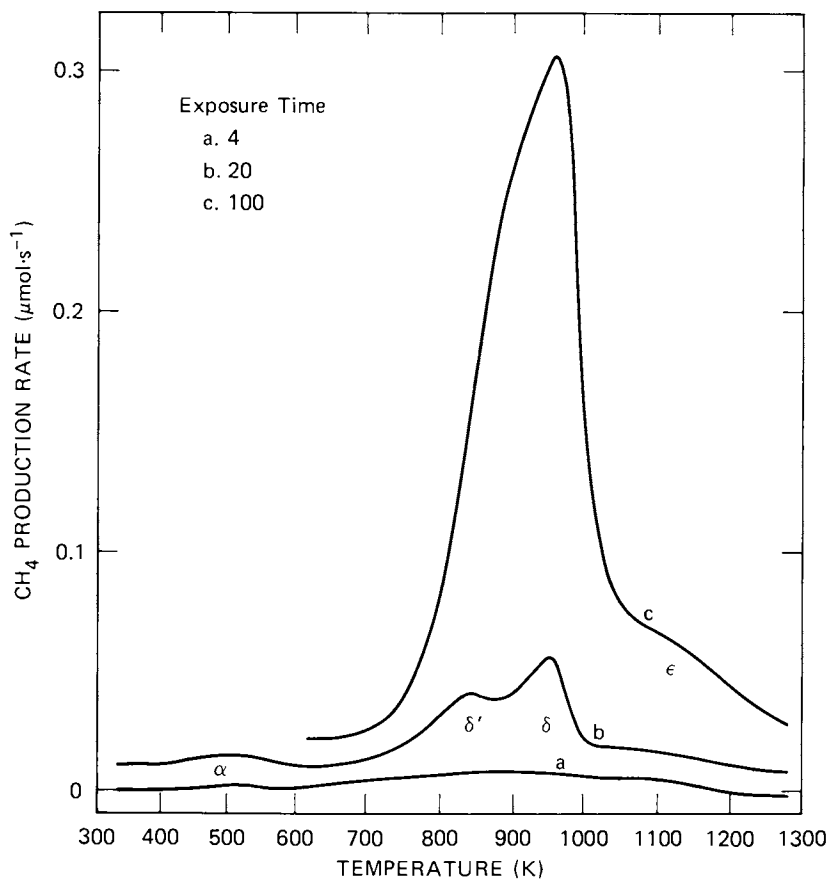


Figure 3. TPSR with hydrogen of carbon deposited on G-56H at 873 K by increasing exposure to ethylene.

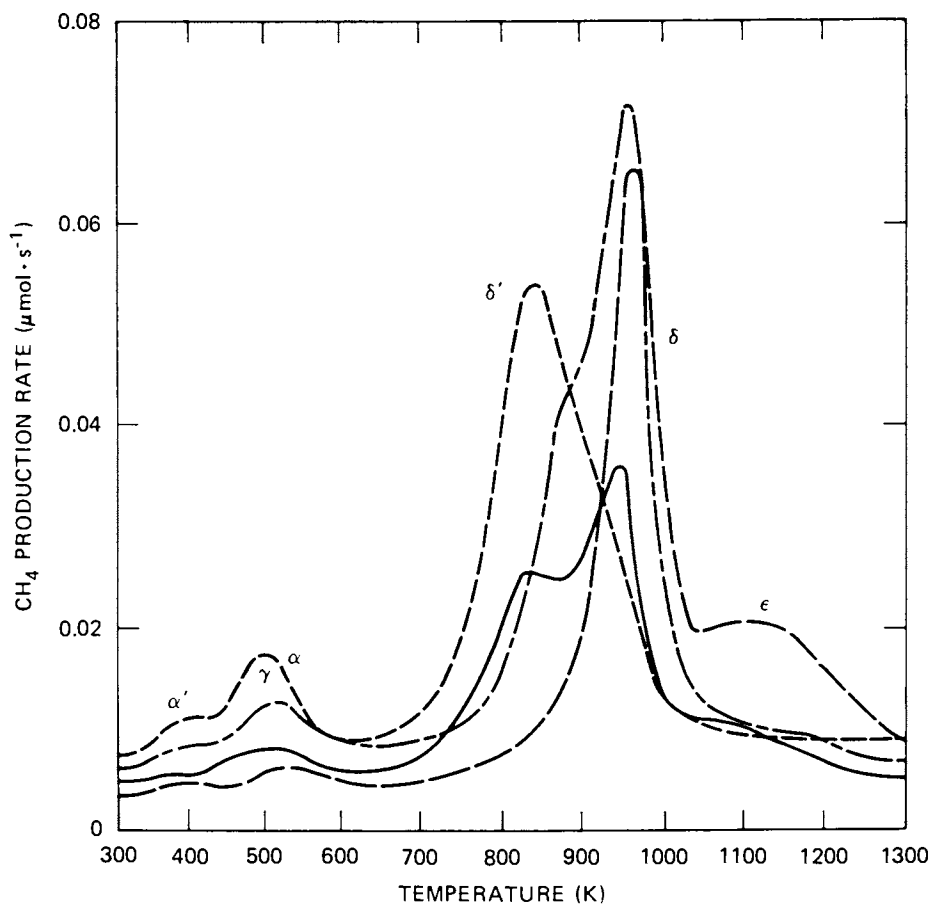


Figure 4. TPSR with hydrogen of the δ' carbon state deposited on G-56H by exposure to ethylene. Key to carbon deposition temperature: ---, 773 K; —, 873 K; — · —, 973 K; and — —, 1073 K.

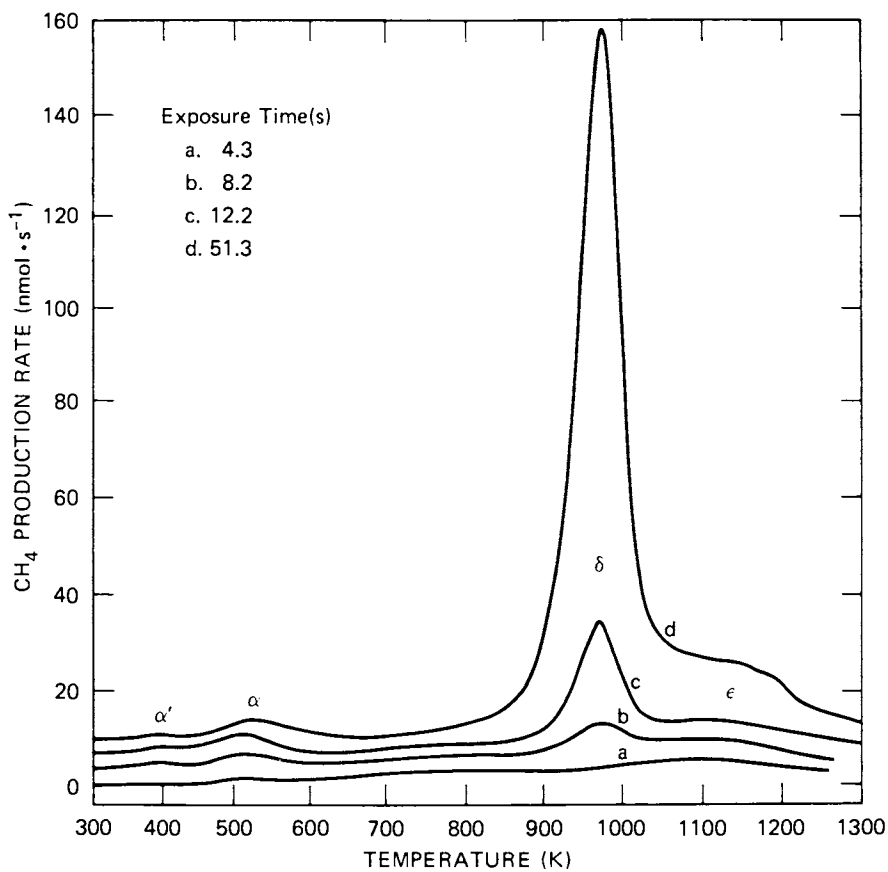


Figure 5. TPSR with hydrogen of carbon deposited on G-56H at 1073 K by increasing exposure to ethylene.

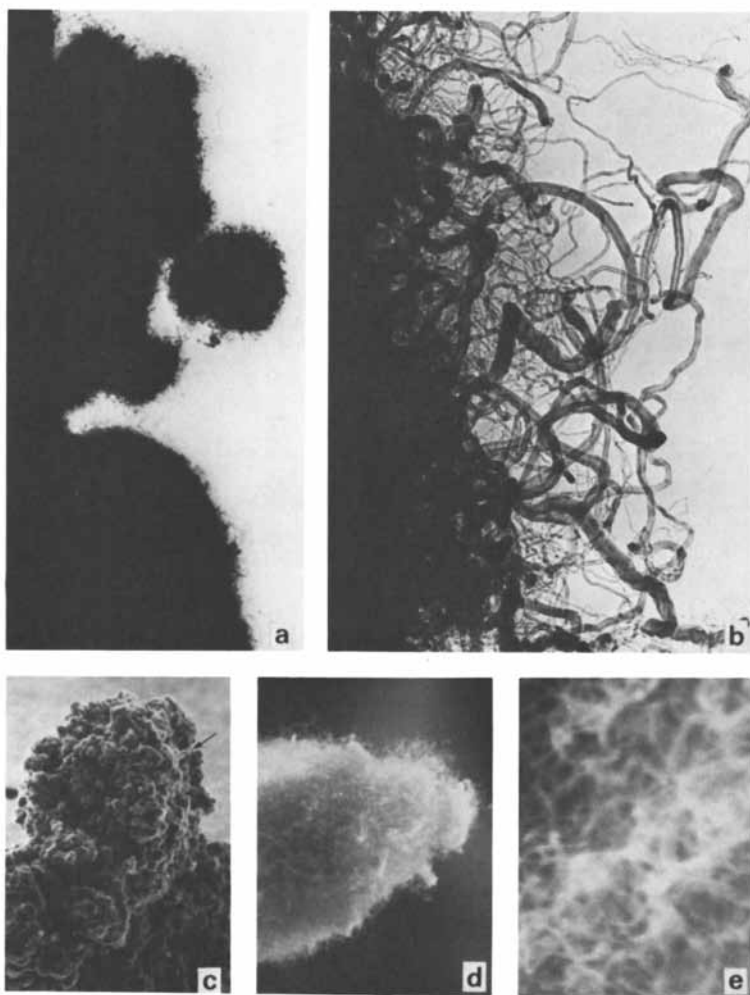


Figure 6. Electron micrographs of carbon deposited on G-56H by decomposition of ethylene at 875 K and 1073 K.

Key: a, low-magnification (2340 \times) transmission electron micrograph (TEM) of carbon deposited at 875 K; b, high-magnification (21,775 \times) TEM of the same sample as in a; c, low magnification (65 \times) scanning electron micrograph (SEM) of a G-56H catalyst particle exposed to ethylene at 875 K; d, medium-magnification (3,250 \times) SEM of the protrusion arrowed in c; and e, SEM micrograph of the same sample at near the limit of resolution (32,500 \times).

representing the ϵ carbon state in particular, is that the rate not only decreases with increasing temperature as expected but increases again upon cooling. Apparently the concentration of CH_4 in the effluent gas is limited by the opposing reactions of carbon gasification with H_2 and methane decomposition, i.e., the methane-carbon equilibrium. It is also apparent that at 1 K s^{-1} heating rates and $1 \text{ cm}^3 \text{ s}^{-1}$ gas flow rates, the TPSR (H_2) experiments cannot completely gasify the ϵ carbon state except when very little is present ($< 5 \mu\text{mol}$). Gasification with steam does not approach the equilibrium concentrations under TPSR conditions and allows a more complete examination of the carbon state.

Carbon Deposited on Nickel Catalysts by Exposure to Carbon Monoxide. In a previous TPSR study (9) carbon was deposited on at 25-wt% $\text{Ni}/\text{Al}_2\text{O}_3$ catalyst (G-65) by exposure to CO at temperatures between 550 and 610 K. TPSR (H_2) of carbon produced by the dissociation/disproportionation of chemisorbed CO showed the presence of large α and β states (Figure 7). Although some chemisorbed CO may have contributed to the α states, it was conclusively shown that most of the α carbon state was more reactive than a monolayer of chemisorbed CO. In this study, we extended the deposition of carbon by CO exposure to higher temperatures to determine if the δ' and δ filament carbon states in addition to the α and β states can be populated by a hydrogen-free source. The TPSR (H_2) results (Figure 8) clearly show the presence of the filament carbon (δ' carbon) state at 773 K. Comparison of the peak temperatures for carbon deposited by C_2H_4 and CO exposure (Table IV) shows little difference in the reactivity of the carbon states.

Table IV
TPSR* CARBON STATES ON G-56H
AFTER EXPOSURE TO C_2H_4 AND CO

Carbon State	Identification	Temperature (K at Maximum Rate [T_p])	
		C_2H_4 Exposure	CO Exposure
α'	Reactive carbon	410 \pm 15	380 \pm 15
α	Chemisorbed carbon	480 \pm 25	460 \pm 20
β	Carbon film	660 \pm 30	660 \pm 20
γ	Ni_3C	\sim 555	\sim 480
δ'	Filament carbon	875 \pm 20	850 \pm 40
δ	Encapsulating carbon	960 \pm 15	-
ϵ	Platelet carbon	1120 \pm 20	-

* Methane production from TPSR with 1-atm hydrogen.

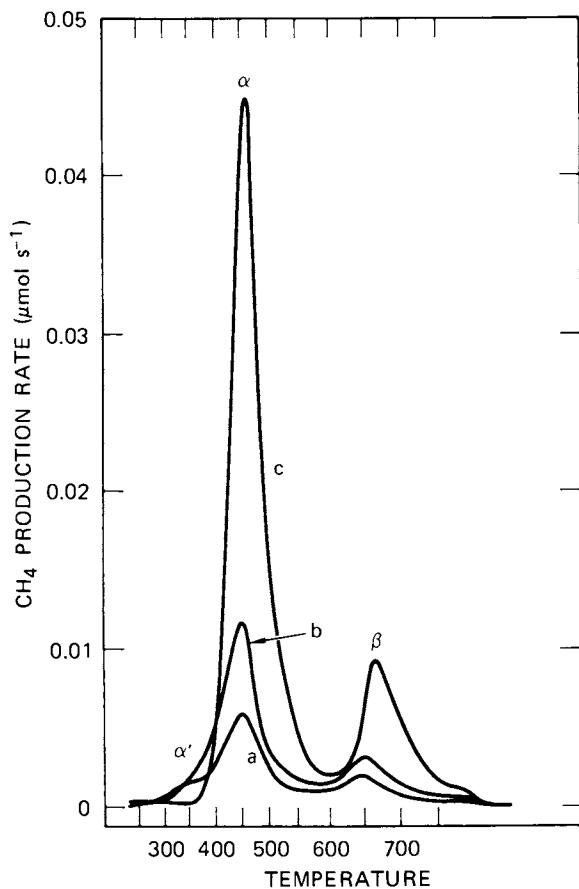


Figure 7. TPSR with hydrogen of carbon deposited on G-65 by CO exposure at 550 K. Key to relative carbon deposit: a, 0.48; b, 1.19; and c, 3.14 normalized to CO adsorption at 300 K.

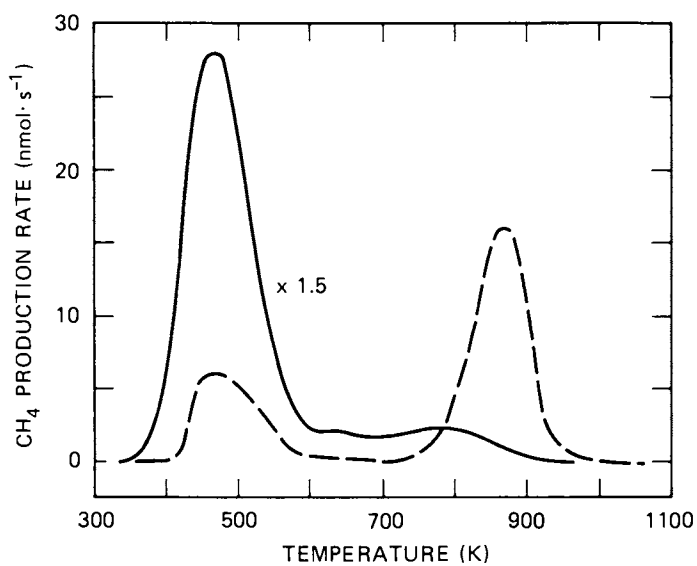


Figure 8. TPSR with hydrogen of carbon deposited on Ni/Al₂O₃ by exposure to CO. Key: —, 573 K; and ---, 773 K.

TPSR with 0.03-atm H₂O of Carbon Deposited on Nickel via C₂H₄ Exposure. The gasification of carbon deposits with 0.03-atm steam (Figure 9 and Table V) shows that the δ state carbon reacts more rapidly with 0.03-atm H₂O than with 1-atm H₂, as indicated by the lower temperature (some 50 to 120 K) at which the gasification rate reaches a maximum. The yield of carbon deposited above 873 K during exposure to 0.01-atm C₂H₄ decreases with increasing catalyst temperatures seen by the TPSR (H₂O) results (Figure 9), which is in agreement with the TPSR (H₂) results. However, TPSR (H₂O), unlike TPSR (H₂), does not resolve the low temperature states (Figure 9) and little or no gasification is seen below 475 K.

Table V
COMPARISON OF H₂O AND H₂ TPSR RESULTS AFTER
EXPOSURE OF G-56H TO ETHANE

TPSR States	Temperature (K)		Tentative Identification of Carbon Species
	0.03-atm H ₂ O	1-atm H ₂	
δ'	825	875	Filament carbon
δ	870	960	Encapsulating carbon
ϵ	1000	1120	Pyrolytic carbon

Carbon Formation on Nickel Catalysts

Morphology of Carbon Deposits on Nickel. The morphology of carbon deposited on nickel by exposure to hydrocarbons and CO varies dramatically with deposition conditions, as shown previously by numerous investigations with electron microscopy (1). The most dramatic finding of these studies is the growing carbon filaments with nickel crystallites attached at their tips (1), (2), (6), (12-20). The carbon filaments (often hollow) can grow rapidly, pulverizing catalyst pellets (21) and forming a thick, viscous mat of carbon. The mechanism of formation of filamentous carbon is believed to be the concentration-driven (20) or temperature-driven (1) diffusion of carbon through entrained, small (~ 10 nm) nickel crystallites. Because carbon is continuously removed by diffusion from the surface regions where it first deposits and is transferred to the growing filament, the surface where carbon is first deposited need not deactivate. Thus coking proceeds rapidly and continuously, as long as carbon continues to move from the exposed metal surface into the growing filament. The TEM data, especially at higher temperature, also show that the filaments may stop growing and that a carbon shell may encapsulate the metal crystallites. Such a passivating shell stops further filament

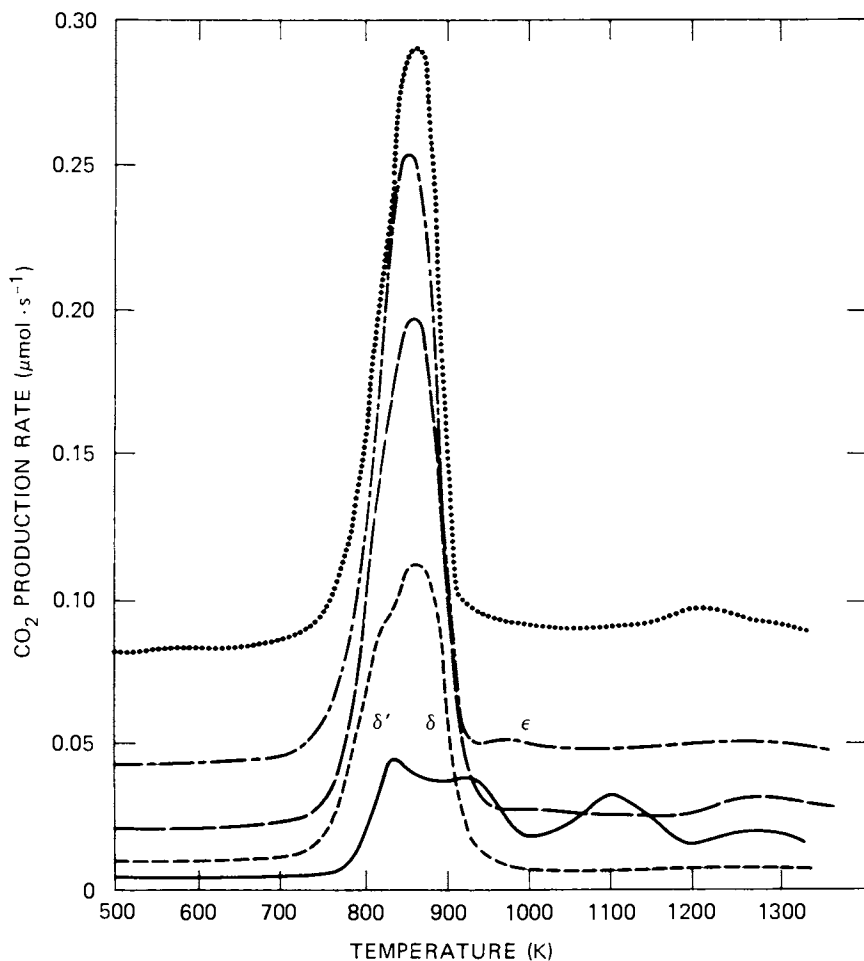


Figure 9. TPSR with 0.03 atm H₂O in He of carbon deposited on G-56H by exposure to ethylene. Key to carbon deposition temperature: —, 1273 K; ---, 1073 K; - - -, 973 K; — · —, 873 K; and · · ·, 773 K.

growth and presumably slows any catalyzed reactions such as hydrocarbon steam reforming.

Other types of carbonaceous deposits found on nickel surfaces following exposure to hydrocarbons include encapsulating polymer films possibly containing hydrogen) formed at low temperature, (20) crystalline flake or platelet carbon formed on flat metal surfaces at high temperatures (1), (20), (22), and amorphous carbon films also formed at high temperature (1). In addition, pyrolytic carbon (essentially formed in the gas phase) can collect on the exterior surfaces of catalyst particles and may eventually coat the catalyst particles with a layer of carbon (20) and block the pores that lead to their interiors (23), (24). A description of the various forms and properties of carbonaceous deposits are summarized in Table VI. Given the wide range in morphology, we expected, as observed in our TPSR studies, that these various carbon forms would have quite different reactivities with H_2 and H_2O .

We have been able to show that particular forms of carbon have characteristic TPSR spectra in flowing H_2 and H_2O/He mixtures. Such carbon states can be quantitatively identified by their characteristic TPSR spectra.

In particular, the α' and α states have been identified as individual carbon atoms, probably chemisorbed at two different sites (perhaps terrace and ledge or step sites (25)). We made this identification because (9) (1) these states are very reactive with hydrogen to produce methane, as we expect for C atoms; (2) they are populated only up to about monolayer quantities in terms of CO adsorption capacity; (3) they are not hydrocarbon fragments because they are populated by CO dissociation as well as hydrocarbon decomposition; and (4) their reactivity is only a little greater than the γ carbon state, which we believe is bulk nickel carbide because there are no nickel lines in the x-ray diffraction of G-56H catalyst with a carbon deposit composed of the γ carbon state. Thus the α and γ carbon states both have metal-carbon bonding rather than carbon-carbon bonding.

Identifying the β carbon states as the polymeric "beta" carbon film mentioned in the literature (6) is less certain than assignments for α' , α , and γ carbon TPSR states. Rostrup-Nielsen (6), (11) and others (25) have referred to this state on nickel catalysts as a polymeric surface carbonaceous deposit, which includes within it a considerable amount of hydrogen. The formation of the β carbon state by CO exposure suggests that this film may not contain hydrogen; however, there are several reasons to believe that our β carbon state is a surface hydrocarbon polymeric film: (1) the maximum amount of the β carbon state was produced by C_2H_4 decomposition at moderate temperature (573 K); (2) the β carbon state was only observed after TPSR in H_2 of the α (or γ) carbon state and in the case of CO exposure may be formed by transformation of the α or γ carbon states during TPSR; (3) finally, the maximum amount of the β carbon state was observed was 3 to 4 times the amount of CO adsorbed on freshly reduced 25 wt% Ni/Al₂O₃

(G-65), or about 4.5×10^{15} carbon atoms per cm^2 Ni surface area (assuming 1.1×10^{15} molecules adsorbed CO/cm^2 Ni at 298 K). Such a mass of carbon is less than expected for a bulk phase but more than expected for a surface layer, and therefore we consider it a polymeric hydrocarbon surface film.

The TPSR results strongly suggest that the δ' carbon state is associated with the long, rapidly growing carbon filaments observed by TEM. Filamentous carbon was observed in transmission electron micrographs of catalysts exposed to C_2H_4 at 873 K and 1073 K, but not for those exposed at 573 K and 1273 K (Figure 2). X-ray diffraction studies of the same samples showed no lines attributable to graphitized carbon. The detailed TPSR (H_2) studies (Figure 4) clearly showed that the population of the lower δ' state appears only with the higher temperature δ state, but at 1073 and 1273 K the δ state appears alone. This observation leads to our speculation that the δ' carbon state is the soft, more reactive carbon observed (1) occupying the core of filaments, whereas δ carbon is the hard outer shell of filaments and perhaps is also the encapsulating carbon often observed (19) surrounding nickel particles during high temperature exposure to hydrocarbons. TPSR and gravimetric observations of the rapid decrease in the rate of δ carbon state formation with increasing time exposure at 1073 K also support the view that the δ carbon state could include the encapsulating form of carbon.

Whether the δ' or δ carbon states are formed depends entirely on the temperature during carbon deposition. There is a gradual transition between deposition into δ' carbon and deposition into δ carbon for C_2H_4 exposure to $\text{Ni}/\text{Al}_2\text{O}_3$ with temperature between 773 K and 1073 K (Figure 2).

The nature of the ϵ carbon state seen during TPSR with H_2O is uncertain. TPSR with H_2 could not be used to resolve the ϵ carbon state from free graphitic carbon because at 1100 K and higher temperatures, CH_4 decomposition becomes favored over carbon gasification by H_2 . The ϵ state seen during TPSR with 0.03-atm H_2O was often small amounting to several monolayers carbon, and difficult to reproducibly populate. For this reason, we speculate that the ϵ state may represent a film of platelet carbon (22), a highly graphitized monolayer of carbon often observed following precipitation from carbon dissolved in large specimens of metallic nickel (26). However, the ϵ state could also represent H_2O gasification of carbon catalyzed by the support materials, such as Al_2O_3 or especially CaO , a known catalyst for H_2O gasification of carbon (27, 28).

The formation of catalyst carbon as carbon filaments or encapsulating carbon could profoundly influence carbon fouling during reforming. Carbon filaments can grow very rapidly, block the catalyst pores, and ultimately lead to restricted flow and a large pressure drop through the reactor (Table VI). The restricted flow could lead to increased pyrolysis of unsaturated hydrocarbons and further carbon fouling. Encapsulating carbon would lead to a much

Table VI. CHARACTERISTICS OF DEACTIVATING CARBON DEPOSITS ON

<u>Carbon TPSR State</u>	<u>Carbon Morphology</u>	<u>Mechanism of Formation</u>
β	Carbon film	Slow polymerization of CH_x radicals on Ni surfaces into an amorphous film (containing some H)
δ'	Filaments, whisker-like growth, helical (δ') growth	Diffusion of carbon through Ni crystallite and precipitation at favored sites creating long (often hollow) filaments carrying the crystallite
δ	Encapsulating carbon shell	Formation similar to filament carbon except carbon layers precipitate and grow on all crystal planes
ϵ	Platelet carbon	Precipitation of (crystalline) graphitic carbon from dissolved carbon
G	Pyrolytic carbon	Thermal cracking of hydrocarbon and deposition of carbon precursors on exterior of catalyst
G	Soot	Homogeneous nucleation and growth of carbon particles

NICKEL HYDROCARBON REFORMING AND SYNTHESIS CATALYSTS

<u>Effect on Catalyst and Reactor</u>	<u>Parameters Favoring Deposition</u>	<u>References</u>
<ul style="list-style-type: none"> • Progressive, reversible deactivation • Little carbon buildup 	<ul style="list-style-type: none"> • Low temperature (< 625 K) • Low H₂O/C ratio • Aromatics and olefins in feed 	2, 6, 20
<ul style="list-style-type: none"> • No deactivation • Catalyst breakdown • Rapid increase in reactor ΔP • Massive deposit 	<ul style="list-style-type: none"> • High temperature (> 625 K) • Low H₂O/C ratio • Aromatics and olefins in feed • Low activity 	1, 2, 6 19, 20, 21
<ul style="list-style-type: none"> • Deactivation • Slow carbon buildup 	<ul style="list-style-type: none"> • High temperature (> 800 K) • Low H₂O/C ratio • Rapid rate of carbon deposition 	2, 17, 18, 19 22
<ul style="list-style-type: none"> • Deactivation • Small carbon buildup • Difficult to remove deposit 	<ul style="list-style-type: none"> • High temperature (> 900 K) • Low pressure • Aging deposit 	1, 25
<ul style="list-style-type: none"> • Encapsulation of catalyst particles • Deactivation due to pore blocking • Increase ΔP 	<ul style="list-style-type: none"> • High temperature (> 900 K) • High void fraction • Low H₂O/C • High pressure • Low space velocity • Acidic catalyst support 	1, 20
<ul style="list-style-type: none"> • Increasing ΔP • Large carbon deposit 	<ul style="list-style-type: none"> • Low reforming activity • Low space velocity • High temperature • High pressure 	20

reduced level of catalytic activity for H_2O reforming with a corresponding increase in the residence time for reactive hydrocarbons, again leading to pyrolysis.

The Reaction Network. The chemisorbed carbon states are likely reforming intermediates. Chemisorbed carbon is formed by the absorption and rapid dissociation of C_2H_4 and is removed as CO by reaction with surface oxygen, which is produced in turn by dissociative adsorption of H_2O or CO_2 (Figure 10). Given the high reactivity of chemisorbed carbon, the α (including α') state is probably an intermediate in the production of other forms of catalyst carbon, δ and ϵ , and at lower temperature δ' , β , and γ . A similar set of equations would apply to other reactive hydrocarbons, other hydrocarbon products, and CH_4 .

The selectivity between reforming and carbon growth is determined in this mechanistic scheme by the thermochemical potential of chemisorbed carbon, $C(a)$. If there is a high concentration of surface oxygen from the dissociative adsorption of H_2O and relatively low concentration of $C(a)$, then we expect only reforming products and no bulk carbon formation. However, if the $C(a)$ formation rate is very high and the $O(a)$ concentration low, then the thermochemical potential of $C(a)$ could be high enough to produce filament carbon $C_\delta(a)$. If filament carbon is produced, and subsequently the concentration of $C(a)$ again falls due either to lower partial pressure of $C_2H_4(g)$ or a greater concentration of $O(a)$ via increased partial pressure of $H_2O(g)$, then $C_\delta(a)$ could be consumed by the reversal of the α to δ transformation.

Other reactions important to reforming are also considered in the reaction network in Figure 10, include the water-gas-shift reaction and its reverse, the reversible adsorption and decomposition of water, the desorption and adsorption of reforming products like CO, CO_2 , and H_2 , and the formation of hydrocarbons like CH_4 . The formation of dissolved carbon, oxygen, and hydrogen in bulk nickel is also considered. Dissolved C, O, or H may be important in the transport of those elements to or from interfaces with other solid phase (carbon, carbides, oxides, support). The possible formation of NiO from H_2O is also shown. Finally, an important reaction to consider is the formation of a deactivating layer of carbons (δ or ϵ carbon states).

Carbon Gasification Rates. Because the reforming rates we observed during this work were often controlled by diffusion, it was not possible to determine individual reaction rates and rate constants. However, from the TPSR measurements we were able to estimate rate constants for the gasification of catalyst and non-catalyst carbons. These rates are listed in Table VII along with selected results taken from the literature (29, 30, 31). We found that the catalyst carbon gasification rates were first order in carbon amounts up to equivalent (CO adsorption) monolayer

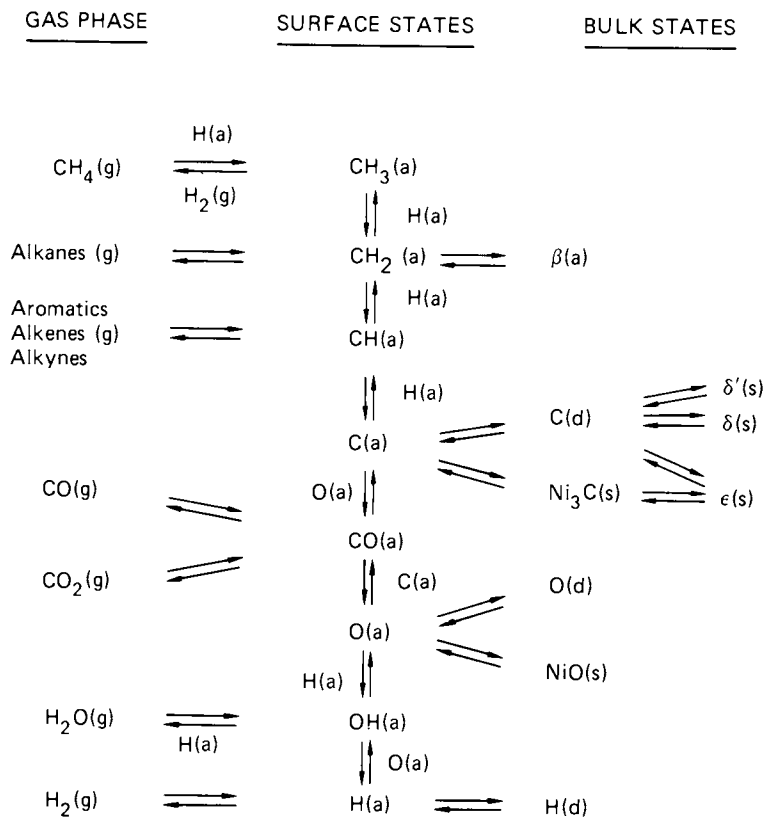


Figure 10. Hydrocarbon synthesis and reforming reaction network on nickel surfaces. Key: a, adsorbed phase; g, gas phase; s, solid phase; and d, bulk solution.

Table VII. Carbon Gasification Rate Parameters

Carbon State	Reactant Gas	Product Gas	Activation Energy (kJ·mol ⁻¹)*	Pre-Exponential Factor (S ⁻¹ ·μmolC ^{1-m})*
α	1 x 10 ⁻¹⁺¹ -atm H ₂	CH ₄	71 ± 10	3 x 10 ⁶⁺¹
γ	1-atm H ₂	CH ₄	84	3 x 10 ⁶⁺
β	1-atm H ₂	CH ₄	130 ± 40	2 x 10 ⁹⁺³
δ'	1-atm H ₂	CH ₄	108 ± 20	7 x 10 ^{2+1.5}
δ'	3 x 10 ⁻² -atm H ₂ O	CO ₂	210 ± 40	2 x 10 ^{10+1.9}
δ', δ	1-atm H ₂	CH ₄	134	3 x 10 ⁴
δ', δ	1.5x10 ^{-1+0.3} -atm H ₂ O	CO _x	185	8 x 10 ⁷
δ	1-atm H ₂	CH ₄	182 ± 20	1 x 10 ^{6+1.2}
δ(?)	1 x 10 ⁻³ -atm H ₂	CH ₄	220 ± 40	-
δ	3 x 10 ⁻² -atm H ₂ O	CO ₂	212 ± 45	2 x 10 ^{11+2.6}
G(char)	1-atm H ₂	CH ₄	172	2 x 10 ²
G(soot)	3 x 10 ⁻² -atm H ₂ O	CO	238 ± 30	3 x 10 ^{7+1.6}
G(char)	1-atm H ₂ O	CO _x	146	8 x 10 ¹
G(char)	5 x 10 ⁻³⁺¹ -atm H ₂ O	CO _x	227	2 x 10 ⁹

* The uncertainty in pre-exponential factor directly follows the uncertainty in activation energy within the specific temperature range.

+ Assigned same as α state.

from Temperature-Programmed Surface Reactions

Experimental Method [†]	Temperature Range (K)	Reaction Order Carbon	Reaction Order Gas	Literature Reference
TPSR/HRV	450-520	1	~0.2	9
TPSR	530-550	≤ 1	-	9
TPSR/HRV	680-720	≤ 1	-	9
TPSR/IR	630-760	§	-	-
TPSR/IR	700-750	§	§	-
GA	773-927	1	2	29
GA	821-895	1	0	29
TPSR/IR	810-820	§	-	-
TEM	975-1240	-	-	22
TPSR/IR	710-810	§	■	-
GA	900-1400	§	-	31
TPSR/IR	920-1240	§	■	-
GA	820-1400	§	≤ 1	31
GA	1003-1123	1	0-1	38

[†] Methods include: TPSR/HRV - variation of heating rate with TPSR; TPSR-IR - initial rates with TPSR; GA - microbalance studies; TEM - movement of Ni particles on a carbon substrate during TEM studies.

[§] Initial rates only.

■ Assumed first order.

quantities, and nearly first order ($n = 0.5$ to 1.0) in carbon up to 30 monolayers for filament carbon.

We did not attempt to determine reaction orders for gasification with H_2O and H_2 ; however, we did note that the hydrogasification of the α carbon state was nearly zero order with respect to H_2 partial pressure. At higher temperature (~ 800 K) we expect the reaction order for hydrogen to increase due to the desorption of hydrogen, and indeed Figureiredo (20) reports second-order reaction in H_2 for hydrogasification of carbon deposited on nickel foil by decomposition of propylene at 720 ± 30 K. Under Figureirdo's conditions, we would expect the δ' carbon state to comprise most of the deposit. The reaction order for steam gasification of such carbon filament deposits varies between 0 and 1 depending on temperature (29, 30).

Apparent activation energies for gasification of the filament carbon states were also determined from initial rates of the TPSR results (Table VII). Because the rates were first order in our studies (i.e., directly proportional to the mass of deposited carbon), plots of the logarithm of normalized rates (rate divided by remaining carbon state mass) vs. reciprocal temperature for the leading edge of the TPSR curves have slopes proportional to the apparent activation energy (E_a). Our values of E_a are generally in good agreement with the literature values given the experimental uncertainties in this type of data. Rates extrapolated to 1273 K are very large for the δ' carbon state; thus under typical high temperature adiabatic steam reforming conditions we do not expect this form of carbon to be present. However, the δ carbon state is not so readily gasified and could be stable and accumulate under ATR conditions.

It is likely that the δ carbon TPSR on Ni/Al_2O_3 represents gasification of relatively dense carbon in contact with nickel surfaces. In fact, the transition from low density filament (δ) to encapsulating shell catalyst carbon is gradual (see Figure 3). At 1073 K and higher temperatures the range of carbon formation decreased rapidly (< 50 s) probably because of the formation of a carbon shell around the nickel crystallites.

Gasification of dense catalyst carbon shells or tubes may be similar to catalytic gasification of a graphite substrate by small nickel particles. Direct controlled atmosphere electron microscopy (CAEM) of nickel-catalyzed hydrogasification of crystalline graphite (22, 23) has provided many interesting observations about the nature of the gasification process; one is that the nickel crystallites soften and change shape as they start to gasify graphite at temperatures well below the melting point of nickel (~ 100 K) (32). The interaction of graphite lowers the surface energy of the nickel crystallites with diameters of ~ 100 nm, and at 1075 K the nickel dissolves into the graphite substrate. This may explain why long filaments can be gasified by metal crystallites; the "wetting" action of the carbon keeps the metal in contact with the filament even as gasification proceeds. With

metal carbon contact assured, gasification proceeds as long as the reactant gas has diffusional access to the crystallite.

Another important CAEM observation is that some nickel crystals deactivate at elevated temperature 1175 K and become immobile (22, 32). This phenomena was attributed to dissolution of carbon into the nickel crystallites and its eventual precipitation as graphite platelets, similar to observations on well-defined nickel (33), platinum, (34) and iron (35, 36) surfaces. Under CAEM pressure (< 1 -torr H_2) platelet carbon is not fully gasified and remains a hollow shell as the nickel crystal dissolves away at 1225 K. Similar phenomena may give rise to the ϵ TPSR carbon state, which at 1-atm H_2 or 20-torr H_2O is gasified at higher temperature. In H_2O , nickel crystallites observed in CAEM are stable and do not dissolve into the bulk at elevated temperature. However, even in the presence of H_2O , the initial step in cracking open a layer of platelet carbon or the carbon shell surrounding an immobilized Ni crystallite may be penetration by fluid metal.

The rates of nickel-catalyzed gasification of graphite are in reasonable accord with our TPSR results for the δ carbon state. For the δ carbon state, our E_a was 182 ± 20 kJ mol $^{-1}$ in good agreement with the results of Keep et al. (22) 220 ± 40 kJ mol $^{-1}$. Because of the differences in H_2 pressure and technique, it is difficult to compare actual rates. Tomita et al. (37) observed substantially lower apparent activation energies 130 ± 12 kJ mol $^{-1}$ for nickel-impregnated carbons, but those rates may have been limited by diffusion (22).

Literature Cited

1. Baker, R. T. K.; Harris, P. S., The Formation of Filamentous Carbon, in "Chemistry and Physics of Carbon; Walker, P., Jr.; Thrower, P. A., Eds.; Marcel Dekker: New York, 1978, Vol. 14.
2. Trimm, D. L. Catal. Rev. 1977, 16, 155.
3. Ekerdt, J. G.; Bell, A. T. J. Catal. 1977, 48, 155.
4. Ponec, V. Catal. Rev. Sci. Eng. 1978 18, 151.
5. Niemantsverdriet, J. W.; van der Kraan, A. M. J. Catal. 1981, 72, 385.
6. Rostrup-Nielsen, J. R.; Trimm, D. L. J. Catal. 1977, 48, 155.
7. Munster, P.; Grabke, H. J. J. Catal. 1981, 72, 279.
8. Martin, G. A. J. Catal. 1979, 60, 345.
9. McCarty, J. G.; Wise, H. J. Catal. 1979, 57, 406.
10. Nagakura, S. J. Phys. Soc. Japan 1957, 12, 482; 1958, 13, 1005.
11. Rostrup-Nielsen, private communication.
12. Baker, R. T. K. Catal. Rev. 1979, 19, 161.
13. Hofer, L. J. E.; Sterling, E.; McCartney, J. T. J. Phys. Chem. 1955, 59, 1153.
14. Benschaw, G. D.; Roscoe, C.; Walker, P. L. J. Catal., 22, 394.

15. Baker, R. T. K.; Barber, M. A.; Harris P. S.; Feates, F. S.; Waite, R. J. J. Catal. 1977, 26, 51.
16. Bohm, H. P. Carbon 1973, 11 583.
17. Baird, T.; Fryter, J. B.; Grant, B. Carbon 1974, 12, 591.
18. Audier, M.; Coulon, M.; Oberlin, A. Carbon, 1980, 18, 73.
19. Audier, M.; Oberlin, A.; Oberlin, M; Coulon, M.; Bonnetain, L. Carbon 1981, 19, 217.
20. Rostrup-Nielsen, J. R.; Trimm, D. L. J. Catal. 1977, 48, 155.
21. Rostrup-Nielsen, J. R.; Tottrup, P. B., Steam Reforming of Heavy Feedstocks in "Symposium on Science of Catalysis and Its Application in Industry;" FPDIL Sindri, India, 22-24 February 1979, paper 39 p. 397.
22. Keep, C. W.; Terry, S.; Wells, M. J. Catal. 1980, 66, 451.
23. Froment, G. F. Proc. Int. Congr. Catal., 6th, The Chemical Society: Letchworth, England, p. 976.
24. Beeckman, J. W.; Froment, G. F. Chem. Eng. Sci. 1980, 35, 805.
25. Jackson, S. D.; Thomson, S. J. Webb, G. J. Catal. 1981, 70, 249.
26. Isett, L. E.; Blakley, J. M. Surf. Sci. 1976, 58, 397.
27. McKee, D. W. Fuel, 1980, 59, 308.
28. Otto, K.; Bartosiewicz, L.; Shelef, M. Carbon 1979, 17, 351.
29. Figueiredo, J. L. Carbon 1981, 19, 146.
30. Bernardo, C. A.; Trimm, D. L. Carbon 1979, 17, 115.
31. Wen, C. Y. Dutta, S. in "Coal Conversion Technology;" Wen, C. Y.; Lee, E. S., Eds.; Addison Wesley, 1979.
32. Baker, R. T. K.; Sherwood, R. D. J. Catal. 1981, 70, 198.
33. Derbyshire, F. J.; Presland, A.; Trimm, D. L. Carbon 1978, 13, 111.
34. Baker, R. T. K.; Sherwood, R. D., Dumesic, J. A. J. Catal. 1980, 66, 56.
35. Baker, R. T. K.; Feats, F. S.; Harris, P. S. Carbon 1972, 10, 93.
36. Brown, M. A.; Hill, M. P. Carbon 1981, 19, 51.
37. Tomita, A.; Sato, N.; Tamari, Y. Carbon 1974, 12, 143.
38. Chihara, K.; Matsui, I.; Smith, J. M. AIChE Journal 1981, 220.

RECEIVED August 15, 1982.

Reaction of Steam with Coke on Solid Substrates

T. Y. YAN and M. P. ROSYNEK¹

Mobil Research and Development Corporation, Central Research Division,
Princeton, NJ 08540

The kinetics of coke gasification are markedly influenced by the nature of the substrate on which the coke is deposited. Steam gasification of coke deposited on a silica-alumina substrate followed first-order kinetics, with respect to carbon remaining, with an activation energy of 55.5 kcal/mole and a reaction rate constant of $5 \times 10^{-3} \text{ min}^{-1}$ at 1500°F. Prior impregnation of the substrate with copper, iron, or vanadium oxides had virtually no effect on the rate of subsequent coke gasification. Nickel oxide, on the other hand, caused a three-fold increase in initial gasification rate, up to 30% of coke conversion. Coke deposited on an alumina substrate was three to six times more reactive toward steam gasification at 1500°F than that on silica-alumina. Alumina apparently influences both the rate and the structure of coke deposited on it.

Reaction of steam with carbon is one of the basic processes involved in the gasification of coals or chars to produce clean fuels. The industrial importance of this reaction is considerable, particularly at this time of spiraling energy costs. In addition, the steam-carbon reaction finds other important industrial applications, such as preventing or minimizing the coking of olefin-plant cracker-tubes. Because of its commercial importance, the steam-carbon reaction has been studied extensively, and excellent reviews are available (1,2). In addition to reaction kinetics and mechanisms, the effects of carbon structure, catalysis by metals, and impurities (anions) have been investigated (3,4,5).

¹ Current address: Texas A&M University, Department of Chemistry, College Station, TX 77843.

Except for spectroscopic graphite, carbons used in the steam-carbon reaction, viz., active carbon, coke, and char, typically contain varying amounts of hydrogen, i.e., the "carbons" are hydrocarbons in a broader sense. In addition to impurities, variations in the compositions of the carbons (e.g., hydrogen content) complicate the measurements and are a cause of discrepancies among previous studies. The reactions of steam with coals, cokes and chars have been reported and compared with the corresponding steam-graphite reactions (6-9). References in the open literature to the reaction of steam with carbon that has been deposited on various inorganic solid substrates, however, are lacking.

In the catalytic processing of heavy oil and residua over solid cracking or hydrocracking catalysts, a significant amount of "coke" is deposited on the catalysts, thus lowering the catalytic activities. Such coked catalysts are regenerated by burning off the coke with air. When the level of coke on the catalyst is high, excessive heat can be generated during regeneration, causing temperature run-away, and resulting in possible irreversible catalyst sintering and permanent loss of activity. Furthermore, the potential heating value of the coke is lost, because recovery of waste heat from the flue gas is relatively expensive. Various schemes have been suggested for regenerating severely coked catalysts using steam and oxygen (10,11). We have previously reported a process for upgrading petroleum residua that involves contacting it with a solid catalyst, followed by gasification of the coke-laden substrate with steam and oxygen (12).

The present study was undertaken in an effort to gain a better understanding of certain aspects of the reactions involved in the gasification of cokes deposited on catalyst substrates in these applications. Solid substrates were coked with a petroleum residuum under simulated conditions and the substrate-supported coke was then reacted with steam. Effluent gases were analyzed, and the kinetics of gasification and the effects of substrates identities and metal impregnations were examined.

Experimental Methods

Materials. Physical properties of the solid substrates employed in this study are summarized in Table I. The silica-alumina was an equilibrated Durabead TCC catalyst from Mobil Oil Corp., with an activity index of ~50. The bauxite extrudate was of the North American variety used in the Claus process for sulfur recovery, and contained 2.3 and 12.5 wt % of iron and SiO₂, respectively. The montmorillonite catalyst was obtained from Chemetron Corp. (No. K306), and was used in the form of irregular 14/60 mesh granules. Its wt % composition was SiO₂, 71.7; Al₂O₃, 12.5; Fe₂O₃, 5.2; CaO, 2.7; MgO, 3.6; ignition

loss, 4.0. The two γ -alumina substrates were obtained from Continental Oil Co. (Catapal S, in pelleted form) and from Harshaw Chemical Co. (Al-1706E, 1/8 in. extrudate). All substrates were calcined in air for 16 hrs at 1000°F before use.

Table I
Physical Properties of Solid Substrates

Substrate	S.A. (m ² /g)	Pore Vol. (cc/g)	Ave. Pore Diam. (Å)	App. Dens. (g/cc)	Real Dens. (g/cc)
Silica-Alumina (Durabead)	150	0.46	92	1.13	2.35
Silica-Alumina (Montmorillonite)	250	0.54	--	0.65	--
γ -Alumina (Catapal S)	250	0.53	65	0.69	3.32
γ -Alumina (Harshaw)	218	0.77	--	0.51	--
Bauxite	62	0.44	261	1.39	3.55

For experiments involving metal-containing substrates, samples of the Durabead silica-alumina were impregnated with the nitrate salts of copper, iron, or nickel, or with vanadyl sulfate, at a level of 5 wt % metal, and then calcined in air for 10 hrs at 1000°F. The resulting metal oxide-containing materials were then subjected to the coking procedure described below without further treatment.

Residuum boiling at >650°F and derived from an Agha Jari crude oil was used for the coking procedure. The residuum had an API gravity of 17.3°, a pour point of 75°F, a kinematic viscosity of 800 cs. at 100°F, and nitrogen and sulfur contents of 2.42 and 0.33 wt %, respectively.

Procedures. Coke was deposited on each of the various solid substrates by intimately mixing with Agha Jari residuum at a solid/oil ratio of 0.5 by weight in a reactor equipped with a stirrer and a reflux condenser. The coking reaction was allowed to proceed at 900°F for 24 hrs under 1 atm. of nitrogen. The coked substrate was then stripped for 3 hours with flowing nitrogen in a tubular reactor at 950°F, and finally cooled under nitrogen to room temperature. The composition of cokes on the substrates were determined by a combustion method. The composition of coke on the silica-alumina catalyst was CH_{0.25}. The resulting levels of coke deposited on the various substrates are contained in Table II.

Table II
Steam/Coke Reaction Rates At 1500°F

Run	Material	Basic Substrate	Total Coke (wt %)	First Order Rate Const. ($\times 10^2 \text{ min}^{-1}$)
17	Durabead	Silica-Alumina	4.9	0.50
59	Montmorillonite	Silica-Alumina	10.0	0.45
56	Catapal Pellets	Alumina	7.0	2.17
58	Catapal Pellets	Alumina	11.4	1.37
52	γ -Alumina Extrudate	Alumina	15.2	1.31
60	Bauxite Extrudate	Alumina	8.1	2.83

Two grams of externally-coked substrate were charged to a 1/2" OD x 12" long Vycor, downflow reactor that contained a thin-walled longitudinal thermowell. The reactor space above and below the substrate bed was packed with 10-20 mesh Vycor chips. Water was fed with a syringe pump at 2 g/hr, and vaporized upon contact with the hot Vycor chips. Unreacted steam was condensed at the reactor exit, and the total volume of gas flow was measured with a wet test meter. Samples of the effluent gas were taken periodically and analyzed mass spectrometrically for H_2 , CO , CO_2 , N_2 and O_2 . From these analyses, the rates of disappearance of carbon and appearance of carbon monoxide and carbon dioxide were calculated. The gasification reactions were carried out in the temperature range 1400-1600°F.

Results and Discussion

Gasification Kinetics of Coke Deposited on Silica-Alumina. Within the temperature range 1400 to 1600°F and in the presence of excess steam, the gasification reaction of coke deposited on the silica-alumina cracking catalyst closely followed first-order kinetics with respect to unreacted carbon (Figure 1). First-order rate constants were calculated from the slopes of these plots (Table III), and yielded an activation energy of 55.5 Kcal/mole.

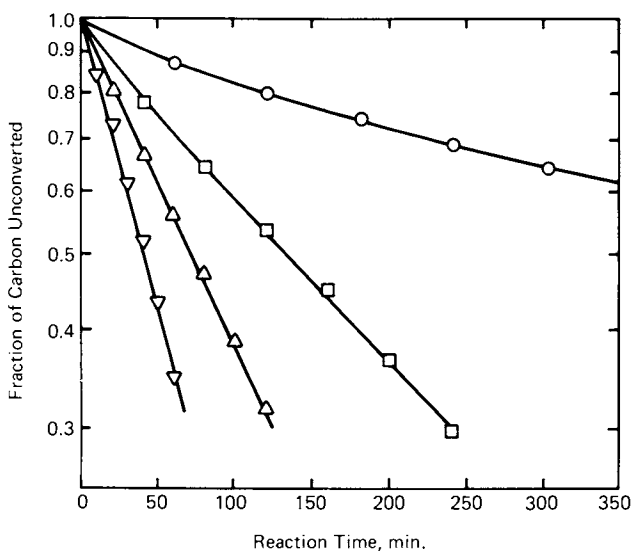


Figure 1. Kinetics of steam gasification of coke deposited on silica-alumina, for reaction temperatures of 1400°F (○), 1500°F (□), 1550°F (△), and 1600°F (▽).

Table III
Rate Constants for Carbon + Steam Reaction
on Silica-Alumina Substrate

<u>T (°F)</u>	<u>First-Order Reaction Rate Constant (min⁻¹)</u>
1400	.00121
1500	.00463
1550	.00906
1600	.01668

The reaction rate constant at 1500°F of $4.6 \times 10^{-3} \text{ min}^{-1}$ is strikingly similar to that observed for chars from the Hydrane and Synthane processes ($\sim 9 \times 10^{-3} \text{ min}^{-1}$ via interpolation of the results of Fuchs et al.) (6). The activation energy of 55.5 Kcal/mole is within the range (51.3 to 56.6 Kcal/mole) reported previously by Tyler and Smith for gasification of petroleum coke and electrode materials (13). In addition, our result is much lower than the 83 ± 5 Kcal/mole found by Long and Sykes (14) for gasification of purified charcoal, but close to the 55 ± 7 Kcal/mole that they observed for contaminated charcoal.

Effect of Impregnated Metals on Coke Gasification Rate.
The steam-carbon reaction is known to be catalyzed by metals, particularly transition metals (3,4). In an effort to improve the rate of gasification, separate samples of the silica-alumina (Durabead) catalyst were impregnated with one of various metals prior to coke deposition, and the results for the subsequent steam-carbon reaction at 1500°F over these materials are shown in Figure 2 and Table IV. The effects of the deposited metal oxides can be summarized as follows:

- Cu, V, Fe: No effect on the gasification reaction rate.
- Ni: Acceleration of the initial gasification rate (for coke conversions up to $\sim 30\%$).

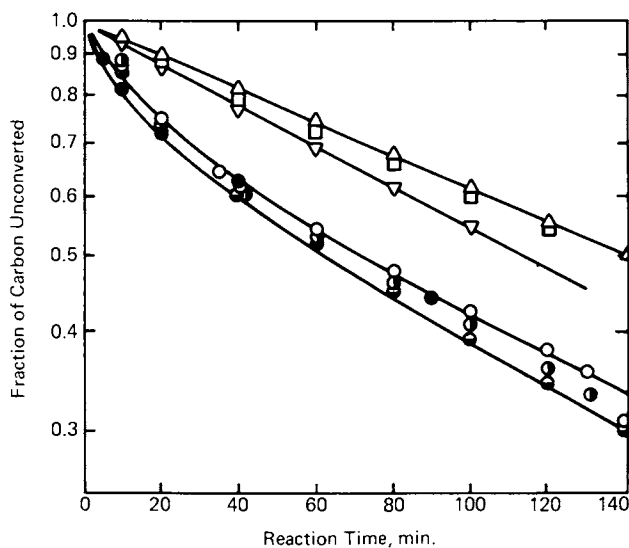


Figure 2. Kinetics of steam gasification at 1500°F of coke deposited on silica-alumina impregnated with oxides of copper (Δ), vanadium (\square), iron (∇), and nickel (\circ , \bullet , \ominus , \bullet [various preparations]).

Table IV
Coke/Steam Reaction Rates on Metal-Impregnated Durabead
(Silica-Alumina) TCC Catalysts at 1500°F

Run	Metal	Wt %	Rate Constant (min ⁻¹)		Relative Rate Constant	
			0-30% Conv.	>30% Conv.	0-30% Conv.	>30% Conv.
17	--	--	.0046	--	1.00	--
39	Fe	5	.0058	--	1.25	--
40	Cu	5	.0049	--	1.05	--
41	V	5	.0046	--	1.00	--
38	Ni	5	.0139	.0059	3.00	1.28
42	Ni	5	.0137	.0063	2.96	1.37
43	Ni	5	.0140	.0067	3.02	1.46

Impregnated Cu, V, and Fe oxides had no effect on the rate of subsequent coke gasification. Hall and Rase (15) found that for a silica-alumina cracking catalyst contaminated with metals up to a level of ~0.2 wt %, the rate of oxidation of deposited coke did not increase in comparison with that over the uncontaminated catalyst. These metals are known to accelerate the reaction, however, when they are admixed intimately with the coke. It is apparent in this case that contact between the impregnated metals and the coke was not sufficiently close to be catalytically significant. Haldeman and Botty (16) found that on a silica-alumina cracking catalyst containing 6% coke by weight, the dimensions of the average coke pseudocrystallite were 17 and 10-12 Å for Le (normal to layers) and La (in place of layers), respectively. For an interlayer spacing of 3.47 Å, this represents about 5 parallel layer groups. Coke deposits were also found to be located preferentially on the metal sites. At higher coke levels, the pseudocrystallites should be larger and contain more layers. Thus, at the coking level of ~10% used in this study, the metals could be completely covered with coke, be impermeable to steam, and, hence, ineffective catalytically. Since the gasification reaction followed first-order kinetics up to coke conversion levels of 50%, it is apparent that, assuming uniform gasification, even pseudocrystallites one-half the original size are still too large for the metals to be effective. An alternative, but less likely, explanation for the catalytic ineffectiveness of deposited Fe, Cu, and V is that these metals react with silica-alumina at the high gasification temperatures to form catalytically inactive silicates, aluminates, or solid mixtures.

There is another possible explanation for the apparent lack of effect of metals on the steam gasification reaction rate. The metals deposited on substrates could catalyze the dehydrogenation reaction during the coking step leading to "coke" of lower hydrogen content. Such low-hydrogen "coke" is known to react with steam more slowly. Thus, the metals could affect the

steam carbon reaction in two opposite ways; viz., to increase the rate by catalyzing the reaction on one hand and to decrease the reaction rate by forming slow reacting cokes on the other hand. Except for nickel, these two effects counteract each other so that the deposited metal shows no overall effect on the rate of steam coke reaction.

In marked contrast to the effects observed with iron, vanadium and copper oxides, prior impregnation of silica-alumina with nickel oxide led to a considerable increase in the initial rate of subsequent coke gasification, up to a coke conversion level of ~30% (Figure 2).

The kinetics of carbon deposition on nickel have been studied in detail previously (17,18,19), and a mechanism which explains most observations has been advanced. Coke precursors proceed through a series of dehydrogenation steps on the nickel surface, resulting eventually in carbonaceous species. These species dissolve in, and precipitate from, the metal phase detaching nickel crystallites from the surface of the bulk nickel or the silica-alumina surface. Further coke deposition incorporates additional nickel into the growing carbon layer, as shown by electron microscopic examination of the deposits (18).

In the experiments reported here, some nickel may, therefore, be transported by the growing carbon crystallites to the solid surface during coke deposition. When the carbon-steam reaction is subsequently begun, this nickel is particularly accessible and reactive, and results in an increased initial reaction rate. In addition, however, there is apparently a second fraction of coke, deposited on the silica-alumina substrate, which is not associated with the nickel. This coke is not affected by impregnated nickel and reacts more slowly, paralleling the behavior of coke on metal-free silica-alumina. The presence of these two types of coke results in the observed kinetic behavior. Our data indicate that about 30% of the coke reacts at a rate approximately 3 times greater than that deposited in the absence of nickel, while the remaining 70% of the coke reacts at the same rate as that without nickel (Table III). This result suggests that the fraction of coke associated with the nickel is about 30%.

Effect of Substrate on Coke Gasification Rate. The effect of substrate variations on the steam-carbon reaction rate at 1500°F is shown in Table II and in Figure 3. The substrates can be classified into two categories according to their effect on coke gasification reaction rates:

- Low activity: Silica-alumina (cracking catalyst and Montmorillonite)
- High activity: Alumina, (calcined Catapal, alumina and bauxite).

At 1500°F, the steam-coke reaction on alumina occurs approximately three to six times faster than on silica-alumina type substrates. Comparison of results from Runs 56 and 58 indicates the extent of reproducibility of the experiments. In comparison with this reproducibility and in consideration of the observed consistency, the increased gasification rates on the alumina substrates are significant. All alumina-based materials tested, viz., γ -alumina, calcined Catapal, and bauxite, showed equally high activities.

The activation energies for coke gasification on the three substrates shown in Figure 4 were ~ 33 Kcal/mole for the three alumina-based materials and 54 Kcal/mole, for the silica-alumina catalysts. The increased activity and lower activation energy for the coke deposited on the aluminas (compared to that on the silica-aluminas) cannot be due to a direct catalytic effect of alumina on the gasification reaction, but rather to an indirect effect of the alumina that controls the nature and structure (surface area and structural disorder) of the coke during its deposition.

The coke formed on alumina appears to be more structurally disordered. It is less graphitic, more porous, higher in surface area, and lower in density than that deposited on the silica-alumina catalyst. This type of coke will be more reactive in the gasification reaction (6). Qualitatively, it was also observed that the various aluminas coked more quickly and at lower temperatures during the coking procedure than did the silica-aluminas. This is in agreement with the results of Tantarov et al., who found that during catalytic cracking of α -methyl styrene at 450°C, the initial coking rate on alumina was twice that on silica-alumina (20). The alumina catalyzes the coke deposition on the substrate and, perhaps, promotes formation of more reactive coke. The enhanced reactivity of coke on alumina could be the result of increased surface area (higher porosity), but the nature of the coke could be altered as well, as suggested by the lower activation energy (54 vs. 33 Kcal/mole) of gasification. This conclusion is consistent with the observation that coke which is deposited quickly is generally less dense and more reactive to gasification. An investigation of the nature and physical properties of cokes deposited on various substrates may be helpful in elucidating the mechanism.

The high carbon reaction rate on alumina makes this material the substrate of choice for the proposed petroleum upgrading scheme (12). For example, if a reaction rate constant of 0.011 min^{-1} is required (corresponding to about 210 min residence time for 90% coke removal), a temperature advantage of 65°F (1495 vs. 1560°F) would exist for alumina over silica-alumina.

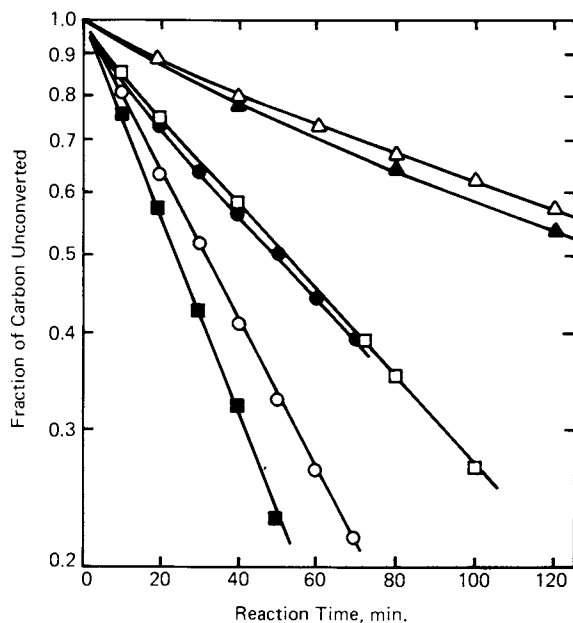


Figure 3. Kinetics of steam gasification at 1500°F of coke deposited on montmorillonite (Δ), silica-alumina (\blacktriangle), American Cyanamid alumina (\square), Catapal alumina, Run 58 (\bullet), Catapal alumina, Run 56 (\circ), and fresh bauxite (\blacksquare).

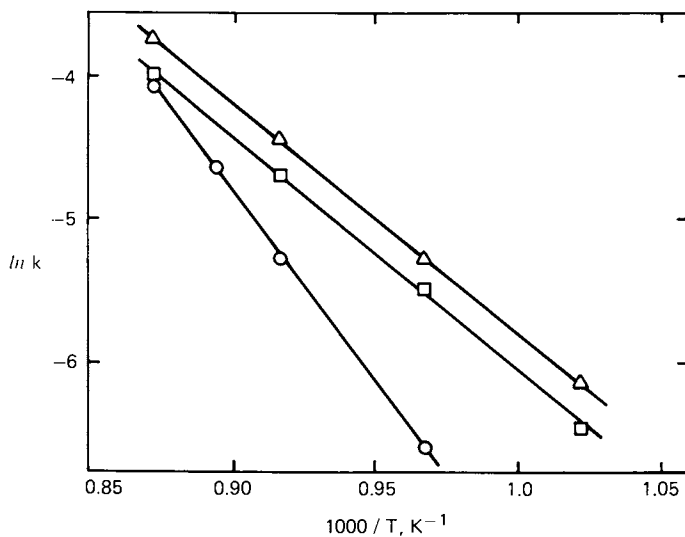


Figure 4. Arrhenius plots for steam gasification of coke deposited on American Cyanamid alumina (Δ), fresh bauxite (\square), and silica-alumina (\circ). Corresponding activation energies are 32.6, 33.8, and 53.1 kcal/mol, respectively.

Acknowledgment

The authors wish to thank Dr. W. K. Bell for valuable discussions.

Literature Cited

1. Walker, P.L., Jr.; Rusinko, J.F., Jr.; Austin, L.G. "Advances in Catalysis"; Eley, D.D., Selwood, P.W., Weisz, P.B., Eds.; Academic Press: New York, 1959; Vol. XI, 133.
2. Ergun, S.; Mentser, M. "Chemistry and Physics of Carbon"; Walker, P.L., Jr., Ed.; Marcel Dekker: New York, 1965; Vol. 1, 203.
3. Walker, P.L., Jr.; Shelef, M.; Anderson, R.A. "Chemistry and Physics of Carbon"; Walker, P.L., Jr., Ed.; Marcel Dekker: New York, 1968; Vol. 4, 287.
4. Rewick, R.T.; Wentreck, P.R.; Wise, H. Fuel 1974, 53, 274.
5. Wilks, K.A.; Gardner, N.C.; Angus, J.C. Symposium on Structure and Reactivity of Coal and Char; 170th National ACS Meeting, Chicago, 1975.
6. Fuchs, W.; Yavorsky, P.M. Symposium on Structure and Reactivity of Coal and Char; 170th National ACS Meeting, Chicago, 1975.
7. Nandi, S.P.; Lo, R.; Fischer, J. Symposium on Structure and Reactivity of Coal and Char; 170th National ACS Meeting, Chicago, 1975.
8. Johnson, J.L. "Coal Gasification"; Massey, L.G., Ed.; ACS Advances in Chemistry Series, No. 131, 1974; 145.
9. Willson, W.G.; Sealock, L.J., Jr.; Hoodmaker, F.C.; Hoffman, R.W.; Stinson, D.L.; Cox, J.L. "Coal Gasification"; Massey, L.G., Ed.; ACS Advances in Chemistry Series, No. 131, 1974; 203.
10. Kirk, M.C., Jr. U.S. Patent 3,691,063, 1972.
11. Kimberlin, C.N., Jr.; Hamner, G.P. U.S. Patent 3,726,791, 1973.
12. Rosynek, M.P.; Shipman, G.F.; Yan, T.Y. U.S. Patent 3,983,030, 1976.
13. Tyler, R.J.; Smith, I.W. Fuel, 1975, 54, 99.
14. Long, F.J.; Sykes, K.W. J. Chim. Phys. 1950, 47, 361.
15. Hall, J.W.; Rase, H.F. Ind. Eng. Chem. Process Design Develop. 1963, 2, 25.
16. Haldeman, R.G.; Botty, M.C. J. Phys. Chem. 1959, 63, 489.
17. Lobo, L.S.; Trimm, D.L. J. Catal. 1973, 29, 15.
18. Lobo, L.S.; Trimm, D.L.; Figueiredo, S.L. Proc. 5th Intern. Congr. Catal. 1972; Vol. 2, 1125.
19. Figueiredo, S.L.; Trimm, D.L. J. Catal. 1975, 40, 154.
20. Tanatarov, M.A.; Akhmetshina, M.I.; Levinter, M.E. Kinet. Katal. 1971, 12, 511.

RECEIVED June 28, 1982.

Process of Coke Formation in Delayed Coking

C. A. AUDEH and T. Y. YAN

Mobil Research and Development Corporation, Central Research Division,
Princeton, NJ 08540

The process of coke formation in a delayed coker has been studied. Rates of reaction and selectivities have been determined from which an overall sequence of coke development is suggested.

Kinetic, tracer and quenching studies have shown that feed entering the coker at the incipient coking temperature undergoes a two stage thermal decomposition to gas and liquid products and coke. In the first stage, thermal cracking takes place producing gas and liquid products at a fast rate R_f , with simultaneous condensation reactions which result in the formation of non-volatile semicoke. The volatiles leave the coking zone rapidly. Steam injected with the feed facilitates the removal of volatiles to minimize secondary cracking.

Hot feed continues to enter the drum and pushes the semicoke upward with little or no mixing. Meanwhile, in the second stage, the semicoke continues to undergo pyrolysis, leading to more gas, liquid and coke, at a slower rate R_s .

At 915°F, in the first stage the reaction rate is 10.9 times that of the second stage ($R_f/R_s=10.9$) and the liquid yield is higher. The product selectivities for gas, liquid and coke were 4, 57 and 39 and 7, 21 and 72% wt. for the fast and slow stages respectively.

In connection with thermal and catalytic processes such as coking, pyrolysis and catalytic cracking for the conversion of petroleum fractions, there is considerable interest in the mechanism of the transformation of various

0097-6156/82/0202-0295\$06.00/0

© 1982 American Chemical Society

organic materials into coke. In particular, Singer (1) studied the initial steps associated with the coking of a series of pure organic compounds. Whittaker et.al., (2) concentrated on the coking of residual oils and studied the nature of coke precursors and their plasticity. Others (3,4) have studied other aspects, with particular emphasis on kinetics, and have developed complex mathematical models to describe the coking process (4). All these studies agree that coking is a thermal process in which feed is decomposed to generate free radicals and light products. Some free radicals undergo condensation/polymerization reactions which result in the formation of coke.

Published kinetic data were generally obtained in batch reactors (1-5). The data obtained were observed to fit first order kinetics notwithstanding the complexity of the feeds studied and the constant change in the nature of the product-forming intermediates. It has been shown (3,5) that batch coking has a definite induction period and that the usually observed first order coking behavior of complex feeds is only apparent. Also it was determined that the rates observed could fit third order kinetics for decomposition and fourth order for polymerization/condensation (5). Clearly, kinetics of batch coking are only approximations.

Delayed coking is a well developed commercial process (6), and operates on a semi-continuous basis. Feed, usually vacuum residue, mixed with steam, is continuously pumped through tubular heaters in which it is heated to its incipient coking temperature. At this temperature the feed is injected into an insulated drum where coking takes place. The vapors produced in the drum during coking are continuously removed and fractionated. The fractions usually include coker naphtha and light and heavy coker gas oils. As a drum fills up, feed is switched to another drum. Meanwhile, the full drum is steam stripped, cooled and the coke drilled out. Whereas feed is continuously supplied to the drum, the coke is recovered intermittently.

In considering the nature of delayed coking in a continuous process it is clear that no specific amount of feed is under consideration if only part of the coking period is studied. Also, feed is continuously transformed during the coking process. Volatiles, with the help of steam, leave the coking zone continuously as soon as they are formed and pass through layers of material that are at various stages of the coking process. It would appear that a yet more involved model would be needed to describe the coking process in the continuous mode than in the case of batch coking.

An aspect of coking which has received little or no attention in the published literature (7) concerns the gross

physical changes involved in delayed coking. Such information could be helpful in commercial unit design and in the interpretation of commercial unit performance. Some information is, however, available about the apparent densities of the vapor phase within a commercial coke drum (8). Apparent density is a measure of the relative position of the solid phase in a coke drum. Usually such information is used as an aid in determining optimum operating levels of a specific coke drum.

We have studied the process of coke formation in a laboratory-scale continuous coker from which the overall sequence of coke development could be described.

Experimental

Figure 1 depicts the 100 ml, 7/8" ID steel coker drum used in these experiments. The coker was heated in a furnace, fitted with three independently controlled zones, and was equipped with gas and liquid measurement and recovery systems. Coke recovery in the form of plugs was carried out by the use of a hydraulic ram or lathe operating on an aluminum rod with the same diameter as the preheater plug.

The feed used was a 1050°F+ residue from a commercially operated unit and was processed at typical commercial conditions, 915°F and 40 psig. In addition, operation at lower temperatures and pressures as well as higher temperatures were explored in these studies. In all the coking experiments, steam, 2% by wt. of the feed, was introduced with feed in the preheating zone.

For tracer experiments, where two residues with different metals content were used, feed to the coker was interrupted to allow for the feed change. Metals profile in the coke was obtained by taking sections from the coke plug and determining the metals concentration in each section. The metals, nickel and vanadium, were determined by atomic absorption.

In the quenching experiments, the usual coking procedure was initially followed. However, after the required amount of feed was pumped into the drum, the experiment was stopped by quickly removing the drum from the furnace and immersing it in a mixture of ice and water. The quenched contents were carefully removed from the drum, inspected and sectioned. Each section was then extracted in a Soxhlet extractor with toluene, until the toluene extract became colorless.

Results and Discussion

Formation of Coke. Tracer and quenching studies were

carried out to follow the progress of feed conversion from the point of entry into the coking drum. In the tracer studies two residues with different metals concentrations were used. Initially it was determined that coke prepared from each of the residues had a significantly different concentration of metals. Thus by taking contiguous sections from the coke plug and determining the metals concentration, the metals profile of the coke plug recovered from the coker could be determined. Since coke produced from each of the feeds has a known metals concentration, it is possible to determine from which feed the coke was derived and thus assess the flow pattern of each residue.

Figure 2 depicts the concentration profile of the metals in the coke. It is apparent that the coke formation is representative of plug flow through the coker. The top portion of the coke has a metals concentration of 425 ppm V and 125 ppm Ni, and the bottom portion 855 ppm V and 300 ppm Ni. These metals concentrations correspond to those of coke derived from the first residue followed by coke from the second residue.

This observation shows that feed entering the drum does not penetrate and mix with the material already in the coke drum. The carbonizing mass continues its reaction process with little or no co-mingling of the materials at the various intermediate stages that, ultimately lead to coke formation. Early (9) and recent (2) reports have shown that coking of residues involves a sequence of phase changes with different plasticity characteristics. Whittaker (2) found that, depending on the feed, the carbonizing mass retains plasticity up to 95% of the residence time at the coking temperature. Quenching experiments, Table I, show that the carbonization progresses continuously from the entrance of the feed and that the carbonizing mass would have the plasticity required for flow at the coking temperature.

Formation of Products. The rate of conversion of feed into products was determined in terms of the rate of formation of volatiles, gas and liquid products, and by difference the non-volatiles. The gaseous product includes C_1-C_4 hydrocarbons and the liquid $C_5-1000^\circ F$. Gas rates were obtained from the composition and volume of the gas generated during each experiment. Similarly, the rate of liquid product was obtained by determining the weight of liquid product condensed at room temperature for each coking experiment.

It was found that, at the temperatures studied, volatiles formed at a constant rate as long as feed is introduced into the coker; upon stopping the feed, however, the rate drops (Figure 3). Similarly the rate behavior of gas formation was also observed (Figure 4).

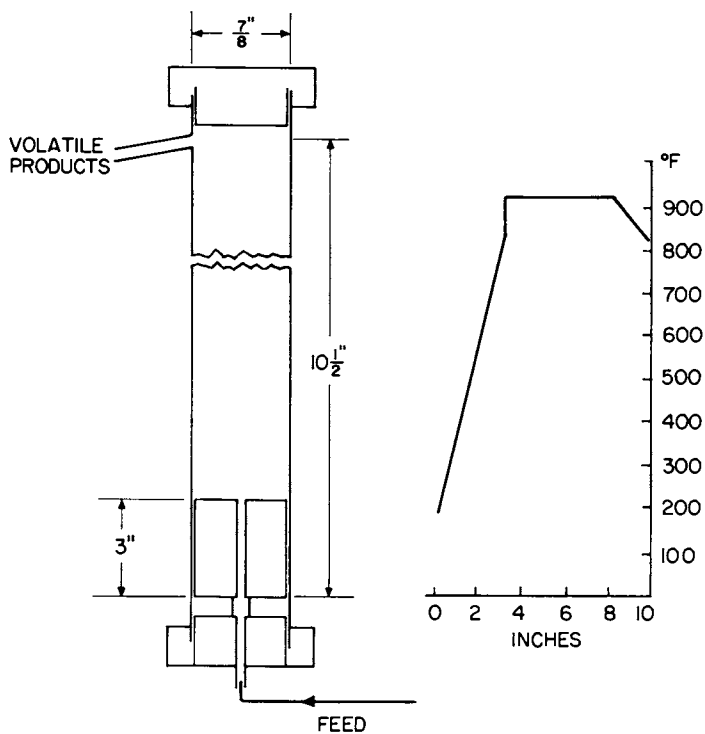


Figure 1. Experimental coker drum and typical temperature profile.

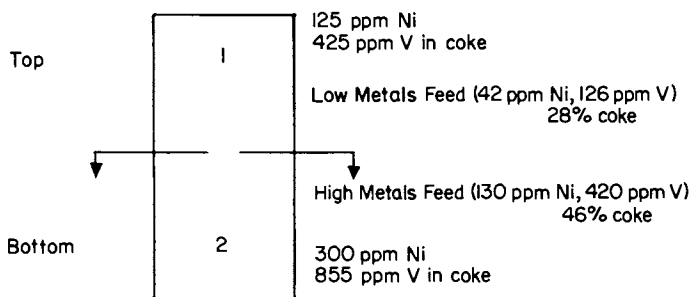


Figure 2. Consecutive coking of two residues with different metal content. Key: low metals, 90 cm³; and high metals, 50 cm³. Conditions: temperature, 915°F; pressure, atmospheric; and steam, 2% by weight.

Table I
Toluene Solubles Determined for a
Quenched Coking Reaction in a Continuous Coker

Temperature: 915°F
 Pressure: atmospheric
 Steam: 2% by weight
 Operation time, min: 320

a. Coke Plug	Approximate Position in Drum, in.	% of Total "Coke"	Toluene Soluble % wt.	Approximate "Residence" Time, min.
Section 1	0-1/4	4	35	3-12
Section 2	1/4-1 1/4	24	5	12-80
Section 3	1 1/4-4 1/2	56	<1	80-320
Section 4	4 1/2	16	<1	

b. Solubility of Vacuum Residue and Dry Coke in Toluene

	% Wt.
Vacuum Residue	100
Dry Coke	<1

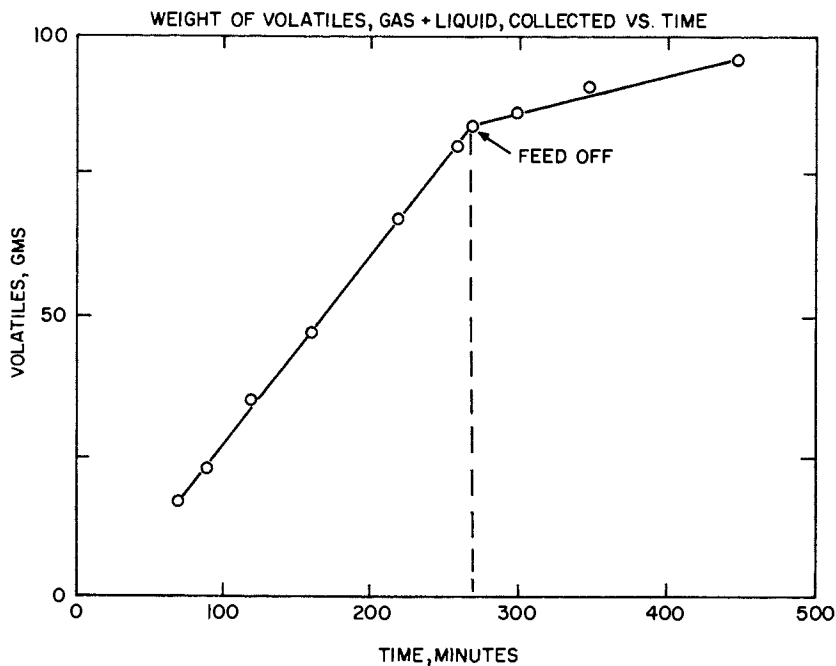


Figure 3. Coking of a vacuum residue at 1035°F.

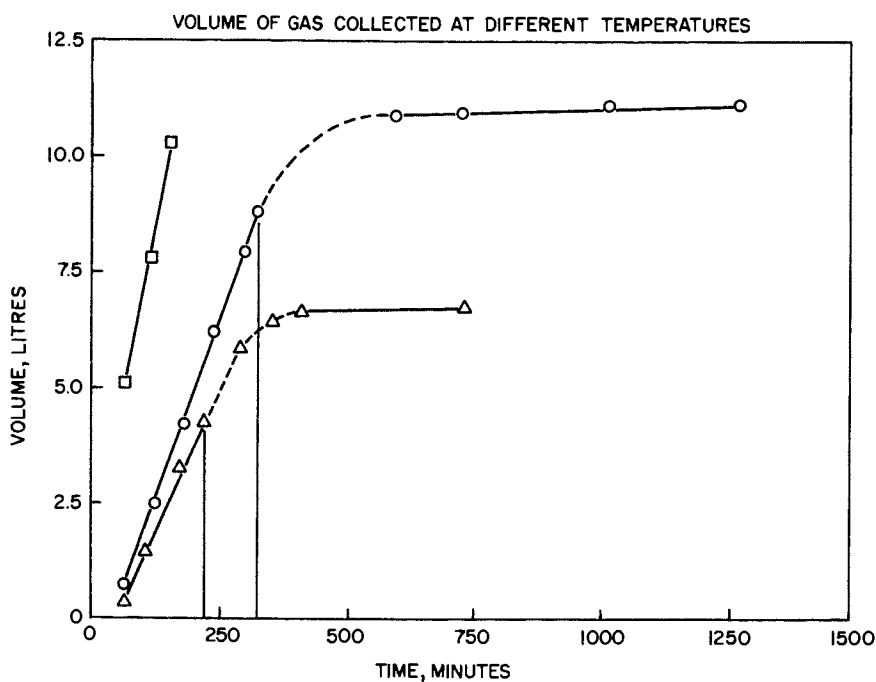
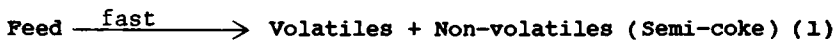


Figure 4. Coking of a vacuum residue at 1035°F (□), 915°F (○), and 835°F (△).

The above observations suggest that volatiles are formed at two rates; an initial fast rate (R_f) and a final slow rate (R_s). This indicates that the conversion of feed into coke takes place in two gross steps: First a fast conversion of feed into a volatile product, gas and liquid, and a non-volatile product, semi-coke; secondly, a slower conversion of the non-volatiles into more volatiles and, ultimately, coke, equations 1 and 2.



In a delayed coking process only the volatiles are removed while feed is continuously added to the carbonizing mass. Both the fast and slow reactions are consecutive for the incremental feed and concurrent with the material already in the coker which is in the process of coking. Thus, when the coker is being fed the amount of volatile products measured is the sum of the products produced by the fast reaction and by the slow reaction. After the feed is stopped and the rate drops, another constant but slow rate of product formation is observed. From the calculated slow rate of product formation R_s , the proportion contributed by the slow reaction during conventional operation could be backed-out and the rate of the fast reaction, alone, calculated.

Table II shows the product yield for coking a vacuum residue at 3 temperatures and the percent of gas and liquid produced by the slow and fast reactions, respectively. Coking at 835°F gives proportionately more liquid in the total volatiles as a result of the slow reaction than at 915°F and 1035°F. The data available are insufficient to determine an overall rate constant for the process, equation 3.



However, based on the model proposed the relative rates of the fast and slow reactions, R_f/R_s , may be derived. These are 5.4, 10.9 and 8.9 for 835°F, 915°F, and 1035°F respectively, Table II.

At 1035°F a considerable increase in the yield of gas was observed. This is the result of secondary cracking of liquid product formed during the coking process which results in a reduced yield of liquid and a higher proportion of the gas component in the volatiles. From the relationships between the products it is possible to calculate selectivities for the fast and slow reactions, Table III. A pictorial representation of these data is

Table II
 Yields of Gas and Liquids Products and
 Their Rates of Formation for the Coking
 of Vacuum Residue at Different Temperatures

Temperature, °F	835	915	1035
Gas Collected, %wt			
Reaction 1, fast	1.68	4.06	11.32
Reaction 2, slow	<u>4.32</u>	<u>2.94</u>	<u>7.68</u>
	6.00	7.00	19.00
Liquid Collected, %wt			
Reaction 1, fast	45.63	56.81	52.66
Reaction 2, slow	<u>15.37</u>	<u>8.19</u>	<u>6.34</u>
	61.00	65.00	59.00
Volatiles* Collected, %wt			
Reaction 1, fast	47.31	60.87	63.98
Reaction 2, slow	<u>19.69</u>	<u>11.13</u>	<u>14.02</u>
	67.00	72.00	78.00
Rates of Formation, 10 ² x gm/min			
Reaction 1, R _f	23.7	30.4	32.0
Reaction 2, R _g	4.4	2.8	3.6
Reaction rate ratio, R _f /R _g	5.4	10.9	8.9

*Volatiles: gas and liquid combined.

Table III
Selectivities for Gas and Liquid Products for the Coking
of a Vacuum Residue at Different Temperatures

Temp., °F	Coking Reaction	% wt.	Selectivity, %		
			gas	liquid	"semi-coke" or coke
835	Overall	100.0	6.0	61.0	33.0
	Fast	47.3	3.6	96.4	-
	Slow	52.7	8.2	29.2	62.6
915	Overall	100.0	7.0	65.0	28.0
	Fast	60.9	6.7	93.3	-
	Slow	39.1	7.5	20.9	71.6
1035	Overall	100.0	19.0	59.0	22.0
	Fast	64.0	17.7	82.3	-
	Slow	36.0	21.3	17.6	61.1

shown in Figure 5 and the overall coking yield in Figure 6. As an example, at 915°F, in the first stage, the feed is converted into about 4% gas, 57% liquid (61% volatiles) and 39% solid. In the second stage, the 39% solid formed in the first stage is further converted to about 7% gas, 21% liquid and 72% coke. These data are summarized as overall coking yields, 7% gas, 65% liquid and 28% coke.

Overall Coking Model. From the tracer experiments, quenching and toluene solubility experiments, rates and product selectivities, the following model appears to describe the gross behavior of residue in a delayed coking process.

- a. Feed and steam enter an empty coke drum and the feed in part is deposited on the surface of the drum with the remainder falling to the bottom of the drum. The feed decomposes at a fast rate to give a volatile product and a carbonizing mass called semi-coke.
- b. As more feed and steam are pumped into the drum, accumulation of the carbonizing mass continues together with the generation of volatiles. The steam helps in stripping heavier liquid product from the carbonizing mass.
- c. Hot feed continues to enter the drum and pushes the non-volatile carbonizing mass upwards with little or no mixing. Concurrently semi-coke is further pyrolyzed by the action of the hot vapors and the steam. This decomposition takes place at a slower rate than that of the feed and also gives gaseous, liquid and solid products.
- d. Above the solid carbonizing mass a gradation of vapor density exists, with the least dense vapors nearest the top of the drum. Some of the more dense vapors could be converted to coke. Their contribution is, however, probably minimal; most of the vapors leave the coke drum to form the gaseous product and the coker liquid.

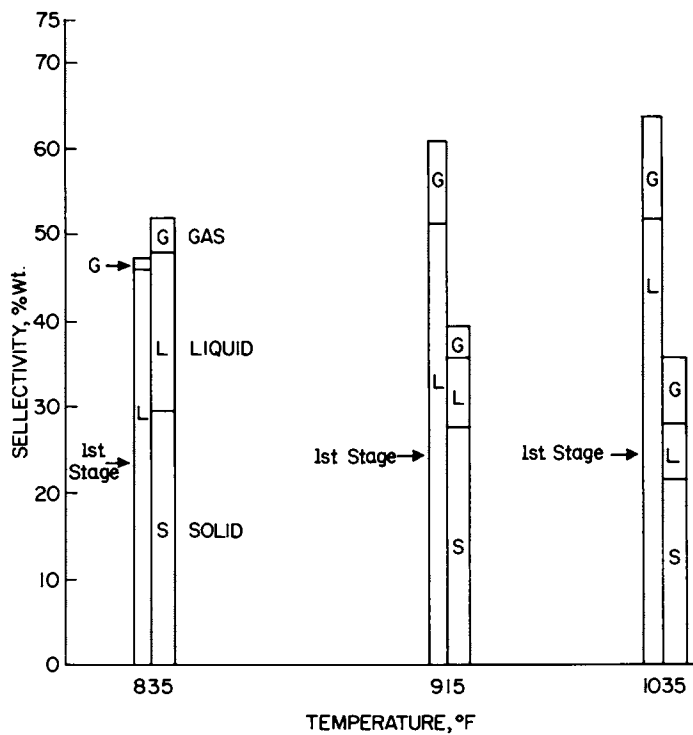


Figure 5. Product selectivity of the two stages in the coking of a vacuum residue at different temperatures.

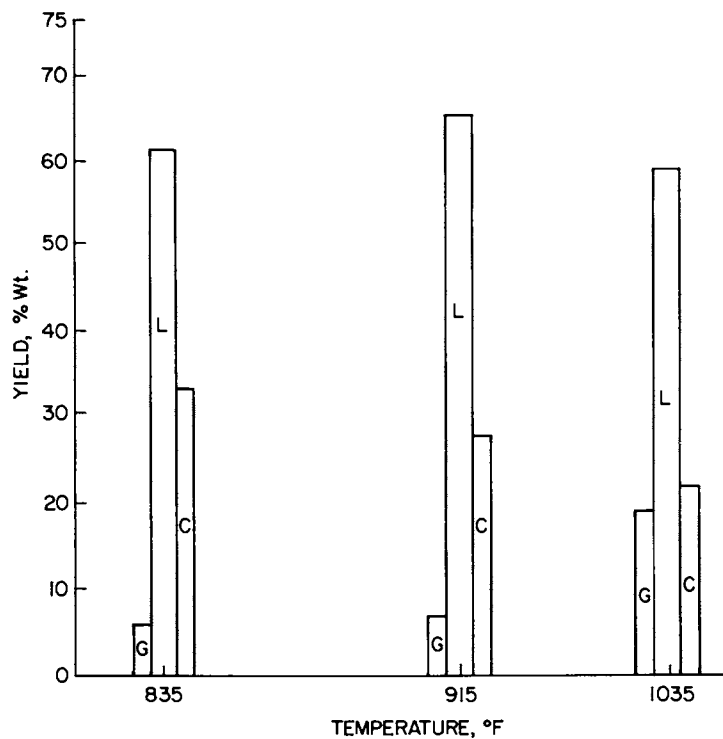


Figure 6. Overall product yields for coking a vacuum residue at different temperatures. Key: G, gas; L, liquid; and C, coke.

Literature Cited

1. Singer, L. S., J. Chim. Phys. Special Vol. 1969, April, p. 21.
2. Whittaker, M. P. and Grindstaff, L. I., Carbon 1972, 10, 165.
3. Kabak, H. N., Ivanov, S. K. and Anghelova, G. K., Dokl. Bolg. Akad. Nauk, 1978, 31, No. 9, 1135, Levinter, M. E., Medvedeva, M. I., Panchenkov, G. M., and Agpov, G. I., Khimiya i Tekhnologiya Topliv i Masel, 1966, No. 11, 25.
4. Valyavin, G. G., Fryazinov, V. V., Gimaev, R. N., Syunyaev, Z. I., Vyatkin, Yu. L., and Mulyukov, Sh. F., Chemistry and Technology of Fuels and Oils, 1979, 15, No. 7-8, 562.
5. Ozaki, H., Murakami, T., and Yamane, M., Fifth International Carbon Graphite Conference, London 1978, p. 205.
6. Cantrell, A., Oil and Gas J., 1982, March 22, p. 128.
7. Hayashitani, M., Bennison, D. W., Donnelly, J. K. and Moore, R. G., Oil Sands, 1977, 233.
8. Werstler, C. E., Niederstadt, R. J., and Lutz, H. A., Oil and Gas J., 1954, August 9, p. 98.
9. Berry, A. and Edgewood-Johnstone, R., I. E. Chem. 1944, 1140.

RECEIVED June 28, 1982.

INDEX

- A**
- Abrasion 61, 63
- Acetone, carbon deposition,
sulfiding effects 226*t*
- Acetone, heterogeneous
decomposition 223–238
- Acetone decomposition
mechanism 236
- by niobium, stainless steel, sulfur
effects 230*t*
- on triiron tetraoxide, sulfur effects.. 232*t*
- on triiron tetraoxide, thiophene
effects 231*t*
- reaction features 236
- Acetone deposition on stainless
steel, sulfiding 227
- Acetylene 123
- Alkali metal carbonates 76
- Alkaline earth oxides 76
- Alonized Incoloy 800 125
- Alumina, differential thermal
analysis 250*f*
- Aluminized Incoloy 800 153
- advantages 174
- coke deposit morphology 138
- coke deposits 168*f*, 170*f*
- coking results 125, 126
- coking/decoking sequence 143
- hydrogen sulfide treatment 155
- oxygen treatment 155
- steam treatment 155
- Aluminized Incoloy 800 coupons
hydrogen sulfide treatment 164
- inorganic gaseous treatment
157*f*–158*f*, 161*f*
- metal oxide formation 164
- reaction order 133
- surface composition 160
- Aluminized surfaces 151
- Aluminum 125
- Amorphous carbon 2
- Amorphous carbon film 258, 261
- Argon 60
- Auger electrons 11
- B**
- Barium oxide 76
- Benzene, carbon formation, hydrogen
effect 89–106
- Benzene, chemisorbed on nickel 101*f*
- Benzene on iron, heats of adsorption .. 104
- Benzene pyrolysis
carbon deposit morphology 112
- conditions 112
- surface carbon formation, mech-
anism 109–120
- Beta carbon film 272
- Bifunctional catalyst 249
- Bismuth 60
- Butane 69, 73
- Butene 23
- C**
- CAEM—*See* Controlled atmosphere
electron microscopy
- Carbide nucleation 219
- Carbide particle growth, mech-
anism 219
- Carbon, filamentous 2, 177
- growth mechanism 2, 7*f*
- Carbon, filamentous growth,
hydrogen effect 100
- Carbon, scanning Auger map 201
- Carbon, transport 5
- Carbon buildup 2
- Carbon deposit
characterization 8
- crystalline particles 207
- particulate development 207
- Carbon deposit morphology 193–221
- metal structure influences 217
- Carbon deposition
catalyst 191
- cementite formation 185
- gas residence time effect 96*f*
- mechanisms 194
- presence of carbide 185
- rate 119
- solution-precipitation processes 193–221
- supports 194
- Carbon deposition from acetone,
sulfiding effect 228*t*
- Carbon deposition on
copper 109–120, 115*f*
- Carbon deposition on iron
activation energy 103
- Arrhenius plot 94*f*
- mechanism 103–105
- rate comparison 105*f*

Carbon deposition on iron— <i>Continued</i>	
rate expression	103
SEM photograph	97f
Carbon deposition on iron foils	
benzene concentration effects	93–95
deposit structure	95, 96f
gas flow rate effect	95
hydrogen effect	95
temperature effect	93–95
Carbon deposition on iron-oxide foils	17f
Carbon deposition on nickel	
activation energy	102
carbon monoxide exposure	267, 268f
by carbon monoxide exposure	269f
by ethylene	258–267
forms	253
hydrogen effect	96f
morphology	270
reaction network	276
reaction order	101f
SEM photograph	97f
steam gasification	267
x-ray diffraction	98f
Carbon deposition on nickel foils	
benzene concentration effects	93
deposit structure	95, 96f
hydrogen effect	95
temperature effects	93
Carbon deposition on silica-alumina, rate constants	288t
Carbon deposition rate	
gas residence time effect	114f
hydrogen partial pressure effect	114f
temperature effect	112f
Carbon deposits via decomposition of ethylene, electron micrographs	266f
Carbon diffusion, activation energies	4t
Carbon dioxide	223
Carbon dissolution	205f
Carbon fibers	177
Carbon filament	3f
formation	6f
growth mechanism	90
problems with growth	273
spiral	6f
Carbon film, amorphous	258, 261
Carbon formation	
catalyst	184f
filamentous, macro-scale formation	16
filamentous, over iron surfaces	1–20
hydrogen:naphtha ratio effects	250f
iron and nickel-catalyzed	89–106
pressure effects	250f
solid phase catalyst	180
Carbon formation on nickel	
mechanism	100–103
rate comparison	105f
rate expression	100–103
Carbon gasification rates	276, 278–279t
apparent activation energies	280
interaction of graphite	280
Carbon monoxide	
disproportionation, iron-catalyzed	5
exposure to nickel catalysts	267
radiation-induced degradation	223
Carbon mound growth	201, 203f, 206f, 207
development	219
growth kinetics	207
particulates	210f
Carbon oxidation	
butane effect	69, 71f, 74f, 73
hydrogen effect	69, 71f–72f
oxygen transfer mechanism	83
temperature effect	63
water vapor partial pressure effect	63
Carbon oxide, formation	50, 56
Carbon precipitate, lateral spreading	204f
Carbon precipitation	201, 202f, 217
Carbon reprecipitation	205f
Carbonaceous deposits	
CAEM	14
formation	9f
Mössbauer spectroscopy	14
Carbonyl sulfide	232t, 235
Carbon–water vapor reaction, activation energy	83
Catalyst, carbon diffusion	2
Catalytic reforming of naphtha, purpose	239
Cementite	184f, 191
Cesium	76
Channeling	76
Chemical vapor deposition	
of silica	27
Chemisorbed carbon	276
Chromium	24, 57, 84, 125, 173
Chromium(III) oxide	
carbon deposition	227
sulfiding effects	229t
gas phase poisons	227, 223, 234
sulfiding	227
sulfur poisoning	233
surface area	225t
Clean fuels, production	283
Cobalt	76
Coke	
effect on hydrogenolysis	249
filamentous, growth and initiation mechanism	177–191
metals in, concentration profile	298

- Coke—*Continued*
 reaction with steam on solids 283–293
 Coke content, measurement 240
 Coke deposit 39*f*, 41*f*
 bulk metals concentrations 24
 filamentous 42*f*
 oxidation rates 85*t*
 removal 141–143
 structure effect 64*f*
 Coke deposit oxidation 67*f*–68*f*
 enhancement by inorganic
 catalysts 59–87
 in water vapor 61
 Coke deposition
 coke structure 38
 effect of cracking times 38
 measurement 34
 procedure 285
 Coke deposition on alumina, steam
 gasification 293*f*
 Coke deposition on impregnated
 silica–alumina, kinetics of
 steam gasification 289*f*
 Coke deposition on montmorillonite,
 kinetics of steam gasification 293*f*
 Coke deposition on Pt/Al₂O₃ 251
 Coke deposition on silica–alumina
 activation energy 286
 gasification kinetics 286
 kinetics of steam gasification 287*f*
 Coke deposition on stainless steel 123–148
 Coke deposition on Vycor surfaces
 123–148
 Coke effects 23
 Coke formation
 acetylene 127
 after coking/decoking 144
 from carbon monoxide 223
 catalysts 26, 30, 56
 decoking effect 34
 edge phenomena effect 138
 factors affecting the rate 151
 geometrical effect 138, 140–141
 heterogeneities effect 138
 H₂:hydrocarbon ratio effect 239–252
 hydrogen partial pressure effect 127
 inhibition 23–42
 α-iron–cementite equilibria 180
 iron–iron oxide–iron carbide–gas
 equilibria 182*f*
 α-iron–wustite equilibria 180
 nature 245
 preoxidized quartz reactor 54*f*
 preoxidized steel reactor 53*f*
 prerduced steel reactor 52*f*, 53*f*
 pressure effect 239–252
 procedure 285
 quenched coking 300*t*
 Coke formation—*Continued*
 quenching studies 297, 298
 reactor material effect 48
 role of the surface 172
 surface comparison 133
 surface effects 45
 surface passivation 26
 tracer studies 297, 298
 Coke formation in delayed coking 295–307
 Coke formation from ethylene 127
 Coke formation from methane 223
 Coke formation over naphtha
 reforming catalyst 239–252
 catalyst behavior, H₂:naphtha
 molar ratio effect 246*t*, 248*f*
 H₂:hydrocarbon ratio effect 245
 pressure effects 241*f*, 242–244
 standard test 241*f*
 Coke gasification 283–293
 activation energy 283
 impregnated metal effects 290
 reaction rate 286*t*
 reaction rate constant 283
 Coke gasification rate
 deposited metal oxides effect 288
 impregnated metals effect 288–291
 substrate effect 291–293
 Coke oxidation
 alkali metal salt effect 78*f*
 argon effect 62*f*
 barium oxide effect 79*f*
 cobalt effect 81*f*
 conditions 77*t*
 experimental measurement 73
 inorganic contaminants 73
 iron effect 80*f*
 nickel effect 81*f*
 strontium oxide effect 79*f*
 transition metal effectiveness 84
 water vapor effect 65*f*–66*f*
 Coke reaction with steam, im-
 pregnated metal effects 290
 Coke reaction with steam, reaction
 rates 286*t*
 Coke reforming, catalyst behavior
 and pressure effects 243*t*
 Coke skin, hard 40*f*
 Coke types 127
 Coked catalysts 284
 Coker drum 298*f*
 Coking 33*f*
 Coking, delayed
See also Delayed coking
 coke formation 295–307
 Coking, microbalance system 32*f*
 Coking/decoking sequences, coke
 formation after 144
 Coking model, overall 305

- Coking rate measurements 30
- Coking of residue, metal content
effect 299f
- Coking of vacuum residue 301f
product selectivity 306f
product yields 307f
selectivities for gas and liquid
products 304f
yields of gas and liquid products 303f
- Condensation mechanism 110, 112
- Controlled atmosphere electron
microscopy 13, 26, 194
description 8
- Copper 84
carbon deposition 115f
carbon formation 109-120
effect on coke gasification 288
- Copper foils, preparation 111
- Core type particles 215f
- Coupons, metal alloy 124
- Cracking, coking deposition 23
- Cracking temperature, gas com-
position effects 36f
- Cr₂O₃—*See* Chromium(III) oxide
- CVD—*See* Chemical vapor deposition
- D**
- Decoking 23, 143
- Delayed coking 296
coke formation 295-307
feed 296
process 302
- Delayed coking process, gross
behavior of residue 305
- 1,2-Dichloroethane 123
- Differential thermal analysis of
alumina 250f
- E**
- Electron microscopy, carbon deposit
characterization 257
- ESC—*See* Ethylene steam crackers
- ESCA—*See* X-ray photoelectron
spectroscopy
- Ethane, reaction with iron 19
- Ethylene 23, 123
- Ethylene steam cracker
butane effect 69
carbon deposits 224
coke formation 59-87
coke inhibition 34-38
coke structure 86
coke surface contamination 86
coke yields 37f
deposit oxidation conditions 75f
deposit structure effect 61, 63
- Ethylene steam cracker—*Continued*
gasification 86
gas flow rate effect 61
hydrogen effect 69
inhibition of coke formation 23-42
inorganic contaminants 73
oxidation of deposit 59-87
oxidized deposit, surface
topography 82f
plant materials investigation 24-26
presence of metals 26
sample containment 61
silica coated tubes 34-38
surface contamination 60
surface passivation 26, 27
See also Surface passivation
temperature effect 63
water vapor effect 63
water vapor oxidation 86
- Extrusion filaments 5
- F**
- Fe₃C—*See* Iron carbide and Cementite
- Fe₃O₄—*See* Triiron tetraoxide 225
- Ferromagnetic metals, carbon
formation 1
- Filament growth, activation energies 4f
- Filamentary growth 219, 220
- Filamentous carbon 2, 177, 193
delta states 261
extrusion mode growth 7f
formation 2
formation studies 11
growth center 178
growth inhibition 2, 5
growth mechanism, extrusion
mode 5, 7f
spiral filaments 5
- Filamentous carbon formation
CAEM 13
macro-scale formation 16
Mössbauer spectroscopy 10
over iron surfaces 1-20
temperature effects 13
- Filamentous coke
catalyst 191
growth
apparatus 179f
composition 186f
reactor support 181f
growth and initiation
mechanism 177-191
surface effects 185 191
- Foil pretreatment 48

G

Gasification, influence of inorganic contaminants	73
Gas-phase carbon formation	110
Gas-phase reactions, homogenous	124
Gas-phase poisons	
carbonly sulfide	235
hydrogen sulfide	235
sulfur dioxide	235
thiophene	233
Gold	225
Graphite	280
crystal	10
iron deposition	10
nickel-catalyzed gasification, rates	281
spectroscopic	284
Graphite platelet deposit	5
Graphitic laminar films	193

H

Hard coke skin	40f
Heavy oil, catalytic processing	284
Helium	153
Heterogeneous metal-catalyzed reactions	124
High activity substrates	291
High alloy steel	24
Homogenous gas-phase reactions	124
H ₂ S—See Hydrogen sulfide	
Hydrocarbon-metal reaction, carbon atom formation	90
Hydrocarbon surface film, polymeric	273
Hydrocarbon synthesis, on nickel surfaces	277f
Hydrocracking, comparison with hydrogenolysis	249
Hydrogen:hydrocarbon ratio effect	239–252
Hydrogen sulfide	151, 164, 228, 232t, 235
effect on acetone decomposition	230t
effect on chromium(III) oxide	229t
Hydrogenolysis, coke effects	249
Hydrogenolysis, comparison with hydrocracking	249

I

Impregnated silica-alumina, coke deposits on, kinetics of steam gasification	289f
In situ scanning electron microscopy, benefits	194
Incoloy 800	24, 25f, 152
coking results	125, 126

Incoloy 800—Continued

aluminized, hydrogen sulfide treatment	155
aluminized, oxygen treatment	155
aluminized, steam treatment	155
hydrogen sulfide treatment	155
oxygen treatment	155
steam treatment	155
inorganic gaseous treatments	156f, 159f
metal oxide formation	164
polished aluminized, coke deposits	171f
polished, inorganic gaseous treatment	156f
reaction order	133
surface composition	160
surface composition after treatment	162f
titanium content	164
Incoloy 800, aluminized	153
advantages	174
coke deposit morphology	138
coke deposits	168f, 170f
coking/decoking sequence	143
hydrogen sulfide treatment	164
inorganic gaseous treatment	157f–158f, 161f
metal oxide formation	164
surface composition	160
Incoloy 800 chromium contact	164
Incoloy 800 tube, uncoated	40f
Inorganic contaminants	73
Ion etching	197, 213f
Iron	24, 56, 125, 173, 194
effect on coke gasification	288
metallic	19
Iron, carbon formation	1
activation energy	103
mechanism	103–105
rate expression	103
Iron carbide	10, 14, 16
Iron carbide as catalyst	19
Iron-carbon phase diagram	198f
α -Iron-cementite equilibria, coke formation	180
Iron contamination	207
Iron foil	
metallic, Mössbauer spectra	15f
structure	200f
surface preparation	199f
Iron foils, carbon deposition	
benzene concentration effect	93–95
deposit structure	95, 96f
gas flow rate effect	95
hydrogen effect	95
temperature effect	93–95
Iron levels, etching effects	211
Iron oxide	10, 18f, 76

Iron oxide— <i>Continued</i>			
identification	11		
production	16		
samples	11		
Iron surface, pretreatment			
with steam	16		
α -Iron-wüstite equilibria,			
coke formation	180		
			K
Ketone decomposition, poisoning	224		
			L
Lead	76		
Lithium	76		
Low activity substrates	291		
			M
Manganese	57, 84		
Mass transfer limitations	90		
Metal-catalyzed reactions,			
heterogeneous	124		
Metal alloy coupons	124		
coke deposits	164		
coke thickness	167		
coking rates	165 <i>t</i>		
filamentous coke formation	169		
morphology change	155		
polishing	152		
pretreatment effect	164		
surface composition	162		
surface morphology	153		
Metal foil, surface preparation	197		
Metallic iron	19		
Mössbauer spectra	15 <i>f</i>		
Metals in coke, concentration			
profile	298		
Metal-support interaction	90		
Methane, filament growth	220		
Methane radiation-induced			
degradation	223		
Microbalance	47 <i>f</i>		
Microbalance reactor	91, 92 <i>f</i>		
Molybdenum	48		
Monticular growth— <i>See</i> Mound			
growth			
Montmorillonite, coke deposits on,			
kinetics of steam gasification	293 <i>f</i>		
Mössbauer spectroscopy	10		
Mössbauer spectroscopy experiments,			
carbonaceous deposits	14		
Mound growth	193		
carbon	201, 203 <i>f</i> , 206 <i>f</i> , 207		
development	219		
growth kinetics	207		
particulates	210 <i>f</i>		
Mounting systems	195		
			N
Naphtha	23		
catalytic reforming, purpose	239		
properties	240		
Naphtha reforming catalyst	239–252		
Naphtha reforming catalyst, coke			
formation over			
catalyst behavior, H ₂ :naphtha			
molar ratio effect	247 <i>t</i> , 248 <i>f</i>		
pressure effect	241 <i>f</i> , 242–244		
standard test	241 <i>f</i>		
Nickel-catalyzed gasification of			
graphite, rates	281		
Nickel	56, 76, 173, 194		
carbon deposits on, via ethylene	258–267		
carbon formation			
mechanism	100–103		
rate expression	100–103		
effect on coke gasification	288		
Nickel catalyst	257		
carbon deposits on			
carbon monoxide exposure	267		
ethylene exposure	270		
morphology	270		
steam gasification	267		
properties	257 <i>t</i>		
surface carbon reactivity	253–281		
temperature-programmed			
surface reaction	253–281		
deactivation	281		
Nickel foils, carbon deposition			
benzene concentration effects	93		
deposit structure	95, 96 <i>f</i>		
gas flow rate effect	95		
hydrogen effect	95		
temperature effects	93		
Nickel reactor, preoxidation effects	50		
Nickel–niobium stabilized stainless			
steel	223		
Nickel sulfides	151		
Niobium stainless steel, acetone			
decomposition by, sulfur effects	230 <i>t</i>		
Niobium stainless steel, sulfur			
poisoning	233, 235		
			O
Octane number	240		
Olefin, sources	45		
Overall coking model	305		
Oxidation–reduction cycle	83		
Oxygen	153		
Oxygen transfer mechanisms	83		
			P
Particulate deposit	212 <i>f</i>		
core particles	211		
crystalline particles	207		
filamentary deposits	211		

- Particulate deposit—*Continued*
 shell particles 211
 Particulate growth 219, 220
 Petroleum chemicals operation 23
 Phase diagram 180
 iron-carbon 198f
 Platelet carbon 272
 Platinum 5
 Platinum-alumina catalyst,
 coke deposition 251
 Poisons 224
 Polished aluminized Incoloy 800,
 coke deposits 171f
 Polished Incoloy 800, inorganic
 gaseous treatment 156f
 Polymeric hydrocarbon surface film .. 273
 Pore blockage 90
 Potassium 76
 Preoxidation 30, 48, 56
 Prereduction 48
 Presulfiding treatments 26
 Product formation, rate of
 conversion from feed 298
 Propane steam cracking 45-57
 apparatus 47f
 coke formation 49f, 53f
 preoxidized quartz reactor 54f
 preoxidized steel reactor 53f-54f
 prereduced steel reactor 51f-52f
 prereduced vs. preoxidized
 quartz reactor with steel 49f
 Propylene 23
 Pseudocrystallites 290
 Pyrolysis, effect of inorganic gases .. 151-175
 Pyrolysis, surface phenomena
 during 151-175
 Pyrolysis reactor, oxidation 151
 Pyrolytic carbon 272
- Q**
- Quartz reactor, coke formation 48
 Quenched coking 300t
- R**
- Radiant coils 24
 Reforming reaction network on
 nickel surfaces 277f
 Rough surfaces 147
 Roughness 155
 minimization in analysis 197
 Rubidium 76
- S**
- Salts 61
 Scanning Auger map, carbon 201
 Scanning electron micrograph, silica
 coated steel 31f
 Scanning electron microscopy, carbon
 deposit morphology 193-221
 Semi-coke 302
 Shell thickness 211
 Shell type particles 215f
 Silica-alumina, coke deposits on
 activation energy 286
 gasification kinetics 286
 kinetics of steam gasification 287f
 Silica-alumina, impregnated, coke
 deposits on, kinetics of
 steam gasification 289f
 Silica-rich surfaces 151
 Silica coating 34
 of steel alloys 27-33
 Silica films 30
 Silicon-rich surfaces 151
 Silver 84
 Sodium 76
 Specimen, mounting systems 195
 Spectroscopic graphite 284
 coke deposition 123-148
 nickel-niobium stabilized 223
 niobium, sulfur poisoning 233, 235
 removal of coke deposits 123-148
 Stainless steel surfaces 151
 Steam 59
 Steam cracking
 coke yields 37f
 coking deposition 23
 ethylene, inhibiting coke
 formation 23-42
 Steam cracking of propane,
 surface effect 45-57
 Steam reaction with coke
 impregnated metal effects 290
 reaction rates 286t
 on solids 283-293
 Steam reforming, carbon oxide
 formation 56
 Steel, high alloy 24
 Steel, silica-coated 31f
 Steel alloy, silica coating 27-33
 Steel alloy, steam treated 28f
 Steel coupons, silica coating,
 apparatus 29f
 Steel foils, preoxidation 48
 Steel reactor
 carbon oxide formation 50
 preoxidation effects 50
 quartz liner effects 50
 Strontium oxide 76
 Substrate, high activity 291
 Substrate, low activity 291
 Sulfide surface layer 224
 Sulfided stainless steel, carbon
 deposition 227
 Sulfided surfaces, coke formation 169
 Sulfiding 227

Sulfur dioxide	232t, 235	Transmission electron microscopy,	
effect on acetone decomposition	230t	benefits	194
Sulfur poisoning	223-238	Triiron tetraoxide	
thiophene	233	acetone decomposition on	
Surface carbon, reactivity on		sulfur effects	232t
nickel catalyst	253-281	thiophene effects	231t
Surface carbon, temperature-		carbon deposition	227
programmed surface reaction	253-281	from acetone	228t
Surface carbon formation,		gas phase poisons	227, 233, 234
mechanism	109-120	sulfiding	227
Surface contamination, with		sulfur poisoning	233, 235
inorganic salts	60	surface area	225t
Surface corrosion	147	Tubular reactor, quartz	46
Surface metal carburization	147	Tubular reactor, stainless steel	46
Surface passivation			
high temperature team		V	
pretreatments	26	Vacuum residue, coking	
preoxidation	26	product selectivity	306f
presulfiding treatments	26	product yields	307f
Surface phenomena during		selectivities for gas and liquid	
pyrolysis	151-175	products	304t
Surface roughness	155	yields of gas and liquid products	303t
Surface sulfiding	151	Vanadium, effect on coke gasification	288
T		Vinyl chloride	123
Temperature run-away	284	Volatile formation	302
Temperature-programmed surface		Volatiles	296
reaction	253-281	Vycor	152
carbon deposits by		Vycor glass, coking results	125, 126
ethylene	259f, 263f, 264f, 270	Vycor glass, rate of carbon formation	138
carbon monoxide exposure	267t	Vycor reactor	124
ethylene exposure	267t	Vycor surfaces, coke deposition	
microreactor system	254	and removal	123-148
system	255f	Vycor tubes, filamentous	
Tetraethoxysilane	34	coke formation	169
Thermal annealing	197	X	
Thiophene	225, 229t, 230t	X-ray photoelectron spectroscopy,	
Titanium	24, 125, 140	steam treated steel alloys	27
Toluene solubles	300t	Z	
TSPSR— <i>See</i> Temperature-programmed		Zirconium	60
surface reaction			
Tracer studies	298		
Transition metals	177		

Jacket design by Martha Sewall.

Indexing and production by Deborah Corson and Anne Bigler

Elements typeset by Service Composition Co., Baltimore, MD

Printed and bound by Maple Press Co., York, PA